

An Experimental Study of Shale-Water Interactions for Applications in
Hydraulic Fracturing

by

Mingxiang Xu

A thesis submitted in partial fulfillment of the requirements for the degree of

Doctor of Philosophy

in

Petroleum Engineering

Department of Civil & Environmental Engineering
University of Alberta

© Mingxiang Xu, 2018

Abstract

The increasing demand for fossil energy and the decreasing trend of conventional resources have shifted the focus of industry towards unconventional resources including shale gas, shale oil, tight gas, tight oil, and coalbed methane. Recent advances in stimulation techniques, including horizontal drilling and multi-stage hydraulic fracturing have led to economic production of previously inaccessible hydrocarbon trapped in ultra-low permeability reservoirs. During a hydraulic fracturing operation, fracturing fluids are pumped into the well to create fractures, which produces a pathway for hydrocarbon flow towards the wellbore. However, a significant fraction of injected fracturing fluid leaks off into natural fractures and shale matrix, which causes the reservoir damage and environmental concerns.

Recent experiments show that gas shales which are strongly oil wet based on contact angle measurements might have strong water uptake during imbibition. Clay hydration, microfracture induction, lamination, and osmotic effect may be collectively responsible for the strong water uptake. However, the previous measurements are not sufficient to isolate the above factors nor to explain why the bulk of shale samples can hardly imbibe the oil which completely spreads on their surface. This study aims at interpretation of low flowback efficiency by conducting a series of shale-water interaction experiments. The objective of this research is to investigate the reasons behind low water recovery in flowback process and quantify the impacts of interactions between the lost water and reservoir rock.

Extensive imbibition experiments are performed to investigate shale-water interactions at different conditions. Effects of pore network connectivity, salinity of imbibing brine, clay swelling, and air blockage in shale samples are investigated through measuring the imbibed mass, induced strain

and stress during imbibition process, and concentrations of dissolved oxygen and ions in the imbibing water. The hypothesis is then tested by 1) measuring imbibed mass of water and oil in crushed shale samples and intact shale samples, 2) measuring soluble/leachable ions in shale samples, 3) measuring hydration-induced strain and stress during water imbibition, 4) conducting imbibition experiments in degassed and oxic conditions, and 5) SEM and EDS imaging of organic and inorganic pores in shale.

The comparative study of water imbibition into crushed shale packs and intact shale samples suggests that the connected pore network of the intact samples is water wet while the majority of rock including poorly connected pores is oil wet. In contrast to the artificial pores of crushed rock, the pores of intact rock are already wetted by a film of water and/or covered by precipitated salt. This makes the pores of intact rock prefer to be water-wet than oil-wet. Furthermore, the precipitated salt provides an additional force for water uptake through osmotic effect.

By calculating the characteristic thickness of electrostatic double layer (also known as Debye length, κ^{-1}) around the charged shale powders, it shows that the imbibition rate is positively correlated to the κ^{-1} values. Electrostatic interactions are part of the disjoining pressure which is not considered in the Young-Laplace equation. A higher κ^{-1} value leads to a higher disjoining pressure value. In turn, this forms a larger hydration shell around the shale powder surface and increases the imbibition rate.

The induced strain and stress during water imbibition show a strong correlation among imbibed water mass, induced strain and stress, and clay content of the shale samples. Increasing clay content increases the induced strain and stress caused by water imbibition. For unconfined samples, water imbibition leads to significant pore volume enhancement (up to 0.72% of sample total volume).

For partially confined samples, water imbibition induces a relatively low expansive stress. This induced stress can be described as a logarithmic function of confining pressure.

Comparative study of water imbibition shows that the imbibition rate and imbibed volume are higher under degassed condition than under oxic condition. These differences are mainly due to the enhanced dissolution of air into water in the shale pore network during water imbibition under degassed conditions. This dissolution will consequently increase the relative permeability of water. The results also suggest that pyrite oxidation from dissolved oxygen produces sulfate ions, iron ions, and iron-compound precipitates. This is supported by SEM/EDS images which show abundant pores in the vicinity of pyrite minerals.

Preface

All or parts of Chapters 2 to 4 have been published as peer reviewed journal papers. Chapter 2 has been published as “Advances in understanding wettability of gas shales. *Energy & Fuels*, 2014, 28(7), 4362-4375.” Chapter 3 has been published as “Effect of electrostatic interactions on water uptake of gas shales: the interplay of solution ionic strength and electrostatic double layer. *Energy & Fuels*, 2016, 30(2), 992-1001.” Chapter 5 has been published as “Effects of Dissolved Oxygen on Water Imbibition in Gas Shales. *Energy & Fuels*, 2018, 32(4), 4695-4704.” The contents of Chapter 5 have been submitted for publication in *Journal of Petroleum Science and Engineering* in August 2018. The reference style from the Society of Petroleum Engineers was used in this study.

I was responsible for experimental design, running the experiments, model development, writing and editing the papers. My co-authors were responsible for providing relevant data from their respective companies, helping me with the experiments, providing useful comments and discussions on field practices, and reviewing the manuscript drafts.

Dedication

To my dearest parents, Hui Xu and Ming Wan

To my beloved wife, Min Yue

To my grandmother in heaven, Yuqing Liang

For their unconditional love, endless support and encouragement.

Acknowledgements

I would like to express my sincere appreciation to my supervisor, Dr. Hassan Dehghanpour for giving me the opportunity to pursue this degree, having faith in me, and supporting me throughout this study. It is impossible to complete this dissertation without his patient encouragement, invaluable advice and insightful guidance.

I would like to thank my supervisory committee members, Dr. David Potter and Dr. Japan Trivedi for their guidance and technical advices through this work. I am also grateful to Dr. Derek Apel, Dr. Lijun Deng and Dr. Rouzbeh Ghanbarnezhad Moghanloo for being my examining members.

I would also like to express my gratitude to Mr. Doug Beringer for the informative discussions and valuable suggestions. I am very thankful to our technician, Mr. Todd Kinnee, for providing technical assistance in lab and helping me out with my experiments.

I gratefully acknowledge the Natural Sciences and Engineering Research Council of Canada (NSERC) and Nexen Energy ULC for providing the research funding for this study. Special thanks British Columbia Oil and Gas Commission, INPEX Gas British Columbia Ltd and Nexen Energy ULC for providing shale samples.

I would also like to thank my colleagues (Mojtaba Binazadeh, Obinna Ezulike, Ashkan Zolfaghari Sharak, Ali Habibi, Yingkun Fu, Yanmin Xu, Mahmood Yassin, Sara Eghbali, Tamer Moussa, Lin Yuan, Son Tran, Khan Athar, Maryam Eghbalvala, Serge Pegov, Ebrahim Ghanbari, Mahdie Mojarad, Hamidreza Yarveicy, Taregh Soleiman Asl, Qing Lan) for their insightful contributions and fruitful discussions.

Finally, I would like to express my appreciation to all those who helped and inspired with me throughout my research.

Table of Contents

Abstract.....	ii
Preface.....	v
Dedication	vi
Acknowledgements	vii
Table of Contents	viii
List of Tables	xiii
List of Figures.....	xv
Nomenclature	xxiii
Chapter 1: General Introduction	1
1.1 Overview.....	1
1.1.1 Unconventional Reservoirs	1
1.1.2 Drilling and Completion Process	5
1.1.3 Pore Network in Unconventional Reservoirs.....	9
1.1.4 Spontaneous Imbibition	12
1.2 Research Motivation	13
1.3 Research Objectives.....	13
1.4 Organization of Thesis	14
Chapter 2: Effect of Pore Connectivity on Water Uptake of Gas Shales.....	16
2.1 Introduction.....	16
2.2 Materials	18
2.3 Methodology.....	22
2.3.1 Set 1 (Co-current Imbibition of Kerosene and DI Water)	23

2.3.2	Set 2 (Counter-current Imbibition Experiments)	25
2.3.3	Set 3 (Spontaneous Imbibition of Brine)	26
2.3.4	Set 4 (Pore-scale Visualization).....	26
2.4	Results.....	26
2.4.1	Set 1.....	28
2.4.2	Set 2.....	28
2.4.3	Set 3.....	28
2.4.4	Set 4.....	30
2.5	Quantitative Interpretation of Imbibition Data	33
2.5.1	Modelling Imbibition Rate.....	33
2.5.2	Modelling Front Position	36
2.5.3	Dimensionless Time.....	39
2.6	Summary and Discussion.....	42
Chapter 3: Effect of Electrostatic Interactions on Water Uptake of Gas Shales: The Interplay of Solution Ionic Strength and Electrostatic Double Layer		44
3.1	Introduction.....	44
3.2	Theory.....	44
3.3	Materials and Methods.....	48
3.3.1	Shale Samples	48
3.3.2	Washing Shale Powder and Preparing Brine Solutions	48
3.3.3	Imbibition Experiments.....	51
3.3.4	Zeta Potential Analysis	52
3.4	Results and Discussions.....	53
3.4.1	Water and Brine Imbibition in Unwashed and Washed Powder	53

3.4.2	Zeta Potential Analysis of Shale Powder	55
3.4.3	Slope Analysis of Water and Brine Imbibition	55
3.4.4	Debye Length of the In-situ Formed Brines	57
3.5	Summary	60
Chapter 4:	Effects of Dissolved Oxygen on Water Uptake of Gas Shales.....	62
4.1	Introduction.....	62
4.2	Materials and Methods.....	63
4.2.1	Shale Samples	63
4.2.2	Imbibition Experiment	64
4.2.3	SEM-EDS Imaging	66
4.3	Results and Discussion	66
4.3.1	Imbibition Profiles	66
4.3.2	Dissolved Oxygen Profiles.....	68
4.3.3	Ion Concentration Profiles	71
4.3.4	SEM and EDS Images.....	78
4.4	Summary	80
Chapter 5:	Impact of Clay Swelling on Water Imbibition in Gas Shales	81
5.1	Introduction.....	81
5.2	Methodology	83
5.2.1	Set 1 (Spontaneous Imbibition Experiment).....	83
5.2.2	Set 2 (Induced Strain Measurement).....	84
5.2.3	Set 3 (Induced Stress Measurement).....	87
5.3	Materials	88
5.3.1	Fluids.....	88

5.3.2	Rock Sample	88
5.4	Results.....	92
5.4.1	Induced Strain during Water and Oil Imbibition	92
5.4.2	Induced Stress during Water Imbibition	96
5.4.3	Effects of Ion Concentrations on Induced Strain and Stress.....	97
5.5	Discussion.....	100
5.5.1	Water Imbibition Affected by Sample Expansion	100
5.5.2	Induced Strain/Stress versus Imbibed Water Mass.....	102
5.5.3	Induced Strain/Stress versus Clay Content of Shale.....	104
5.5.4	Induced Strain/Stress versus Ion Concentration of Imbibed Brine.....	105
5.6	Summary.....	107
Chapter 6:	Modelling of Water Uptake into Shales	109
6.1	Introduction.....	109
6.2	Experiments	112
6.2.1	Materials.....	112
6.2.2	Contact Angle Measurements.	113
6.2.3	Imbibition Experiments.....	113
6.2.4	Sample Expansion Measurements.	114
6.3	Experiments	115
6.3.1	Contact Angle	115
6.3.2	Imbibition.....	116
6.3.3	Expansion.....	117
6.4	Decoupling the Total Water Imbibition Profile	118
6.5	Decoupling the Imbibition and Adsorption	121

6.6	Summary	124
Chapter 7:	Conclusions and Recommendations for Future Work.....	125
7.1	Conclusions	125
7.1.1	Effect of Pore Network Connectivity.....	125
7.1.2	Effect of Salt Concentration.....	125
7.1.3	Effect of Dissolved Gas	126
7.1.4	Effect of Clay Swelling.....	126
7.2	Recommendations for Future Work.....	126
Bibliography		128
Appendix A:	Permeability Measurement	154
Appendix B:	Calculation of Average Pore Diameter	155
Appendix C:	Chemical Analysis of Precipitated Salts.....	156
Appendix D:	Oven Heating Process	158
Appendix E:	Effect of Heterogeneity on Expansion Behavior	160
Appendix F:	Mechanisms of Clay Swelling.....	161

List of Tables

Table 1-1. Typical chemical additives used in the fracturing fluids (Petrowiki, 2018).....	6
Table 2-1. Density, viscosity and surface tension of different fluids used for the imbibition experiments.	18
Table 2-2. Average mineral concentration (wt %) of the shale sections determined by XRD.	19
Table 2-3. Average TVD, matrix density determined by XRD data (ρ_{XRD}), matrix density after the Adjustment for TOC content (ρ), TOC, Length, Cross-Sectional Area, Pack Density, Porosity and Permeability of all the Samples Used in the Crushed-Shale Pack Experiments.....	19
Table 2-4. Mass, depth and geometry of the intact shale samples used in imbibition experiments.	20
Table 2-5. The values of water and oil contact angles, the R value defined by Eqs. (4) and obtained from Eqs. (5) (R_C), horizontal (R_H) and vertical (R_V) imbibition experiments. Subscripts o , w , a represent kerosene, water, air, respectively.	34
Table 3-1. Representative mineralogy of shale samples used in 1-D imbibition experiments measured by XRD.	48
Table 3-2. Ion concentration and ionic strength, I , of different brine solutions	50
Table 3-3. Zeta potential of the unwashed and washed HRB shale powder samples in DI water and brine	55
Table 3-4. Calculated capillary pressure at front saturation from imbibition slope	57
Table 4-1. Approximate depth, porosity, permeability and average rock mineralogy for shale samples.....	64
Table 5-1. The maximum and average values of clay content measured by XRD analysis of shale samples from different shale plays*	81
Table 5-2. Imbibition fluid, number of shale samples used in each set of experiment, and the parameters for the experimental measurements.....	83

Table 5-3. Approximate depth, porosity, and permeability of representative samples from each group. 89

Table 5-4. Mineral concentration (wt %) for a representative sample from each group determined by XRD analysis. 90

Table 5-5. Porosity of the HRB shale samples before and after 10 days of water imbibition... 101

Table 6-1. The dimensions and petrophysical data of shale samples used in 1-D imbibition experiments. The labels of “Water” and “Oil” stands for the samples are used for water and oil imbibition experiments. The label of “Exp” stands for the samples are used for sample expansion measurement. 112

Table 6-2. Representative mineralogy of shale samples used in 1-D imbibition experiments measured by XRD..... 113

Table 6-3. The original porosity before water imbibition, pore volume enhancement, porosity and porosity enhancement after 815 hours water imbibition..... 117

Table 6-4. Values of adsorption coefficient from analytical interpretation of imbibition experimental data..... 124

List of Figures

Figure 1-1. Comparative analysis of matrix permeability of various unconventional reservoirs (CSUR, 2018).	1
Figure 1-2. Geographical distribution of major unconventional reservoirs in North America (EIA, 2011). The approximate location of the Horn River Basin is highlighted and shown by the red circle.....	2
Figure 1-3. Natural gas production by type in China, Canada, and the United States in 2012 and the predicted production in 2040 (EIA, 2016).	3
Figure 1-4. Schematic stratigraphic cross-section of the Horn River basin and its adjacent Liard Basin (B. C. Oil & Gas Commission, 2014).....	4
Figure 1-5. Production history in the Horn River Basin from 2007 to 2013 (B. C. Oil & Gas Commission, 2014).	4
Figure 1-6. Schematic of cross-sectional view of a horizontal well (Northern Territory Department of Mines and Energy, 2018).....	6
Figure 1-7. Typical volumetric composition of a water-based fracturing fluid (Arthur et al., 2009). Data is collected at Fayetteville shale fracturing stimulation (GWPC and ALL Consulting, 2009).	7
Figure 1-8. Schematic of cross-sectional view of horizontal well and hydraulic fractures (zoomed-in area) drilled in an unconventional reservoir (Modified from NaturPhilosophie, 2014).	8
Figure 1-9. (a) Transverse and (b) longitudinal fracture propagation patterns in horizontal well relative to the minimum and maximum horizontal in-situ stress (Salah et al., 2016).	11
Figure 1-10. Scanning electron microscope images of (a) Montney tight sandstone sample (Yassin et al., 2016) and (b) Barnett shale sample (Sondergeld et al., 2010).	12
Figure 1-11. Schematics of (a) counter-current and (b) co-current imbibition. Blue and green colors represent the wetting and nonwetting phases, respectively. The arrow represents the direction of imbibition flow (Makhanov, 2013).....	13

Figure 2-1. The particles of shales from (a) FS, (b) M and (c) OP sections visualized using microscope. 22

Figure 2-2. A 25-cm-long crushed-shale pack used in the horizontal and vertical imbibition experiments. 22

Figure 2-3. The schematic illustration the set-up for horizontal experiments. The fluid is imbibed from left to the right and displaces the air in the crushed-shale pack. The air is collected in an inverted cylinder. 23

Figure 2-4. The water (left) and oil (right) imbibition front position at 4.5 hours (a, b), 12.5 hours (c, d), 30.5 hours (e) and 25.5 hours (f) for Muskwa crushed sample packs. 24

Figure 2-5. The front position for vertical imbibition of water (left) and kerosene (right) into Muskwa crushed-shale packs (a) after 3.5 hours, (b) after 9 hours, (c) after 69 hours. 25

Figure 2-6. Comparison between imbibition rate of DI water and kerosene in horizontal (a,c,e) and vertical (b,d,f) crushed-shale packs from FS (a,b), M (c,d) and OP (e,f) sections. 28

Figure 2-7. Pictures of FS, M and OP shale samples used in the spontaneous imbibition experiments using 20 wt% NaCl brine, 10 wt% NaCl brine and DI water. 29

Figure 2-8. NaCl brine and de-ionized water normalized imbibed mass versus time in (a) FS, (b) M and (c) OP samples. The curves stop for M8, M9, FS8 and FS9 samples because of their reaction with water, which leads to sample expansion, and thus the imbibition mass can not be measured. 30

Figure 2-9. SEM image of a focused area on an OP shale sample and the corresponding elemental maps of carbon, silica, iron, aluminum, calcium and sulfur on the same focused area. Magnified area-A shows pores in organic; magnified area-B shows small pores in organic and two large pores in Quartz. Darker area in elemental maps represents higher element density. 32

Figure 2-10. Square of imbibed volume versus time for the imbibition of DI water and kerosene into horizontal (a,c,e) and vertical (b,d,f) crushed-shale packs from FS (a,b), M (c,d) and OP (e,f) sections. 36

Figure 2-11. Mathematical solution of imbibition front position (L_s) versus time (t) from Eq. 2.6 for (a) FS, (c) M and (e) OP samples and experimental imbibition front position versus time for (b) FS, (d) M and (f) OP samples. 38

Figure 2-12. Mathematical solution of imbibition front position (L_s) versus time (t) from Eq. 2.8 for (a) FS, (c) M and (c) OP samples and experimental imbibition front position versus time for (b) FS, (d) M and (f) OP samples. 39

Figure 2-13. Imbibition volume versus dimensionless time of DI water and kerosene for horizontal (a,c,e) and vertical (b,d,f) crushed-shale packs from FS (a,b), M (c,d) and OP (e,f) sections. 41

Figure 3-1. Schematic of double layer structure around a negatively charged surface in an electrolyte solution (Binazadeh, 2013). 46

Figure 3-2. Flowchart of sample preparation and experimental procedure. 51

Figure 3-3. The schematic of 1-D imbibition set-up. Liquid imbibes from bottom to the top. 52

Figure 3-4. The normalized imbibed volume of DI water and brine in unwashed and washed HRB shale powder (a) sample 1, (b) sample 2, (c) sample 3, and (d) sample 4. 54

Figure 3-5. The imbibed volume of DI water and brine solutions in (a) sample 1, (b) sample 2, (c) sample 3, and (d) sample 4 of HRB shale powder packs as a function of square root of time. ... 56

Figure 3-6. (a) Calculated Debye length, κ^{-1} , of the in-situ formed brine after mixing the imbibed fluid (DI water or brine solution) with the unwashed or washed HRB shale powder samples during the imbibition. (b) The correlation between P_c and κ^{-1} 58

Figure 3-7. (a) Representative imbibition (Vol. fraction vs. square root of time) of aqueous solutions (DI water and brine) in shale powders of sample 2 (washed and unwashed) pack, (b) schematics of DI water imbibition into washed shale powders, (c) schematics of DI water imbibition into unwashed shale powders, (d) Schematics of brine imbibition into unwashed shale powders. Faster imbibition is shown by thicker arrows and thicker electrostatic double layer is shown by larger blue circles. 60

Figure 4-1. The schematic of the vacuum set-up used for the imbibition tests under degassed conditions. 66

Figure 4-2. Normalized mass of imbibed oxic and degassed water for (a) EV-1, (b) EV-2, and (c) EV-3 samples. 67

Figure 4-3. The surface of EV-1 shale samples in a. oxic water and b. degassed water 2 hours after starting the imbibition experiment. The blue areas in the figure are reference areas used for determining the sample depth. 68

Figure 4-4. Normalized mass of imbibed oxic and degassed water versus square root of time for (a) EV-1, (b) EV-2, and (c) EV-3 samples. The trendlines show the initial imbibition rate. 70

Figure 4-5. The concentration of (a, c, e) potassium and (b, d, f) sodium ions in degassed/oxic water during imbibition experiments with (a, b) EV-1, (c, d) Ev-2, and (e, f) EV-3 shale samples measured by ICP-MS. 73

Figure 4-6. The K^+/Cl^- (a, c, e) and Na^+/Cl^- (b, d, f) molar ratios in degassed/oxic water during imbibition with EV-1 (a, b), EV-2 (c, d), and EV-3 (e, f) shale samples. 74

Figure 4-7. The concentration of (a, c, e) iron and (b, d, f) sulfate ions in degassed/oxic water during imbibition experiments with (a, b) EV-1, (c, d) Ev-2, and (e, f) EV-3 shale samples measured by ICP-MS. 76

Figure 4-8. (a) SEM image of a focused area on a EV-2 shale sample; (b) magnified SEM image showing pores in pyrite; (c) sulfur elemental map and (d) iron elemental map obtained by EDS of the EV-2 shale sample. Darker area in elemental maps represents higher element density. 79

Figure 4-9. SHIM image of the EV-2 shale sample. Nano pores are observed around pyrite framboid. 80

Figure 5-1. Schematic of a rock sample and its depositional lamination (red dashed line). The horizontal direction represents the direction parallel to the lamination. The vertical direction represents the direction perpendicular to the lamination. 84

Figure 5-2. Schematic illustrations of the custom-designed linear variable differential transformers (LVDT) set-up for measuring ϵ . (a) full experimental set-up and (b) LVDT mechanism for measuring sample expansion. 85

Figure 5-3. (a) Displacement data measured on a dry rock using LVDT, and (b) the distribution of the measured data..... 87

Figure 5-4. Schematic illustration of the experimental set-up for measuring induced expansive stress during water imbibition..... 87

Figure 5-5. (a) Ternary diagram of the mineralogy and (b) clay content versus TVD for the Muskwa, Otter Park, and Evie members from the HRB. The three groups shown on the ternary diagram are quartz, clay, and other minerals (sum of feldspar, plagioclase, calcite, dolomite, pyrite, etc)..... 89

Figure 5-6. SEM image of a focus area (a) and two magnified SEM images of clay areas (b and c) for a shale sample from Group 2. The layered and curled-flakes structure indicates illite/smectite in the zoomed-in area..... 91

Figure 5-7. SEM image of a focused area (a) and a magnified clay area (b) for a shale sample from Group 2. The layered and curled-flakes structure indicates the illite/smectite in the zoomed-in area. 91

Figure 5-8. ϵ_x , ϵ_y and S_w during water imbibition into the shale samples. (a) Group 1, (b) Group 2, (c) Group 3, (d) Group 4 and (e) Group 5..... 94

Figure 5-9. Microcracks along the depositional lamination observed on a randomly-picked HRB shale sample..... 94

Figure 5-10. ϵ_y and S_o during oil imbibition into the shale samples. (a) Group 1, (b) Group 2, (c) Group 3, (d) Group 4 and (e) Group 5..... 95

Figure 5-11. σ of the shale samples in vertical direction versus the time of water imbibition. S_w measured at the end of the experiments (6 days) are presented on the plot..... 96

Figure 5-12. (a) σ of shale samples in vertical direction versus the time of water imbibition. Five Horn River shale samples are selected from 0.5-m depth interval of the same well. The samples are confined in the vertical direction with different confining pressures (125 psi, 65 psi, 40 psi, 25 psi, 15 psi) during the tests. 97

Figure 5-13. ϵ_y measured during imbibition of DI water, 10 wt% NaCl brine and 20 wt% NaCl brine for the samples of (a) Group 1, (b) Group 2, (c) Group 3, (d) Group 4 and (e) Group 5. S_w measured at the end of the experiments (6 days) are presented on the plot. ϵ_y curves of Group-5 are zoomed-in due to the relatively low ϵ_y values. 98

Figure 5-14. σ measured during imbibition of DI water, 10 wt% NaCl brine and 20 wt% NaCl brine for the samples of (a) Group 1, (b) Group 2, (c) Group 3, (d) Group 4 and (e) Group 5. S_w measured at the end of the experiments (6 days) are presented on the plot..... 99

Figure 5-15. Excess water imbibition due to sample expansion versus (a) the total clay content and (b) illite/smectite content of the samples. 102

Figure 5-16. (a) ϵ_x versus normalized M_{imb} and (b) ϵ_y versus normalized M_{imb} for the shale samples. (a) ϵ_x are zoomed-in due to the relatively low ϵ_x -values..... 103

Figure 5-17. The correlations of (a) ϵ_x and (b) ϵ_y with normalized M_{imb} for the shale samples. 103

Figure 5-18. σ versus the normalized M_{imb} for the shale samples applied with 40 psi confining pressure 104

Figure 5-19. (a) ϵ_x and (c) ϵ_y versus time of water imbibition. (b) ϵ_x and (d) ϵ_y after 10 days of water imbibition versus total clay content of the shale samples. 105

Figure 5-20. (a) σ of the shale samples versus water imbibition time, and (b) σ after 6 days of water imbibition versus total clay content of the samples. 40 psi of confining pressure is applied vertically on all the shale samples. 105

Figure 5-21. (a) ϵ_y and (b) σ at the end of water/brine imbibition experiment (6 days) versus NaCl concentration in the bulk solution. 107

Figure 6-1. Schematic of 1-D imbibition set-up. Imbibed fluid (water or oil) is imbibed from the bottom to the top. 114

Figure 6-2. Schematic of the LVDT set-up for measuring sample expansion during 1-D imbibition set-up. Imbibed fluid (water or oil) is imbibed from the bottom to the top. Two LVDTs are placed

horizontally and vertically to measure the sample expansion in the horizontal and vertical direction.	115
Figure 6-3. Water contact angles of the shale samples. Oil is completely spread on all the rock surface, which has 0° contact angles.	116
Figure 6-4. Results of 1-D spontaneous imbibition experiment.	116
Figure 6-5. Sample expansion results on (a) vertical (perpendicular to the depositional lamination) and (b) horizontal (parallel to the depositional lamination) directions during water imbibition. Expansion curves in vertical direction is zoomed-in due to their relatively low values.....	118
Figure 6-6. Porosity enhancement versus the time of water imbibition into shale samples.	118
Figure 6-7. Experimental imbibition curve of oil (green dashed line) and water (blue dashed line), calculated water imbibition curve excluded expansion effect (black dotted line) and calculated water imbibition curve using Handy’s model (red dotted line). (a) Sample-1, (b) sample-2, (c) sample -3, (d) sample-4 and (e) sample-5.....	121
Figure 6-8. Comparisons of the imbibed water concentration predicted by the presented model (Eq. 6.16) with the imbibition experimental data excluding the sample expansion effect (Eq. 6.11). (a) Sample-1, (b) sample-2, (c) sample -3, (d) sample-4 and (e) sample-5.....	123
Figure A-1. The schematic of permeability test.....	154
Figure C-1. The EC of salt solutions obtained after washing of HRB shale powders with DI water as a function of number of washing stages	156
Figure C-2. Individual ion concentration of the salt solutions obtained after washing of HRB shale powders with DI water as a function of number of washing stages.	157
Figure D-1. Normalized weight loss of shale samples at different temperatures. The weight-loss is normalized by dividing by the initial weight of dry sample.	158
Figure D-2. Normalized weight loss of shale samples heated at 100°C. The measured weight does not change after 24 hours.....	159

Figure E-1. (a) ϵ_y and (b) σ of ten shale samples from HR Formation during water imbibition process. The maximum differences and standard deviations in measured values of ϵ_y and σ are 0.10% and 7.01 psi and 0.03% and 2.07 psi respectively. 160

Figure F-1. Structure of smectite clay before and after hydration. Water molecules bind to the cations in interlayer spaces, resulting in clay swelling. (b) Structure of tetrahedral and octahedral sheets. Modified from Holtz and Kovacs (1981) and Mitchell, J.K. (1993). 162

Nomenclature

a	Langmuir adsorption constant
A	Cross-sectional area of rock sample
C	Concentration of water in rock sample
Q	Volume of imbibed liquid
L_s	Distance of imbibition front
Q'	Imbibed liquid volume at the end of imbibition experiment
q	Liquid imbibition flow rate
S	Liquid saturation behind the imbibition front
P_c	capillary pressure at the saturation of S
ΔS	Excess water saturation due to sample expansion.
ϕ	Porosity of rock sample
$\Delta\phi$	Enhanced porosity due to sample expansion
ϕ_{dry}	Porosity of dry rock sample (before imbibition test)
ϕ_{wet}	Porosity of wet rock sample (after imbibition test)
q_{ad}	Amount of water molecules adsorbed on unit mass of rock matrix
M	Molar mass
M_{imb}	mass of fluid imbibed into rock sample
ρ	Density of imbibing fluid
k	Absolute permeability of rock sample
k_{rw}	Relative permeability of liquid
μ	Viscosity of liquid
γ	Surface tension
λ	effective pore diameter
θ	Contact angle
V_{dry}	Bulk volume of dry rock sample (before imbibition test).
V_{wet}	Bulk volume of wet rock sample (after imbibition test).
ΔV	Change in volume of the rock sample.
ε	Strain induced by imbibition of fluid into the rock sample.

ε_x	Induced strain in the horizontal direction.
ε_y	Induced strain in the vertical direction.
ε_v	Volumetric strain.
σ	Stress induced by imbibition of fluid into the rock sample.
d	Diameter of the rock sample.
Δd	Change in diameter of the rock sample.
r	Radius of the rock sample.
Δr	Change in radius of the rock sample.
h	Height of the rock sample.
Δh	Change in height of the rock sample.
κ^{-1}	Thickness of the electrical double layer.
ε_0	Vacuum permittivity.
ε_r	Relative permittivity of medium.
k_B	the Boltzmann constant.
e	Electron charge.
N_A	Avogadro number.
I	ionic strength of an electrolyte solution.

Chapter 1: General Introduction

1.1 Overview

This chapter briefly describes the key technologies and common field practices mentioned in relevant chapters. Also, it presents the objective, study scope and thesis structure.

1.1.1 Unconventional Reservoirs

Unconventional reservoirs usually have extremely low permeability (in the scale of nano-Darcy) compared to conventional reservoirs (see Figure 1-1). Examples of unconventional reservoirs include tight-gas sands, gas and oil shales, coalbed methane, heavy oil and tar sands, and gas-hydrate deposits.

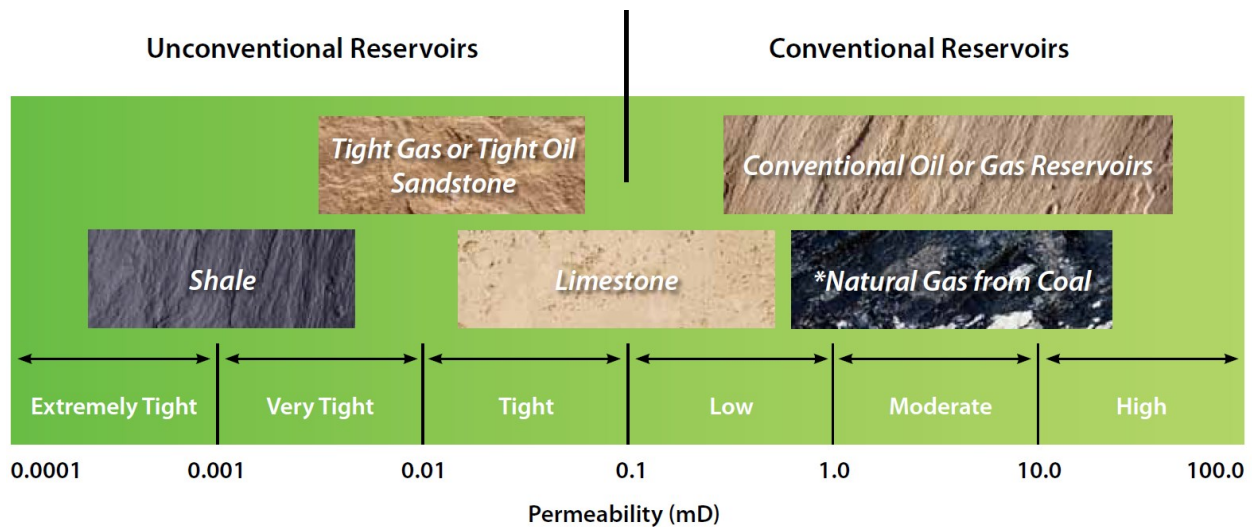


Figure 1-1. Comparative analysis of matrix permeability of various unconventional reservoirs (CSUR, 2018).

1.1.1 Oil and Gas Shale Plays in North America

Oil and gas shales are widely distributed in east- and west-central of North America (see Figure 1-2). By the end of 2011, there were 28 shale basins with 56 identified shale plays in North America. Major commercial shale plays include Horn River and Montney located in Canada, and Barnett, Haynesville, Fayetteville, Marcellus, and Eagle Ford located in the U.S. The rock samples

used in this study are gas shales from Horn River Group of the Western Canadian Sedimentary Basin.

In the past two decades, unconventional resources have become an important energy source for the production of hydrocarbon in North America, and are being explored as a resource in other continents as well. From 2000 to 2012, the contribution of shale gas to the total natural gas production increased from 1% in the United States and Canada, to 39% in the United States and 15% in Canada (EIA, 2013; Stevens, 2012). The shale gas and tight gas production projects a substantial increase, especially in China, the U.S, and Canada, as shown in Figure 1-3 (EIA, 2016).



Figure 1-2. Geographical distribution of major unconventional reservoirs in North America (EIA, 2011). The approximate location of the Horn River Basin is highlighted and shown by the red circle.

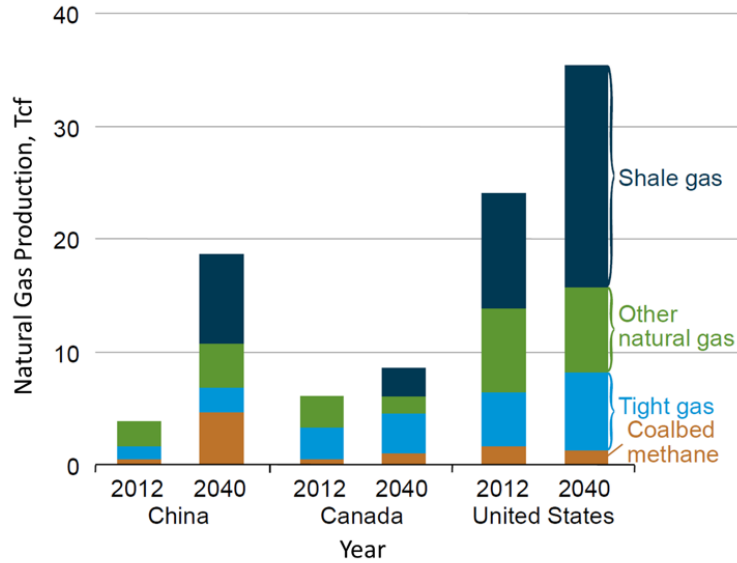


Figure 1-3. Natural gas production by type in China, Canada, and the United States in 2012 and the predicted production in 2040 (EIA, 2016).

1.1.2 Horn River Gas Shale Play

The Horn River Basin is a major gas shale play in North America. It is located in Northeast British Columbia and covers an approximate areal extent of 1.1 million hectares. It is Middle to Upper Devonian in age with main pay zones in the Fort Simpson, Muskwa, Otter Park, and Evie members. The Fort Simpson member is categorized as clay-rich formation, and the other three members are dominantly composed of organic and silica-rich shale (National Energy Board, 2011). The estimated gas in place in the Horn River Basin is $12.6 \times 10^{12} \text{ m}^3$ (448 Tcf), and the marketable resource base is expected around $2.2 \times 10^{12} \text{ m}^3$ (78 Tcf) (National Energy Board, 2011). Production in the Horn River Basin has been steadily increasing in the past decade. As shown in Figure 1-4, the daily gas production from 203 producing wells has reached 580 mmcf per day by the end of 2013.

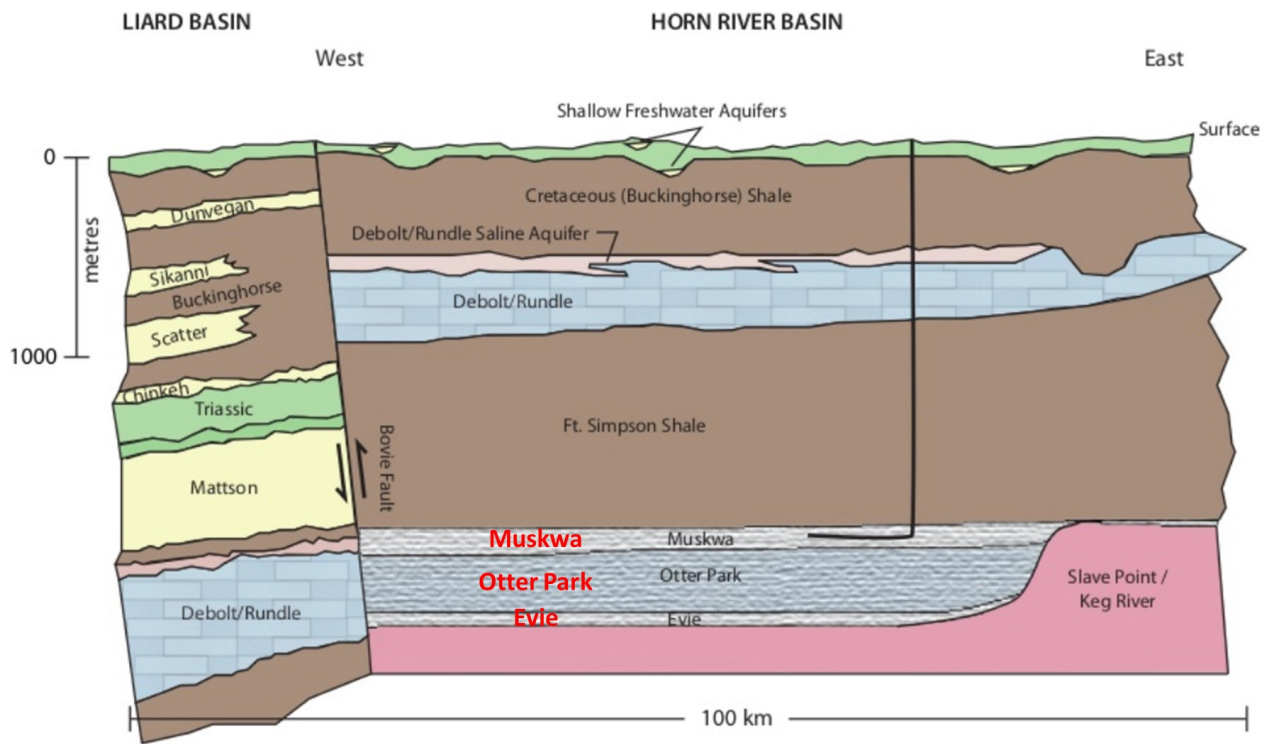


Figure 1-4. Schematic stratigraphic cross-section of the Horn River basin and its adjacent Liard Basin (B. C. Oil & Gas Commission, 2014).

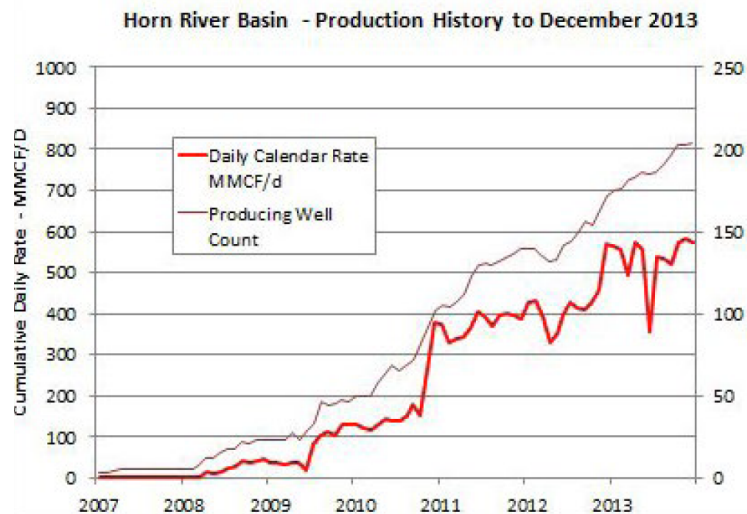


Figure 1-5. Production history in the Horn River Basin from 2007 to 2013 (B. C. Oil & Gas Commission, 2014).

1.1.2 Drilling and Completion Process

It is a great challenge to produce oil and natural gas on a commercial scale, due to the low porosity and ultra-low permeability of unconventional reservoir rocks. Thus, special techniques such as horizontal drilling and multi-stage hydraulic fracturing are required to enhance hydrocarbon recovery and overcome economic constraints, in order to produce hydrocarbons from these reservoirs monetarily viable.

1.1.2.1 Horizontal Drilling

Horizontal drilling, which is also known as directional drilling, is the process of drilling a well that intersects the reservoir with a near-horizontal inclination, and maintaining that inclination within the reservoir until the desired bottom hole location is reached (Helms, 2008). A typical horizontal well is mainly composed of vertical well section, build section and horizontal well section, as can be seen from Figure 1-6. Traditional vertical well is drilled a thousand or more metres deep until it reaches the kick-off point above the target formation at the first step. The well is then deviated from the vertical plane around a curve until it runs parallel to the target formation (hydrocarbon zone), which is usually nearly horizontal. The horizontal legs of the wells may extend up to 3,000 metres within the target formation, thereby accessing a greater volume of the reservoir and creating more borehole-reservoir contact area, compared with a traditional vertical well. Multiple horizontal wells can be drilled from one well pad to minimize the costs, reduce the total amount of land and production equipment needed, and reduce the associated environmental impacts (i.e. surface disruption).

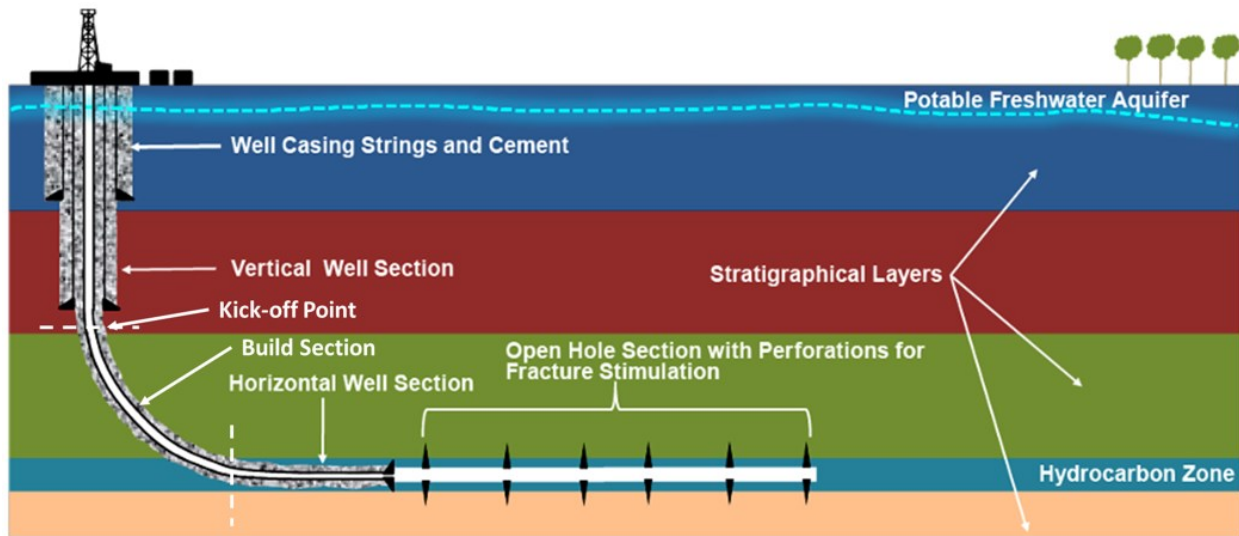


Figure 1-6. Schematic of cross-sectional view of a horizontal well (Northern Territory Department of Mines and Energy, 2018).

1.1.2.2 Hydraulic Fracturing

To produce the hydrocarbon at economic flow rate, the unconventional reservoir needs to be hydraulically fractured to create additional pathway for hydrocarbon flow. Multi-stage hydraulic fracturing is a common formation stimulation practice to facilitate hydrocarbon flow from the low-permeable unconventional reservoir to the wellbore (Gidley, 1989). Following the drilling and perforating the casing in the well, the mixture of water, proppant (i.e. appropriately sized grains of silica sand or ceramic beads) and chemicals is injected at high pressure into a wellbore to create fractures during hydraulic fracturing operation. A typical composition of water-based fracturing fluid is shown in Figure 1-7 and the typical chemical additives is listed in Table 1-1. The pressure exerted by the fracturing fluids should be in excess of the minimum stress fields and overcome the tensile strength of the reservoir rocks, to open existing fractures and create new fractures in the formation.

Table 1-1. Typical chemical additives used in the fracturing fluids (Petrowiki, 2018).

Additive	Function Performed	Typical Product
Biocide	Kill bacteria	Gluteraldehyde carbonate
Breaker	Reduce viscosity	Acid, oxidizer, enzyme breaker

Buffer	Control pH	Sodium bicarbonate, fumaric acid
Clay stabilizer	Prevent clay swelling	KCl, NHCl, KCl substitutes
Diverting agent	Divert fluid flow	Ball sealers, rock salt, boric acid
Fluid loss additive	Improve fluid efficiency	Diesel, particulates, fine sand
Friction reducer	Reduce friction	Polyacrylamide derivatives
Iron controller	Keep iron in solution	Acetic and citric acid
Surfactant	Modify surface tension and wettability	Fluorocarbon, Isopropanol
Gel stabilizer	Reduce thermal degradation	MEOH, sodium thiosulphate
Scale Inhibitors	Reduce scale formation	Inorganic and organic phosphates

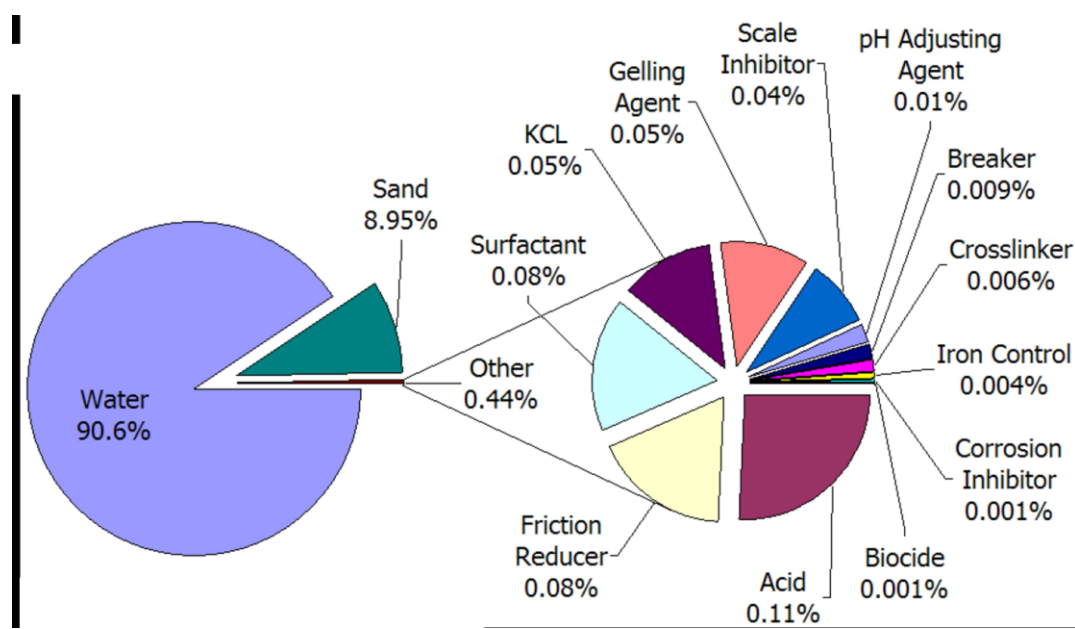


Figure 1-7. Typical volumetric composition of a water-based fracturing fluid (Arthur et al., 2009). Data is collected at Fayetteville shale fracturing stimulation (GWPC and ALL Consulting, 2009).

The hydraulic fracturing usually occurs in several stages (generally 10 to 15 stages) along the horizontal wellbore (Alessi et al., 2017), as shown in Figure 1-8. Each fracturing stage is isolated by a packer or plug and performed within the isolated interval (~150 metres). The staged fracturing is performed from the toe to heel of the horizontal well. Once hydraulic pressure is removed from the well, small grains of proppant hold these fractures open. Consequently, an extensive surface area of the reservoir is exposed to the fracturing fluids after the hydraulic fracturing operation.

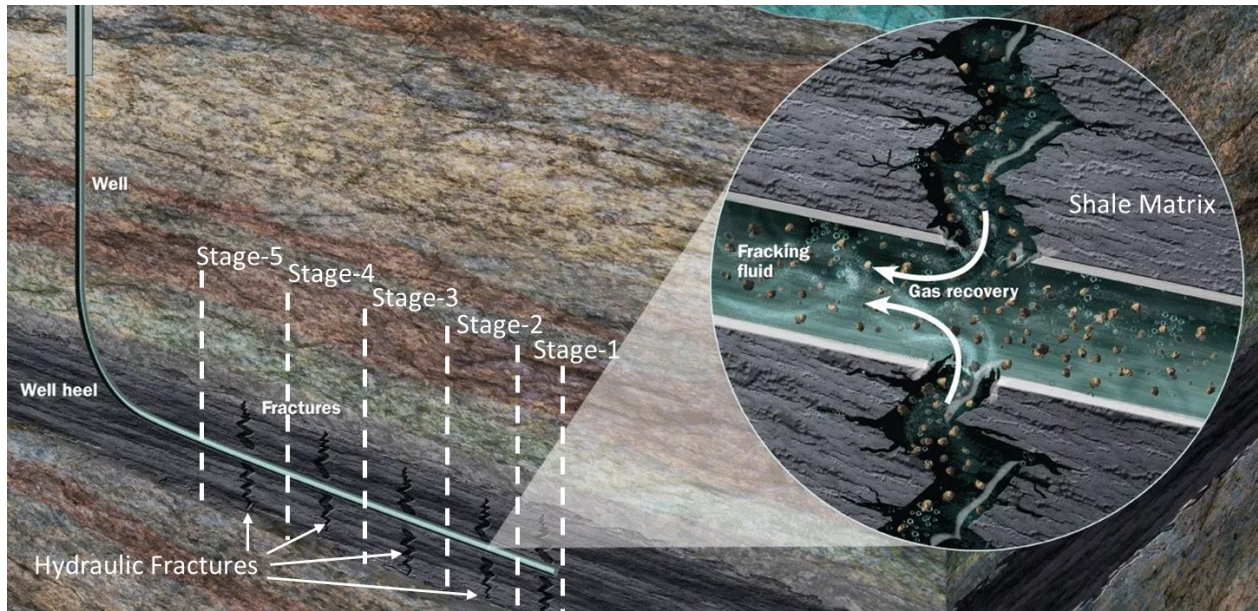


Figure 1-8. Schematic of cross-sectional view of horizontal well and hydraulic fractures (zoomed-in area) drilled in an unconventional reservoir (Modified from NaturPhilosophie, 2014).

1.1.2.3 Shut-in Process

After hydraulic fracturing, the well undergoes shut-in for some time (i.e., 1 to 5 weeks). This enables operators to prepare surface facilities for production. Also, it allows the bottom hole pressure of the well to build-up. During shut-in, the fracturing fluid leaks off into the rock matrix, which is considered to have a dual effect.

Firstly, imbibition of the fracturing fluid into the shale matrix, during the shut-in period, can result in the displacement of the hydrocarbons to the fracture which may ultimately enhance hydrocarbon production from the well (King, 2012; Lan et al., 2014; Makhanov et al., 2014). Extended shut-in period may increase hydrocarbon production in the early time (Fakcharoenphol et al., 2014). According to the well production data available from four different shale plays - the Bossier (Settari et al., 2002) and the Marcellus (Cheng, 2012) formations in the U.S., the Montney (Kanfar and Clarkson, 2016) and the Monteith (Zambrano et al., 2016) Formations in Canada, hydrocarbon flow rate is higher and water flow rate is lower after shut-in, compared with their rates before shut-in period.

Secondly, fracturing fluid imbibition into the shale matrix may damage the reservoir (Bahrami et al., 2012; Bennion et al., 2005) via an increased water saturation in the vicinity of the fractures (water blockage) which can reduce the relative permeability of the hydrocarbon. Reduction of the hydrocarbon permeability may drastically impede hydrocarbon flow in the reservoir (Shaoul et al. 2011). A complete design of a hydraulic fracturing operation for a specific unconventional reservoir, requires an in depth understanding of the mechanisms responsible for the retention of the injected fracturing fluid into the rock matrix.

1.1.2.4 Flowback Process

In order to clean-up the injected fracturing fluids, the well is open for a brief period (~10 days) before or after the shut-in period. Large volume of water (10 to 20 million litres per well) is injected into shale formations during fracturing operation. However, only ~10% of the injected water is recovered during flowback process (Matthew and Mantell, 2013; Roychaudhuri et al., 2013; Vandecasteele et al., 2015). Some wells in the Eagle Ford shale formation produced less than 20% of the injected fracturing fluid in their entire production history (Nicot and Scanlon, 2012). For the wells completed in Horn River basin, the flowback efficiency is only ~1.5% after 72 hours of production (Ghanbari and Dehghanpour, 2016).

The unrecovered part of fracturing fluids is believed to be imbibed by fractures, micro-fractures and shale matrix, where the fluids stay as an immobile phase due to capillarity, fracture closure and gravity segregation (Gdanski et al., 2006; Fan et al., 2010; Ehlig-Economides and Economides, 2011; Parmar et al., 2014). Imbibition is an immiscible displacement process, whereby the wetting fluid spontaneously imbibe into the porous media driven by capillary pressure and expel the non-wetting fluid (Akin et al., 2000).

1.1.3 Pore Network in Unconventional Reservoirs

Pore structure of unconventional reservoirs is a complex system of pores in matrix, natural fractures, and hydraulic fractures (Loucks et al., 2012; Gale et al., 2014).

1.1.3.1 Natural Fractures

Natural fractures are macroscopic planar discontinuities generated via natural processes (i.e. local stress perturbations, regional burial, tectonic forces; lithification processes such as diagenesis) (Saidi, 1987; Nelson, 2001; Gale and Holder, 2010). Natural fractures in unconventional reservoirs are prone to be sealed or partially filled by minerals (e.g. calcite), and poorly connected (Gale et al., 2007). The connectivity of natural fractures could be effectively reactivated by drilling and fracturing operations. Slippage and shear dilation of natural fractures are caused by injected fracturing fluids and microseismic events (Blanton, 1982; Warpinski and Teufel, 1987; Moradian et al., 2016).

In addition, microfractures can be created during water uptake into clay-rich shales (Makhanov et al., 2014; Meng et al., 2015; Sun et al., 2015). These induced microfractures might be due to 1) collapse clay swelling (Ghanbari and Dehghanpour, 2015; Roshan et al., 2015), 2) high internal pore pressure generated by the capillary pressure (Yang et al., 2015), and 3) shear and tensile failure (Nygård et al., 2006; Zhou et al., 2016). These induced microfractures may further imbibe a significant amount of water.

1.1.3.2 Hydraulic Fractures

Hydraulic fractures are tensile fractures which propagate perpendicular to the direction of minimum horizontal in-situ stress in a normal fault environment, as shown in Figure 1-9 (Nolen-Hoeksema, 2013). Some geologic discontinuities (joints, bedding planes, faults and stress contrasts) have significant influences on hydraulic fracture, including reducing total length of hydraulic fracture by fluid leak-off or difficulty of proppant transport and placement (Warpinski and Teufel, 1987). The most common practice to estimate hydraulic fracture volume is through the percentage of the fracturing fluid injected which does not leak off into the reservoir. In the past decade, microcosmic imaging has been used to characterize the fracture network (i.e., fracture spacing, conductivity, complexity, azimuth and dimensions) and approximate fracture geometry (Maxwell et al., 2002; Mayerhofer et al., 2006; Nejadi et al., 2015). It relies on the detection of micro-earthquakes and acoustic emissions associated with fracture creation and extension (Urbancic et al., 1999).

Generally, the fracture width is in the scale of millimetre (Geertsma and de Klerk, 1969) and the fracture half-length is from 50 to 300 metres (Fisher et al., 2002; Ezulike, 2017). The closure of

hydraulic fracture occurs when the bottom-hole pressure is less than the minimum principal stress (Raaen et al., 2001; Fjar et al., 2008), resulting in smaller aperture size and lower fracture permeability (Walsh, 1981).

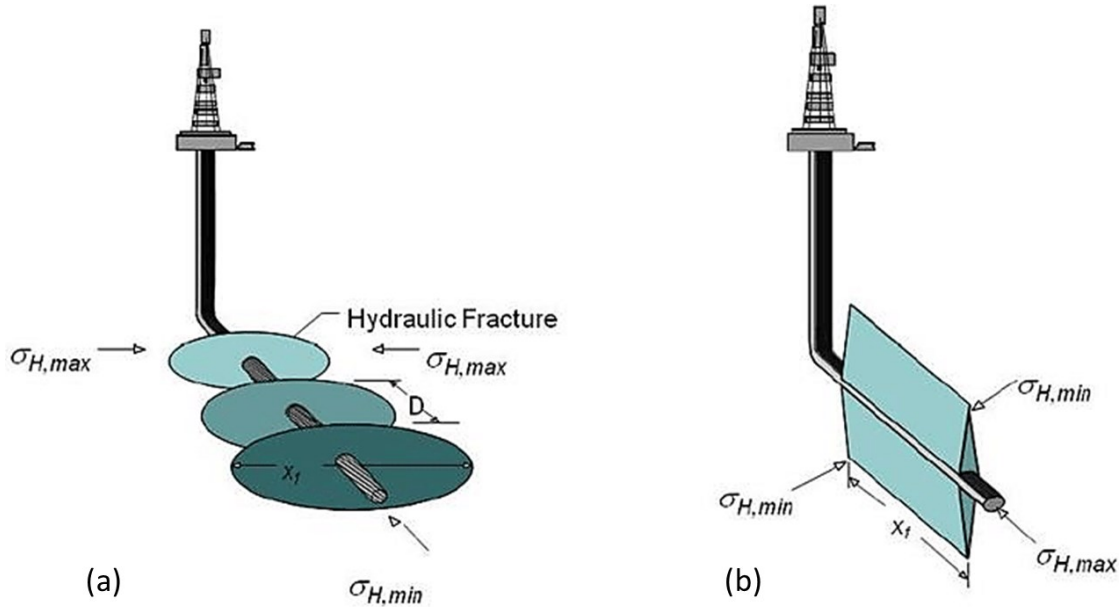


Figure 1-9. (a) Transverse and (b) longitudinal fracture propagation patterns in horizontal well relative to the minimum and maximum horizontal in-situ stress (Salah et al., 2016).

1.1.3.3 Pores in Matrix

Rocks in unconventional reservoirs typically have lower porosity (less than 10% of total bulk volume) compared to rock in conventional reservoirs (more than 15% of total bulk volume) (Kulia et al., 2014). For example, the averaged porosity of Horn River gas shales is around 3 to 6% (B. C. Oil and Gas Commission, 2014). Scanning electron microscope images in Figure 1-10 show two types of pores in Montney tight sandstone and Barnett shale: 1) abundant number of small nanopores within the organic matter, and 2) a few micropores bordered by inorganic minerals.

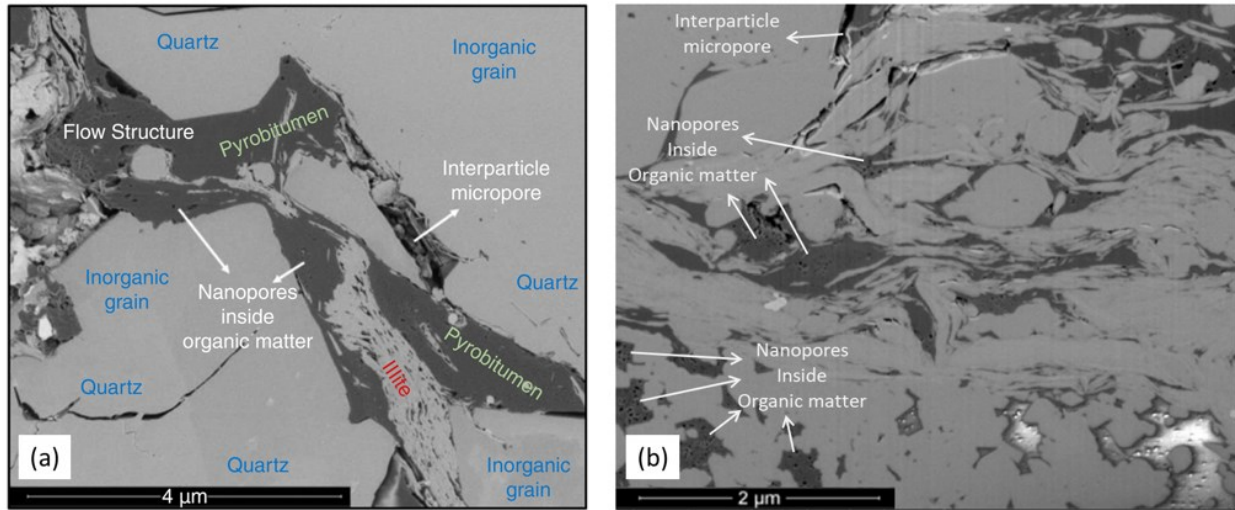


Figure 1-10. Scanning electron microscope images of (a) Montney tight sandstone sample (Yassin et al., 2016) and (b) Barnett shale sample (Sondergeld et al., 2010).

1.1.4 Spontaneous Imbibition

Spontaneous imbibition is driven by capillary pressure, which is a function of rock wettability, interfacial tension, and pore radius (Balcerak, 2012; Singh, 2016). Wettability is in general the affinity of a particular fluid to wet the surface of the target rock (Agbalaka et al., 2008). The wetting state of a reservoir rock can be identified by measuring equilibrium contact angle, the Amott wettability index (Amott, 1959), the United States Bureau of Mines (USBM) wettability index (Donaldson et al., 1969), spontaneous imbibition rate/volume (Morrow, 1990), hysteresis of the relative permeability curves (Jones and Roszelle, 1978), and Nuclear Magnetic Relaxation (NMR) (Brown and Fatt, 1956). Contact angle measurement is the most common method to evaluate the liquid wettability in rock.

Figure 1-11 shows the schematic of counter-current and co-current imbibition. Counter-current imbibition means the wetting phase and nonwetting phase move in opposite directions. Co-current imbibition means wetting phase flows in the same direction as nonwetting phase. The imbibition rate is strongly influenced by (1) petrophysical properties including permeability, porosity and wettability (Mattax and KYTE, 1962), (2) fluid properties including viscosity, interfacial tension (Shouxiang et al., 1997; Li and Horne, 2001) and (3) geometrical parameters such as sample shape, size and boundary conditions (Kazemi et al., 1992; Zhang et al., 1996).

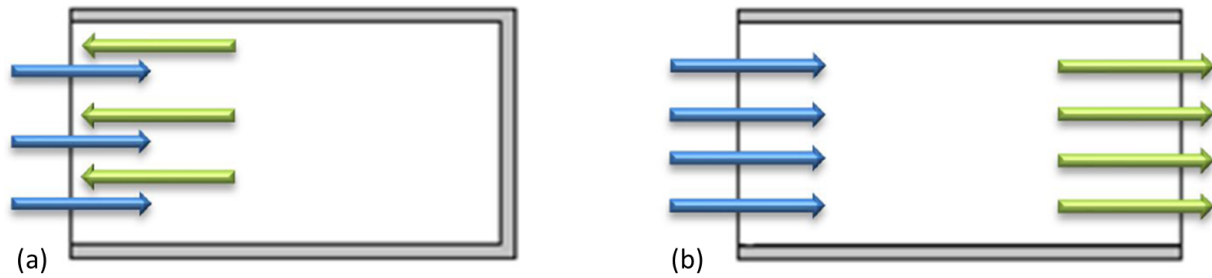


Figure 1-11. Schematics of (a) counter-current and (b) co-current imbibition. Blue and green colors represent the wetting and nonwetting phases, respectively. The arrow represents the direction of imbibition flow (Makhanov, 2013).

1.2 Research Motivation

Although high water uptake in shales has been observed both in field and laboratory conditions, its reasons are poorly understood. Capillary pressure is one key driving force for the liquid uptake in shales (Handy, 1960; Roychaudhuri et al., 2013; Lan et al., 2014). However, it is insufficient to explain this strong water uptake in shales.

The presence of large amount of clays and complex pore structure, variation in pore location (i.e. pores in organic or inorganic matrix) (Mitchell et al., 1990; Al-Maamari and Buckley, 2003) and size (Toumelin et al., 2006) pose additional challenges to investigating the mechanisms for excess water uptake in shales. Also, clay swelling and electrostatic interactions between charged clay and water may drastically influence water uptake in shales.

All these factors affecting overall water uptake of shales are hardly isolated and investigated using conventional techniques. Therefore, an improved understanding of fluid-shale interaction is critical for optimizing the chemical formulation of fracturing and treatment fluids, estimating the field-scale imbibition rate, and evaluating the environmental impact during hydraulic fracturing process.

1.3 Research Objectives

The primary objectives of this research are:

- Investigating the existence and connectivity of hydrophobic and hydrophilic pore networks, and its effect on water uptake in shale.
- Investigating the interaction effects of clays in rock samples and salts in imbibing fluids during water imbibition in shales.
- Investigating the interaction effects of air/water blockage on water imbibition and flowback efficiency.

1.4 Organization of Thesis

This thesis consists of five chapters.

Chapter 1 presents a brief overview of the research background and introduces the research gap and objectives of this study.

Chapter 2 presents the comparative study of water imbibition into crushed shale packs and intact shale samples to investigate the connected pore network on water imbibition. The effect of osmotic potential is also investigated by imbibition experiments using brine with different salinities.

Chapter 3 extends the study of osmotic potential in Chapter 2 and investigate the effect of salts content of the samples and the salt concentration in the fluid on imbibition potential of shale samples. The effects of imbibing solution ionic strength, rock zeta potential, and salts content of the shale powder on the imbibition process are discussed based on electrostatic interactions.

Chapter 4 presents the results of imbibition experiments using air-saturated de-ionized water (oxic water) and degassed de-ionized water (degassed water) to investigate the role of dissolved oxygen on water imbibition rate/volume and evaluate the effects of dissolved oxygen on concentration of major ions and redox-sensitive ions in flowback water.

Chapter 5 presents the measured strain and stress induced during imbibition of water, brine and oil into shale samples, in order to estimate the enhancement in porosity and water uptake due to clay swelling, and investigate the existence of correlations among clay content of gas shales, imbibed water mass, and induced strain and stress.

Chapter 6 applies an imbibition model to quantitatively interpret the effect of capillary pressure, water adsorption and clay swelling on water imbibition.

Chapter 7 summarizes the important findings and results of this research and provides recommendations for future studies.

Chapter 2: Effect of Pore Connectivity on Water Uptake of Gas Shales

2.1 Introduction

Spontaneous imbibition is a reliable technique used to quantify the wettability of reservoir rocks such as sandstones and carbonates. However, quantification of shales wettability is challenging due to the adsorption of water by clay minerals and oil by organic material, and also the complexity of their pore structure. Recent imbibition studies (Dehghanpour et al., 2012; Dehghanpour et al., 2013) show that brine and water uptake of several samples from the Horn River Basin, are considerably higher than their oil uptake. Contact angle measurements show that oil completely spreads on the fresh break of these samples while water does not. This shows that the samples are oil-wet and should not imbibe much water. However, this is contrary to the imbibition results which show that they imbibe significantly more water than oil. The following paragraphs outline and discuss some possible reasons for this anomalous excess water uptake:

1) Sample Expansion: Clay minerals in shale samples can adsorb a considerable amount of water. This adsorption is controlled by clay chemistry and water salinity (Chenevert, 1970; Hensen, 2002). The negatively charged clay platelets strongly attract polar water molecules, and this driving force is absent in the case of oil imbibition. The previous imbibition experiments, using confined and unconfined intact shale samples (Ghanbari and Dehghanpour, 2015), showed that water uptake induces microfractures in some of the shale samples. The clay hydration leads to sample expansion, which also increases the porosity and permeability of the samples, and results in higher water imbibition rate and volume.

2) Depositional Lamination: It is well known that shales have a layered structure. Previous measurements show that imbibition parallel to the bedding plane is faster than that perpendicular to the bedding plane (Makhanov et al., 2012). The result suggests that permeability parallel to the bedding plane is higher than that perpendicular to the bedding plane. Furthermore, the clay swelling during water imbibition tests enhances the anisotropy by increasing the distance between the clay platelets, which leads to more water imbibition than oil imbibition along the bedding plane.

3) Chemical Osmosis: The higher chemical potential of fresh water provides some additional force for water imbibition. It is possible that some salt precipitates are present inside the shales pore network, due to the sample dehydration. During water imbibition tests, the salt dissolves into the imbibed water and results in the chemical potential difference between the pore water and the external water. This chemical potential difference acts as an additional driving force for the transport of water molecules into the sample.

4) Connectivity of Hydrophobic and Hydrophilic Pore Networks: Shale pores can be in its organic and non-organic constituent materials (Sondergeld et al., 2010). The organic part of the rock is hydrophobic. The non-organic part can be hydrophilic, especially in the presence of clay minerals. Therefore, organic shales are usually a mixture of hydrophilic and hydrophobic materials. Significant water uptake of gas shales may indicate that the hydrophilic pore network is relatively well-connected. Furthermore, this network may be coated by water film and salt which increase its affinity to water, as discussed above. On the other hand, insignificant oil uptake of gas shales may indicate that the hydrophobic pore space, mainly coated by organic carbon, is poorly connected.

The overall water uptake of gas shales is controlled by the above factors, which cannot be isolated by the imbibition experiments conducted on unconfined intact samples. This study measures and compares spontaneous imbibition of oil and water into the crushed Horn River shale packs. Recent studies (Borysenko et al., 2009; Pagels et al., 2012a, 2012b) show that using crushed-shale packs is a good way to investigate the petrophysical properties such as wettability of organic-rich shales. A crushed-shale pack has a confined volume which is not allowed to expand during the imbibition process. Furthermore, a crushed-shale pack is relatively isotropic compared with intact samples which are significantly anisotropic. In addition, both hydrophobic and hydrophilic pore networks of crushed shale packs are artificially well-connected. Imbibition tests using similar intact rocks and high salinity water to investigate the osmotic effect are also conducted. The rest of the chapter is organized as follows: Section 2.2 describes the materials and methods. Section 4.3 shows the water and oil imbibition profiles of crushed and intact shale samples. Section 4.4 describes the conclusions of this study.

2.2 Materials

Spontaneous imbibition experiment of DI water and kerosene is conducted using crushed-shale packs from Fort Simpson (FS), Muskwa (M) and Otter Park (OP) formations of the Horn River Basin (HRB). Detailed information regarding this shale play can be found in existing literature (Reynolds et al., 2010; Pond et al., 2010; Dehghanpour et al., 2012). The imbibed mass of various concentrations of NaCl brine and deionized (DI) water in intact rock samples are also measured.

2.2.1 Fluids

Kerosene, DI water and NaCl solutions of various concentrations were used for the imbibition tests. The density, viscosity and surface tension of different fluids used for the imbibition experiments are listed in Table 2-1.

Table 2-1. Density, viscosity and surface tension of different fluids used for the imbibition experiments.

Fluid	Density (g/cm ³)	Viscosity (cp)	Surface Tension (dyne/cm)
DI water	1.0	0.9	72
10 wt% NaCl	1.06	1.04	76
20 wt% NaCl	1.12	1.26	79
Kerosene	0.8	1.32	28

2.2.2 Intact Shale Samples and Crushed Shale Packs

A total of fifty crushed-shale packs and nine intact shale samples were selected for this study. All the shale powders and shale samples are from two wells drilled in the Horn River Basin. The powders and samples are classified into three sections corresponding to the FS, M and OP. The average mineral concentration of the shale sections determined by X-Ray Diffraction (XRD) data is listed in Table 2-2. The average true vertical depth (TVD), total organic carbon (TOC), matrix density before and after considering TOC content, length, cross-sectional area, porosity and permeability of the crushed-shale packs are presented in Table 2-3. The mass, depth and geometry of the intact shale samples for brine and water imbibition experiments are listed in Table 2-4. The porosity of crushed-shale packs was calculated by:

$$\phi = \frac{V - \frac{m}{\rho_m}}{V} \quad (2.1)$$

where \emptyset is porosity. m and V are the mass and volume of the crushed-shale pack, respectively. ρ_m is matrix density of the sample after adjustment for the TOC content. ρ_m was calculated by using the weight fractions of each mineral obtained from XRD analysis and TOC:

$$\rho_m = (1 - \omega_{TOC}) \times (\sum_{i=1}^n \omega_i * \rho_i) + \omega_{TOC} \times \rho_{TOC} \quad (2.2)$$

Here, ω_i and ρ_i are mass fraction and density of each mineral. ω_{TOC} and ρ_{TOC} are the weight fraction and density of TOC. ρ_{TOC} is close to water density and ranges between (0.94-0.98 g/cm³) (Crain's Petrophysical Handbook, 2012). In this study, ρ_{TOC} is assumed to be 1 g/cm³.

Permeability of each sample is measured independently using Darcy's Law. The permeability is only measured on one sample from each layer. It is assumed that all samples from the same layer have almost the same permeability. The procedure and set-up schematic of permeability test are presented in Appendix A.

Table 2-2. Average mineral concentration (wt %) of the shale sections determined by XRD.

label	Calcite	Quartz	Dolomite	Chlorite IIB2	Illite 1Mt	Plagioclase Albite	Pyrite	Matrix Density
FS	0.5±0.4	29±1.3	2.7±0.3	6.5±0.8	55.4±1.7	4.1±0.5	1.7±0.2	2.747
M	0	36.7±1.2	5.2±0.4	4.4±0.4	48.3±1.5	3.6±0.5	1.7±0.2	2.744
OP	12.9±0.4	43.6±1.1	2.2±0.5	0	33.8±1.2	4.4±0.4	3.2±0.2	2.772

Table 2-3. Average TVD, matrix density determined by XRD data (ρ_{XRD}), matrix density after the Adjustment for TOC content (ρ), TOC, Length, Cross-Sectional Area, Pack Density, Porosity and Permeability of all the Samples Used in the Crushed-Shale Pack Experiments.

Label	Layer	TVD, m	ρ_{XRD} , g/cm ³	ρ_m , g/cm ³	TOC, wt. %	Length , cm	Area , cm ²	Pack Density, g/cm ³	Porosity, %	Permeability, mD
FS1	Fort Simpson	1755	2.748	2.717	1.73	25	5.067	1.973	27.36	21
FS2	Fort Simpson	1755	2.748	2.717	1.73	25	5.067	1.973	27.36	21
FS3	Fort Simpson	1755	2.748	2.717	1.73	25	5.067	1.973	27.36	21

FS4	Fort Simpson	1755	2.748	2.717	1.73	25	5.067	1.973	27.36	21
FS5	Fort Simpson	1755	2.748	2.717	1.73	5	5.067	1.973	27.36	21
FS6	Fort Simpson	1755	2.748	2.717	1.73	5	5.067	1.973	27.36	21
FS7	Fort Simpson	1755	2.748	2.717	1.73	5	5.067	1.973	27.36	21
M1	Muskwa	1758	2.744	2.704	2.25	25	5.067	1.973	27.01	35
M2	Muskwa	1758	2.744	2.704	2.25	25	5.067	1.973	27.01	35
M3	Muskwa	1758	2.744	2.704	2.25	25	5.067	1.973	27.01	35
M4	Muskwa	1758	2.744	2.704	2.25	25	5.067	1.973	27.01	35
M5	Muskwa	1758	2.744	2.704	2.25	5	5.067	1.973	27.01	35
M6	Muskwa	1758	2.744	2.704	2.25	5	5.067	1.973	27.01	35
M7	Muskwa	1758	2.744	2.704	2.25	5	5.067	1.973	27.01	35
OP1	Otter Park	2639	2.772	2.718	3.01	25	5.067	1.973	27.39	32
OP2	Otter Park	2639	2.772	2.718	3.01	25	5.067	1.973	27.39	32
OP3	Otter Park	2639	2.772	2.718	3.01	25	5.067	1.973	27.39	32
OP4	Otter Park	2639	2.772	2.718	3.01	25	5.067	1.973	27.39	32
OP5	Otter Park	2639	2.772	2.718	3.01	5	5.067	1.973	27.39	32
OP6	Otter Park	2639	2.772	2.718	3.01	5	5.067	1.973	27.39	32
OP7	Otter Park	2639	2.772	2.718	3.01	5	5.067	1.973	27.39	32

Table 2-4. Mass, depth and geometry of the intact shale samples used in imbibition experiments.

Label	Mass, g	Area, cm²	Thickness, cm	Diameter, cm	Depth, m
FS8	149.17	78.5	1.0	10	1755

FS9	149.40	78.5	1.1	10	1755
FS10	144.02	78.5	1.1	10	1755
M8	179.96	78.5	1.3	10	1758
M9	187.91	78.5	1.2	10	1758
M10	168.76	78.5	1.3	10	1758
OP8	217.58	78.5	1.4	10	2639
OP9	187.50	78.5	1.3	10	2639
OP10	215.21	78.5	1.4	10	2639

2.2.3 Preparation of Crushed Shale Packs

The crushed-shale packs were prepared in the following steps:

- 1) Break the shale cores into pieces less than 1 cm³ using a hammer.
- 2) Clean the grinding container with ethanol and silicon before grinding the rock samples from different layers.
- 3) Pour the shale pieces into the dish-shaped grinding container in shatter box. Set the grinding time to 1 minute.
- 4) Measure the particle size of the powders by using microscope. Figure 2-1 shows the shale particles visualized by the microscope.
- 5) Heat the powder in an oven at 100°C for 24 hours to ensure moisture evaporation.
- 6) Pack the shale powders into a 1-inch inner diameter (ID) plastic tube. Both ends of the tube are fixed to prevent expansion of the shale powder during the imbibition test.

Figure 2-1 shows that the shale powder diameter is in the order of 1 μm. A crushed-shale pack used for the imbibition experiment is shown in Figure 2-2. A plastic-plug with a nozzle was mounted on one side (plug side) and a cloth-screen was mounted on the other side (mesh side). During the imbibition experiment, fluid was imbibed from the mesh side toward the plug side.

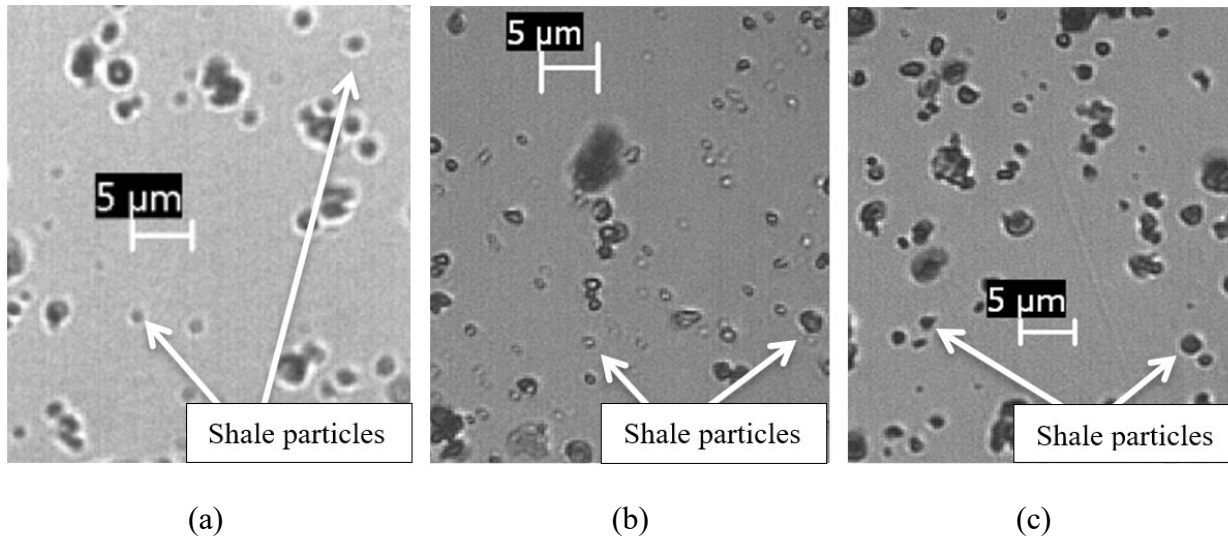


Figure 2-1. The particles of shales from (a) FS, (b) M and (c) OP sections visualized using microscope.



Figure 2-2. A 25-cm-long crushed-shale pack used in the horizontal and vertical imbibition experiments.

2.3 Methodology

A total of 27 imbibition tests are conducted. They can be categorized into three sets. In Set 1, the co-current imbibition of water and oil in dry, crushed-shale packs is measured. The use of crushed-shale packs is to minimize the effects of anisotropy, expansion, and pore connectivity. In Set 2, the counter-current imbibition of water (or oil) into the shale packs saturated with oil (or water) is measured. This is to investigate the imbibition in samples initially saturated with a liquid phase. In Set 3, the spontaneous imbibition of brine of different salinities in intact samples is measured. This is to investigate the effect of osmotic potential on the imbibition behavior.

2.3.1 Set 1 (Co-current Imbibition of Kerosene and DI Water)

The spontaneous imbibition experiments for crushed-shale packs were conducted to compare the imbibition volume of kerosene and DI water. A total of 12 crushed-shale packs were made from the shale powders from the three formations. Both horizontal and vertical imbibition experiments are designed to measure and compare the imbibition with and without gravity effect.

In horizontal imbibition experiments, the 25-cm-long crushed-shale pack was put into a container filled with DI water or kerosene (Figure 2-3). During the test, the fluid gradually imbibe from the screen-side to the plug-side (Figure 2-4). In order to get the co-current imbibition volume, a graduated cylinder is placed on the outlet to collect the air bubbles displaced by the fluid.

In vertical imbibition experiments, before starting the experiment, the weight of dry crushed-shale packs (M_0) is measured. The crushed shale pack is placed on a mesh stand inside an imbibition cell. The fluid level in the imbibition cell is slightly above the mesh to ensure continuous fluid exposure during the test. The mass of the imbibed sample at time T_i is recorded as M_i . Therefore, the imbibed mass is given by $M_i - M_0$. The imbibition front of oil and water at different T_i values are shown in Figure 2-5.

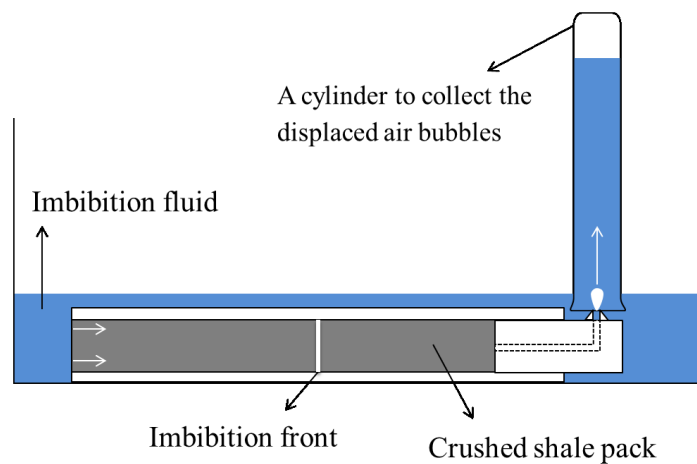
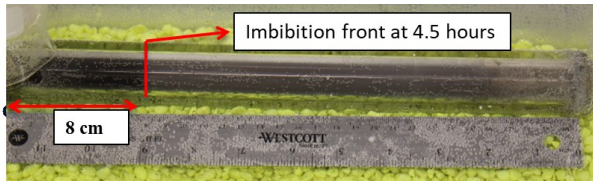
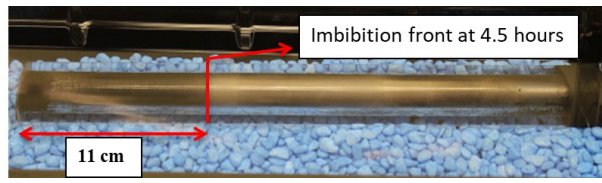


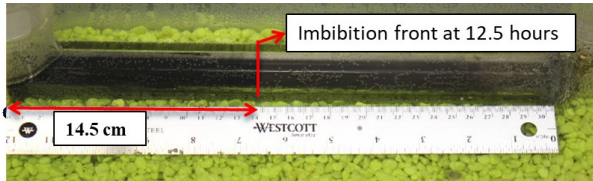
Figure 2-3. The schematic illustration the set-up for horizontal experiments. The fluid is imbibed from left to the right and displaces the air in the crushed-shale pack. The air is collected in an inverted cylinder.



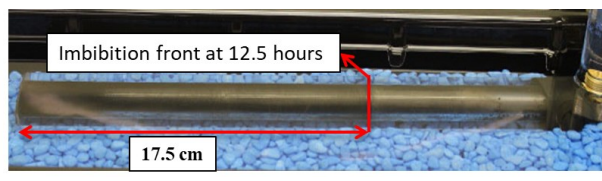
(a)



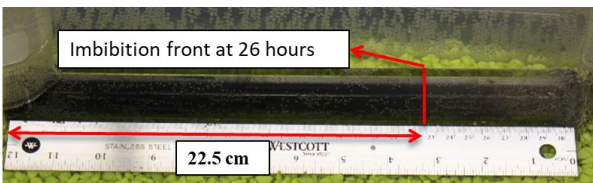
(b)



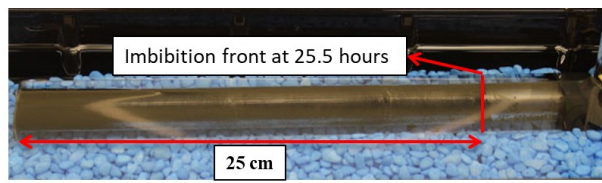
(c)



(d)



(e)



(f)

Figure 2-4. The water (left) and oil (right) imbibition front position at 4.5 hours (a, b), 12.5 hours (c, d), 30.5 hours (e) and 25.5 hours (f) for Muskwa crushed sample packs.

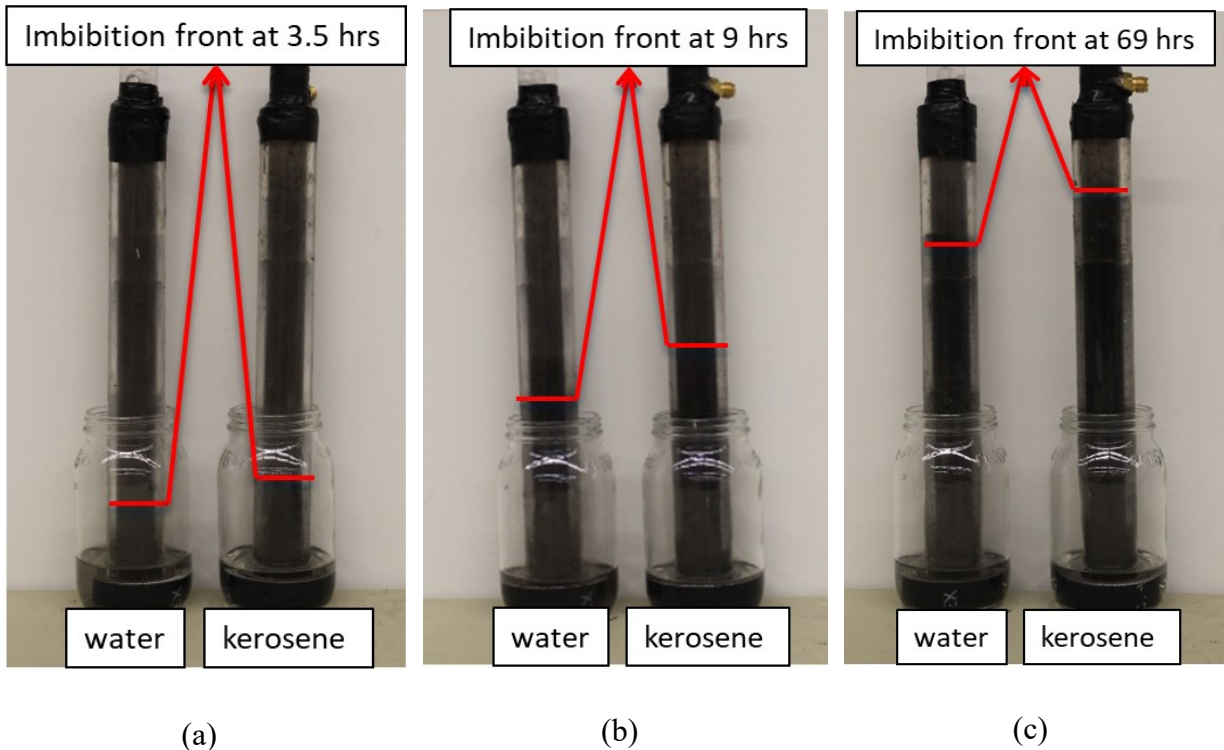


Figure 2-5. The front position for vertical imbibition of water (left) and kerosene (right) into Muskwa crushed-shale packs (a) after 3.5 hours, (b) after 9 hours, (c) after 69 hours.

2.3.2 Set 2 (Counter-current Imbibition Experiments)

The counter-current imbibition experiments compare the water uptake of oil-saturated samples with oil uptake of water-saturated samples. The objective of Set 2 is to know whether the samples still have the same affinity to oil (or water) when their pore space is initially saturated with water (or oil). A total of 6 crushed-shale packs (FS6-FS7, M6-M7, OP6-OP7) were made for the counter-current tests with the following procedure:

- 1) Immerse a 5-cm-long crushed-shale pack into DI water or kerosene until the weight gain is stabilized.
- 2) Put the water/oil-saturated crushed-shale pack into oil/water for 72 hours and visualize the occurrence of counter-current imbibition

2.3.3 Set 3 (Spontaneous Imbibition of Brine)

Set 3 compares the imbibition rate of water and brine of 20 wt% and 10 wt% NaCl. The objective is to investigate the role of osmotic potential on water uptake. It is possible that salt precipitates are present in the pore space. In this case, increasing the salt concentration of imbibing water is expected to decrease the concentration gradient, the osmotic potential, and in turn, water imbibition volume. The general test procedure includes the following steps:

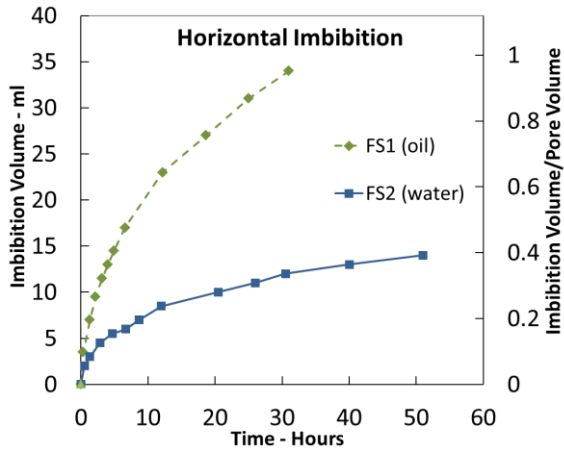
- 1) Heat selected shale samples at 100°C for 24 hours to ensure moisture evaporation.
- 2) Measure the mass and bulk volume of shale samples
- 3) Place the shale samples in imbibition cell and measure the sample weight at selected time intervals.
- 4) Stop the experiment when the shale samples' weight does not increase with time.

2.3.4 Set 4 (Pore-scale Visualization)

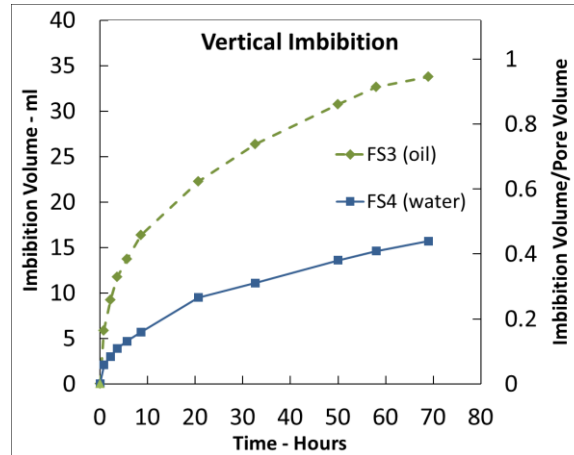
Scanning electron microscope (SEM), scanning helium ion microscope (SHIM), and energy-dispersive x-ray spectroscopy (EDS) are used to visualize the pores and obtain the elemental maps from OP sample. One end piece from OP sample is prepared for SEM-EDS imaging. The sample are first cut into 1×1×0.5 cm cubes. The surface of the sample is then mechanically polished using 600-, 1000-, and 2000-grit polishing pads. Then, the sample surface is further polished using argon-ion milling to minimize the influence of roughness and artifacts of the sample surface on the SEM images. All SEM/SHIM images are obtained using ~15 Kv beam energy.

2.4 Results

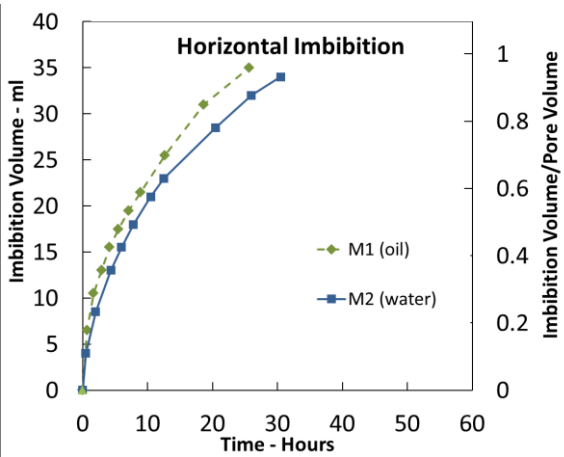
This section presents and discusses the results of three sets of imbibition experiments.



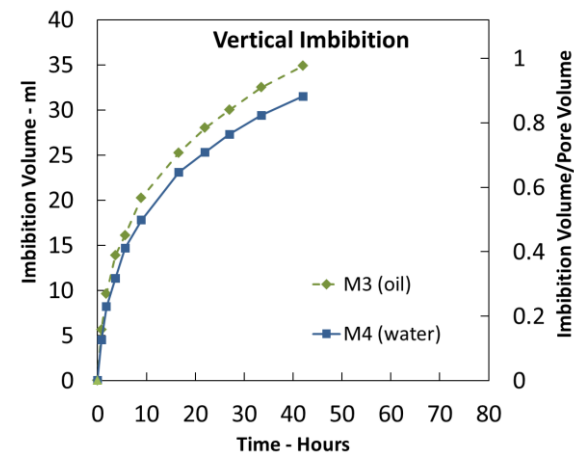
(a)



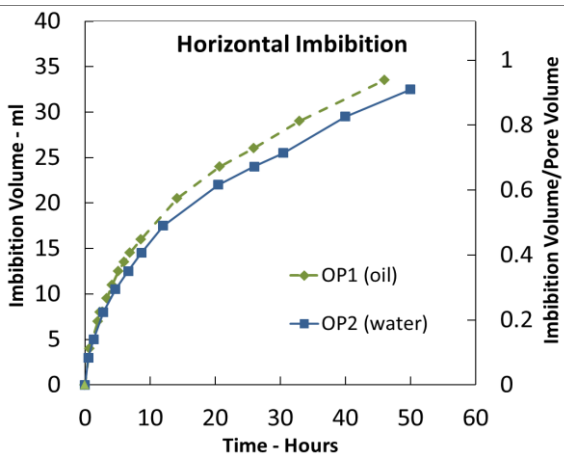
(b)



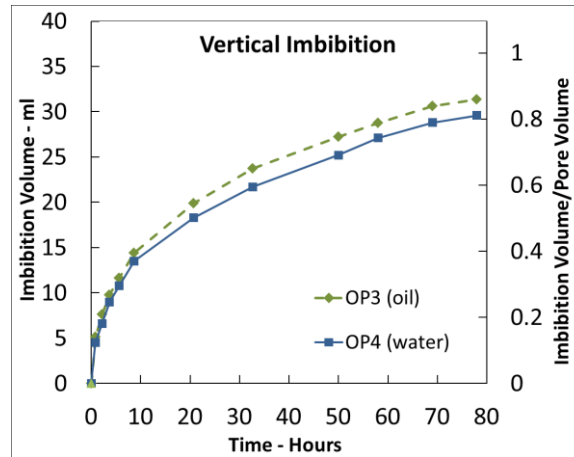
(c)



(d)



(e)



(f)

Figure 2-6. Comparison between imbibition rate of DI water and kerosene in horizontal (a,c,e) and vertical (b,d,f) crushed-shale packs from FS (a,b), M (c,d) and OP (e,f) sections.

2.4.1 Set 1.

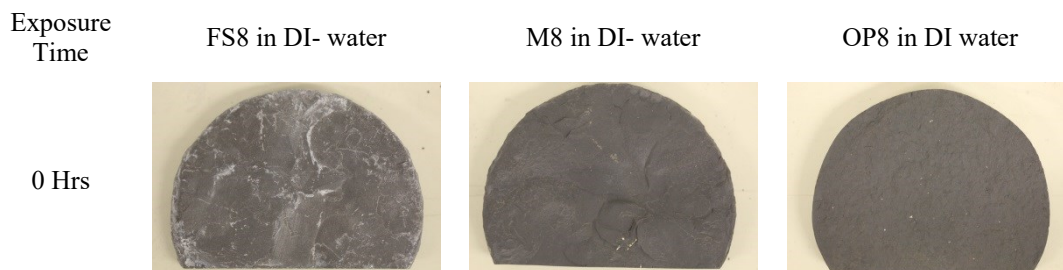
Figure 2-6 shows the cumulative imbibition volume versus time for crushed packs. It is observed that oil imbibes faster than DI water especially for FS samples. However, previous experiments (Dehghanpour et al., 2013) show water imbibes considerably faster than oil in intact samples. Therefore, based on the imbibition behavior, the crushed packs are preferentially oil wet while the intact shale samples are preferentially water wet. This contradiction will be discussed later.

2.4.2 Set 2.

The results of Set 2 show that oil (or water) does not imbibe into water (or oil) saturated packs, even after 72 hours. The results indicate that if the pore space is initially covered by oil (or water), its wetting affinity to water (or oil) will be significantly reduced.

2.4.3 Set 3.

Figure 2-7 shows that increasing the brine salinity from 0 to 20 wt% reduces the degree of physical alteration of M and FS samples. Comparing the pictures before and after 12 hours imbibition tests shows that increasing the salt concentration significantly reduces the degree of physical alteration in the samples. For OP samples, no observed induced crack indicates the lack of swelling clays. Figure 2-8 compares the imbibition profiles of water and brine of different salinities. Water uptake of all samples is significantly higher than their brine uptake. Furthermore, the imbibition rate of low salinity brine (10 wt% NaCl) is higher than that of high salinity brine (20 wt% NaCl).



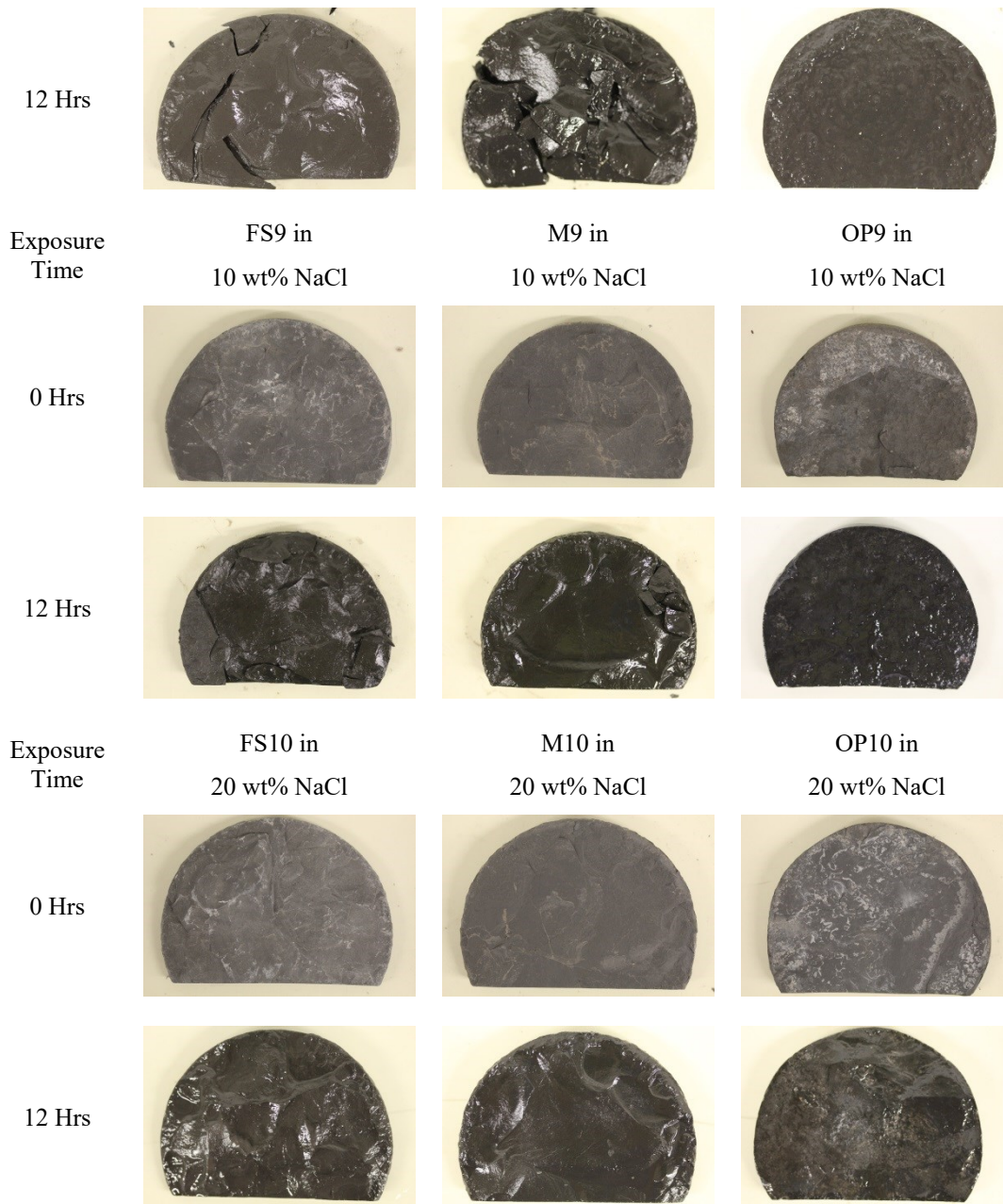


Figure 2-7. Pictures of FS, M and OP shale samples used in the spontaneous imbibition experiments using 20 wt% NaCl brine, 10 wt% NaCl brine and DI water.

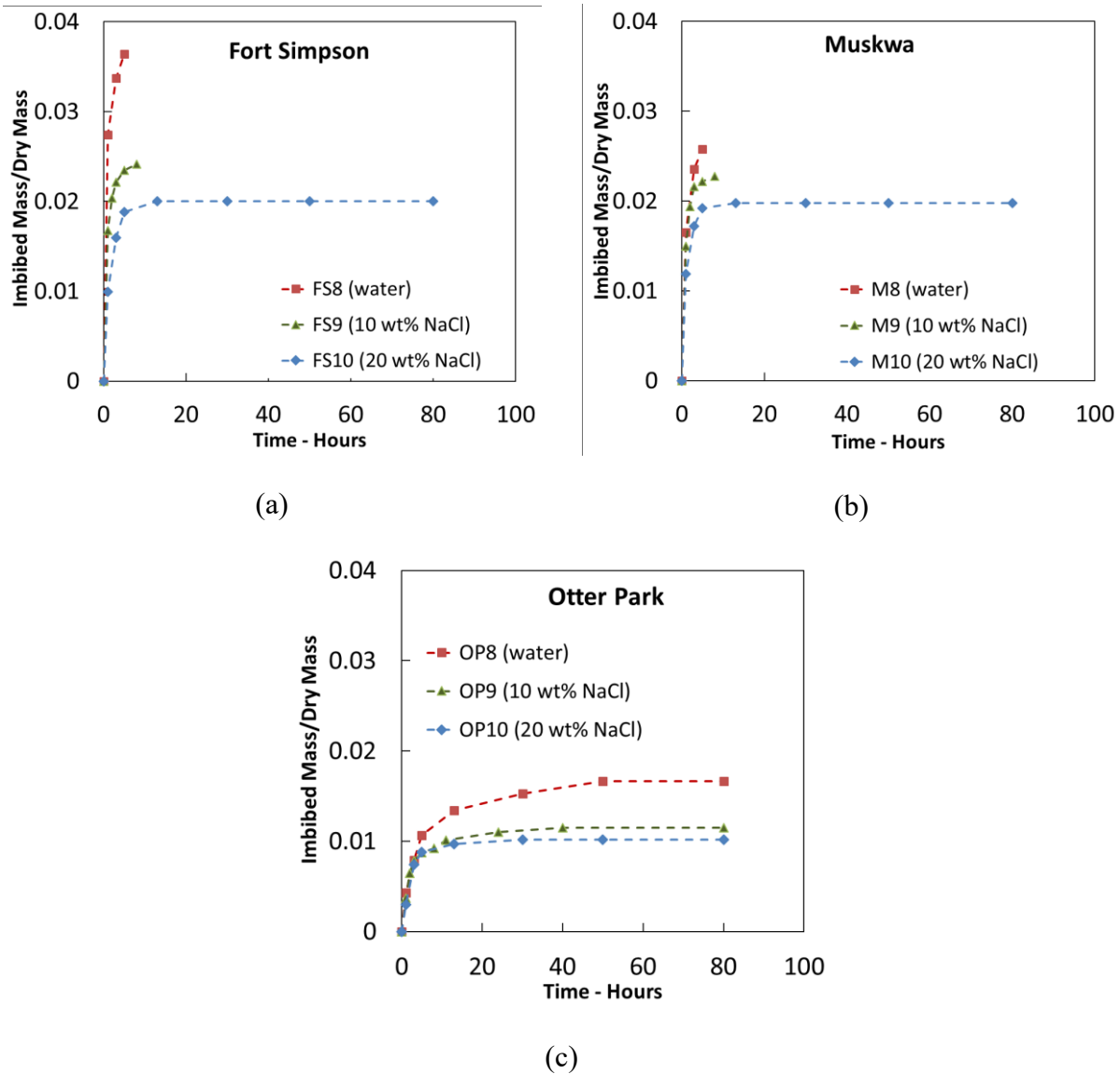


Figure 2-8. NaCl brine and de-ionized water normalized imbibed mass versus time in (a) FS, (b) M and (c) OP samples. The curves stop for M8, M9, FS8 and FS9 samples because of their reaction with water, which leads to sample expansion, and thus the imbibition mass can not be measured.

2.4.4 Set 4

Figure 2-9 displays an SEM image of a focus area and the corresponding elemental maps of carbon, silica, iron, aluminum, calcium and sulfur showing the distribution of pores, organic content and inorganic minerals. Magnified area-A shows that many pores with a throat size of 5 to 50 nm exist in the organic content. Magnified area-B shows two large (~100 nm) pores in Quartz. These large inorganic pores may have better connectivity than that of organic pores. The inorganic pores have

more affinity to water than oil (Lopes et al., 2006), which makes more water imbibed into the large pores in a higher rate.

Table 2-3 shows that the total organic carbon in the shale samples is relatively low (1.73% - 3.01%). However, since organic matter is often deposited on pore surfaces (Tissot et al., 1974), a significant number of pores are coated by organic matter and form hydrophobic pores.

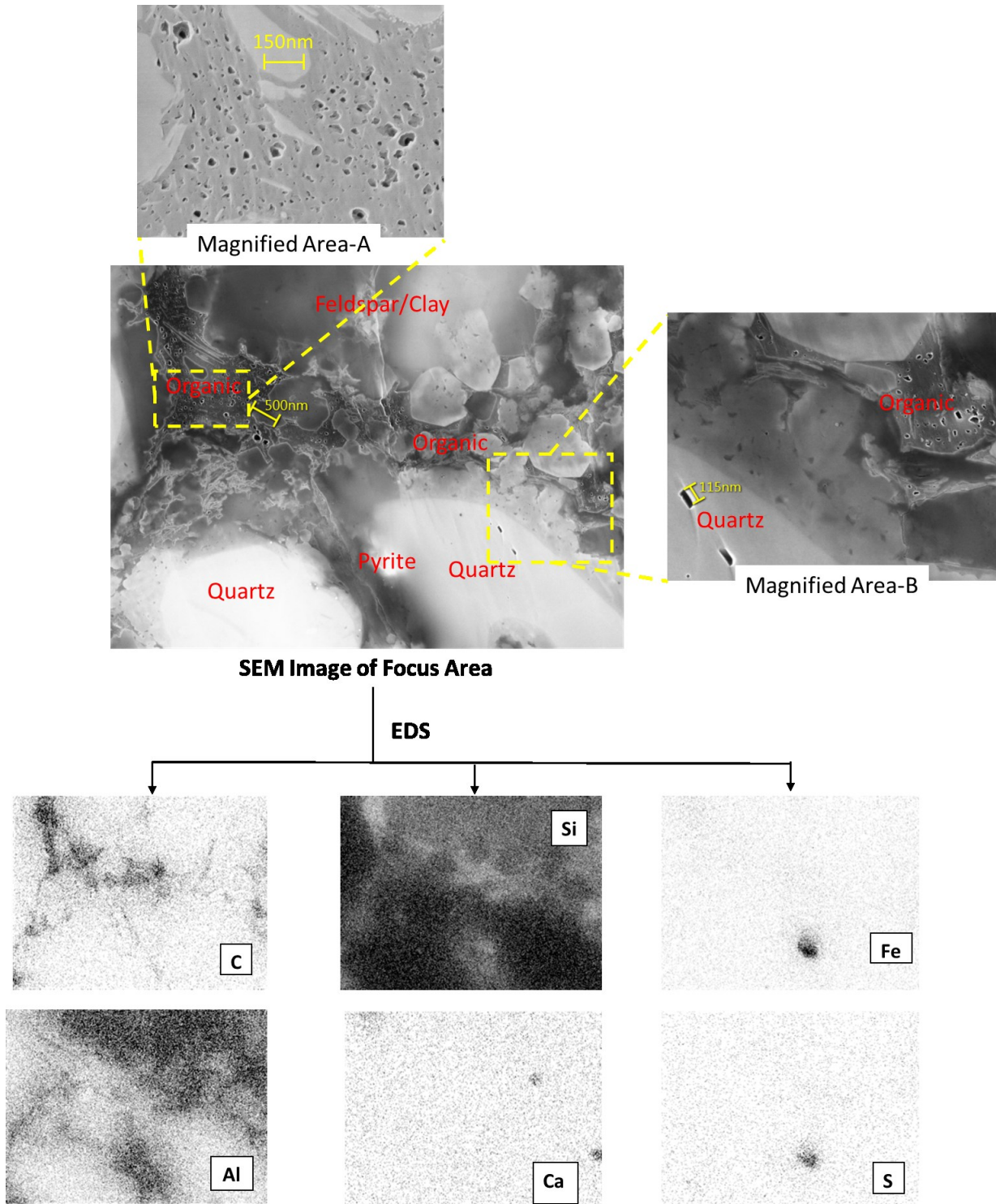


Figure 2-9. SEM image of a focused area on an OP shale sample and the corresponding elemental maps of carbon, silica, iron, aluminum, calcium and sulfur on the same focused area. Magnified area-A shows pores in organic; magnified area-B shows small pores in organic and two large pores in Quartz. Darker area in elemental maps represents higher element density.

2.5 Quantitative Interpretation of Imbibition Data

The results of co-current imbibition show that oil imbibition rate is higher than water imbibition rate. Capillary pressure calculated by Young-Laplace equation cannot explain the significant water uptake of intact samples compared with their oil uptake. However, the crushed samples show an opposite behavior as presented in Section 4. In this section, 1) Handy's model (Handy, 1960) is used to model the imbibition rate, 2) Lucas and Washburn equation (Lucas, 1918; Washburn, 1921) is used to model imbibition front position, and 3) the dimensionless time is used to investigate the difference between the wettability of the shale samples to oil and water.

2.5.1 Modelling Imbibition Rate

In Set 1, the crushed-shale packs are relatively homogeneous and isotropic, so the fluid imbibition can be assumed as a piston-like displacement process. When the gravity can be ignored, the correlation (Handy, 1960; Li and Horne, 2001) between the time and the imbibition volume is:

$$Q^2 = \left(\frac{2P_c k \phi A^2 S}{\mu} \right) \quad (2.3)$$

where, Q is the volume of imbibed liquid, k is effective liquid permeability, ϕ is fractional porosity, A is cross-sectional area of sample, S is the liquid saturation behind the imbibition front. μ is the liquid viscosity, and P_c is capillary pressure at the saturation of S . The capillary pressure of oil and water can be approximated using Young-Laplace equation.

Figure 2-10 shows Q^2 versus t curves from horizontal and vertical imbibition experiments. It is observed that the slopes of the oil curves are consistently higher than those of water curves, especially for the Fort Simpson samples. The ratio between the slope of water and oil curves can be defined as

$$R = \frac{\left(\frac{Q^2}{t} \right)_{water}}{\left(\frac{Q^2}{t} \right)_{oil}} \quad (2.4)$$

The R value of horizontal experiments (R_H) can be directly obtained from Figure 2-10. The R value of vertical experiments (R_V) can also be obtained from the linear part of the curves. For the vertical experiments, the curves are nearly straight lines when the imbibition height is less than 10 cm.

In Set 1, ϕ , S , k and A are approximately the same for every crushed-shale pack, as listed in Table 1-1. Therefore, from Eq. 2.3, R can also be calculated using:

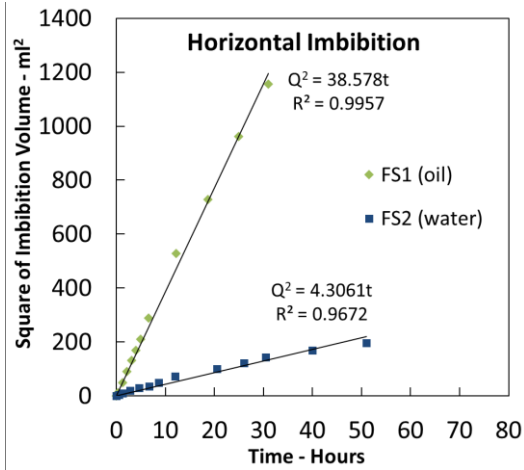
$$R_C = \frac{\left(\frac{P_c}{\mu}\right)_{water}}{\left(\frac{P_c}{\mu}\right)_{oil}} = \frac{\left(\frac{\gamma \cos \theta}{\mu}\right)_{water}}{\left(\frac{\gamma \cos \theta}{\mu}\right)_{oil}} \quad (2.5)$$

The experimental (R_H and R_V) and theoretical (R_C) values of R are listed in Table 2-5. It is observed that R_C values are higher than R_H and R_V values. The R_C values indicate that based on Handy's theory and Young-Laplace equation, the slope of water imbibition curves should be almost 3 times higher than that of oil imbibition curves for Muskwa and Otter Park sections, and should be almost 2.4 times higher than that of oil for Fort Simpson section. In simple, capillary-driven imbibition theory suggests that the water imbibition rate should be much higher than oil imbibition rate, primarily because surface tension of water is considerably higher than that of oil. However, both the horizontal and vertical spontaneous imbibition experiments indicate that oil imbibition rates are higher than water imbibition rates, as the values of R_H and R_V are around 0.8 for Muskwa and Otter Park sections, and around 0.1 for Fort Simpson section.

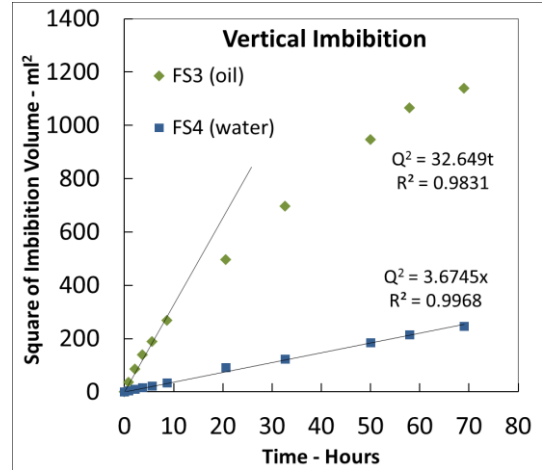
The R_H and R_V values of Fort Simpson samples are significantly lower than those of Muskwa and Otter Park samples. One reason is the high clay content of Fort Simpson samples (see Table 2-2). During water imbibition, clay hydration may cause shale powder swelling and reduce the pore volume of shale sample pack. This can be seen from the significantly lower final imbibed volume of Fort Simpson samples compared with Muskwa and Otter Park samples.

Table 2-5. The values of water and oil contact angles, the R value defined by Eqs. (4) and obtained from Eqs. (5) (R_C), horizontal (R_H) and vertical (R_V) imbibition experiments. Subscripts o , w , a represent kerosene, water, air, respectively.

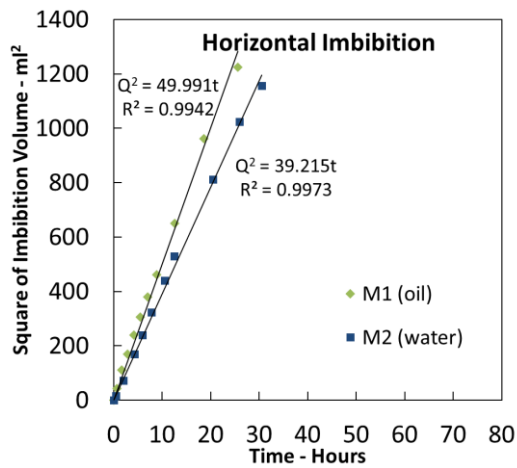
Parameter	Fort Simpson	Muskwa	Otter Park
θ_w (Degree)	27	38	50
θ_o (Degree)	0	0	0
R_C	3.36	2.96	2.42
R_H	0.12	0.78	0.85
R_V	0.11	0.77	0.87



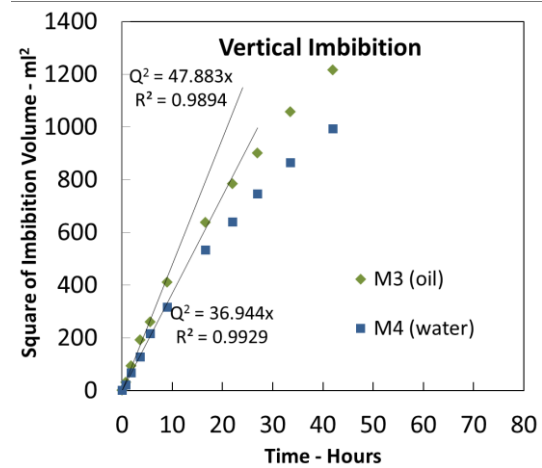
(a)



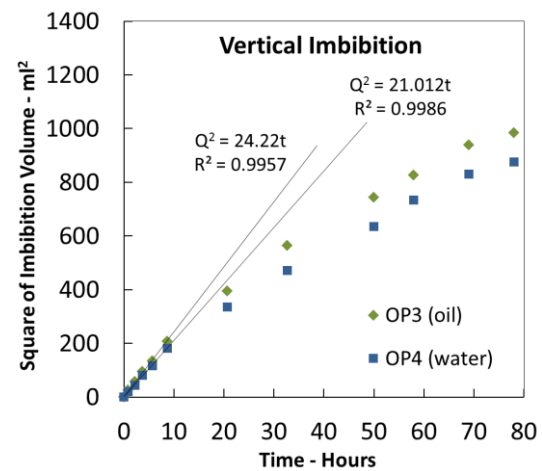
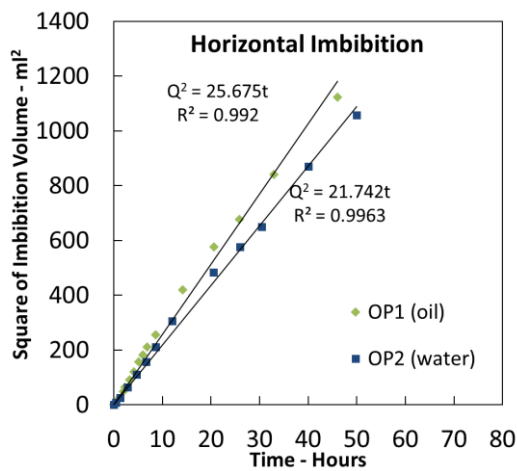
(b)



(c)



(d)



(e)

(f)

Figure 2-10. Square of imbibed volume versus time for the imbibition of DI water and kerosene into horizontal (a,c,e) and vertical (b,d,f) crushed-shale packs from FS (a,b), M (c,d) and OP (e,f) sections.

2.5.2 Modelling Front Position

In this section, the imbibition front position versus time for oil and water is compared using the theory and experimental data. From Lucas and Washburn equation (Lucas, 1918; Washburn, 1921), the horizontal imbibition front is given by

$$L_s(t) = \sqrt{\frac{\lambda\sigma\cos\theta}{4\mu}} t^{\frac{1}{2}} \quad (2.6)$$

Considering the gravity effect, the flux equation for vertical imbibition is given by (Mattax and Kyte, 1962):

$$\frac{dL_s}{dt} = \frac{\lambda^2}{32\mu L_s} \times \left(\frac{4\sigma\cos\theta}{\lambda} - \rho g L_s \right) \quad (2.7)$$

By solving the integration, the relationship between imbibition height (front) and time is given by

$$\frac{\rho g \lambda^2}{32\mu} t = -L_s - \frac{P_c}{\rho g} \ln \left(\frac{\frac{P_c}{\rho g} - L_s}{\frac{P_c}{\rho g}} \right) \quad (2.8)$$

where,

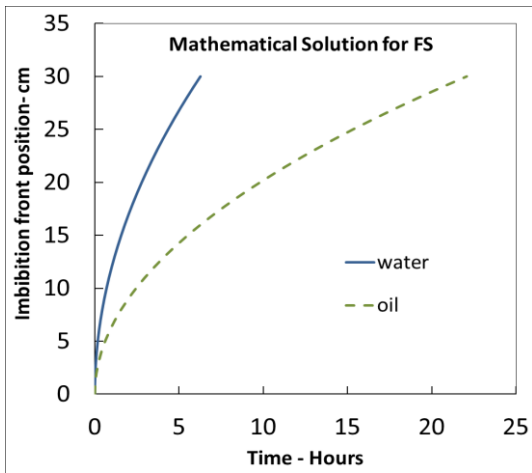
$$P_c = \frac{4\sigma\cos\theta}{\lambda} \quad (2.9)$$

The details of the average pore diameter calculation are presented in Appendix B.

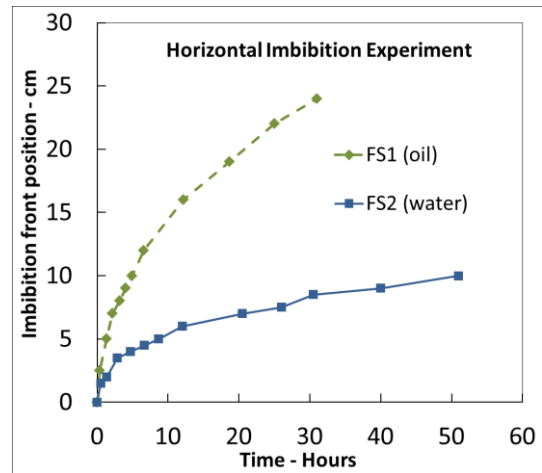
To calculate the front position, the fluid parameters in Table 2-1, the sample parameters in Table I and contact angle values in Table 2-5 are plugged in Eqs. 2.6 and 2.8. The mathematical solution and experimental results from horizontal and vertical imbibition experiments are shown in Figure 2-11 and Figure 2-12, respectively. The mathematical solution shows that the oil imbibition rate should be lower than water imbibition rate, which is contradictory to the experimental results.

In summary, mathematical models for the rate of imbibition volume and frontal advance suggest that water should imbibe faster than oil, while the corresponding measurements show that oil

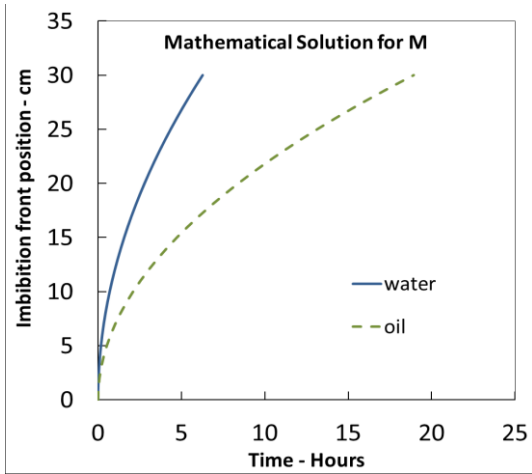
imbibes faster than water. This contradiction indicates that the Young-Laplace equation can not sufficiently account for the strong affinity of crushed-shale media to an oleic phase.



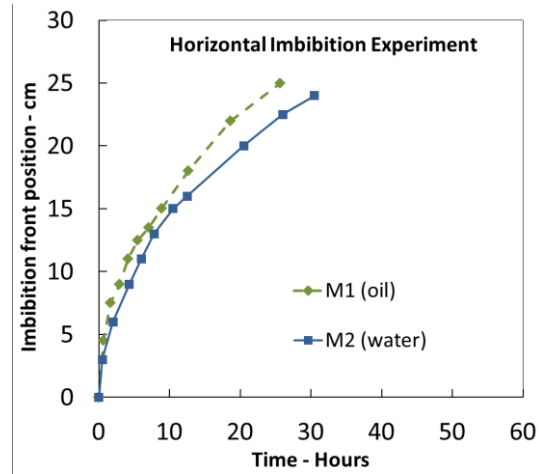
(a)



(b)



(c)



(d)

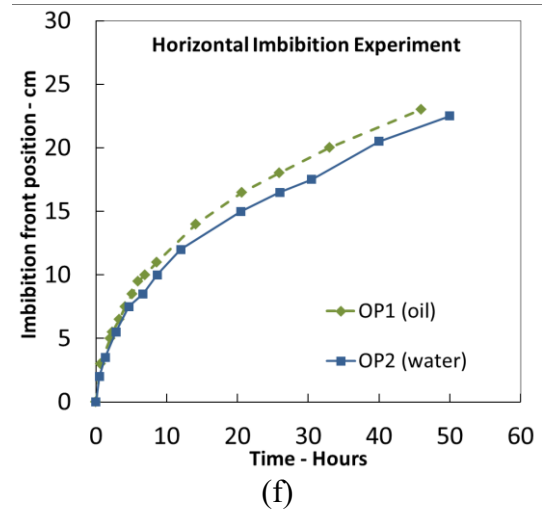
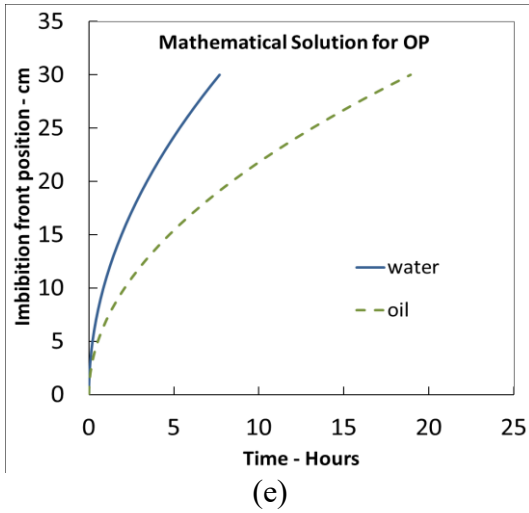
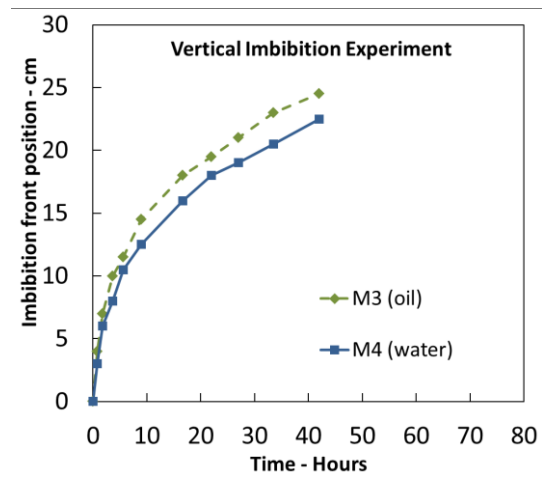
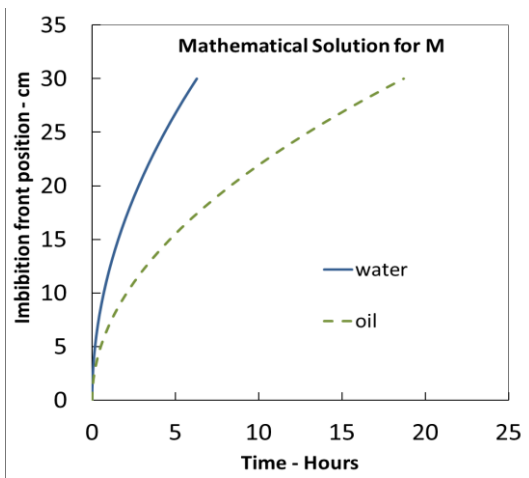
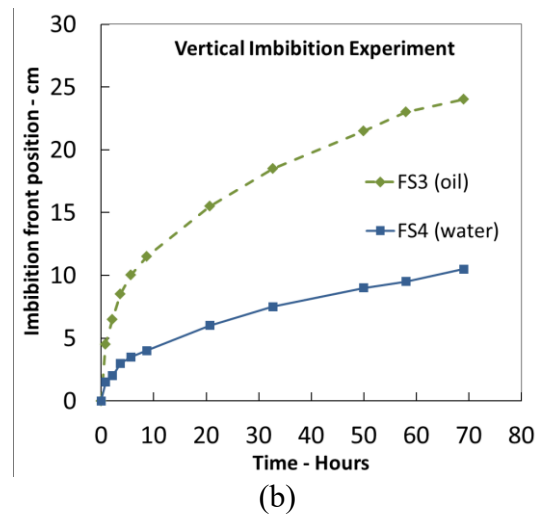
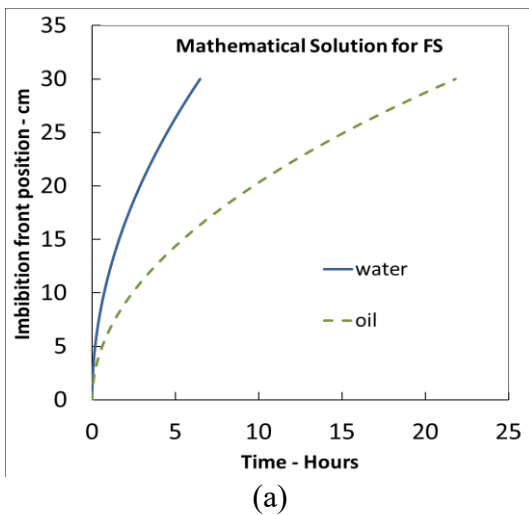


Figure 2-11. Mathematical solution of imbibition front position (L_s) versus time (t) from Eq. 2.6 for (a) FS, (c) M and (e) OP samples and experimental imbibition front position versus time for (b) FS, (d) M and (f) OP samples.



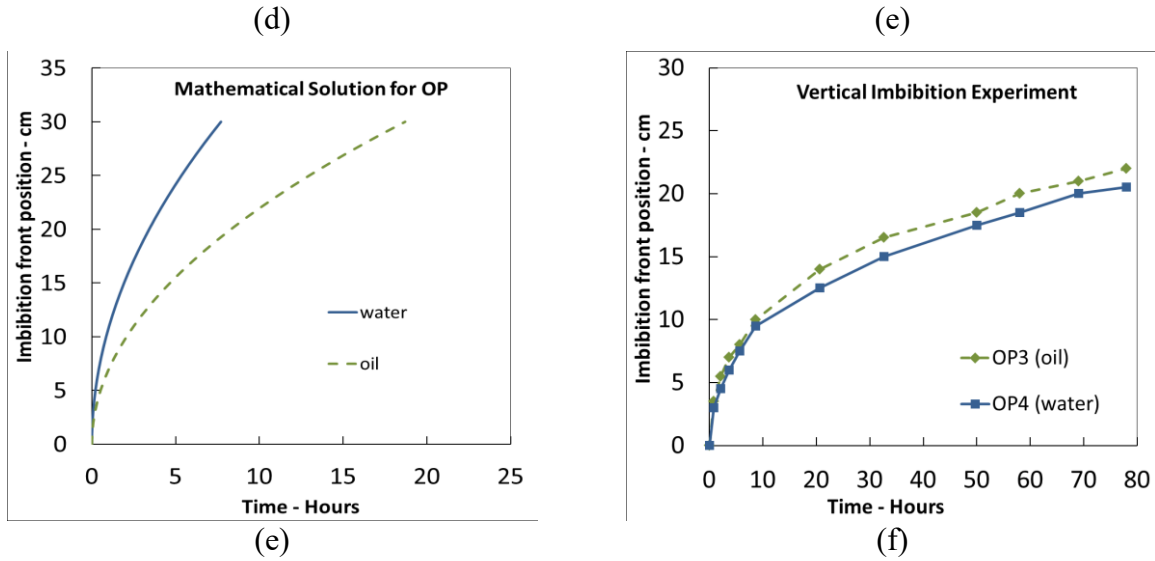


Figure 2-12. Mathematical solution of imbibition front position (L_s) versus time (t) from Eq. 2.8 for (a) FS, (c) M and (e) OP samples and experimental imbibition front position versus time for (b) FS, (d) M and (f) OP samples.

2.5.3 Dimensionless Time

It is well known that the rate of imbibition primarily depends on rock and fluid properties such as porosity and permeability of porous media, fluid viscosity, interfacial tension and wettability. It also depends on geometrical parameters like boundary conditions and sample shape. The basic model for scaling laboratory imbibition data was investigated by Rapoport (1955). For scaling imbibition results for oil/water/rock systems, Mattax and KYTE (1962) proposed the most frequently used dimensionless time (t_D):

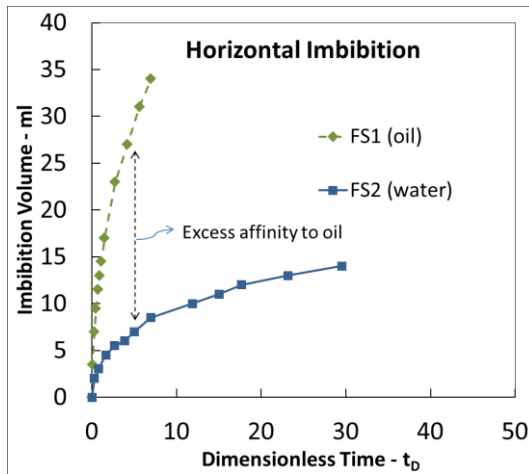
$$t_D = t \sqrt{\frac{k}{\phi} \frac{\sigma}{\mu_{gm}} \frac{1}{L_c^2}} \quad (2.10)$$

Where, μ_{gm} is the geometric mean of water and oil viscosities (Shouxiang et al., 1997) and L_c is the characteristic length that depends on samples' shape and boundary condition. For the two-ends-open boundary condition (Zhang et al., 1996):

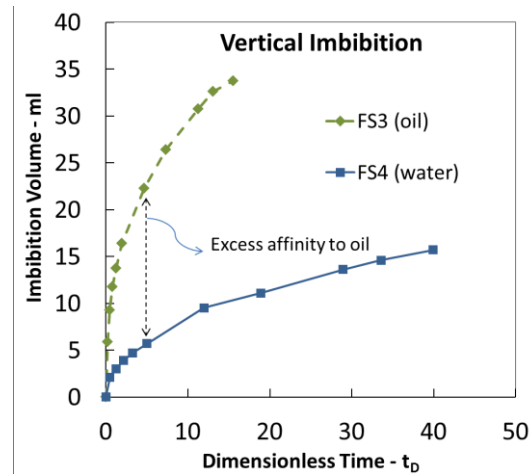
$$L_c = \frac{L}{2} \quad (2.11)$$

The normalized water and oil volume imbibed in the horizontal and vertical crushed-shale packs is plotted versus the corresponding dimensionless time in Figure 2-13. It is observed that all the

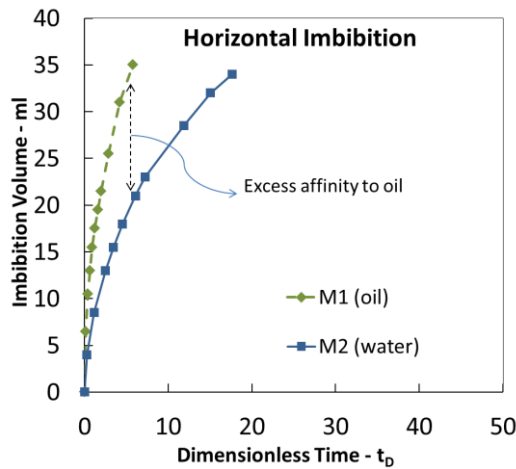
oil curves are much higher than the water curves. The difference between oil and water imbibition rate in dimensionless plots (Figure 2-13) is more pronounced than that in dimensional plots (Figure 2-6). The observed difference between water and oil curves can be explained by the wettability difference. The crushed-shale samples are preferentially oil-wet, while based on the previous research (Dehghanpour et al., 2013), the intact shale samples are preferentially water-wet.



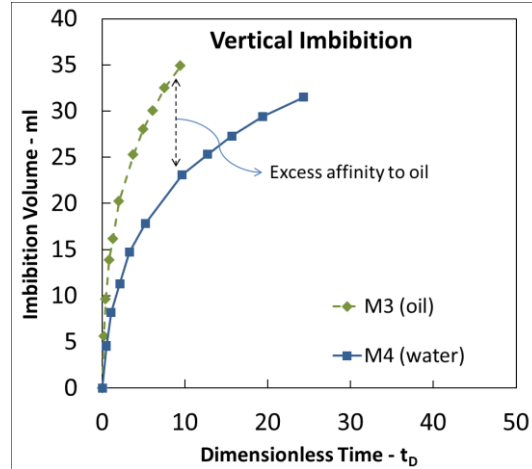
(a)



(b)



(c)



(d)

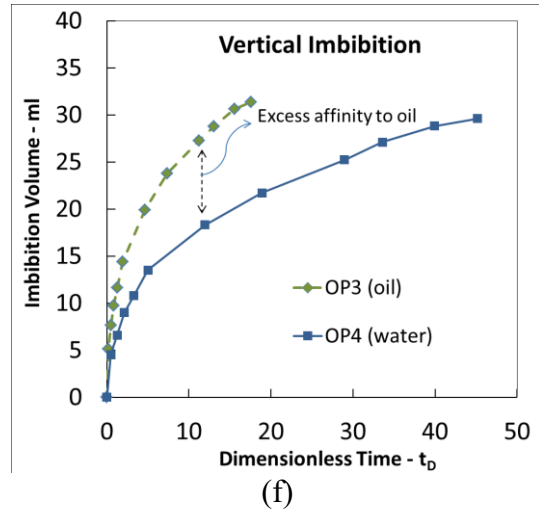
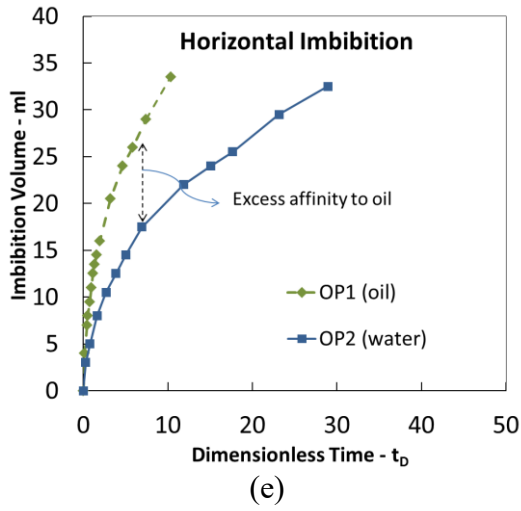


Figure 2-13. Imbibition volume versus dimensionless time of DI water and kerosene for horizontal (a,c,e) and vertical (b,d,f) crushed-shale packs from FS (a,b), M (c,d) and OP (e,f) sections.

2.6 Summary and Discussion

A total of 24 imbibition tests were conducted to compare the water, oil and brine uptake of intact and crushed samples from three different shale formations. The imbibition rate and front position were measured and compared with theories. The key results are summarized as follows:

- 1) Crushed shale samples imbibe more oil than water, but the intact samples from the same formations imbibe more water than oil.
- 2) Hydrophobic organic pores are relatively small compared with the hydrophilic inorganic pores.
- 3) The water (or oil) does not imbibe spontaneously into the crushed samples which are already saturated with oil (or water).
- 4) Increasing the concentration of NaCl inhibits the expansion and physical alteration of intact shale samples.
- 5) Increasing NaCl concentration decreases the brine uptake of all samples.
- 6) Based on capillary-driven imbibition models and Young-Laplace equation, water is expected to imbibe faster than oil into the crushed samples, while the measurements show that oil imbibes faster than water.

Result 1 and 2 indicate that the hydrophobic pore structure of intact samples may not be well-connected. Previous studies (Dehghanpour et al., 2012, 2013) show that water uptake of intact samples is significantly higher than their oil uptake. However, the crushed-shale samples imbibe more oil than water. In a crushed sample, both hydrophobic and hydrophilic pores are well-connected. Therefore, the observed difference between the oil uptake of crushed and intact samples is primarily due to the difference in connectivity of pore network in crushed and intact samples. In simple, the poorly-connected hydrophobic pore network of intact samples becomes artificially well-connected by crushing the samples. This interpretation is backed by the complete spreading of oil on fresh breaks of all samples.

Furthermore, another possible reason for the observed difference between imbibition behavior of crushed and intact samples is related to the laminated structure of intact samples. The lamination

causes more water imbibition along the bedding plane (Makhanov et al., 2012). In contrast to the intact samples, the crushed shale packs are relatively isotropic.

Result 3 indicates that initial exposure of the rock surface to a particular liquid phase increases its affinity to the same phase. In other words, if the pore surface is initially coated by water (or oil) the samples tends to be water-wet (or oil-wet) (Hirasaki et al., 1991). The counter-current imbibition tests reported here, started at zero saturation of imbibing phase.

Results 4 and 5 indicate that the salt precipitates initially present in the shale pore space influence the water uptake and physical alteration of the shale samples. The difference between salt concentration in the pore water and external water creates a chemical potential (osmotic effect) that acts as an additional driving force for water uptake. Therefore, increasing the salt concentration of external water reduces the osmotic effect, and in turn, reduces the water uptake.

Result 6 indicates that the actual driving force imbibing the oleic phase into the crushed samples is stronger than the capillary pressure modeled by Young-Laplace equation. Since the geometry and average pore diameter of the samples used for comparative water and oil imbibition tests are very similar, the observed contradiction indicates that the strong affinity of shale powders to the oleic phase can not be simply modeled by the contact angle of zero (i.e. complete spreading of oil on fresh break of rock samples). It can be hypothesized that the adsorption of oil on the surface of crushed shale grains, partly coated by organic materials, act as an additional driving force for oil uptake, and this mechanism is not accounted for in the Young-Laplace equation through the conventional definition of contact angle. However, detailed examination of this hypothesis needs further experiments which remain the subject of future studies.

Chapter 3: Effect of Electrostatic Interactions on Water Uptake of Gas Shales: The Interplay of Solution Ionic Strength and Electrostatic Double Layer

3.1 Introduction

The objective of this chapter is to investigate the effect of osmotic pressure and electrostatic interactions on water imbibition into shales. Results of section 2 shows dependency of imbibition profile on the salt concentration of imbibing fluid. It suggests that electrostatic interactions may play a role. In fact, imbibition of brine (an electrolyte solution) into a charged porous medium (i.e., shale) cannot be fully described without taking the electrostatic interactions into account. Although the role of salt concentration in the imbibing fluid is presumably described by osmotic pressure, it is largely unknown that what the effect of precipitated salt in the shale matrix is on the imbibition process. To answer this question, this chapter studies the effect of salt content in the media (shale powder) and salt concentration in the fluid (water) on the imbibition potential of the shale powder. The powdered shale samples are sequentially washed with DI water to reduce their salts content. The resulting brine solutions are 10-fold concentrated before imbibition tests. Imbibition is performed on the unwashed and washed shale powder samples. The DI water and different brine solutions are used as the imbibing fluid. The effects of imbibing solution ionic strength, rock zeta potential, and salts content of the shale powder on the imbibition process are discussed based on electrostatic interactions. The results of this study provide additional insight about the poorly understood driving forces that modulate the rock-fluid interactions. Electrostatic interaction theory provides further explanation about the brine-shale interactions. The rest of the chapter is organized as follows: Section 3.2 introduce the theory of disjoining pressure, electric double layer and zeta potential. Section 3.3 describes the materials and methods. Section 3.4 shows the imbibition profiles, measured zeta potential of shale powder and calculated double layer thickness of imbibed water. Section 4.4 describes the conclusions of this study.

3.2 Theory

Inability of Young-Laplace based capillary-driven models in explaining the unexpectedly high-water uptake of Horn River shales (Dehghanpour et al., 2013) is due to neglecting the additional

driving forces. In the Young-Laplace based capillary-driven models, the only term describing the fluid-rock interaction is contact angle, θ . Fluid-rock interfacial properties cannot be completely described by θ . van der Waals, electrostatic, structural, and adsorptive forces can influence the interaction between the fluid and rock and modulate the affinity of the rock to a fluid (Van Oss 2006). To overcome the limitations of the Young-Laplace based capillary-driven models for predicting the fluid uptake in a porous medium, the term disjoining pressure (Desjaguin et al., 1987), P_d , should be considered as part of the total capillary pressure (Hirasaki 1991). Depending on the type of fluid-rock system, the strength of the disjoining pressure may significantly deviate the fluid uptake of shales from what Young-Laplace based capillary pressure models predict (Nitao et al. 1996). To overcome the previously observed discrepancies, total capillary pressure (see Eq. 3.1), must be used to for imbibition studies. Disjoining pressure (see Eq. 3.2) is defined as a negative derivative of Gibbs energy (G) of interaction per unit area with respect to distance (x), at constant temperature, volume, and surface area. As can be seen from Eq. 3.3, the main components of P_d in a porous medium are van der Waals (P_{vdw} , mainly London dispersion), electrostatic (P_{elec}), structural (P_{struc}) and adsorptive (P_{ads}) pressures (Tuller et al., 1999):

$$P_c = \frac{4\sigma\cos\theta}{\lambda} + P_d \quad (3.1)$$

$$P_d = -\frac{1}{A} \left(\frac{\partial G}{\partial x} \right)_{T,V,A} \quad (3.2)$$

$$P_d = P_{vdw} + P_{elec} + P_{struc} + P_{ads} \quad (3.3)$$

P_{vdw} accounts for the van der Waals interactions between dipoles (either permanent or induced) of different components of the fluid and rock surface. P_{elec} is the result of the electrostatic interactions between the charged components of the fluid-rock system. P_{struc} is due to the repulsive forces that the hydration layers at the pore surface exert on particles at the vicinity of the surface. P_{ads} is the result of non-uniform concentration of the fluid components in the hydration shell of the pore wall (Tuller et al., 1999). In order to focus on the effect of electrostatic component of fluid-rock interactions, experiments are designed to maximize the effect of electrostatic interactions in this study.

A charged particle (e.g. negatively charged shale particle) in an aqueous solution interacts with neighboring water molecules and ions in the solution. As can be seen from Figure 3-1, to counter-

balance the charge of the particle, counterions from solution form an ion rich layer (electric double layer) around the particle. The inner layer which is in direct contact with the charged particle surface, the Stern layer (blue color in Figure 3-1), is comprised of a fixed number of immobilized counterions that interact with local charges on the particle surface. The layer between the Stern layer and bulk solution, the Gouy-Chapman or diffuse layer (green color in Figure 3-1), is characterized as having a fixed number of counterions, with respect to the particle surface. The ions in the diffuse layer can diffuse back and forth into the bulk solution while maintaining the overall charge of the layer. The diffuse layer is extended to the point where uniform distribution of ions, i.e. the bulk solution, exists. The characteristic thickness of the electric double layer, Debye length defined in Eq. 3.5, is a function solution ionic strength, temperature, and relative permittivity of the electrolyte solution.

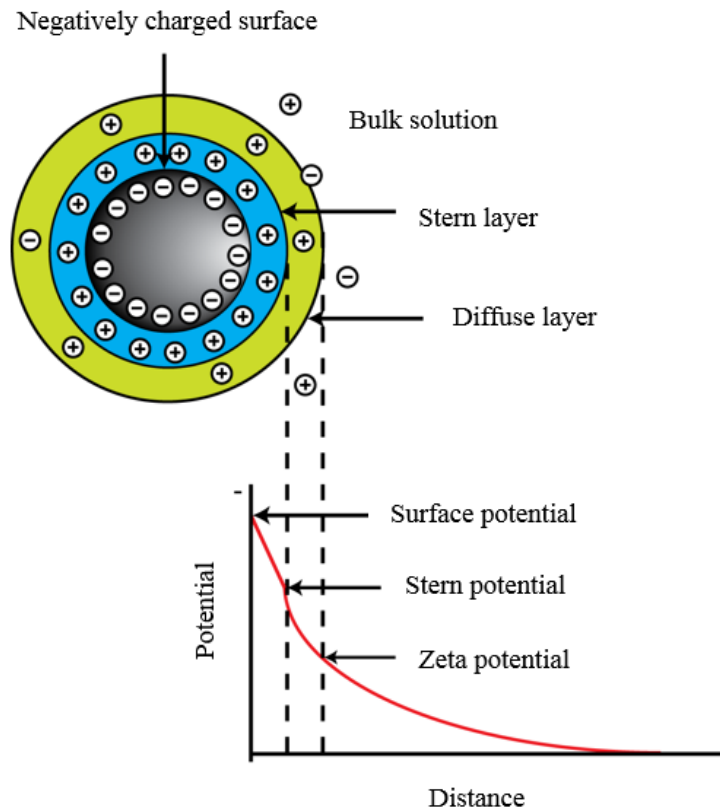


Figure 3-1. Schematic of double layer structure around a negatively charged surface in an electrolyte solution (Binazadeh, 2013).

From the electrostatic point of view, two main factors that affect the hydration shell of a charged surface are stability and thickness of electric double layer around the rock pore surface in electrolyte (e. g. aqueous) solutions. The stability of the electric double layer depends on the rock surface potential (usually estimated by rock zeta potential) (Beckett 1990). As can be seen from Eq. 3.5, the characteristic thickness of the electric double layer, κ^{-1} , is inversely proportional to the square root of ionic strength of the solution, I (Stuart and Mulder, 1985). The ionic strength of an electrolyte solution is calculated by:

$$I = \frac{1}{2} \sum_{i=1}^n C_i Z_i^2 \quad (3.4)$$

Here, C_i and Z_i are the molar concentration and valence of ion “ i ”, respectively. κ^{-1} is given by (Leckband and Israelachvili, 1993)

$$\kappa^{-1} = \sqrt{\frac{\epsilon_0 \epsilon_r k_B T}{2e^2 N_A}} \times \frac{1}{\sqrt{I}} \quad (3.5)$$

Here, ϵ_0 , ϵ_r , k_B , e , and N_A are vacuum permittivity, relative permittivity of medium, Boltzmann constant, electron charge, and Avogadro number, respectively. For a given solution at the constant temperature (constant ϵ and T) κ^{-1} is only a function of I . It means that for a given rock in contact with water at an isothermal condition, I is the only solution property that can directly modulate the strength of electrostatic interactions in a rock-water system. It must be noted that other mechanisms such as clay swelling may also play a role and convolute the rock-water interaction (Dehghanpour et al., 2013). Although both surface and osmotic hydration of clays (Roshan et al., 2015) can be explained by electrostatic interactions, other mechanisms such as cation exchange in clay particles and chemical reactions between the rock and solution may alter the rock-fluid interactions (Zolfaghari et al., 2015). This thesis only focuses on the electrostatic interaction between the rock and fluid and do not consider the source of ions (e.g. cation exchange in clay and chemical reactions between fluid and rock).

Zeta potential of a charged particle is a function of I , pH and ultimately the charge density on the particle surface (Sprycha, 1989; Mullet, 1997). The absolute value of zeta potential decreases as the I value of the solution increases (Hsu and Huang, 2002). The effect of pH on zeta potential is more complicated. Depending on the pH value and the charged groups on the surface, the zeta potential of a charged particle (which can interact with H^+ or OH^-) may become negative, zero, or

positive. For example, the isoelectric point (pI) for calcite is 8-9.5. At a pH lower than its pI, calcite is positively charged. At pH equal to its pI calcite does not carry any charge, and at a pH higher than its pI calcite is negatively charged (Hirasaki, 1991). At a given I and pH, the absolute value of the zeta potential of a particle increases by an increase in the particle surface charge.

3.3 Materials and Methods

3.3.1 Shale Samples

Shale samples from Evie (Sample 1), Lower Keg River (Sample 2), Upper Otter Park (Sample 3), and Lower Otter Park formations (Sample 4) in the HRB are crushed into fine powder. Mineral composition of different samples is reported in Table 3-1. The average particle size of the powder is confirmed by microscope to be $\sim 1 \mu\text{m}$ diameter.

Table 3-1. Representative mineralogy of shale samples used in 1-D imbibition experiments measured by XRD.

Sample	TVD (m)	Quartz (wt %)	Feldspar (wt %)	Plagioclase (wt %)	Calcite (wt %)	Dolomite (wt %)	Pyrite (wt %)	Illite/Smectite (wt %)	Illite/Mica (wt %)	Total Clay (wt %)
1	2677	52	5	6	13	3	3	7	12	19
2	2706	69	5	6	9	2	3	1	3	4
3	2602	79	3	2	0	1	1	6	7	13
4	2612	77	2	2	0	1	1	5	11	16

3.3.2 Washing Shale Powder and Preparing Brine Solutions

The following procedure, schematically shown in Figure 3-2, is performed to prepare washed shale powder and brine solutions for imbibition experiments:

- 1) For the first washing stage, 800 mL of DI water is added to 200 g of shale powder and the resulting mixture is agitated at 200 rpm for 1 hr at room temperature. The mixture is stored for 24 hrs to allow powder settle down. 500 mL of the supernatant is taken out and filtered by filter paper. The supernatant is 10 times concentrated and used as the brine solutions for the imbibition experiments and zeta potential measurements. The ionic concentration of the brine solutions is measured by ICP-MS.

2) 500 mL of DI water is added to the remaining shale powder solution. The resulting mixture is agitated at 200 rpm for 1 hr at room temperature. The mixture is stored for 24 hrs to allow powder settle down. 500 mL of the supernatant is taken out and filtered by filter paper. This step is repeated 9 times to ensure complete removal of the leachable ions from the shale powder of each sample. It can be seen from Figure C1 (in the Appendix) that upon 10 times washing the electrical conductivity (EC) of the supernatant becomes constant and further washing no longer reduces the EC of the supernatant. Maximum removal of leachable ions is required to minimize the effect of precipitated salts on imbibition process.

3) Shale powder at the end of 10th washing stage are dried at 100°C till weight stabilization (72hrs). Washed powder is used for imbibition experiments and zeta potential measurements.

The concentration of major ions in the brine samples obtained by ICP-MS, are reported in Table 3-2. K⁺ and Na⁺ are the most abundant cations in the brine solution of all samples. Similar observations were reported by Zolfaghari et al. (2015). They applied a sequential ion-extraction method to characterize the loosely-, moderately-, and strongly-attached ions in shales. Their results also indicate that majority of the extracted cations at early stages of the ion-extraction process (loosely-attached) are K⁺ and Na⁺. Higher initial concentrations of K⁺ and Na⁺ can be due to higher solubility of the salts that they form (for example NaCl, KCl, Na₂SO₄, K₂SO₄), leaching of clay minerals, or reactions between water and rock. According to Table 3-1, illite, mica, and mixed-layer illite/smectite (I/S) are the major minerals in the clay fraction of our shale samples. Na⁺ is not the major cation in the interlayer of mica and illite (Essington, 2005). Therefore, leaching of the exchangeable Na⁺ in the interlayer of smectite (in the mixed I/S layer) is a possible source for the extracted Na⁺. K⁺ is a common cation in the interlayer of illite and mica (Essington, 2005). Thus, leaching of the exchangeable K⁺ in the interlayer of illite and smectite is another possible source of the extracted K⁺. The ICP-MS analysis also reveals presence of trace amounts of Si⁴⁺, Mo⁶⁺, Ba²⁺, Mn²⁺, Zn²⁺, and Ni²⁺. Due to their relatively low concentration, the influence of these ions on water-rock interactions is neglected. It should be noted that even after the 10th washing stage, the resulting salt solutions contain considerable number of different ions (ICP-MS of the salt solutions after each washing stage is presented in the appendix). Thus, even the washed shale samples have some precipitated salts.

Table 3-2. Ion concentration and ionic strength, I, of different brine solutions

Brine Samples	Ion concentration (mM/L)						<i>I</i> (mM/L)
	K ⁺	Na ⁺	Ca ²⁺	Mg ²⁺	Cl ⁻	SO ₄ ²⁻	
1	2.0	2.3	4.4	5.1	1.4	1.5	70.5
2	10.0	6.1	7.1	1.3	2.1	3.6	71.6
3	17.3	24.3	2.6	2.1	4.4	8.3	106.3
4	22.4	19.2	1.3	1.5	3.3	5.0	82.5

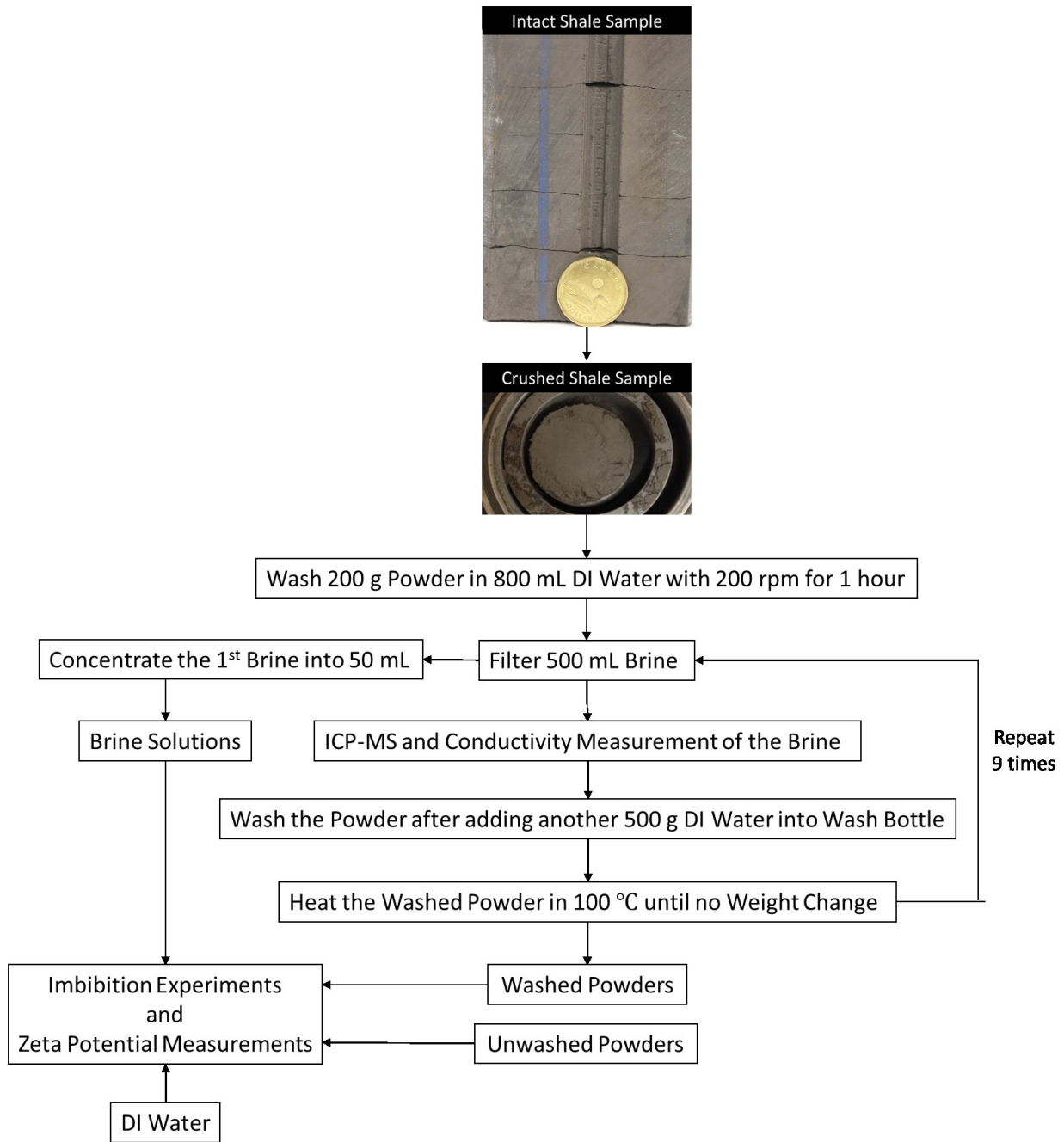


Figure 3-2. Flowchart of sample preparation and experimental procedure.

3.3.3 Imbibition Experiments

Unwashed and washed powders are packed into PVC tubes with 2.54 cm inner diameter and 12 cm length. A cloth mesh which is impermeable to the shale powder is attached to the bottom of the PVC tube to selectively allow fluid transfer up in the tube (see Figure 3-3). The top of the tube

is partially sealed so that shale powder or water cannot flow out of the tube. A small pathway is perforated at the sealed side of the tube to purge the displaced air during the imbibition (Figure 3-3). Similar to the previous chapter, the porosity of powder sample pack is calculated by Eq. 2.1 and the matrix density of all the HRB samples is assumed to be 2.72 g/cm^3 . The calculated average porosity of the packed crushed samples is 27 %. DI water and brines are used as the imbibing fluid into the unwashed/washed crushed sample packs as schematically illustrated in Figure 3-3.

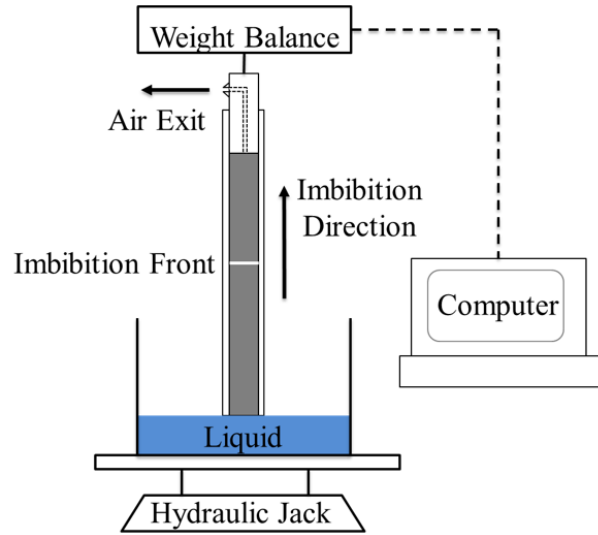


Figure 3-3. The schematic of 1-D imbibition set-up. Liquid imbibes from bottom to the top.

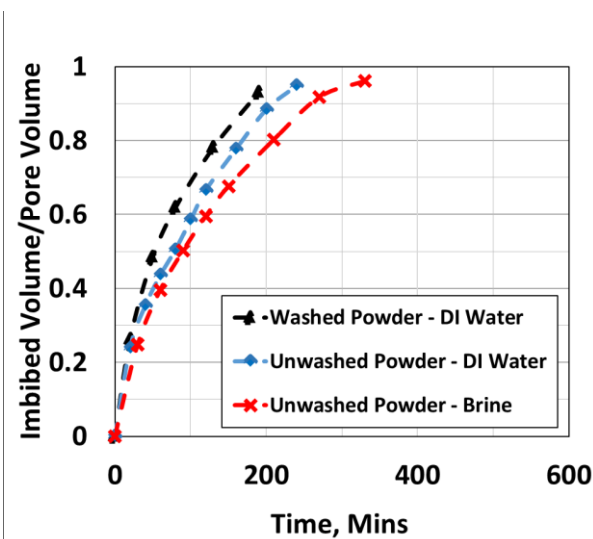
3.3.4 Zeta Potential Analysis

The surface potential of a particle is a measure of the charge density on its surface. Although it is higher than zeta potential (see Figure 3-1), they are typically used interchangeably. As further explained in the section 3.2, presence of salts in the medium affects the magnitude of zeta potential for a given particle. To understand how surface charges on rock particles affects the imbibition process, zeta potentials of the unwashed and washed powder in DI water and brine solutions are measured using Malvern Zetasizer Nano ZS. Samples of 0.1 mg/mL shale powder solution are prepared and transferred into the measurement cell. To avoid interference of impurities in zeta potential measurements, both DI water and brine solutions are initially filtered with $0.22 \text{ }\mu\text{m}$ pore size membrane syringe filters. After temperature stabilization, the zeta potential is measured for at least 5 times. The Zetasizer machine automatically stops the measurement once the zeta potential reading is stable.

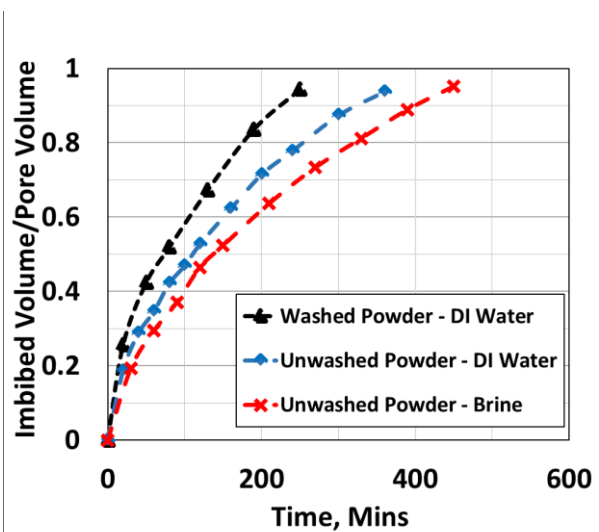
3.4 Results and Discussions

3.4.1 Water and Brine Imbibition in Unwashed and Washed Powder

Results from Chapter 2 shows that higher salt concentrations in imbibition fluid slow down the imbibition process. However, the effect of precipitated salts in the rock matrix on the imbibition process is largely unknown. To understand the effect of dissolved salt in imbibition fluid or precipitated salt in rock matrix, imbibition experiments are performed on three systems of unwashed powder/brine, unwashed powder/ DI water, and washed powder/DI water respectively. Figure 3-4 shows the imbibition profile for unwashed powder/brine, unwashed powder/ DI water, and washed powder/DI water systems for different shale pack samples as a function of time. As can be seen from Figure 3-4, the imbibition of brine solutions into the unwashed shale powder is slower than that of the DI water. This observation could be explained by osmotic effect as described in Chapter 2. Lower salt concentration in the imbibing fluid results in a higher chemical potential (osmotic effect) that acts as a driving force for shale water uptake. According to Figure 3-4, washed powder imbibes DI water faster than unwashed powder.



(a)



(b)

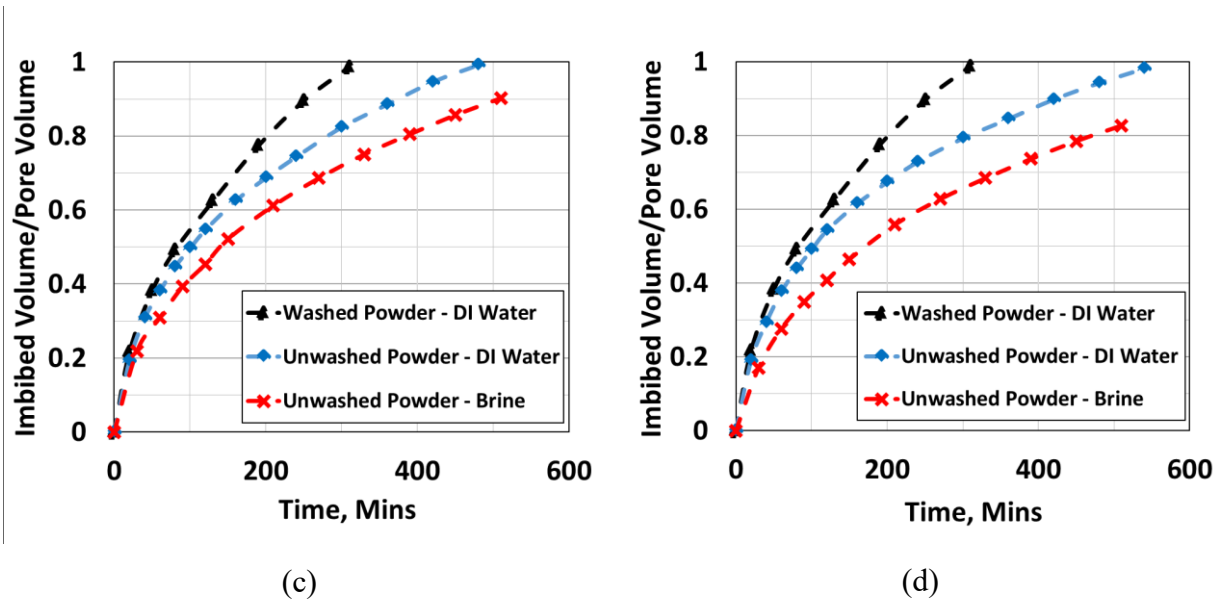


Figure 3-4. The normalized imbibed volume of DI water and brine in unwashed and washed HRB shale powder (a) sample 1, (b) sample 2, (c) sample 3, and (d) sample 4.

It should be noted that all shale samples comprise clay minerals (Table 3-1), which have high affinity for water adsorption (Essington, 2005). Therefore, water can be adsorbed by clays while washing the shale powder. Due to this high adsorption affinity of clay minerals, all adsorbed water may not be released by drying the samples at 100°C. Although the initial hydration of clay minerals reduces their affinity for water, the washed samples imbibe more water compared with the unwashed samples. As explained before, the osmotic effect can explain the difference in the imbibition profile of the unwashed powder/brine and unwashed powder/DI water. Based on the osmotic principle, presence of a semi-permeable membrane which preferentially allows transport of solvent and hinders transport of salt is required for occurrence of an osmotic process. During imbibition of aqueous solution into intact shale samples, the shale matrix may act as the semi-permeable membrane (Schlemmer et al., 2003). Thus, a lower salt concentration in the imbibing aqueous solution results in a faster imbibition process. Interestingly, osmotic effect cannot explain why washed powder imbibes DI water faster than unwashed powder. In fact, osmotic effect predicts the opposite trend. This discrepancy may be due to the fact that crushing the shale samples, destroys the shale matrix. Thus, the hypothetical semi-permeable membrane no longer exists. In order to explain the experimental results, the electrostatic interaction between shale powder and DI water/brines is explained in the theory section. The electrostatic interaction would exist if the

shale particles are charged. Zeta potential measurement, which is an indication of charge density on the shale surface, is performed on the shale powder in DI water and brine solutions.

3.4.2 Zeta Potential Analysis of Shale Powder

In order to employ electrostatic theory, the shale particles must be charged under the imbibition conditions. The results of zeta potential measurements of the shale powders in DI water and brine are summarized in Table 3-3. The zeta potentials of unwashed and washed powders in the DI water are almost the same. This is probably due to the fact that the powder concentration in the zeta potential samples is only 0.1 mg/mL. Such a low concentration of powder cannot change the salt concentration in the solution, and does not influence the zeta potential value. However, the relatively high ion concentration in the brine results in a significant decrease in the zeta potential of the unwashed shale powder.

Table 3-3. Zeta potential of the unwashed and washed HRB shale powder samples in DI water and brine

Samples	Zeta Potential (mV)			
	1	2	3	4
Unwashed Powder in DI Water	-25.6	-31.1	-48.7	-35.2
Washed Powder in DI Water	-25.9	-30.8	-48.4	-35.7
Unwashed Powder in Brine	-20.9	-25.7	-42.3	-29.5

3.4.3 Slope Analysis of Water and Brine Imbibition

In a co-current imbibition experiment, assuming gravity force is negligible compared with capillary force and piston-like displacement of the imbibition process, the correlation between the time and the imbibed volume can be written as (Handy, 1960; Li and Horne, 2001):

$$Q^2 = \left(\frac{2P_c k_m \phi A^2 S}{\mu} \right) t \quad (3.6)$$

Here, Q is the volume of imbibed liquid, P_c is calculated by Eq. 3.1, k_m is effective liquid permeability, ϕ is fractional porosity, A is cross-sectional area of sample, S is liquid saturation behind the imbibition front ($S=1$ for piston-like displacement), and μ is the liquid viscosity.

According to Eq. 3.6, the slope of the imbibed volume curve versus square root of time is

$$S_{imb} = \sqrt{\frac{2P_c k_m \phi A^2 S}{\mu}} \quad (3.7)$$

Here, S_{imb} , A , S , and μ are known. Assuming $k_m=1$ mD, P_c can be calculated.

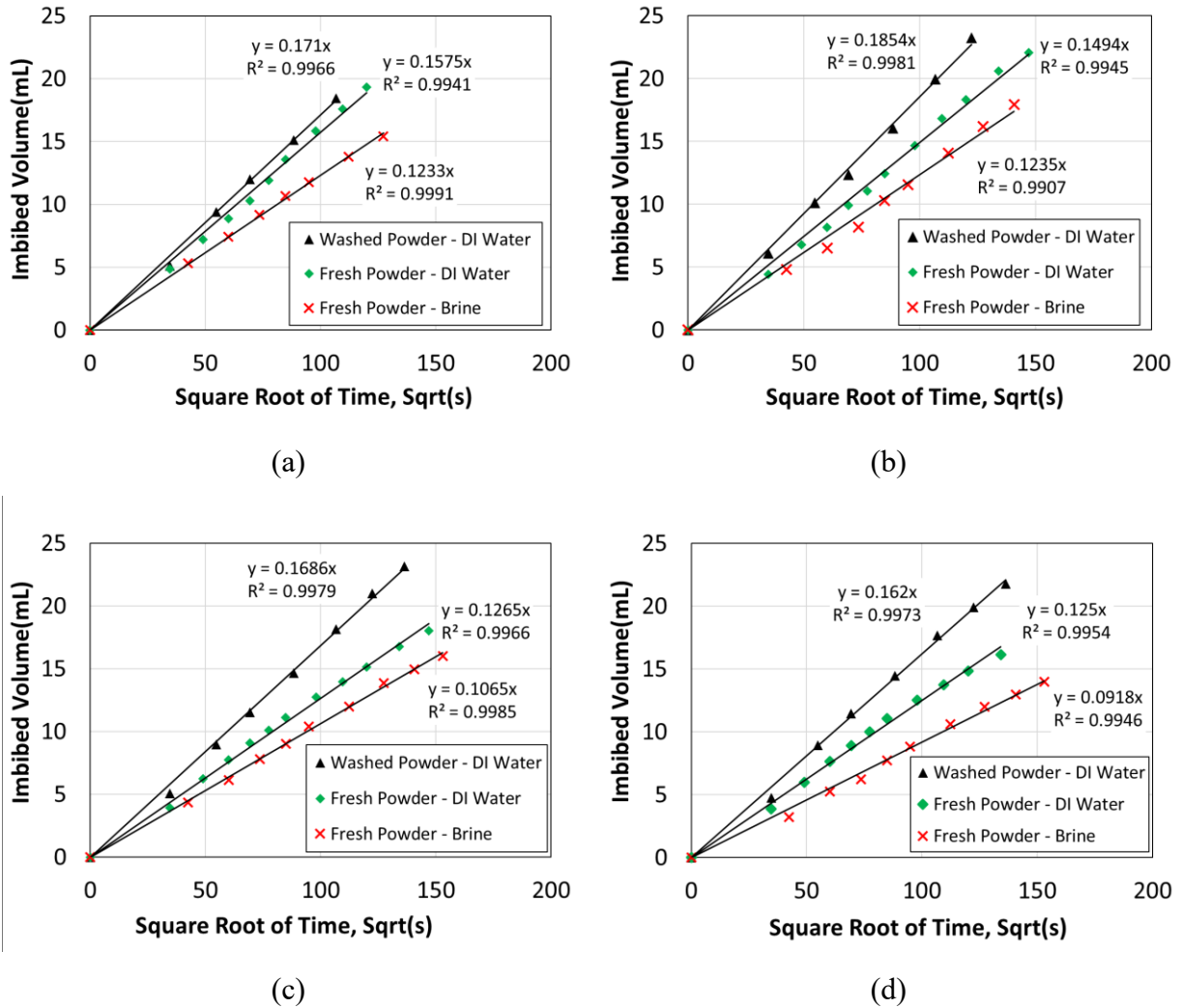


Figure 3-5. The imbibed volume of DI water and brine solutions in (a) sample 1, (b) sample 2, (c) sample 3, and (d) sample 4 of HRB shale powder packs as a function of square root of time.

Table 3-4 shows the calculated P_c using the slopes in Figure 5. The highest P_c corresponds to DI water imbibition in the washed powder from each formation. Use of unwashed powder and DI water reduces the P_c for all powder samples. Evidently washed powder has a higher affinity to DI water as compared with the unwashed powder. This is due to the lower I and higher κ^l of the in-situ formed brine of the washed shale powder in contact with the DI water. The lowest P_c

corresponds to the brine imbibition in the unwashed shale powder. The change in the magnitude of the P_c is mainly attributed to the change in the P_{elec} which cannot be explained by Young-Laplace term of the capillary pressure. Changing the fluid from DI water to brine solution increases the I value which results in reduction of κ^{-l} and zeta potential. A reduction in zeta potential and κ^{-l} , decreases the affinity of powder to the brine solutions.

Table 3-4. Calculated capillary pressure at front saturation from imbibition slope

		Sample			
		1	2	3	4
	Washed Powder – DI Water	180.5	166.6	218.2	185.6
P_c, KPa	Unwashed Powder – DI Water	101.6	99.2	141.7	157.5
	Unwashed Powder – Brine	88.0	65.4	118.3	117.9

3.4.4 Debye Length of the In-situ Formed Brines

As mentioned earlier, for a fluid with constant ϵ and T , κ^{-l} is only a function of I . The individual ion concentration, determined by ICP-MS, are used to calculate the I value of the brine solutions using Eq. 3.4. The I -values of different brines, listed in Table 3-2, are used to calculate κ^{-l} for each of the brines using Eq. 3.4. The I value of the in-situ formed brine after imbibition is estimated based on the ion concentration results obtained by ICP-MS analysis of the salt solutions obtained after the first and 10th washing stage (Figure C2 in the appendix) and the I value of the imbibing fluid. As I drops, the charged particles in the solution interacts with a larger volume of the solution to reach charge neutrality (Figure 3-1), which increases the κ^{-l} value. For instance, the in-situ formed brine during the imbibition of DI water into washed powder has the lowest I value compared to that of other imbibition systems. A lower I value results in the formation of a thicker electric double layer around shale powder (higher κ^{-l}). The κ^{-l} value shows the affinity of the aqueous solution to form a larger hydration shell around the charged shale surface.

As can be seen from Figure 3-4, the imbibition of DI water into the unwashed shale powder is faster than that of brines. This is mainly due to the lower I values and the consequent increase in the κ^{-l} of the in-situ formed brine associated with the imbibition of DI water into unwashed shale powder (Figure 3-6a). A larger hydration shell around the charged shale (higher κ^{-l}) results in a faster imbibition for the washed powder/DI water system. Figure 3-6a shows that changing the

fluid from DI water to brine further decreases in κ^{-1} of the in-situ formed brine and slows down the imbibition process in the unwashed shale powder (Figure 3-4). By comparing the initial slope of the imbibition curves in Figure 3-5 with the corresponding κ^{-1} values in Figure 3-6. it can be concluded that a longer range electrostatic interaction between the charged shale particles and the imbibing electrolyte solution (higher κ^{-1} value) results in a faster imbibition rate. These results suggest that the imbibition behavior is influenced by the electrostatic interactions between the water and shale samples. The same argument can be used to interpret the difference observed during the imbibition of DI water into washed and unwashed shale powder. Removal of leachable ions from the shale powder during washing process, reduces the I of the in-situ formed brine during imbibition, which will ultimately result in higher κ^{-1} . Higher κ^{-1} of the in-situ formed brine during the imbibition of DI water into washed shale powder further accelerates the imbibition of DI water and results in faster imbibition of DI water into washed shale powder as compared to that of the unwashed shale powder.

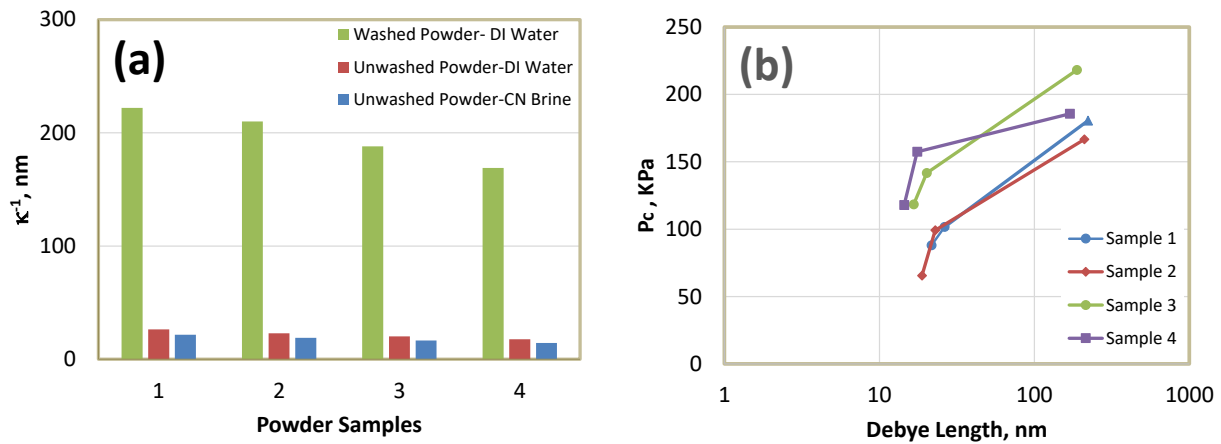


Figure 3-6. (a) Calculated Debye length, κ^{-1} , of the in-situ formed brine after mixing the imbibed fluid (DI water or brine solution) with the unwashed or washed HRB shale powder samples during the imbibition. (b) The correlation between P_c and κ^{-1} .

Figure 3-6b shows the correlation between P_c and κ^{-1} of the in-situ formed brine for each imbibition experiment. It is observed that an increase in the κ^{-1} value results in a higher P_c . A higher value of κ^{-1} indicates longer range electrostatic interaction (thicker electrostatic double layer) as well as a stronger electrostatic interaction between the shale surface and charged particles in the vicinity of

the surface. The highest κ^{-1} value (highest P_c) corresponds to imbibition of DI water into washed powders which is schematically shown in Figure 3-7b. Figure 3-7b shows that the electrostatic double layer around charged clay particles is the thickest. Curve “b” in Figure 3-7a shows that the thickest electrostatic double layer results in the fastest imbibition rate. Use of unwashed powder for the imbibition of DI water reduces the κ^{-1} and P_c value which corresponds to Figure 3-7c and curve “c” in Figure 3-7a. The lowest κ^{-1} value (lowest P_c) corresponds to the imbibition of brine into unwashed shale powders which is shown in Figure 3-7d and curve “d” in Figure 3-7a. It is evident that the κ^{-1} value influences the P_c and imbibition profile.

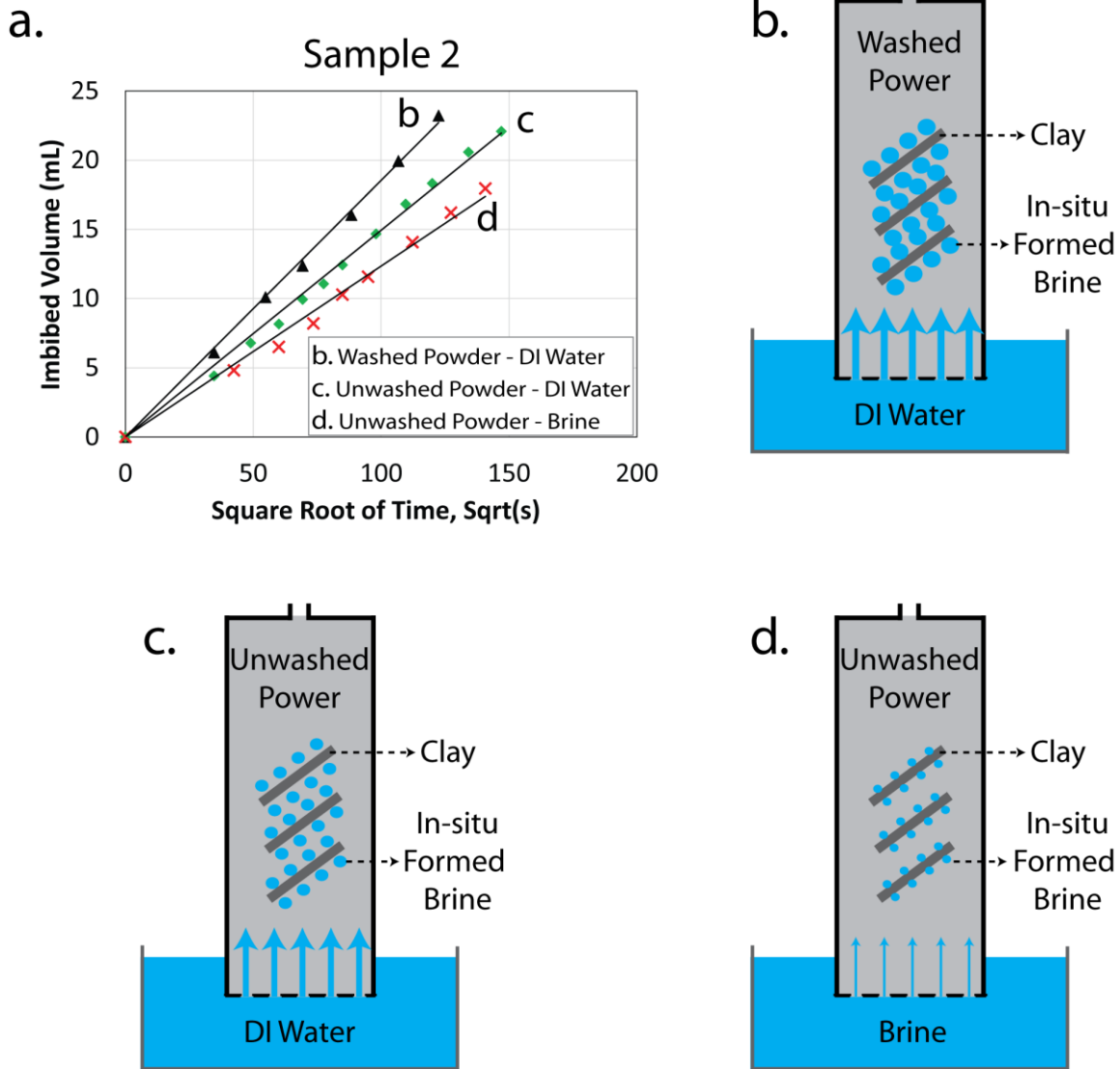


Figure 3-7. (a) Representative imbibition (Vol. fraction vs. square root of time) of aqueous solutions (DI water and brine) in shale powders of sample 2 (washed and unwashed) pack, (b) schematics of DI water imbibition into washed shale powders, (c) schematics of DI water imbibition into unwashed shale powders, (d) Schematics of brine imbibition into unwashed shale powders. Faster imbibition is shown by thicker arrows and thicker electrostatic double layer is shown by larger blue circles.

3.5 Summary

Previous studies reported strong water uptake of shales which cannot be explained by Young-Laplace based capillary-driven imbibition models. Due to the multi-physics nature of the imbibition process, different mechanisms such as the presence of precipitated salts (osmotic effect), hydrophilic pore networks, and imbibition-induced microfractures have been proposed for

unexpected high-water uptake in gas shales. Each of these mechanisms partly explains the experimental observations. The discrepancy between the experimental results and the imbibition models are also partly due to the disregard of disjoining pressure in the conventional models.

In this chapter, the electrostatic interaction concepts are used to describe the strong water uptake of Horn River shale samples. Imbibition profiles for unwashed powder/brine, unwashed powder/DI water, and washed powder/DI water systems for different shale pack samples revealed that the fastest imbibition rate belongs to the washed powder/DI water system. It is concluded that the in-situ formed brine during the imbibition of DI water into washed powder (lowest ionic strength) results in the formation of the thickest electric double layer around shale powder. The thickness of double layer represents the affinity of the aqueous solution to form a larger hydration shell around the charged shale surface.

The experimental results indicate that reduction of the I value, and the consequent increase in the κ^{-1} value, decreases the magnitude of shale zeta potential. It is concluded that a larger hydration shell around the shale surface results in a faster imbibition of the aqueous solution into the shale. Analysis of the initial slope of the imbibition curves show that electrostatic interactions can drastically change the magnitude of P_c . It is not only the I value of the imbibing fluid that affect the imbibition profile. It is the I value of the in-situ formed brine, influenced by both the I value of the injected fluid and the concentration/type of leachable ions in the shale powder, that determines the strength of the electrostatic interactions between the charged shale surface and the imbibed fluid. The results of this study further explain the previously observed strong water uptake by shales and the higher hydrocarbon recovery as a result of low salinity water flooding. This study provides improved understanding of the parameters impacting the water-rock interactions.

Chapter 4: Effects of Dissolved Oxygen on Water Uptake of Gas Shales

4.1 Introduction

Laboratory imbibition experiments have been widely used to investigate the effects of shale-water interactions. A common challenge to applying the results from laboratory imbibition data for the evaluation of fluid-rock interactions during hydraulic fracturing and soaking periods is the differences between laboratory and field conditions. These differences are discussed in the following paragraphs.

1) Temperature. Previous studies indicate that increasing temperature may accelerate the water imbibition by increasing the wetting affinity of rock to water (Tang and Morrow, 1997; Høgenesen et al., 2006). Increasing the temperature increases the activity of divalent ions such as Mg^{2+} and SO_4^{2-} to pair with the surface anions of carbonate minerals, and promotes the affinity of rock toward water (Strand et al., 2008).

2) Pressure. Rock samples are free to expand during laboratory water imbibition experiments (Santos et al., 1996; Wang et al., 2011; Zhou et al., 2014). However, under the field conditions, overburden pressure limits rock expansion (Chenevert, 1992). Ghanbari and Dehghanpour (2015) conducted water imbibition experiments on confined/unconfined shale samples and found that confined samples have less induced microfractures and less water imbibition.

3) Water-Rock Interface Area. The water-rock interface area differs dramatically at the laboratory and field scale imbibition process. Previous studies show that increasing shale-water interface area per unit volume of shale significantly increases the rate and final volume of water imbibition (Zolfaghari et al., 2016). Roshan et al. (2015) showed that the water-rock interface area affects the exchangeable cations in flowback water. Bearinger (2013) showed that the salt concentration in flowback water is related to the complexity of fracture network.

4) Oxygen Concentration. Low oxygen-content under reservoir conditions should also be considered in designing field representative imbibition experiments. Shale reservoirs usually have no (or limited) oxygen content (anoxic conditions) before fracturing process. Anoxic reservoir conditions can be due to oxygen consumption by organic matter and lack of oxygen supply in the

reservoir (Curtis, 2002). Oxygen is introduced by fracturing water into the shale reservoir, creating oxic conditions. Shales usually contain chemically-reactive compounds such as organic matter and pyrite, which may result in participates by oxidation reactions (Evangelou and Zhang, 1995; Hutcheon, 1998; Elie et al., 2000; Marynowski et al., 2011; Marriott et al., 2015). Recent studies show that oxidation of pyrite may change the pore structure and increase the pore connectivity (Jin et al., 2013; Chen et al., 2017). Rowan et al. (2015) observed a positive correlation between oxygen and chloride content in flowback water, which suggests that the oxygen dissolved in injected water may affect the geochemical reactions. Zolfaghari et al. (2016) found that the concentration of dissolved oxygen in flowback water may be lower than that in deionized water. They concluded that the dissolved oxygen may cause oxidation reactions, which could affect salt dissolution, salt precipitation and pH change in the flowback water. Thus, understanding the effects of dissolved oxygen on water imbibition and ion dissolution is important for more accurate interpretation of flowback water chemistry.

The objective of this chapter is to 1) investigate the role of dissolved oxygen on water imbibition rate/mass and 2) evaluate the effects of dissolved oxygen on concentration of major ions (i.e. potassium and sodium) and redox-sensitive ions (i.e. iron and sulfate) in flowback water. Comparative imbibition experiments are performed using air-saturated de-ionized water (oxic water) and degassed de-ionized water (degassed water). The rest of the chapter is organized as follows: Section 4.2 describes the materials and methods. Section 4.3 shows the imbibition profiles and concentration profiles of different ions for the oxic and degassed water. Section 4.4 summarizes the key findings of this study.

4.2 Materials and Methods

4.2.1 Shale Samples

Three pairs of shale samples (EV-1, EV-2, and EV-3) from three different depths of the Evie Formation in the Horn River Basin are used for the imbibition experiments. To eliminate the effect of sample size, all samples are cut into 35×35×25 mm cubes with approximate mass of 100 g. Table 4-1 provides the average depth, porosity, permeability, and mineralogy of the samples. The

porosity, permeability, and mineralogy are measured by helium porosimeter, pulse decay permeameter, and XRD respectively using different samples from similar depths.

Table 4-1. Approximate depth, porosity, permeability and average rock mineralogy for shale samples.

Sample	EV-1	EV-2	EV-3
Depth, m	2672.5	2681.2	2688.2
Porosity, %	6.4	5.0	4.6
Permeability, nD	575	384	372
<i>Non-Clay Content (wt. %)</i>			
Quartz	78.1	51.9	65.4
K-feldspar	5.2	4.9	3.4
Plagioclase	1.3	5.7	5.0
Calcite	3.1	13.3	8.4
Dolomite	0.7	2.6	1.1
Pyrite	1.8	3.0	3.0
Total Non-Clay	90.5	81.4	86.5
<i>Clay Content (wt. %)</i>			
Illite/Smectite	2.9	6.6	5.2
Illite+Mica	6.7	12.0	8.3
Total Clay	9.6	18.6	13.5

4.2.2 Imbibition Experiment

In order to investigate the effects of dissolved oxygen on the water imbibition in shales, one sample from a pair is immersed in air-saturated de-ionized (DI) water (oxic water) and the other sample in degassed DI water (degassed water). The DI water which was in contact with air (air-saturated) for 1 week is considered as oxic water. The dissolved oxygen content of oxic water is about 8.3 mg/L, as measured by rugged dissolved oxygen (RDO) optical electrode. To prepare the degassed water, 500 mL of DI water is placed in a desiccator (vacuum chamber) as shown in Figure 4-1. The desiccator is then sealed and connected to a vacuum of ~1 kPa for one week. The dissolved oxygen content of degassed water is about 0.7 mg/L. Generally, the pressure difference can potentially impact the imbibition results. However, the pressure difference between oxic and degassed experiments is relatively low (100 kPa) compared with that between laboratory and field conditions (usually more than 10,000 kPa). For example, the reservoir pressure in the Horn River

Basin can be as high as 53,000 KPa (B. C. Oil & Gas Commission, 2014). In this study, compared with the huge laboratory and subsurface pressure difference, it is assumed that the relatively small pressure difference between the oxic and degassed experiments has a negligible impact on the pore volume and imbibed mass. The imbibition experiments are conducted according to the following steps:

- 1) All the samples are dried in the oven at 100 °C for 24 hours to remove the moisture in the samples.
- 2) For each pair of samples, one sample is placed in an imbibition cell filled with 500 mL of oxic water. The other sample is placed in an imbibition cell filled with 500 mL degassed water.
- 3) All the imbibition cells filled with degassed water are placed in a vacuum chamber connected to a vacuum pump at 1 kPa to ensure degassed conditions. It is assumed that vacuum pressure during degassed condition has a negligible effect on the pore volume and imbibed mass. The schematic of the vacuum set-up is shown in Figure 4-1.
- 4) At each time step, the shale samples are taken out of the imbibition cell to measure the samples' mass. The normalized imbibed mass is reported by dividing the mass gain by the initial mass of the dried sample. A toploading balances with the accuracy of ± 0.01 g is used to measure the samples' mass. The dissolved oxygen concentrations of the oxic and degassed water are measured using RDO optical electrode.
- 5) 2 mL of the oxic and degassed water are periodically collected for measuring ion concentrations using inductively coupled plasma mass spectrometry (ICP-MS) and ion chromatography (IC).

During the measurements in steps 4 and 5, the shale and water samples are exposed to air. This may cause oxygen adsorption on the rock's surface and oxygen dissolution in degassed water. The vacuum pressure is maintained at 1 kPa during the experiments to reduce potential oxygen adsorption on the shale samples during the measurements. The 2 mL collected degassed water is

sealed in a 2 mL air-tight vial to prevent oxygen contamination.

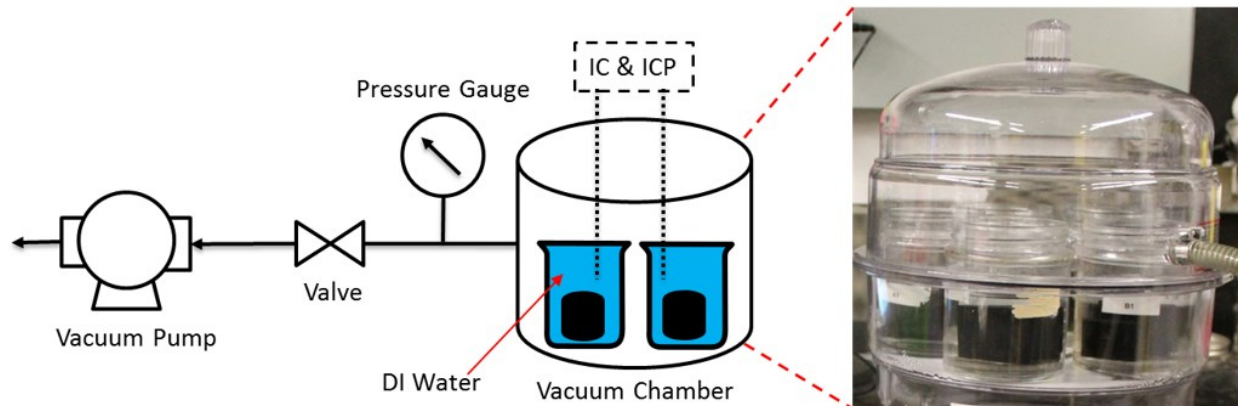


Figure 4-1. The schematic of the vacuum set-up used for the imbibition tests under degassed conditions.

4.2.3 SEM-EDS Imaging

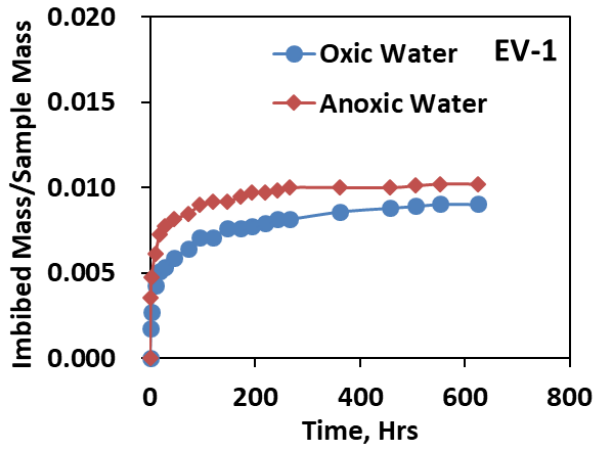
SEM, SHIM, and EDS are used to visualize the pores and obtain the elemental maps from EV-2 sample. End piece from EV-2 sample is prepared for SEM-EDS imaging. The sample preparation procedure is similar with the procedure described in section 2.3.4.

4.3 Results and Discussion

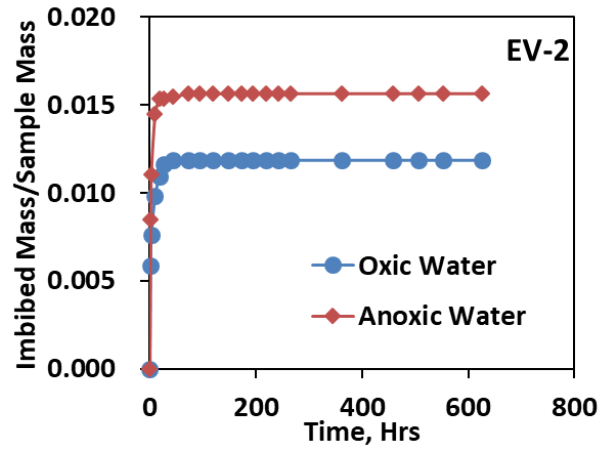
In this section, the imbibition profiles of the oxic and degassed imbibition experiments are compared. Then, the observed difference in ion concentration profiles of the oxic and degassed water samples are discussed.

4.3.1 Imbibition Profiles

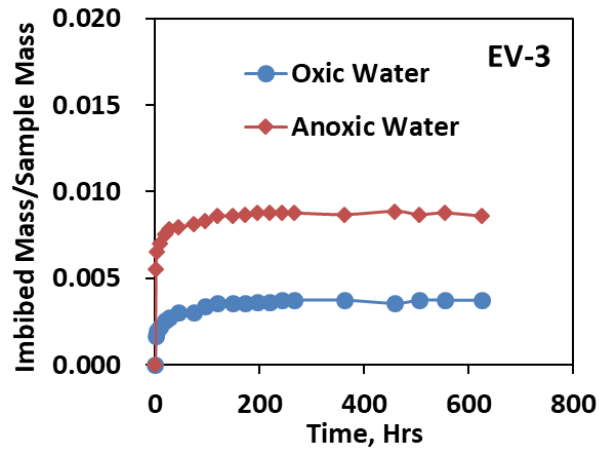
Figure 4-2 shows the water imbibition profiles versus time. The imbibed water mass is normalized through dividing it by the mass of the dry shale sample. The imbibition profiles increase over time and reach to a plateau for both oxic and degassed experiments. It can be observed that 1) the imbibition rate and the final normalized mass of imbibed water are higher for degassed experiments compared with those for oxic experiments, and 2) the EV-1 samples show the smallest gap between oxic/degassed water imbibition profiles while the EV-3 samples show the largest gap. These two observations are explained by investigating the dissolved oxygen in Section 3.2 and ion concentration profiles for both oxic and degassed water samples in Section 3.3.



(a)



(b)



(c)

Figure 4-2. Normalized mass of imbibed oxidic and degassed water for (a) EV-1, (b) EV-2, and (c) EV-3 samples.

4.3.2 Dissolved Oxygen Profiles

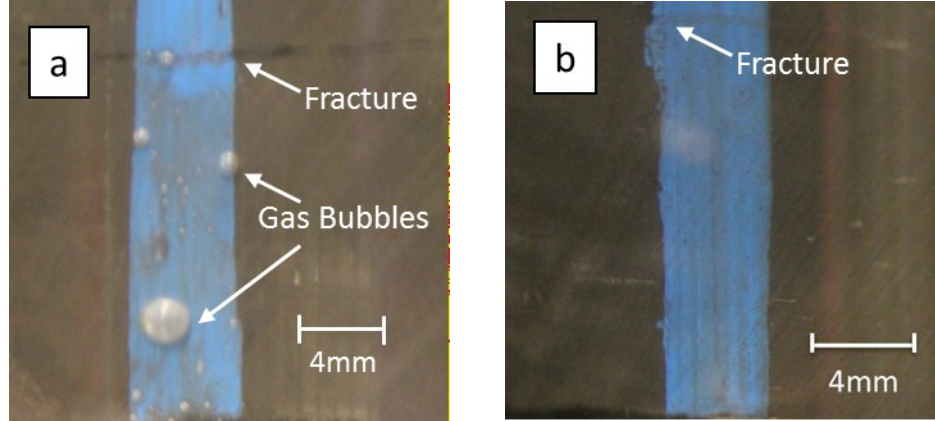
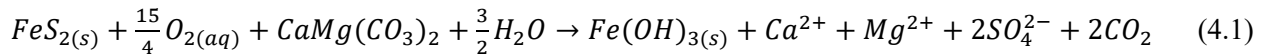


Figure 4-3. The surface of EV-1 shale samples in a. oxic water and b. degassed water 2 hours after starting the imbibition experiment. The blue areas in the figure are reference areas used for determining the sample depth.

Figure 4-3 shows gas bubbles on the surface of shale samples after 2 hours of the imbibition of oxic water. Gas bubbles are not observed for degassed experiments. This could be due to the rapid dissolution of gas initially existing in the pore spaces of the shale samples into the imbibed degassed water. The low pressure in the vacuum chamber (see Figure 4-1) reduces the concentration of dissolved oxygen in degassed water and the concentration of other dissolved gases such as carbon dioxide and nitrogen (Kolev, 2011).

The oxic water imbibing into the shale sample expels gas out of the sample's pore system. Previous studies have also reported similar observations of gas bubble formation on the rock sample during oxic water imbibition (Dehghanpour et al., 2012; Roshan et al., 2015). The gas bubbles in Figure 4-3a are probably the air which is initially presented in the pores of the shale sample. In addition, the gas bubbles observed in Figure 4-3a may contain gas produced from the reaction of rock minerals with water. For example, carbon dioxide may be produced by a reaction between pyrite, dolomite, water and oxygen (Descourvières et al., 2010; Chermak and Schreiber, 2014), which is:



The possibility of pyrite oxidation reaction is discussed in section 4.3.3.

Under degassed conditions, the gas existing in the pore space dissolves into water, while under oxic conditions, gas cannot completely dissolve in the imbibing water. For oxic water imbibition, some of the gas in pore space may be trapped and reduce water saturation and relative permeability (Bennion et al., 1996). The trapped gas during oxic water imbibition may also increase the resistance against the capillary force for water imbibition which will result in the relative permeability effect (Jamin, 1860). According to Figure 4-2, the imbibition rate of degassed water is higher than that of oxic water. For example, for the EV-1 sample, the normalized degassed water imbibition rate for the initial 18.5 hours is about 0.00074 which is higher than that for the normalized oxic water imbibition rate (0.00052).

When the gravity effect is ignored, the imbibed mass is proportional to the square root of time (Handy, 1960),

$$m = \sqrt{\left(\frac{2P_c k k_{rw} \phi A^2 S}{\rho^2 \mu}\right)} \times \sqrt{t} \quad (4.2)$$

Where, m is the mass of imbibed water, μ and ρ are viscosity and density of the imbibed water respectively. S is the water saturation of shale samples at time t , P_c is the capillary pressure at the saturation of S , k_{rw} is water relative permeability, k and ϕ are absolute permeability and porosity of the shale samples, respectively.

Figure 4-4 shows the normalized mass of imbibed water versus square root of time. Compared with the degassed tests, the lower slope for oxic water imbibition can be due to the potential entrapment of gas in the pores of the rock. To be more specific, gas trapping in the pore spaces reduces k_{rw} due to declining water saturation. The potential reduction of k_{rw} can be responsible for the lower imbibition rates during oxic water imbibition compared with that of degassed water imbibition.

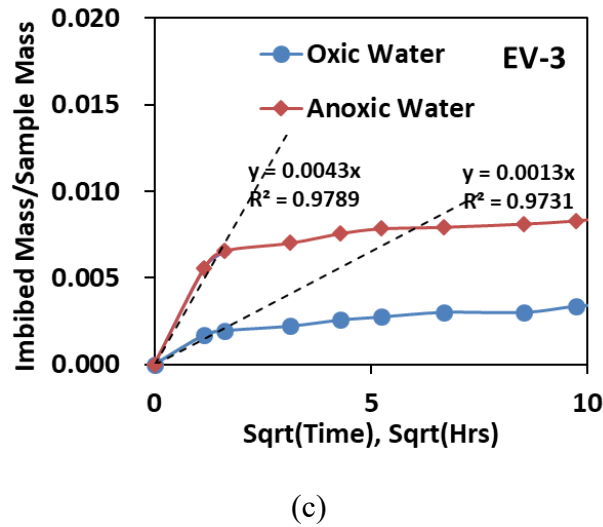
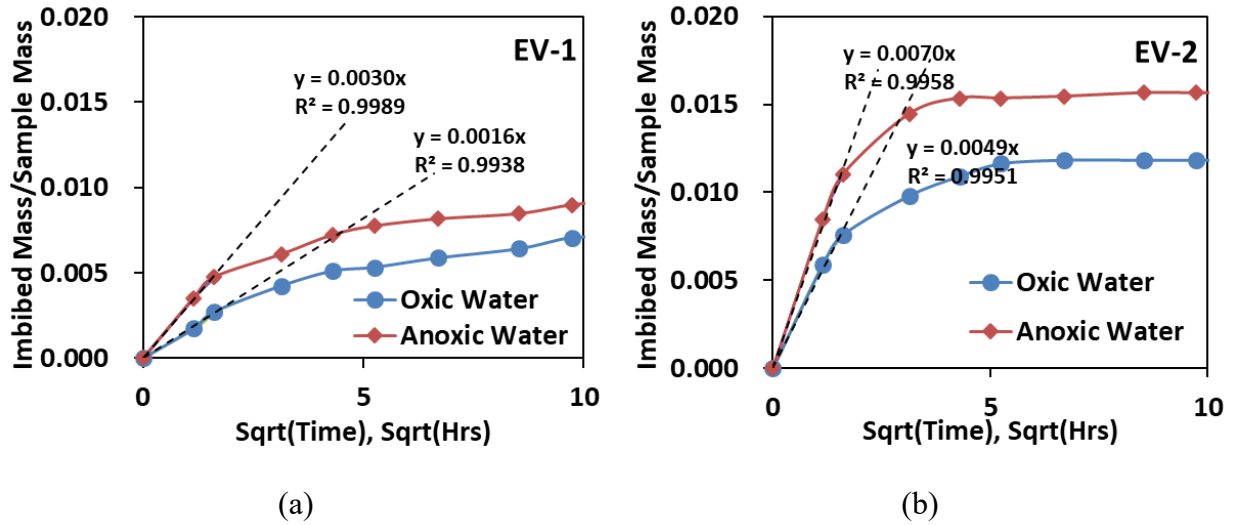


Figure 4-4. Normalized mass of imbibed oxalic and degassed water versus square root of time for (a) EV-1, (b) EV-2, and (c) EV-3 samples. The trendlines show the initial imbibition rate.

During degassed water imbibition, dissolution of gas into the water may provide additional pore space for water imbibition, which explains the difference between the water imbibition curves of oxalic and degassed experiments (see Figure 4-4). On the other hand, the gas trapped in pore space during oxalic water imbibition may partially block the path for water imbibition. In Figure 4-4c, the equilibrated imbibed mass of degassed water is about 2 times higher than that of oxalic water in EV-3 samples which suggests that nearly 50% of the water-accessible pore volume may be occupied by trapped gas during oxalic water imbibition.

4.3.3 Ion Concentration Profiles

In this section, ion concentrations in oxic and degassed water during the imbibition process are presented. Concentration of major ions (such as potassium and sodium) and redox sensitive ions (such as iron and sulfate) are measured to investigate the effects of dissolved oxygen on the ion concentration during water imbibition experiment.

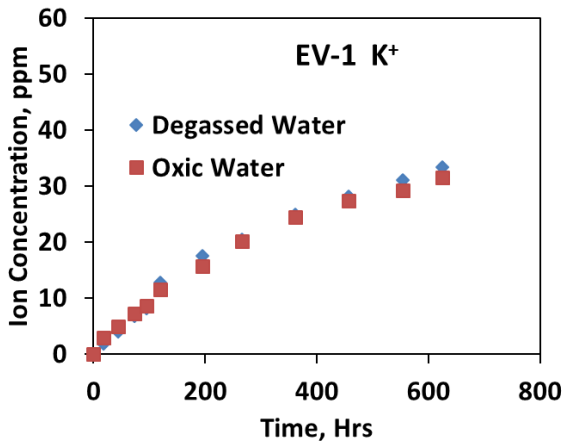
4.3.3.1 Potassium and Sodium Ions

According to Figure 4-5, potassium and sodium ion concentrations increase during both oxic and degassed water imbibition experiments and no considerable difference is observed in the concentration profiles of these ions. The source of potassium and sodium can be 1) dissolution of precipitated salts (such as NaCl and KCl) in shale samples; 2) dissolution of potassium- or sodium-bearing rock constituents (Blauch, et al., 2009) and 3) leaching of exchangeable potassium and sodium ions from the interlayer of clays (Hensen and Smit, 2002; Essington, 2015). The similarity of ion concentration profiles between oxic and degassed water imbibition suggests that the presence of oxygen in the imbibition water has negligible impact on the concentrations of produced Na^+ and K^+ ions.

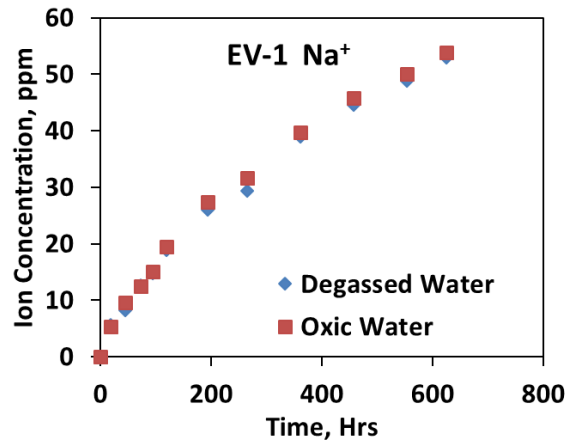
To investigate the potential sources of produced ions during the imbibition experiments, the molar ratio of K^+/Cl^- and Na^+/Cl^- are plotted in Figure 4-6. Both K^+/Cl^- and Na^+/Cl^- molar ratios are more than one. Leaching of exchangeable cations from the interlayer of clay minerals is a possible reason for the excess Na^+ and K^+ (Keller and da Costa, 1989). Both K^+/Cl^- and Na^+/Cl^- molar ratios show an early increase in oxic water. This can be due to the fact that chloride can only be oxidized (not reduced) (Huang et al., 2005). Thus, in an oxic environment, the leached K^+ and Na^+ from the interlayer of clay minerals may be responsible for the early increase in K^+/Cl^- and Na^+/Cl^- molar ratios. Moreover, chloride ion may oxidize and decrease the concentration of Cl^- in the solution. Thus, at early times, both K^+/Cl^- and Na^+/Cl^- molar ratios increase in the oxic environment. At later times, the potential dissolution of chloride-bearing minerals (such as NaCl and KCl) can be responsible for the declining trends of K^+/Cl^- and Na^+/Cl^- molar ratios.

At early times, both K^+/Cl^- and Na^+/Cl^- molar ratios are higher for degassed water compared with that in oxic water. On the other hand, the imbibed volume is higher for the degassed condition

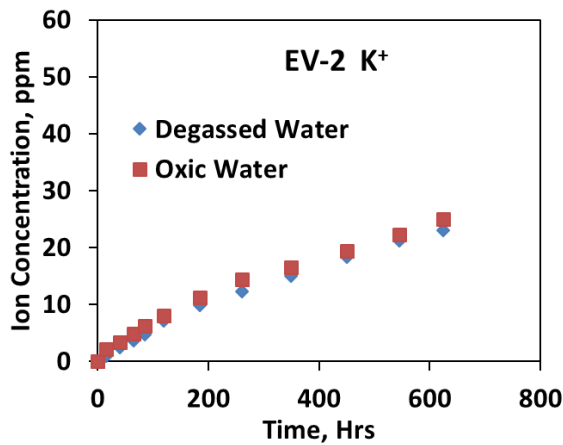
compared with that for the oxic condition (see Figure 4-2). More imbibition can potentially enhance the accessibility to the clay-rich zones, facilitating the ion-exchange reactions. Thus, the probability of leaching exchangeable cations (i.e., K^+ and Na^+) from the interlayer of clay minerals is higher in the degassed condition compared with the oxic condition. Similarly, the possible dissolution of chloride-bearing minerals reduces the K^+/Cl^- and Na^+/Cl^- molar ratios at later times.



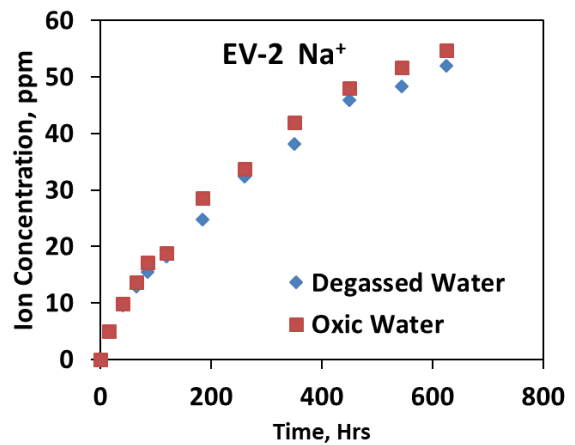
(a)



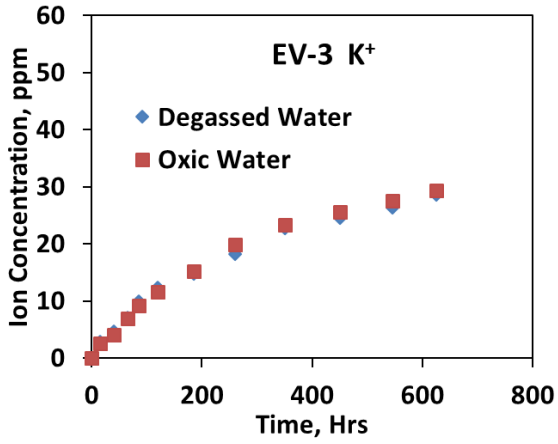
(b)



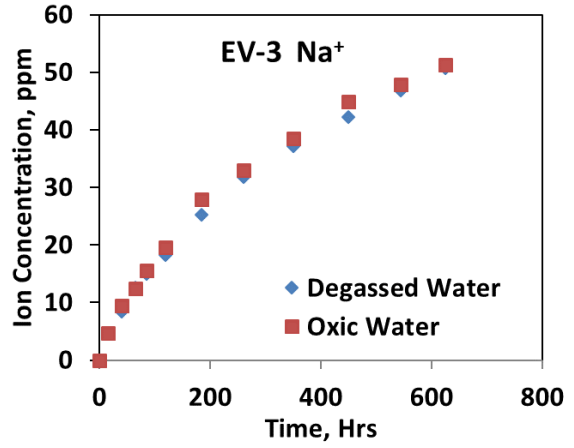
(c)



(d)

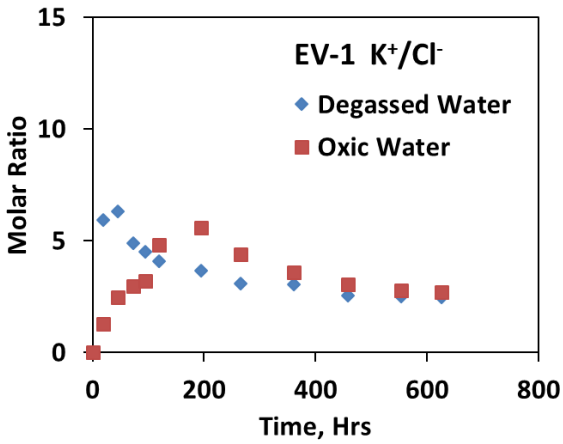


(e)

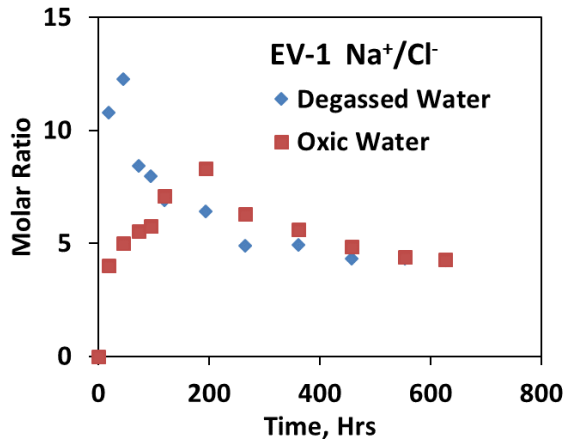


(f)

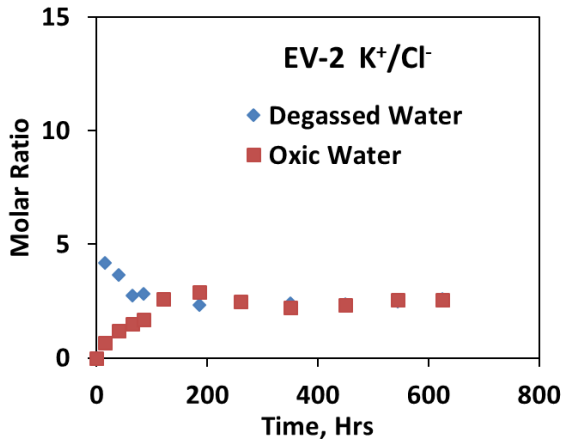
Figure 4-5. The concentration of (a, c, e) potassium and (b, d, f) sodium ions in degassed/oxic water during imbibition experiments with (a, b) EV-1, (c, d) Ev-2, and (e, f) EV-3 shale samples measured by ICP-MS.



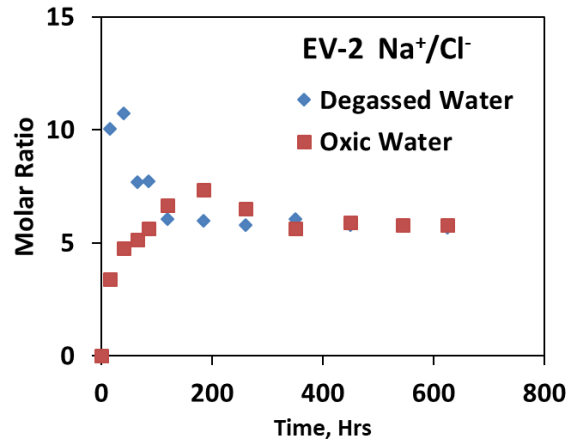
(a)



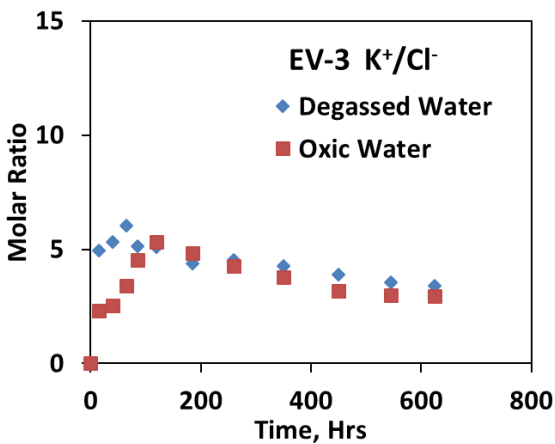
(b)



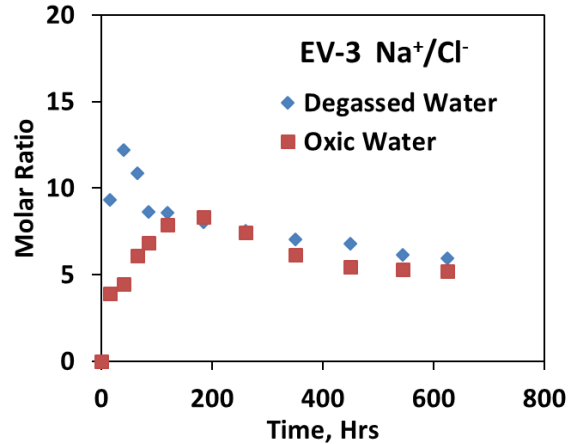
(c)



(d)



(e)



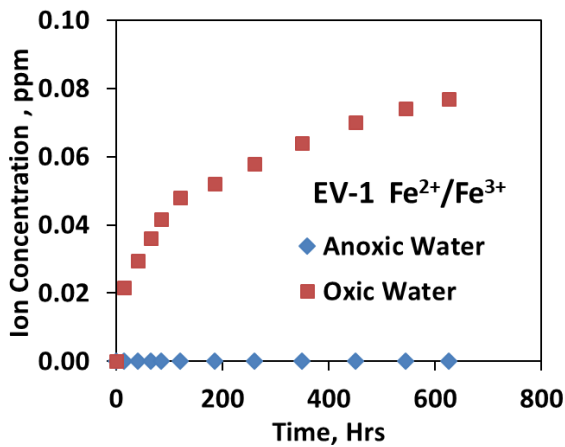
(f)

Figure 4-6. The K^+/Cl^- (a, c, e) and Na^+/Cl^- (b, d, f) molar ratios in degassed/oxic water during imbibition with EV-1 (a, b), EV-2 (c, d), and EV-3 (e, f) shale samples.

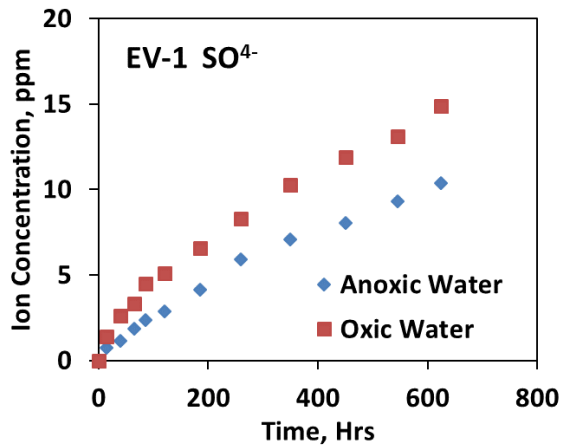
4.3.3.2 Iron and Sulfate Ions

Previous studies have shown that the concentration of redox sensitive elements (such as Fe and S) can be influenced by the presence of oxygen (Xie et al., 2009; Zolfaghari et al., 2016). Figure 4-7 shows concentration profiles of iron and sulfate ions in oxic and degassed imbibition experiments. The concentration of iron ion increases over time during the oxic water imbibition while it is almost zero during degassed water imbibition. According to Table 4-1, pyrite is the major source of iron in our shale samples. Other sources of iron could be the cation exchange of Fe^{2+} in the interlayer of clays during water imbibition. Thus, inhibition of pyrite oxidation reaction during degassed

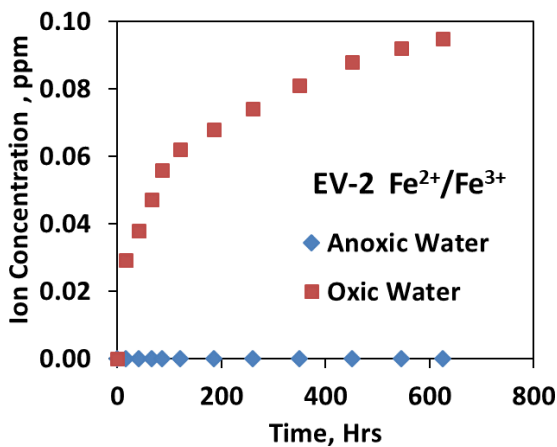
water imbibition can be a reason for negligible production of iron ions. It must be noted that XRD uses very small amount of rock sample for its analysis. Therefore, it is possible that other possible sources of iron element (i.e., goethite, hematite, and magnetite) are missing in the reported rock mineralogy in Table 4-1 due to rock heterogeneity. The reaction of pyrite with water and oxygen may be a possible explanation for the increasing trend of iron concentration profile during oxic water imbibition in Figure 4-7. SEM images presented in the Section 3.4 shows that pyrite minerals are located in vicinity of pores in our shale samples. These pores provide an interface at which imbibed water, dissolved oxygen, and pyrite can potentially co-exist and react.



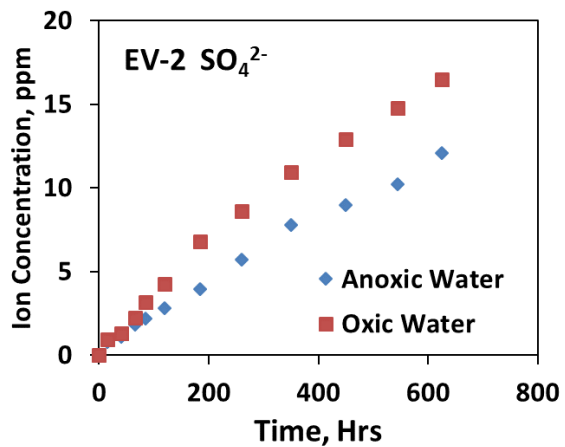
(a)



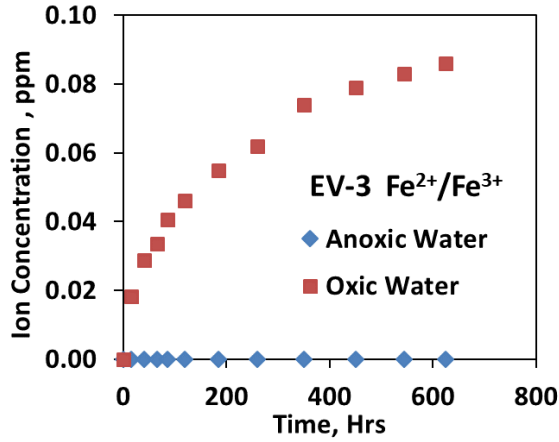
(b)



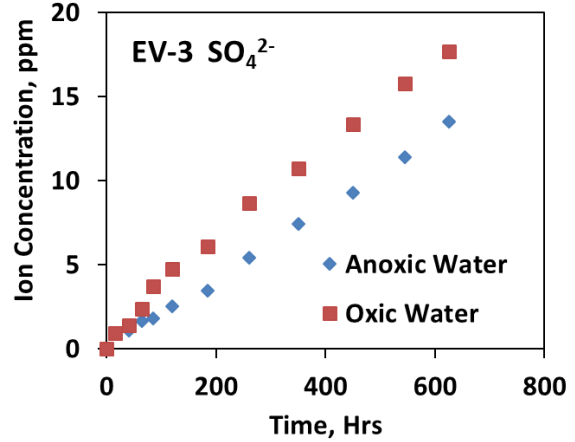
(c)



(d)



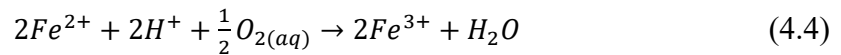
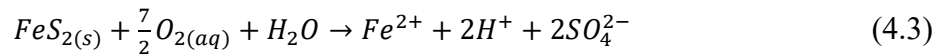
(e)



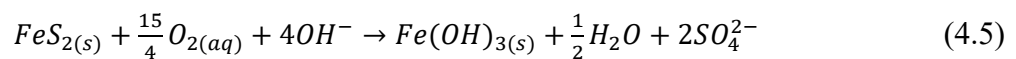
(f)

Figure 4-7. The concentration of (a, c, e) iron and (b, d, f) sulfate ions in degassed/oxic water during imbibition experiments with (a, b) EV-1, (c, d) Ev-2, and (e, f) EV-3 shale samples measured by ICP-MS.

In pyrite oxidation reactions, oxygen atoms from water may react with sulfur atoms in pyrite molecules at the rock-water interface (Biegler and Swift, 1979) to produce ferrous ions (Fe^{2+}) according to the following aqueous reactions (Singer and Stumm, 1968; Bailey and Peters, 1976; Davison and Seed, 1983; McKibben, 1985):



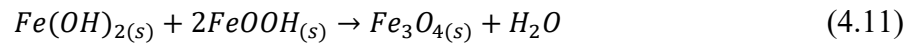
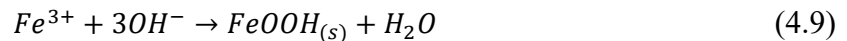
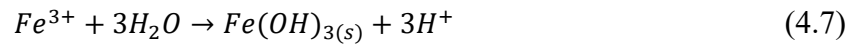
The ferrous ions (Fe^{2+}) can react with dissolved oxygen (Eq. 4.4) to produce ferric ions (Fe^{3+}). Pyrite oxidation rate generally increases with increasing pH and dissolved oxygen concentration (Moses et al., 1987; Holmes and Crundwell, 2000; Manaka, 2009). In the imbibition experiments, the pH value for degassed and oxic imbibing water is between 8.0 to 9.0 and 7.5 to 8.5, respectively. The higher pH of degassed water can be due to the removal of some dissolved carbon dioxide in degassed water by vacuum (Millero, 1995). The overall pyrite oxidation reaction in alkaline solution is as follows (Nicholson et al., 1988; Ciminelli and Osseo-Asare, 1995):



Production of iron and sulfate ions during oxidation of pyrite mineral (Eqs. 4.3 and 4.4) explains why iron and sulfate concentrations in oxic water are higher than that in degassed water, as observed in Figure 4-7. Based on Eq. 4.5, the rate of pyrite oxidation (R_{pyrite}) can be expressed by the rate of sulfate concentration difference (Moses and Herman, 1991):

$$R_{\text{pyrite}} = \frac{d[\text{pyrite}]}{dt} = -\frac{1}{2} \frac{d([\text{SO}_4^{2-}]_{\text{oxic}} - [\text{SO}_4^{2-}]_{\text{anoxic}})}{dt} \quad (4.6)$$

The sulfate concentration difference between oxic and degassed water samples is around 2 orders of magnitude larger than the corresponding $\text{Fe}^{2+}/\text{Fe}^{3+}$ concentration difference. The reacted pyrite will produce either soluble Fe^{3+} (Eq. 4.4) or insoluble Fe^{3+} hydroxide precipitate (Eq. 4.5). Based on Pourbaix diagram of iron (Beverskog and Puigdomenech, 1996), Fe^{3+} -bearing compounds start to precipitate at low pH values. For example, Fe^{3+} -hydroxide starts to precipitate at pH values of about 1 (Taylor et al., 1999). Since the pH range in our experiments is 7.5-9.0, iron released during pyrite oxidation may ultimately form insoluble Fe^{3+} -bearing compounds which cannot be identified by ICP-MS tests. According to the Pourbaix diagram of iron (Beverskog and Puigdomenech, 1996), at pH values of 7.5 to 9.0, the iron oxidation products could be $\text{Fe}(\text{OH})_2$, $\text{Fe}_2\text{O}_3 \cdot n\text{H}_2\text{O}$, and Fe_3O_4 . These are listed in Eqs. 4.8, 4.10, and 4.11. Highly reactive $\text{Fe}^{2+}/\text{Fe}^{3+}$ ions may participate during the production of water insoluble iron hydroxide, goethite, hematite or magnetite according to Eqs. 4.7 to 4.11 (Essington, 2015):



It is worth mentioning that the imbibition experiments are conducted at room temperature, atmospheric pressure and nearly neutral pH, which are different compared with the reservoir condition. For example, Horn River reservoir gas contains about 9-14% of CO_2 (Reynold and Munn, 2010). The reaction of CO_2 with water can potentially produce carbonic acid. It must be noted that although carbonic acid production can reduce the pH, natural buffer systems such as

dolomite and calcite may neutralize the pH under reservoir condition (Zolfaghari et al., 2016). Furthermore, the reservoir temperature in the Horn River Basin is in the range of 135 to 175 °C and the reservoir pressure is between 20,000 to 53,000 kPa (B. C. Oil & Gas Commission. 2014). Different laboratory and reservoir conditions dictate different “speciation and complexation” of ions, which can also alter the pH. Therefore, if individual compounds/complexes are of a particular interest, the different surface and downhole thermodynamic conditions should be taken into account.

4.3.4 SEM and EDS Images

In Figure 4-8, SEM image of a focus area and the corresponding elemental maps of sulfur and iron show that pyrite is widely spread in the shale samples. High density of sulfur and iron elements in Figures 4-8c and 4-8d suggest a pyrite-rich area. Figure 4-8b shows the magnified SEM image of the area surrounded by dashed line in Figure 4-8a, where many pores with a throat size of 50 to 200 nm exist in the pyrite-rich area. Figure 4-9 shows a SHIM image of the pyrite-rich area. Two ~1 μm pyrite framboids and many nanopores between pyrite particles. If these pores are accessible by water, they can provide an interface at which imbibed water, dissolved oxygen, and pyrite likely react. The interaction between these three components may result in precipitation of iron-bearing compounds on the surface of nano pores which may narrow or block the pore size and may ultimately lower the permeability of the shale sample.

Pyrite dissolution and oxidation may have a dual effect: 1) pyrite dissolution may create more pore space and may enhance water imbibition and 2) potential precipitation of iron-bearing compounds formed as a result of pyrite oxidation in the pore space may reduce the flow conductivity for water imbibition. Reduced imbibition rate and lower final imbibed water mass under the oxic conditions in this study suggest that precipitation of iron-bearing compounds potentially formed by pyrite oxidation in the pore space may have a more pronounced effect in comparison with the pore space creation by pyrite dissolution.

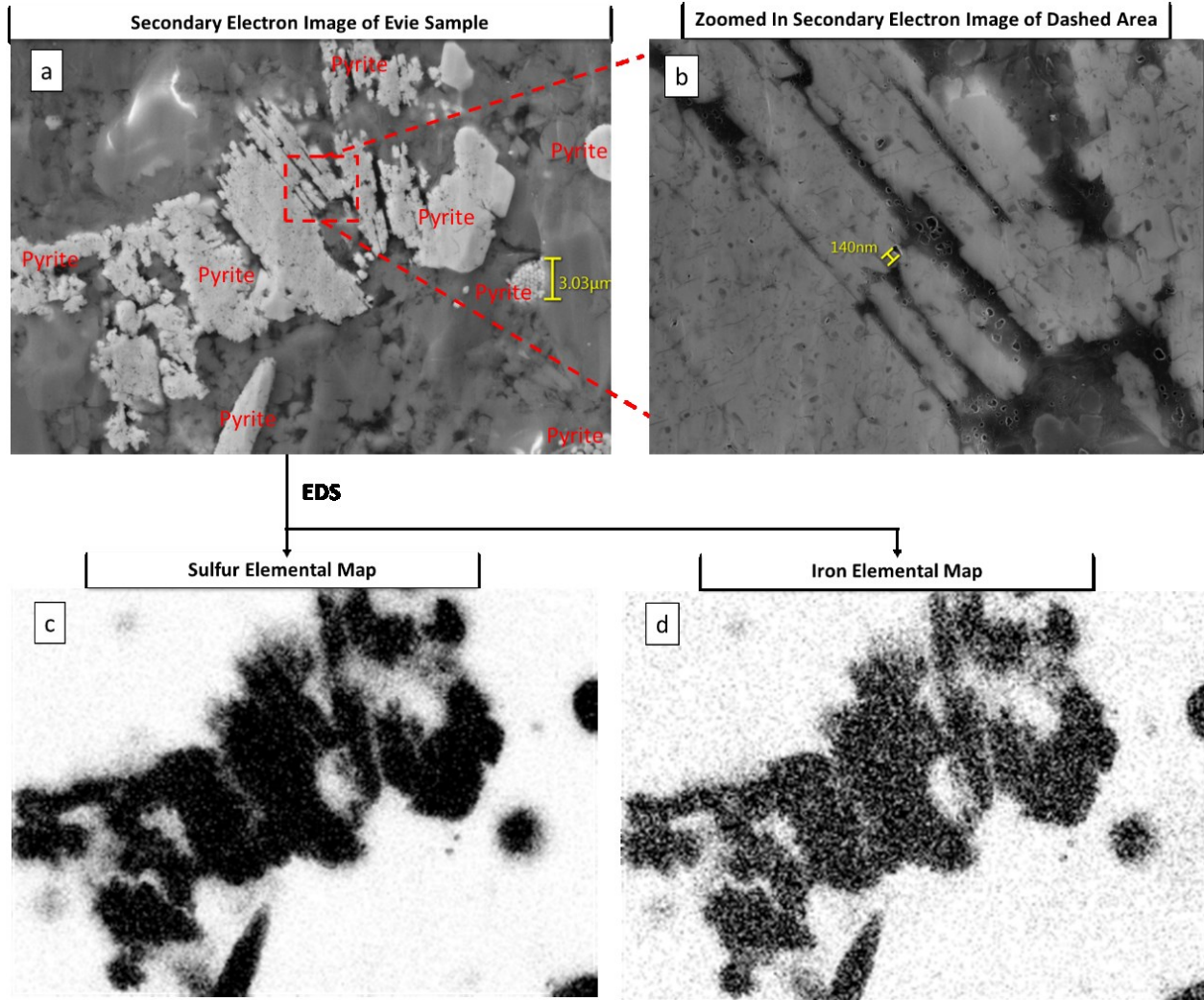


Figure 4-8. (a) SEM image of a focused area on a EV-2 shale sample; (b) magnified SEM image showing pores in pyrite; (c) sulfur elemental map and (d) iron elemental map obtained by EDS of the EV-2 shale sample. Darker area in elemental maps represents higher element density.

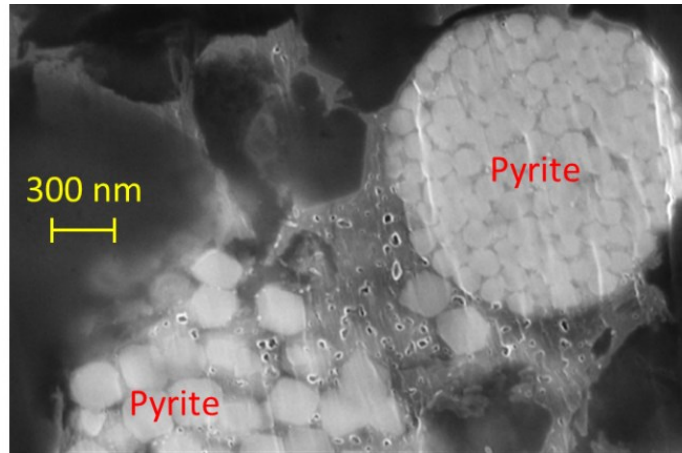


Figure 4-9. SHIM image of the EV-2 shale sample. Nano pores are observed around pyrite framboid.

4.4 Summary

Imbibition experiments using degassed water and oxic water are conducted on shale samples from Evie Formation in the Horn River Basin. Concentration of different ions in water are measured to investigate the effects of dissolved oxygen on water imbibition and produced ions. SEM-EDS analysis is used to visualize the pores and to investigate the elemental composition of the shale's surface. The key results of this study are summarized as:

- Degassed water can dissolve the gas in the shale pore space, contributing to a higher imbibition rate and final imbibed mass, compared with the oxic water. This observation indicates that the initially-degassed conditions in reservoir may accelerate the rate of water imbibition. Less gas entrapment under degassed conditions promote the water imbibition into shale matrix.
- Dissolved oxygen in water can react with pyrite in shale and produce iron and sulfate ions. Interactions of degassed water with shale do not result in iron production. This observation indicates that dissolved oxygen in fracturing fluid can cause pyrite oxidation and dissolution.
- Pores observed by SEM are in the vicinity of both pyrite particles. Although pyrite constitutes only a small portion of shale minerals, the oxygen-water-pyrite interactions cannot be ignored when interpreting the chemistry of water produced during flowback processes.

Chapter 5: Impact of Clay Swelling on Water Imbibition in Gas Shales

5.1 Introduction

The microfractures observed during water imbibition are mainly induced by clay-swelling (Lal, 1999; Guo et al., 2012; Al-Arfaj et al., 2014). Table 5-1 lists the maximum values of clay content measured by x-ray diffraction (XRD) analysis of shale samples from the Horn River Formations in Canada (Ross and Bustin, 2008), the Barnett (Rickman et al., 2008), the Antrim (Manger et al., 1991), the Haysnesville (Quirein et al., 2010), the Woodford (Sierra et al., 2010) and the Eagle Ford (Mullen, 2010) Formations in the U.S., the Stuart Formations (Bhargava et al., 2005; Awaja and Bhargava, 2006) in Australia, and the Niutitian Formation (Yang et al., 2014) in China. Clays are prone to adsorb water into their layered structure. Nano-scale hydrophilic pores in shales (Chalmers et al., 2012) can spontaneously imbibe water due to strong capillary suction (Cai et al., 2014; Wu et al., 2017). This suction accelerates adsorption of water by clays and is the key reason for retention of fracturing water in shale reservoirs after hydraulic fracturing operations (Oduşina et al., 2011; Ghanbari and Dehghanpour, 2015).

Table 5-1. The maximum and average values of clay content measured by XRD analysis of shale samples from different shale plays*.

Formation	Country	Maximum Clay Content, wt. %	Average Clay Content, wt. %	Number of Samples Tested
Horn River Gas Shale ¹	Canada	71	46	58
Barnett Gas Shale ²	U.S.	68	~49	~100
Antrim Gas Shale ³	U.S.	47	42	20
Haysnesville Gas Shale ⁴	U.S.	54	~44	~100
Woodford Gas Shale ⁵	U.S.	31	22	5
Eagle Ford Gas and Oil Shale ⁶	U.S.	41	~20	~100
Stuart Oil Shale ⁷	Australia	65	36	64
Niutitang Gas Shale ⁸	China	48	27	11

* The data of clay content in this table are source from ¹Ross and Bustin (2008), ²Rickman et al. (2008), ³Manger et al. (1991), ⁴Quirein et al. (2010), ⁵Sierra et al. (2010), ⁶Mullen (2010), ⁷Bhargava et al. (2005), ⁷Awaja and Bhargava (2006), and ⁸Yang et al. (2014).

Laboratory experiments show that water uptake of shales during imbibition can be higher than the pore volume initially available in these rocks (Zhou et al., 2014). This excess water uptake can be

partially explained by the expansion of rock samples due to clay swelling. Ghanbari and Dehghanpour (2015) compared water imbibition in confined and unconfined shales from the Horn River Basin. They observed that confinement reduced the water imbibition and physical alteration of the shale samples. Also, they concluded that the physical alteration and induced microfractures lead to excess water uptake of shales. Chenevert (1970) measured expansion of shale samples when exposed to water. He observed that shale expansion is proportional to the amount of water adsorbed. Due to the confined environment in subsurface conditions, shale expansion results in the accumulation of hydrational stress. This hydrational stress can be repulsive or attractive stress depending on clay hydration and ions existing in the interlayer spacing of clays (van Oort, 2003). Clay swelling and hydrational stress can also be affected by the salinity of imbibed brine (Wangler and Scherer, 2008; Rathnaweera et al., 2014). Permeability changes due to clay swelling may depend on clay content and type (Aksu et al., 2015).

Anisotropy is another key player in the water uptake in and physical alteration of shale rocks (Khan et al., 2011; Makhanov et al., 2014). Ghanbari and Dehghanpour (2015) observed that microfractures are primarily induced along rock laminations. Also, they observed that the rate of water imbibition is faster parallel to these laminations than when perpendicular. The anisotropic structure of shales and the layered structure of clay platelets may result in non-uniform hydration stress (Dewhurst and Siggins, 2006). The hydration stress perpendicular to the bedding plane may create secondary fractures which increases the complexity of the fracture network and improves the permeability of the shales (Ji and Geehan, 2013).

It has been hypothesized that water imbibition and clay hydration are partly responsible for the low flowback efficiency in gas shales and the increase in hydrocarbon production rate after prolonged shut-in (Ferrari et al., 2014; Morsy and Sheng, 2014; Xu et al., 2016). Spontaneous water imbibition experiments on shale samples reveal that hydration-induced microfractures may enhance the porosity and permeability (Ghanbari and Dehghanpour, 2015). In this study, the previous studies are extended to 1) quantify the porosity change of shales due to clay swelling, 2) measure the expansive stress during water imbibition, 3) investigate the existence of correlations between clay content and hydration-induced stress and strain, and 4) evaluate the role of ion concentration on clay swelling in shales. The rest of the chapter is organized as follows: Section

5.2 describes the methodology for measuring water/oil imbibition in shales samples and the resulting expansion/stress. Section 5.3 describes the rock and fluid materials used in this study. Section 5.4 shows the results of imbibition, induced strain and stress measurements. Section 5.5 discuss the correlations among water imbibition, sample expansion, expansive stress, rock mineralogy, and depositional lamination. Section 5.6 summarizes key findings of this chapter.

5.2 Methodology

Three sets of experiments are conducted to investigate expansion behavior of shales samples during water imbibition. Table 5-2 lists the measurement parameters, imbibition fluid, and number of shale samples used for each experiment set. The terms “induced strain (ϵ)” and “induced stress (σ)” denotes the strain and stress induced by fluid imbibition into shale samples. The experimental set-up and procedure for each experiment set are described in following three subsections.

Table 5-2. Imbibition fluid, number of shale samples used in each set of experiment, and the parameters for the experimental measurements.

Experiment	Measurement Parameter	Imbibition Fluid	Number of Shale Samples Used
Set 1	Imbibed Mass (M_{imb})	Water, Oil	10
Set 2	Induced strain (ϵ)	Water, Oil 10% and 20% NaCl Brine	20
Set 3	Induced stress (σ)	Water 10% and 20% NaCl Brine	15

5.2.1 Set 1 (Spontaneous Imbibition Experiment)

In this experiment, imbibed mass (M_{imb}) is recorded over time during spontaneous water and oil imbibition experiments. The experiment starts with moisture removal from the shale samples by drying them in the oven at 100 °C until no mass change is observed. The criteria for choosing 100 °C for the oven drying is discussed in Appendix D. Next, the weight and bulk volume (V_{dry}) of each sample are measured and recorded. At each time step, the shale samples are taken out of the imbibition cell to measure the wet samples’ mass. A top loading balance with accuracy of ± 0.01 g

is used to measure the sample mass. M_{imb} is calculated as wet sample mass minus initial dry sample mass. Water/oil saturation of the shale sample is calculated as:

$$S = \frac{M_{imb}}{\rho \phi_{dry} V_{dry}} \quad (5.1)$$

Where, ρ is the density of imbibition fluid, as listed in Table 5-2. ϕ_{dry} is the porosity of dry sample, as listed in Table 5-3. The terms “ S_w ” and “ S_o ” will be used exclusively below for water/brine saturation and oil saturation, respectively.

5.2.2 Set 2 (Induced Strain Measurement)

In this experiment, ϵ due to the imbibition of DI water, oil and NaCl brine with different concentrations into shale samples are measured. ϵ is measured in two directions (see Figure 5-1) – parallel to the depositional lamination (horizontal direction) and perpendicular to the depositional lamination (vertical direction). The shale samples are unconfined and free to expand during the imbibition process.

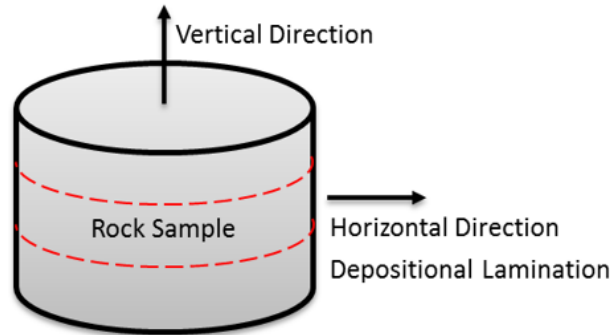


Figure 5-1. Schematic of a rock sample and its depositional lamination (red dashed line). The horizontal direction represents the direction parallel to the lamination. The vertical direction represents the direction perpendicular to the lamination.

Figure 5-2 shows the custom-designed set-up for measuring ϵ . It consists of two linear variable differential transformers (LVDTs). The horizontal and vertical displacement during imbibition experiment are measured by the ferromagnetic rod inside the LVDT (see Figure 5-2b). Before each set of ϵ measurement, the LVDTs are calibrated using a micrometer to ensure the accuracy of the experiments. The vertical displacement is directly measured by the LVDT. The horizontal displacement is transmitted via an L-shaped lever. Stabilizer mounts fixed by bolts are used to

prevent lateral movement of the shale sample. The LVDTs are mounted on a stainless-steel frame through micrometer position adjusters. The micrometer position adjusters allow us to adjust the position of the LVDTs to fit the samples of various sizes. The procedure for the ϵ measurements is as follows:

- 1) Polish the rock surface using 600, 400 and 200 grit grinding pads.
- 2) Dry the sample in oven at 100 °C until no mass change to ensure that all samples have no free water prior to starting the experiments.
- 3) Put the sample into the LVDT set-up and fix the sample by adjusting the stabilizer mounts.
- 4) Adjust the position of LVDT using micrometer position adjusters.
- 5) Increase water or oil level until the sample is fully immersed.
- 6) The vertical and horizontal displacement are acquired and analyzed using LabVIEW software.

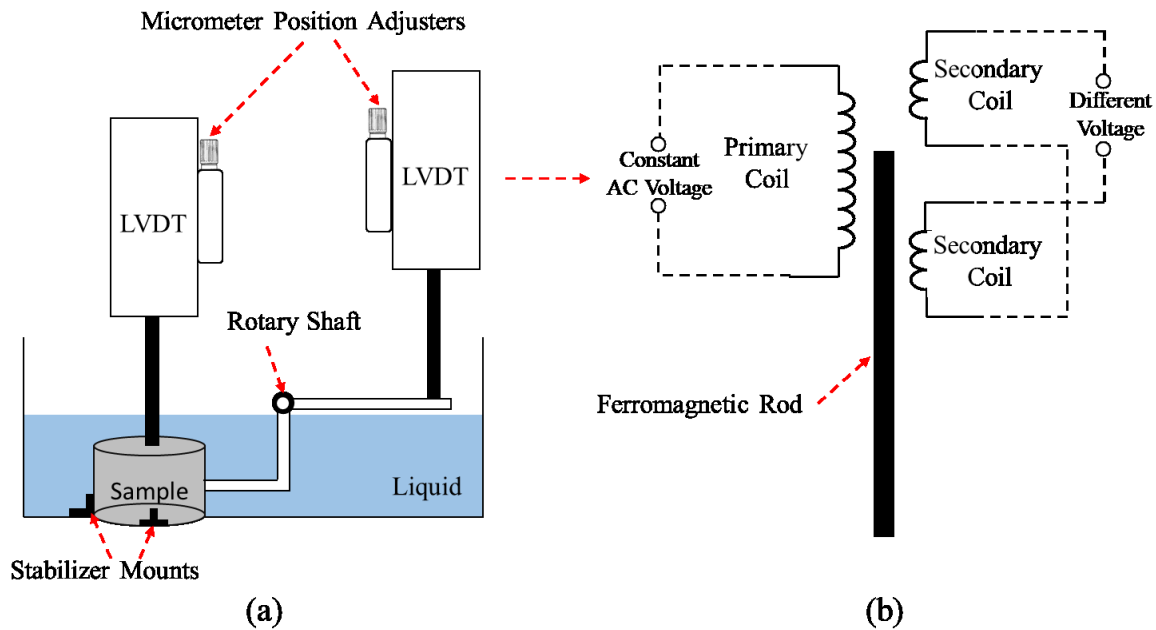


Figure 5-2. Schematic illustrations of the custom-designed linear variable differential transformers (LVDT) set-up for measuring ϵ . (a) full experimental set-up and (b) LVDT mechanism for measuring sample expansion.

Horizontal strain (ϵ_x) and vertical strain (ϵ_y) are defined as:

$$\varepsilon_x = \frac{\Delta r}{r} \quad (5.2)$$

$$\varepsilon_y = \frac{\Delta h}{h} \quad (5.3)$$

Here, h and r are the initial height and radius of the dry cylindrical shale sample, respectively, measured using a caliper with 0.01 mm accuracy. Δh is the change in sample height and is equal to the vertical displacement measured by LVDT. Δr is the change in sample radius and is equal to half of the horizontal displacement measured by LVDT.

Volumetric strain (ε_v) is defined as the change in volume of the sample (ΔV) divided by its original dry volume,

$$\varepsilon_v = \frac{\Delta V}{V_{dry}} \quad (5.4)$$

For a cylindrical sample, ΔV can be determined as

$$\Delta V = V_{wet} - V_{dry} = \pi(r + \Delta r)^2 \times (h + \Delta h) - \pi r^2 \times h \quad (5.5)$$

where, V_{wet} is the sample volume after the imbibition test.

To determine the accuracy of the LVDT set-up, a test is conducted on a dry shale sample without the presence of fluid. The sample size is 4-cm in height and 4-cm in radius. The results of this test (see Figure 5-3a) indicate that the maximum error of the LVDT set-up is $\pm 3.5 \mu\text{m}$. All the shale samples used in this study are more than 4 cm in length and 4 cm in radius. The maximum error of strain value is calculated as $\frac{\pm 3.5 \mu\text{m}}{4 \text{cm}} = \pm 8.75 \times 10^{-5}$. The errors may be due to 1) micro-vibrations in the laboratory, and 2) the system noise of the data acquisition box and LVDT instrument. Figure 5-3b shows that distribution of the displacement data is follow the Gaussian distribution. The mean value of all the data is $0.0087 \mu\text{m}$, and the standard deviation is $1.20 \mu\text{m}$. The error in calculated volume (dV_{err}) is 0.352 cm^3 , which is calculated by,

$$dV_{err} = \left(\frac{\partial V_{dry}}{\partial r} \right)_h dr + \left(\frac{\partial V_{dry}}{\partial h} \right)_r dh = (2\pi hr)dr + (\pi r^2)dh \quad (5.6)$$

Where, dr and dh represent the error in measured height and radius, respectively.

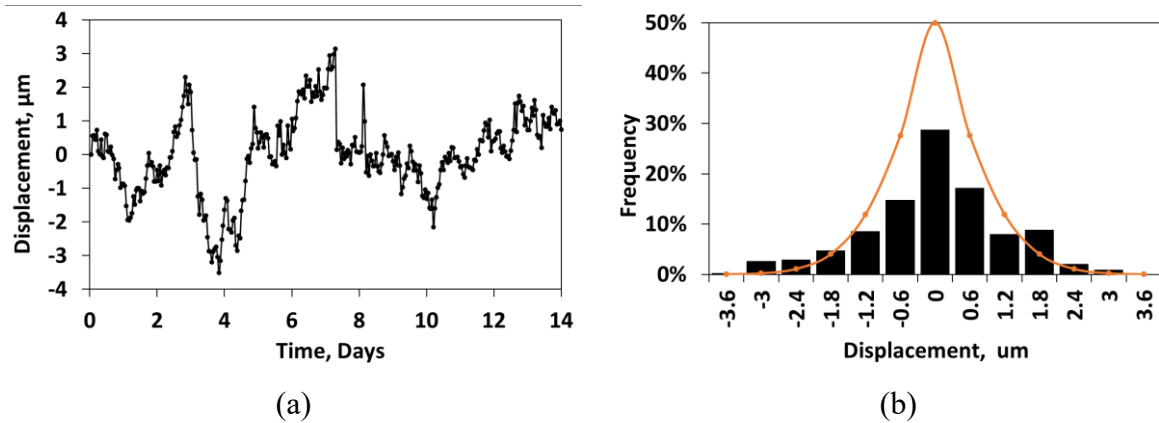


Figure 5-3. (a) Displacement data measured on a dry rock using LVDT, and (b) the distribution of the measured data.

5.2.3 Set 3 (Induced Stress Measurement)

In this experiment, σ is measured when $\varepsilon_y = 0$ during the imbibition of water and brine into the shale samples to investigate the effect of ion concentration on σ . Similar to the experimental procedure of set 2, the experiment starts with moisture removal and surface polishing of shale samples. Figure 5-4 shows the experimental set-up. A constant load (~ 320 lbs) is applied to the shale sample in the vertical direction to ensure that the load cell is fully in contact with the sample's top surface. Then, the sample is immersed in water or brine, and stress changes in the vertical direction are measured by the load cell. This load cell can measure up to 10000 lbs with a systematic error of ± 10 lbs. M_{imb} at the end of test is measured and S_w is calculated using Eq. 1.1.

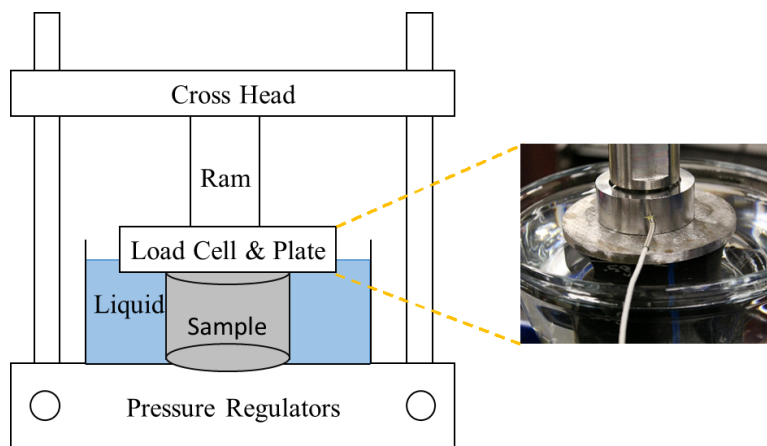


Figure 5-4. Schematic illustration of the experimental set-up for measuring induced expansive stress during water imbibition.

5.3 Materials

Details about the fluids and rock samples used for the experiments are provided in this section.

5.3.1 Fluids

DI water, NaCl brine and kerosene are used for the imbibition tests. The properties of the water, brine and oil are listed Table 2-1.

5.3.2 Rock Sample

Shale samples used in this study are collected from cores drilled in the Horn River (HR) Group in the Western Canadian Sedimentary Basin. It consists of several members including Muskwa, Otter Park, Evie and Lower Keg River (Johnson et al., 2011). Figure 5-5 shows the results of XRD analysis for 78 samples from a single well in HR Formation. The ternary diagram in Figure 5-5a shows the percentage of quartz, clay and other minerals (i.e. carbonate, feldspar, plagioclase, pyrite, etc.) from XRD data. Clay content of these samples ranges from 3 wt. % to 56 wt. %. Figure 5-5b plots the clay content versus the total vertical depth (TVD) of the shale samples. It shows that the sample clay content from the same shale member generally declines with increasing TVD.

A total of 45 shale samples from Muskwa, Otter Park and Evie Formations are categorized into five groups. They are Group 1 (G1) to Group 5 (G5). Samples from the same well and within 0.5-m depth interval are placed in the same group. The cross-sectional area and length of all the samples are $52.0 \pm 3.0 \text{ cm}^2$ and $4.0 \pm 0.3 \text{ cm}$, respectively. Approximate depth, averaged porosity and permeability of the samples in each group are listed in Table 5-3. The porosity and permeability reported in Table 5-3 are measured by a commercial laboratory using helium porosimetry and pulse decay permeameter, respectively. The mineral concentration of all the samples measured by XRD is listed in Table 5-4. All the samples are mainly composed of quartz (29 – 89 wt %), carbonates including calcite and dolomite (4 – 59 wt %) and clay (3 – 19 wt %). The clay minerals mainly consist of illite, smectite, and mica. Due to the limit of XRD analysis, illite, smectite and mica are quantified as mixed layer of illite and smectite, and mixed layer of illite and mica. Smectite has a high affinity to adsorb water into its interlayer space, resulting in clay swelling (Laird, 2006). In contrast, kaolinite has one tetrahedral sheet to one octahedral sheet structure, which makes kaolinite a non-expandable clay (Bergaya and Lagaly, 2013). It must be

noted that only a small amount of rock sample is used for XRD analysis. It is possible that shale samples from the same group have different mineral concentrations compared with XRD results in Table 5-4, due to the heterogeneity. The effect of heterogeneity on ϵ and σ is analyzed in Appendix E.

A $1 \times 1 \times 0.5$ cm shale sample from Group 2 is well-polished to observe the clay structure using scanning electron microscope (SEM). Figure 5-6 and Figure 5-7 show clay structures in two different focus areas. The type of clay in the zoomed-in SEM images of Figure 5-6 and Figure 5-7 is expected to be illite/smectite from its layered and flake structure. The pore size in the clay-rich areas ranges from ~ 5 nm to ~ 100 nm. As a reference, Kodikara et al. (1999) found the size of intra-aggregate pores in compacted clays to be between 3 nm and 1000 nm.

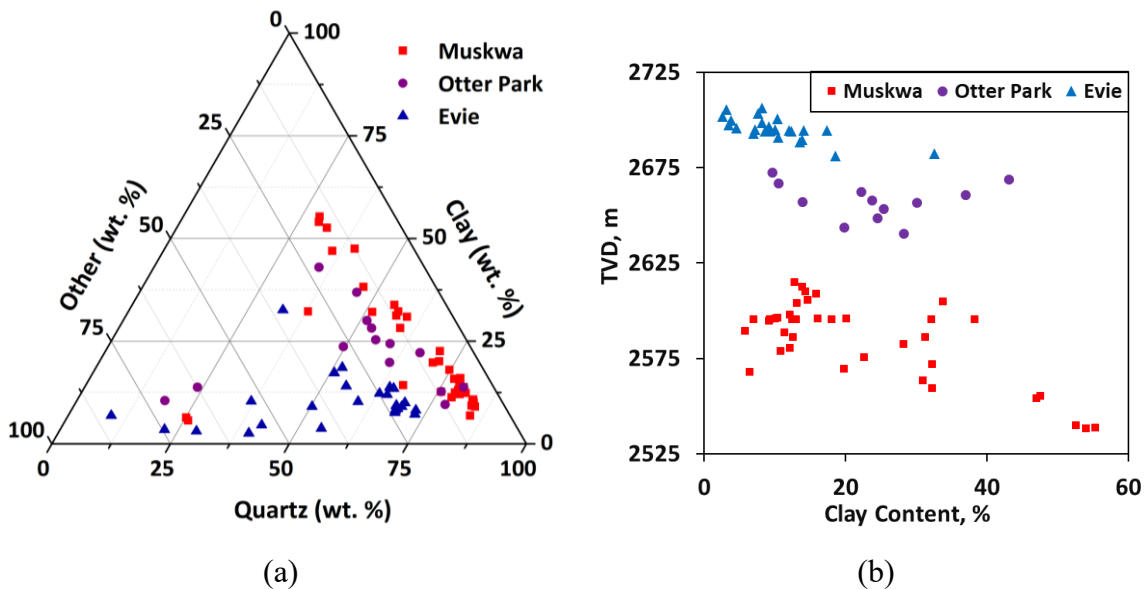


Figure 5-5. (a) Ternary diagram of the mineralogy and (b) clay content versus TVD for the Muskwa, Otter Park, and Evie members from the HRB. The three groups shown on the ternary diagram are quartz, clay, and other minerals (sum of feldspar, plagioclase, calcite, dolomite, pyrite, etc).

Table 5-3. Approximate depth, porosity, and permeability of representative samples from each group.

Group	G1	G2	G3	G4	G5
Formation	Muskwa	Otter Park	Evie	Evie	Evie

Depth, m	2610	2672	2681	2696	2705
Porosity, %	2.92	4.98	6.37	6.40	3.90
Permeability, nD	180	575	384	567	252

Table 5-4. Mineral concentration (wt %) for a representative sample from each group determined by XRD analysis.

Wt %	G1	G2	G3	G4	G5
Quartz	67	78	52	69	29
K-Feldspar	3	5	5	4	5
Plagioclase	3	1	6	5	2
Carbonate	10	4	16	12	59
Pyrite	3	2	3	2	2
Total non-Clay	84	90	81	91	97
Illite/Smectite	5	3	7	2	0
Illite/Mica	11	7	12	7	3
Kaolinite	0	0	0	0	0
Total Clay	16	10	19	9	3

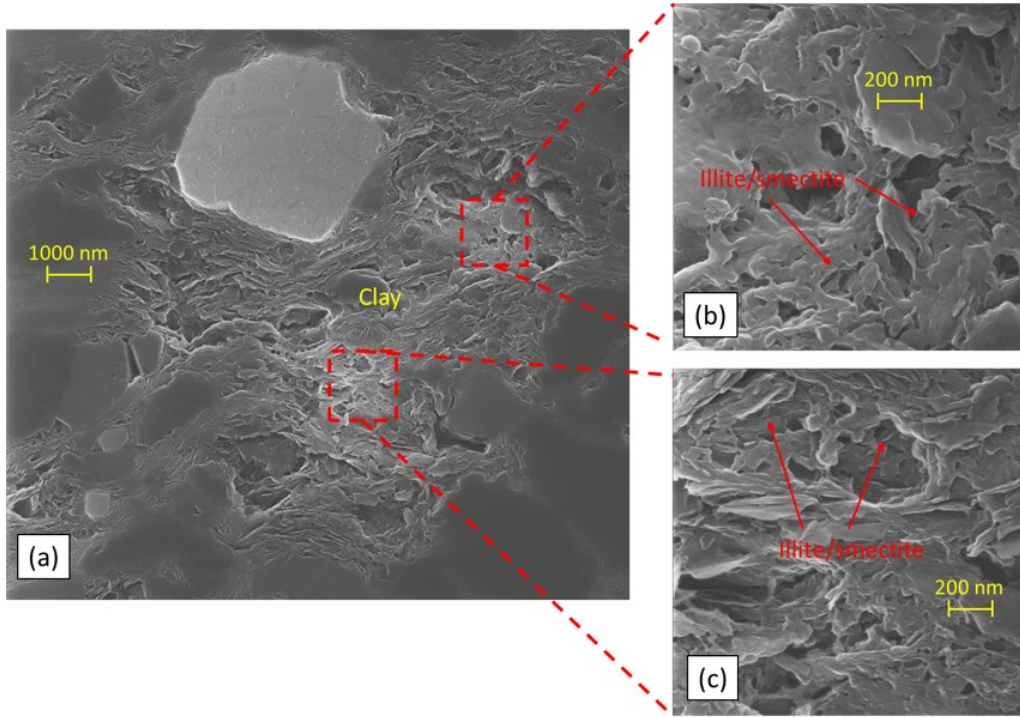


Figure 5-6. SEM image of a focus area (a) and two magnified SEM images of clay areas (b and c) for a shale sample from Group 2. The layered and curled-flakes structure indicates illite/smectite in the zoomed-in area.

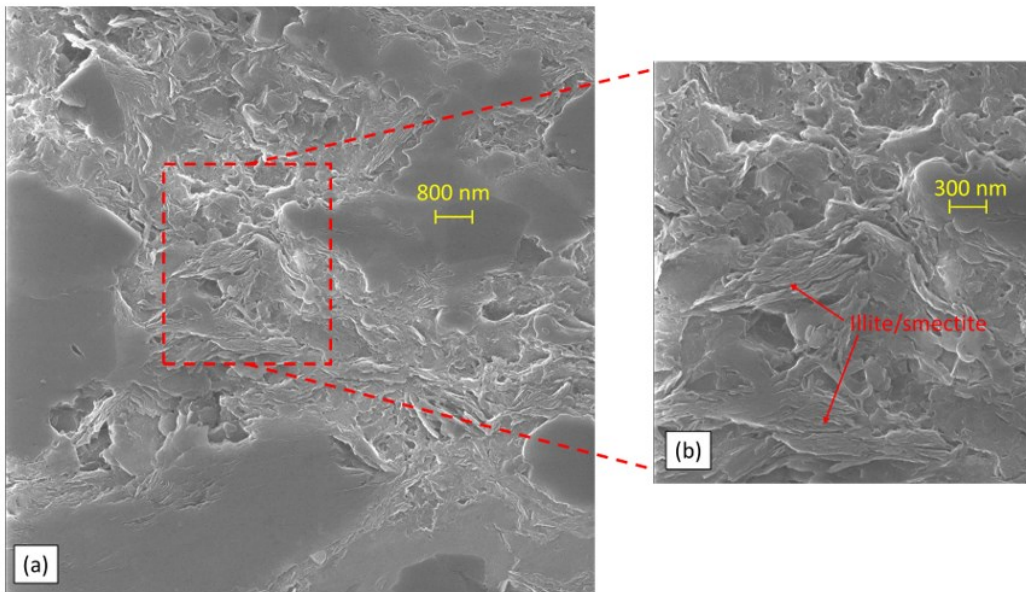


Figure 5-7. SEM image of a focused area (a) and a magnified clay area (b) for a shale sample from Group 2. The layered and curled-flakes structure indicates the illite/smectite in the zoomed-in area.

5.4 Results

This section presents the results of the three sets of experiments. First, the imbibed mass and induced strain for unconfined samples immersed in water or oil is compared. Second, the imbibed mass and induced stress for the samples immersed in water which are confined in the vertical direction is compared. Finally, the results of similar tests by using brine of different salinities are reported to investigate the effects of salt concentration on imbibition-induced stain and stress.

5.4.1 Induced Strain during Water and Oil Imbibition

Figure 5-8 shows the ϵ_x , ϵ_y and S_w measured during water imbibition process. The key observations are as follows:

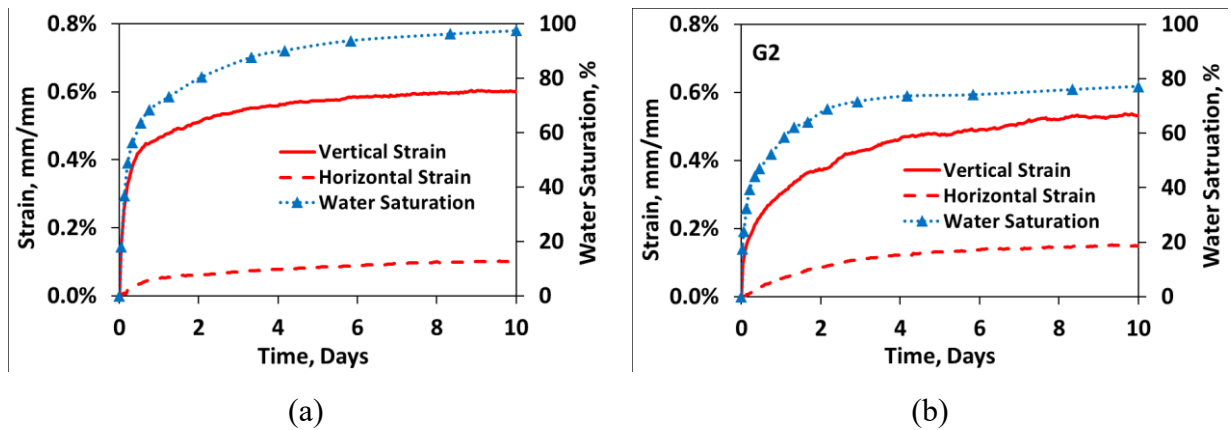
- 1) The final S_w after 10 days of imbibition varies from 66.3% (Group 4) to 97.5% (Group 1).
- 2) Both ϵ_x and ϵ_y are positively correlated to S_w .
- 3) The final ϵ_y ranges from 0.12% (Group 5) to 0.78% (Group 2). The final ϵ_x ranges from 0.04% (Group 5) to 0.18% (Group 2), which is around 4 times lower than the corresponding ϵ_y .
- 4) More than 59% of the final S_w and more than 63% of the final ϵ_y are achieved in the first day of imbibition. The sharp increasing of ϵ_y at early stage of water imbibition is more pronounced for Groups 1, 3, and 4. Unlike ϵ_y , ϵ_x does not rise sharply at the beginning of water imbibition.
- 5) The samples with similar S_w show different ϵ . For example, at $S_w = 60\%$, ϵ_y of Groups 1, 2, and 3 are 0.50 %, 0.38%, and 0.57%, respectively. The observed variations in ϵ_y may be due to the difference in clay content of the shale samples and will be discussed in section 5.5.3.
- 6) The values of ϵ_x and ϵ_y for Group 5 are significantly lower than those for the other groups. It can be explained by the lower clay content of samples from Group 5, resulting in less clay swelling.

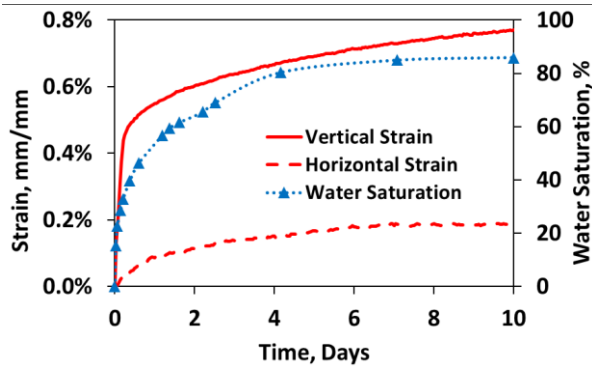
Observations 3 and 4 are supported by the microcracks observed along the depositional lamination of a HR shale sample (see Figure 5-9). These microcracks lead to higher permeability along the lamination direction compared with that against the lamination direction. Thus, enhanced water imbibition along the lamination are observed (Ghanbari and Dehghanpour, 2015). When

imbibition starts, the water imbibing into the microcracks causes the hydration of clay minerals in the vicinity of the microcracks. Clay swelling may further enlarge the microcracks, resulting in sample expansion in the vertical direction at the early stage of water imbibition. However, expansion in the vertical and horizontal directions are usually unequal (see Figure 5-8). This is due to the anisotropic nature of the shale samples.

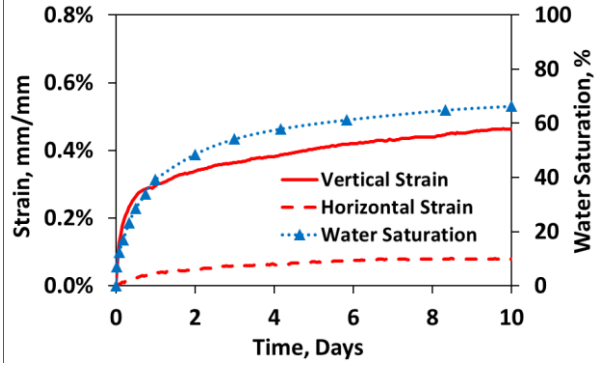
Figure 5-10 shows the values of ϵ_y and S_o for the shale samples during oil imbibition process. Unlike the S_w curves in Figure 5-8, the S_o curves reach equilibrium within 1 day, and the maximum values of S_o is between 44.1% (Group 1) to 53.6% (Group 2). The S_o -values are significantly lower compared with the corresponding S_w -values. Similar imbibition results for the HRB samples were observed in the previous studies (Dehghanpour et al., 2013). ϵ_y shown in Figure 5-10 has the values around zero during the oil imbibition process. ϵ_x is also measured and has similar values with the ϵ_y . The zero value of ϵ_y and ϵ_x suggests that oil imbibition into the shale samples does not result in sample expansion.

A comparison of ϵ_y curves in Figure 5-8 and Figure 5-10 indicates that clay swelling is responsible for sample expansion. Clay swelling stems from hydration of ions (e.g. Na^+ , K^+) in the interlayer spacing of clay platelets, resulting in expansion of shale samples as observed during water imbibition process but not observed during oil imbibition process. The swelling mechanism of a typical swelling clay, smectite, is briefly reviewed in Appendix E.

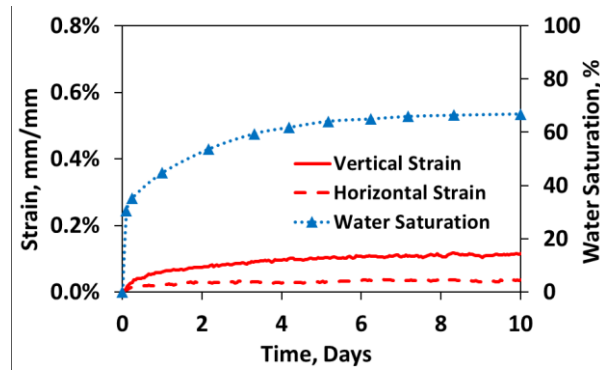




(c)



(d)



(e)

Figure 5-8. ϵ_x , ϵ_y and S_w during water imbibition into the shale samples. (a) Group 1, (b) Group 2, (c) Group 3, (d) Group 4 and (e) Group 5.

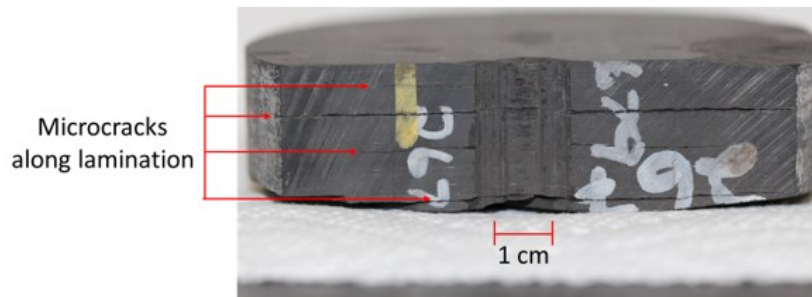
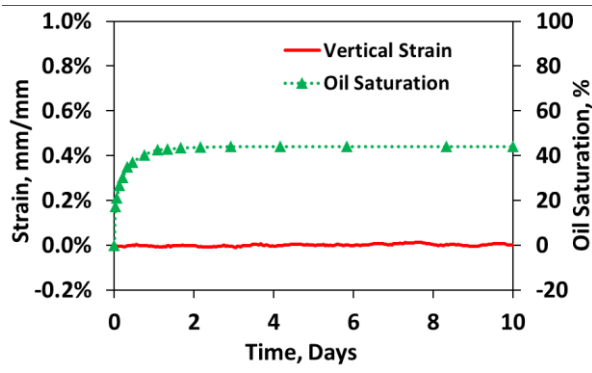
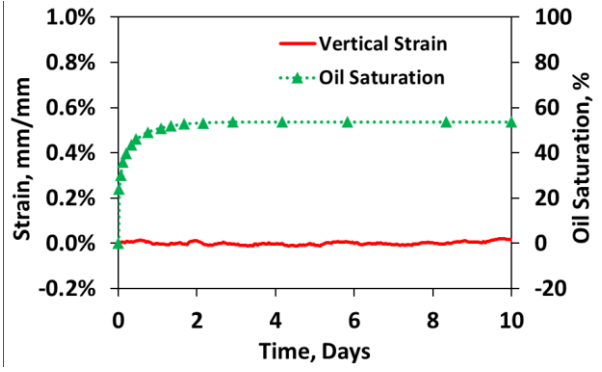


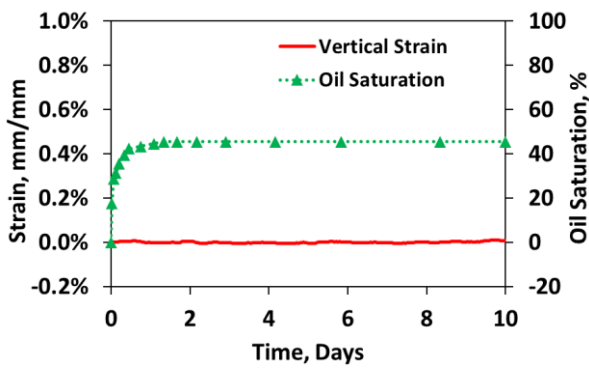
Figure 5-9. Microcracks along the depositional lamination observed on a randomly-picked HRB shale sample.



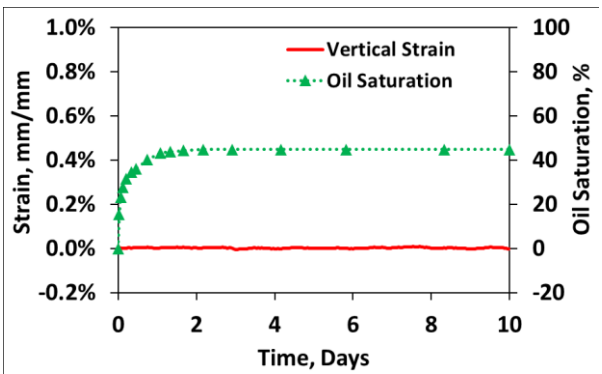
(a)



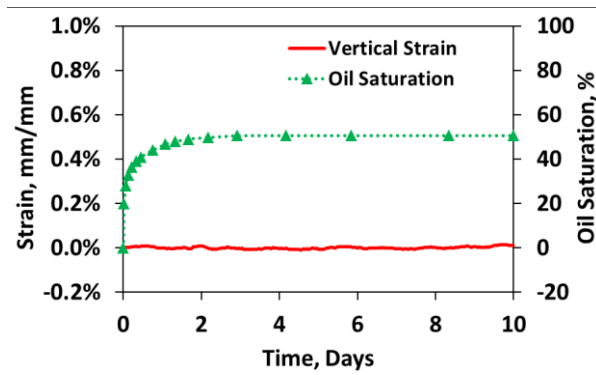
(b)



(c)



(d)



(e)

Figure 5-10. ϵ_y and S_o during oil imbibition into the shale samples. (a) Group 1, (b) Group 2, (c) Group 3, (d) Group 4 and (e) Group 5.

5.4.2 Induced Stress during Water Imbibition

Here, the samples are confined in vertical direction ($\epsilon_y = 0$) and σ are measured in the vertical direction during water imbibition. The measured σ and S_w after the experiments (6 days) are presented in Figure 5-11. σ increases with imbibition time. Samples with higher σ generally have higher S_w at the end of experiments. The correlation of σ with M_{imb} and clay content will be discussed in sections 5.5.2 and 5.5.3, respectively.

The values of σ are relatively low, ranging from 45 to 92 psi after 6 days of water imbibition. The measured σ is negligible compared with the in-situ stress of the target shale formation ($\sim 10,000$ psi for maximum principal stress) (Bell et al., 1990; Oliver et al., 2016). For σ measurement, only 40 psi confining pressure applied on the vertical direction. To investigate the effect of confining pressure on σ values, σ values are measured under different confining pressures (125 psi, 65 psi, 40 psi, 25 psi, 15 psi). Five HRB shale samples are selected from the depth of 2389 m in Evie member. Figure 5-12a shows the measured σ versus imbibition time, and Figure 5-12b shows the semi-log plot of final σ versus confining pressure. Figure 5-12b, σ is proportional to the logarithmic function of the confining pressure applied in the vertical direction. $\sigma \approx 209$ psi is estimated under 10,000 psi confining pressure from the logarithmic function. It must be noted that the shale samples are not restricted to expand in the horizontal direction. Thus, σ may be also affected by the Poisson effect.

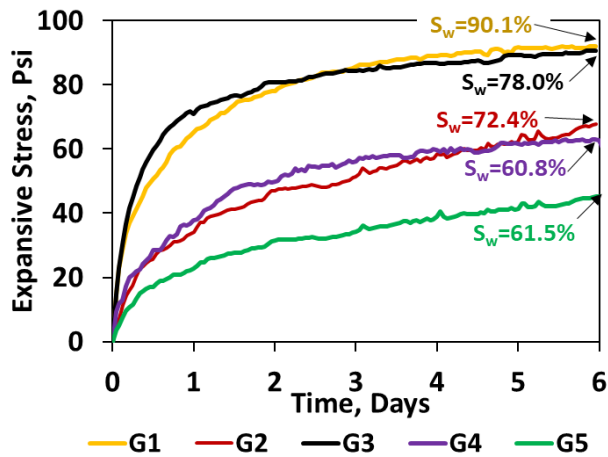
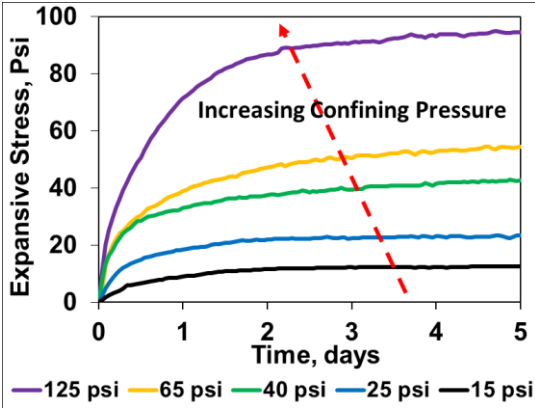
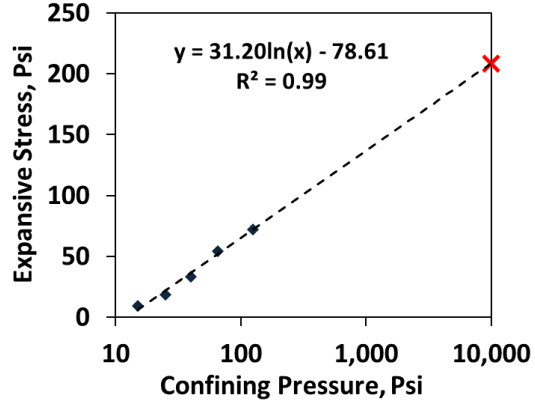


Figure 5-11. σ of the shale samples in vertical direction versus the time of water imbibition. S_w measured at the end of the experiments (6 days) are presented on the plot.



(a)

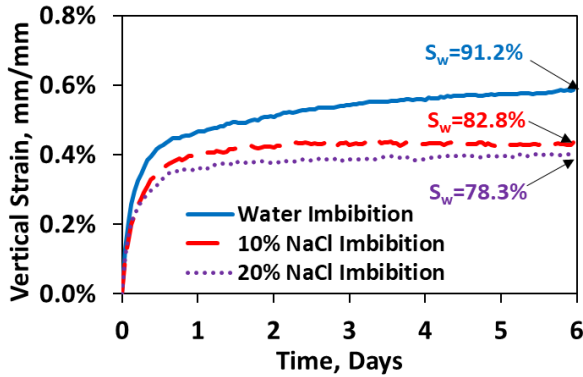


(b)

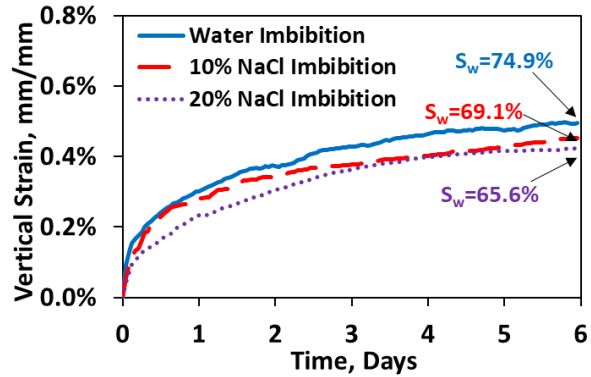
Figure 5-12. (a) σ of shale samples in vertical direction versus the time of water imbibition. Five Horn River shale samples are selected from 0.5-m depth interval of the same well. The samples are confined in the vertical direction with different confining pressures (125 psi, 65 psi, 40 psi, 25 psi, 15 psi) during the tests.

5.4.3 Effects of Ion Concentrations on Induced Strain and Stress.

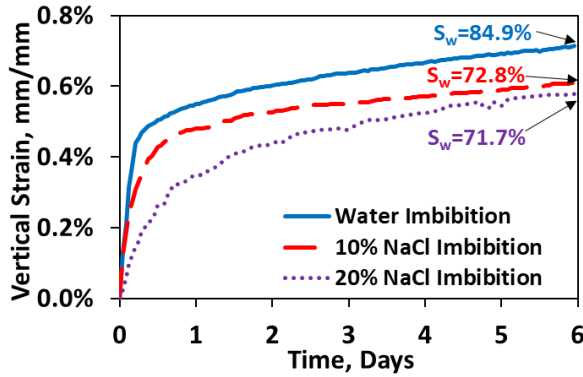
Figure 5-13 shows ϵ_y measured during the imbibition of DI water, 10 wt. % NaCl brine and 20 wt.% NaCl brine. It also shows the estimated S_w after the experiments (6 days). We observe that ϵ_y for samples imbibing DI water is generally higher than that for samples imbibing NaCl brines. Higher NaCl concentration in the imbibing fluid results in lower osmotic potential, leading to less water imbibition and lower ϵ_y . However, the samples of Group 5 have the similar ϵ_y values during water and brine imbibition, possibly due to their relatively low clay content, as listed in Table 5-4.



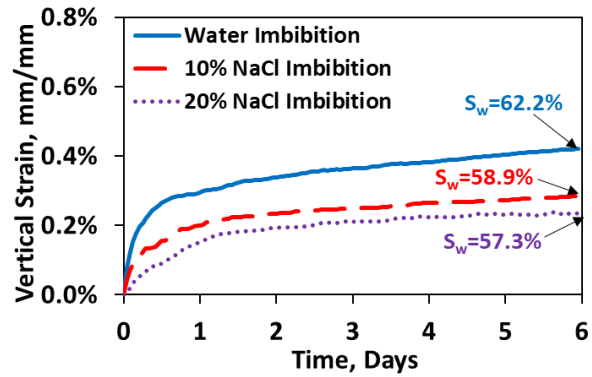
(a)



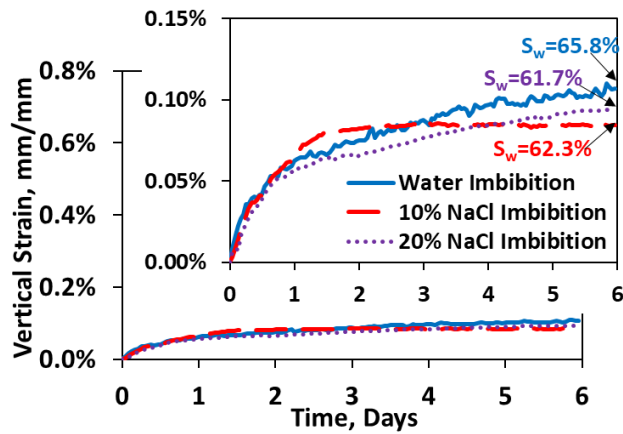
(b)



(c)



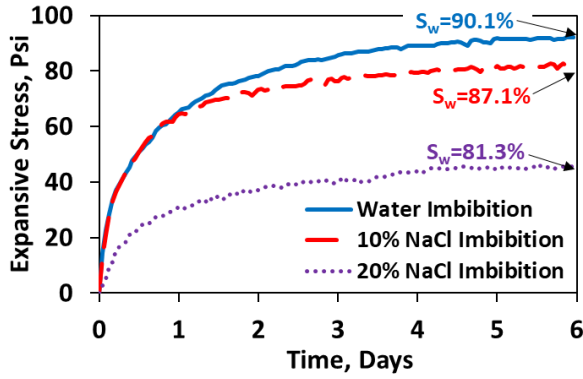
(d)



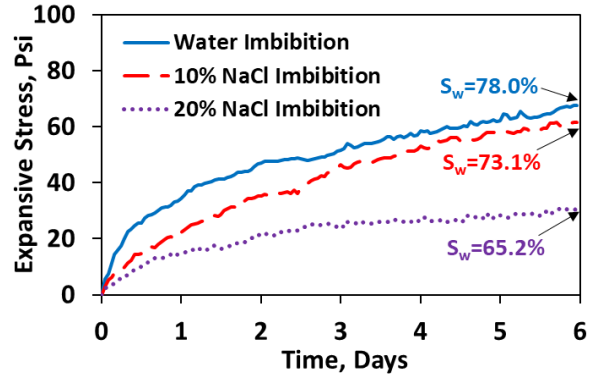
(e)

Figure 5-13. ϵ_y measured during imbibition of DI water, 10 wt% NaCl brine and 20 wt% NaCl brine for the samples of (a) Group 1, (b) Group 2, (c) Group 3, (d) Group 4 and (e) Group 5. S_w measured at the end of the experiments (6 days) are presented on the plot. ϵ_y curves of Group-5 are zoomed-in due to the relatively low ϵ_y values.

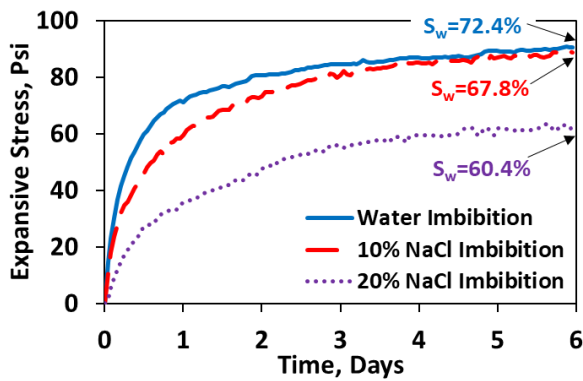
Figure 5-14 shows the measured values of S_w and σ during the imbibition (6 days) of water, 10 wt. % NaCl and 20 wt. % NaCl solutions. The final σ after 6 days of water and brine imbibition ranges from 45 psi to 92 psi for water imbibition, from 41 psi to 89 psi for 10 wt. % NaCl brine imbibition, and from 20 psi to 63 psi for 20 wt. % NaCl brine imbibition. Similar to the observations in Figure 5-13, increasing the ion concentration of imbibed brine reduces the σ and the final S_w . It indicates that σ is mainly caused by clay swelling which can be inhibited by increasing NaCl concentration.



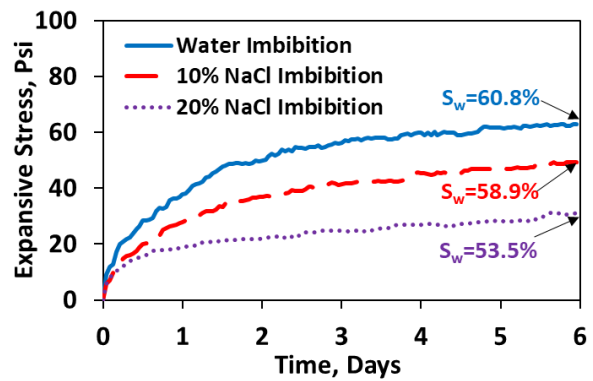
(a)



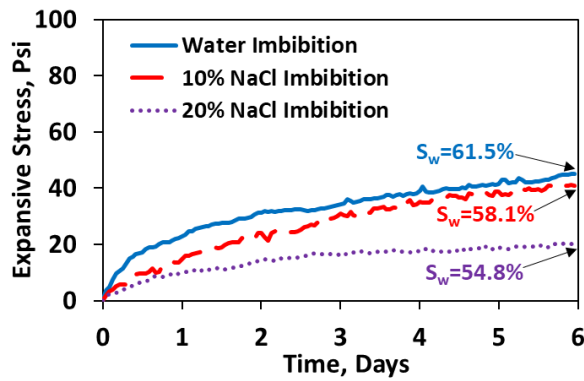
(b)



(c)



(d)



(e)

Figure 5-14. σ measured during imbibition of DI water, 10 wt% NaCl brine and 20 wt% NaCl brine for the samples of (a) Group 1, (b) Group 2, (c) Group 3, (d) Group 4 and (e) Group 5. S_w measured at the end of the experiments (6 days) are presented on the plot.

5.5 Discussion

The measurement of M_{imb} , ε and σ for 45 shale samples soaked in water, brine and oil led to these key results:

- 1) M_{imb} of water is significantly higher than M_{imb} of oil. The difference between S_w and S_o after 10 days imbibition can be up to 53% of the total pore volume.
- 2) ε and σ are observed during water imbibition into the shale samples.
- 3) $\varepsilon \approx 0$ during oil imbibition into the shale samples.
- 4) σ is proportional to the logarithmic function of the confining stress.
- 5) Increasing NaCl concentration decreases the values of ε , σ and M_{imb} for all the shale samples.
- 6) ε_y is significantly higher than ε_x , especially in the early stage of water imbibition.

Based on these results, this section investigates the existence of correlations among clay content of gas shales, imbibed water mass, and induced strain and stress. First, the porosity enhancement and excess water imbibition due to sample expansion are quantitatively evaluated. Second, correlations of clay content and M_{imb} with ε and σ are discussed. Finally, the mechanism of salt concentration in imbibing water on clay swelling inhibition is briefly discussed.

5.5.1 Water Imbibition Affected by Sample Expansion

Water imbibes significantly more than oil in all the shale samples. This observation cannot be explained by the higher capillary pressure of water compared with that of oil (Dehghanpour et al., 2013). Hydration and swelling of clay minerals result in sample expansion, which is a possible reason for the excess water imbibition. It is assumed that the total bulk-volume change during water imbibition is due to the pore-volume enhancement, described as ΔV in Eq. 5.5. Thus, the enhanced porosity ($\Delta\phi$) can be calculated as:

$$\Delta\phi = \phi_{wet} - \phi_{dry} = \frac{\Delta V + V_{dry} \times \phi_{dry}}{\Delta V + V_{dry}} - \phi_{dry} \quad (5.7)$$

where, ϕ_{wet} is the porosity after water imbibition. Table 5-5 lists the original porosity and the estimated enhanced porosity after 10 days of water imbibition. The pore volume of the samples increases up to 1.44 cm³, representing an increase in porosity of up to around 1 %.

Table 5-5. Porosity of the HRB shale samples before and after 10 days of water imbibition.

Sample	Initial Bulk Volume, cm ³	Original Porosity, %	Hydrated Bulk Volume, cm ³	Pore Volume Enhancement, cm ³	Porosity after Hydration, %	Porosity Enhancement, %
G-1	237.26	2.92	238.68	1.42	3.52	0.60
G-2	235.26	4.98	236.62	1.36	5.56	0.58
G-3	235.27	6.37	237.08	1.81	7.14	0.77
G-4	231.69	6.40	232.71	1.02	6.84	0.44
G-5	237.36	3.90	237.62	0.26	4.01	0.11

The total water imbibed into the shale sample is the sum of water that imbibed into ϕ_{dry} and the water that imbibed into $\Delta\phi$. Hence, the excess water imbibition due to sample expansion (ΔS) can be estimated by

$$\Delta S = S_w - S'_w = \frac{M_{imb}}{\rho \times V_{dry}} - \frac{M_{imb}}{(\phi + \Delta\phi) \times V_{dry}} \quad (5.8)$$

Figure 5-15 shows the calculated ΔS after 10 days of water imbibition versus total clay content and illite/smectite content of the samples. The values of ΔS ranges from 1.8% to 27.0% and positively correlates with the total clay content and illite/smectite content of the samples. This indicates that the effect of sample expansion on excess water uptake should not be neglected during imbibition in shales with high clay content. Other possible reasons include chemical osmosis (Neuzil, 2000), water adsorption (Fripiat et al., 1984) and poorly connected hydrophobic pore network (Xu and Dehghanpour, 2014).

It should be noted that different clays have different swelling potentials. For example, mica and illite have less swelling potential than smectite. This is because their interlayer cations (e.g. K⁺) can form strong interlayer bonding with tetrahedral sheets, preventing water from entering the interlayer spacing. Due to the limitation of XRD analysis, the content of swelling clay (i.e. smectite) cannot be precisely identified.

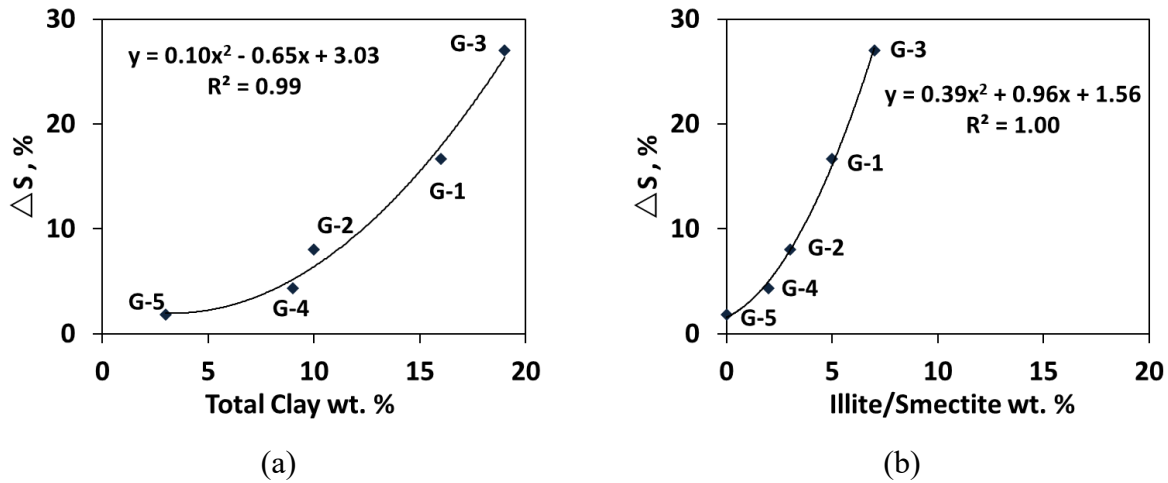


Figure 5-15. Excess water imbibition due to sample expansion versus (a) the total clay content and (b) illite/smectite content of the samples.

5.5.2 Induced Strain/Stress versus Imbibed Water Mass

To investigate the effect of M_{imb} on the sample expansion, the measured ϵ_x and ϵ_y versus normalized M_{imb} are plotted in Figure 5-16. $\epsilon_y > \epsilon_x$ for all samples, and both ϵ_x and ϵ_y are positively correlated to M_{imb} , which can be explained by clay hydration and swelling. Under laboratory conditions, without any confining pressure applied on the samples, sample expansion enhances the pore space during water imbibition process.

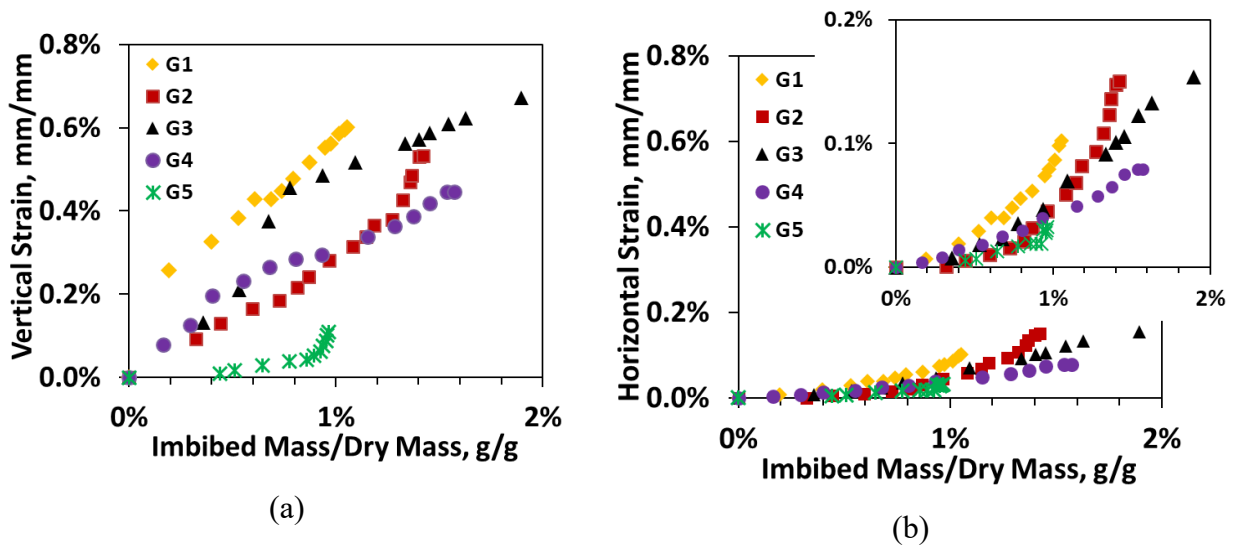


Figure 5-16. (a) ϵ_x versus normalized M_{imb} and (b) ϵ_y versus normalized M_{imb} for the shale samples. (a) ϵ_x are zoomed-in due to the relatively low ϵ_x -values.

Figure 5-17a shows ϵ_x versus the normalized M_{imb} . The convex relationship between ϵ_x and normalized M_{imb} suggests that ϵ_x is more pronounced at late stage of water imbibition. For example, as shown in Figure 5-17a, a normalized M_{imb} of 0.5% results in only $\epsilon_x = 0.02\%$ at early stage. However, the same normalized M_{imb} results in $\epsilon_x = 0.09\%$ at late stage. Unlike ϵ_x in Figure 5-17a, the ϵ_y data are scattered. This is mainly due to the existence of natural and induced fractures along the depositional lamination, as shown in Figure 1-9. Fractures are mainly induced parallel to the depositional lamination. This enhances the heterogeneity perpendicular to the lamination (Mokhtari and Tutuncu, 2015). The existence and intensity of these fractures vary significantly from one sample to another, resulting in different volumes of water imbibing into these fractures. Figure 5-18 shows the σ versus normalized M_{imb} . Unlike the observations from Figure 5-17a, σ does not show a strong correlation with the normalized M_{imb} .

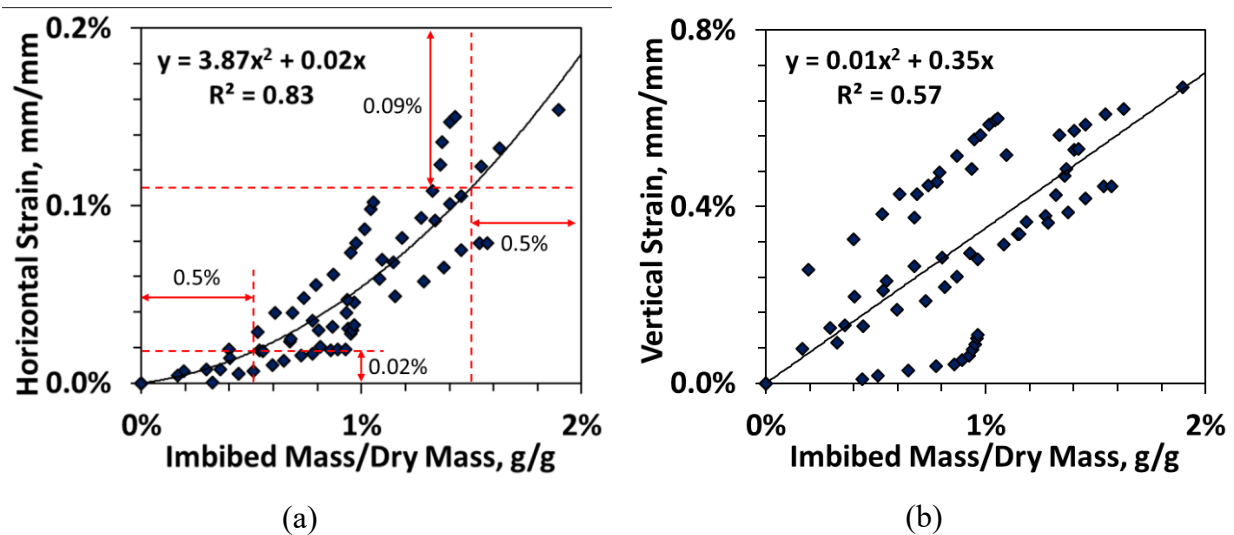


Figure 5-17. The correlations of (a) ϵ_x and (b) ϵ_y with normalized M_{imb} for the shale samples.

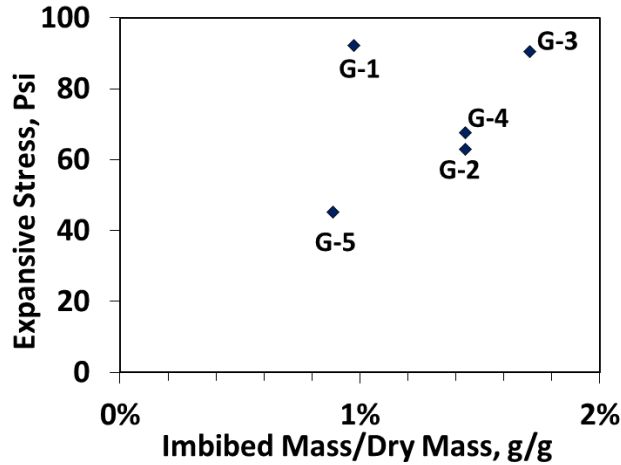
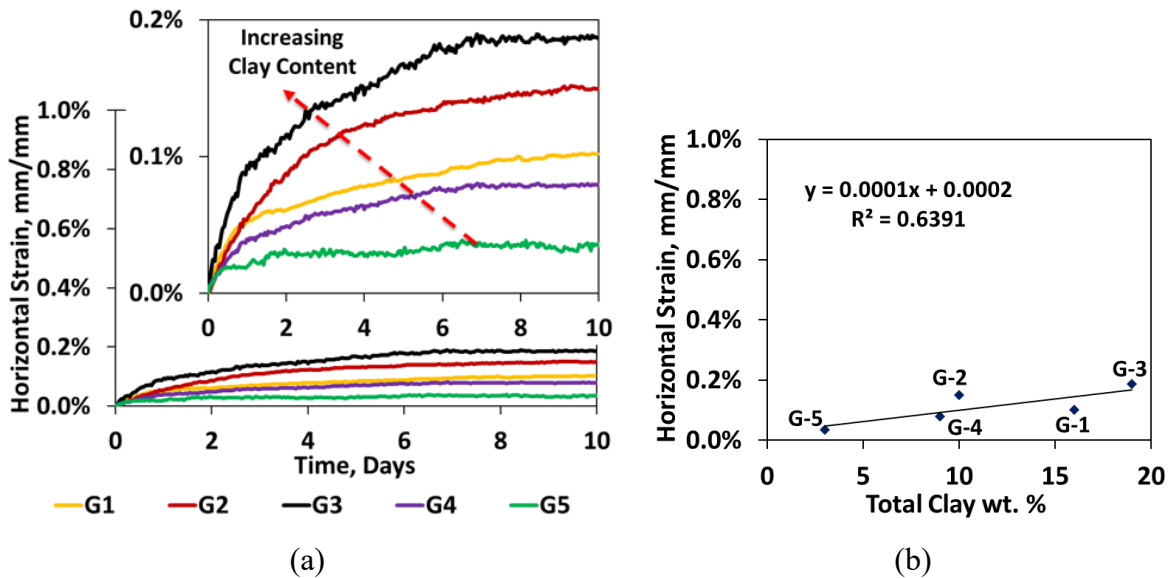
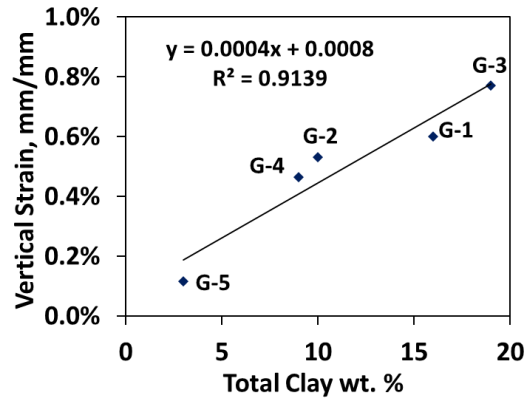
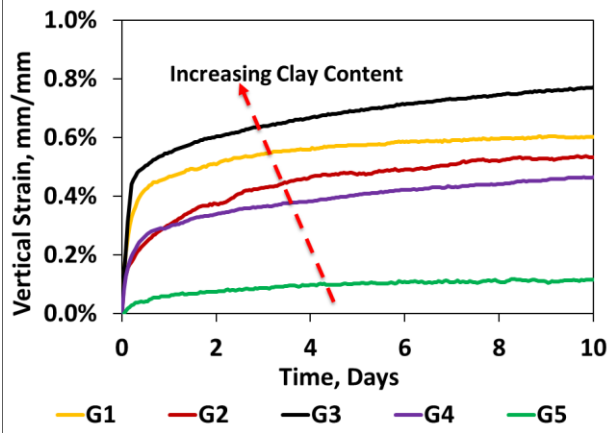


Figure 5-18. σ versus the normalized M_{imb} for the shale samples applied with 40 psi confining pressure

5.5.3 Induced Strain/Stress versus Clay Content of Shale

Figure 5-19a and 5-19c show that ϵ_x and ϵ_y are induced during water imbibition into the samples. Figure 5-19b and 5-19d show the final ϵ_x and ϵ_y after 10 days of water imbibition versus total clay content of the samples. The clay content ranges from 3 wt% to 19 wt%. Samples with higher clay content have higher ϵ_x and ϵ_y . The measured σ versus imbibition time is shown in Figure 5-20a. The final σ after 6 days of water imbibition versus total clay content is shown in Figure 5-20b. Similar to the ϵ_x and ϵ_y , σ is also positively correlated to the clay content of the shale samples.

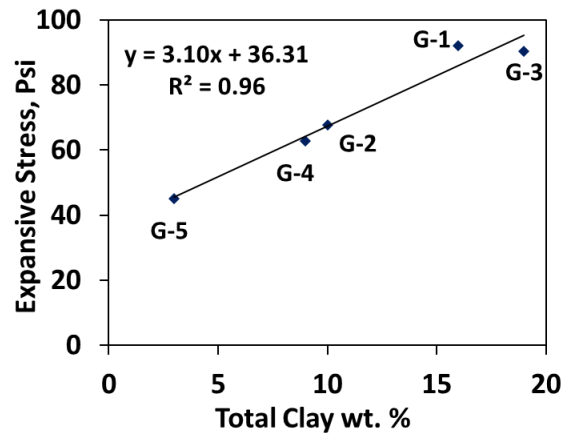
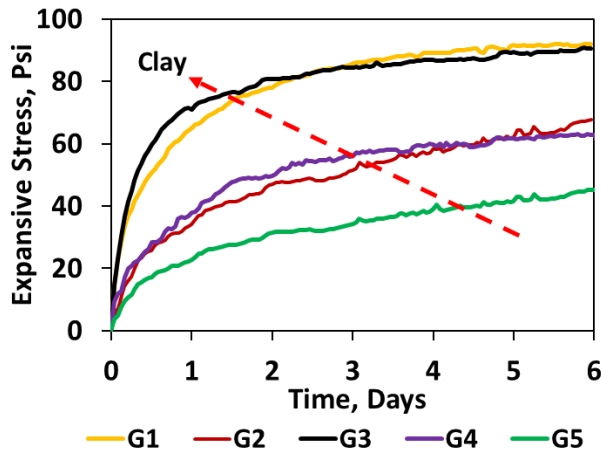




(c)

(d)

Figure 5-19. (a) ϵ_x and (c) ϵ_y versus time of water imbibition. (b) ϵ_x and (d) ϵ_y after 10 days of water imbibition versus total clay content of the shale samples.



(a)

(b)

Figure 5-20. (a) σ of the shale samples versus water imbibition time, and (b) σ after 6 days of water imbibition versus total clay content of the samples. 40 psi of confining pressure is applied vertically on all the shale samples.

5.5.4 Induced Strain/Stress versus Ion Concentration of Imbibed Brine

In section 5.4.3, it is observed that ϵ and σ decrease with increasing salt concentration of water due to the effect of osmotic pressure (Chen et al., 2010) and clay swelling. The final values of ϵ and σ are plot versus NaCl concentration in Figure 5-21. It shows that ϵ and σ are negatively correlated with NaCl concentration.

The imbibed water inside the pore network of shales usually has high salinity due to dissolution of precipitated salt, cation exchange from clays and dissolution of rock minerals. The low-salinity water outside the pore network has high osmotic potential, compared with the imbibed water inside the pore network. It provides additional driving force for water imbibition. Water imbibing into the pore network decreases of salt concentration of imbibed water, resulting in more clay swelling by increasing the interlayer spacing of the clay (Stuart and Mulder, 1985; Chávez-Páez et al., 2001; Boek and Sprik, 2003).

Swelling of diffuse double layer, also known as osmotic swelling, is the dominant mechanism for the clay swelling at relatively large inter-layer separations ($> 22 \text{ \AA}$) (Rao et al., 2013). Water molecules and ions (i.e. Na^+ , K^+) in brine can form electrical double-layer structure to balance the negative charge on the surface of clay platelets. The thickness of electrical double layer, also known as Debye length, can be estimated by (Leckband and Israelachvili, 1993)

$$\kappa^{-1} = \sqrt{\frac{\varepsilon_0 \varepsilon_r k_B T}{2e^2 N_A}} \times \frac{1}{\sqrt{I}} \quad (5.7)$$

Where, κ^{-1} is the thickness of the electrical double layer, ε_0 is the vacuum permittivity, ε_r is the relative permittivity of medium, k_B is the Boltzmann constant, e is the electron charge, N_A is the Avogadro number. I is the ionic strength of an electrolyte solution, which can be calculated by (Stuart and Mulder, 1985),

$$I = \frac{1}{2} \sum_{i=1}^n C_i Z_i^2 \quad (5.8)$$

Where, C_i is the molar concentration and Z_i is the valence of ion “ i ”. For a given solution at the constant temperature (constant ε and T), the thickness of double-layer is only a function of ion concentration. Imbibition of brine with less salt concentration results in higher κ^{-1} , which increases repulsion force between clay platelets (Madsen and Müller-Vonmoos, 1989; Abdullah et al., 1999; de Carvalho Balaban et al., 2015). Therefore, reducing NaCl concentration in the bulk solution increases ε and σ , as shown in Figure 5-21.

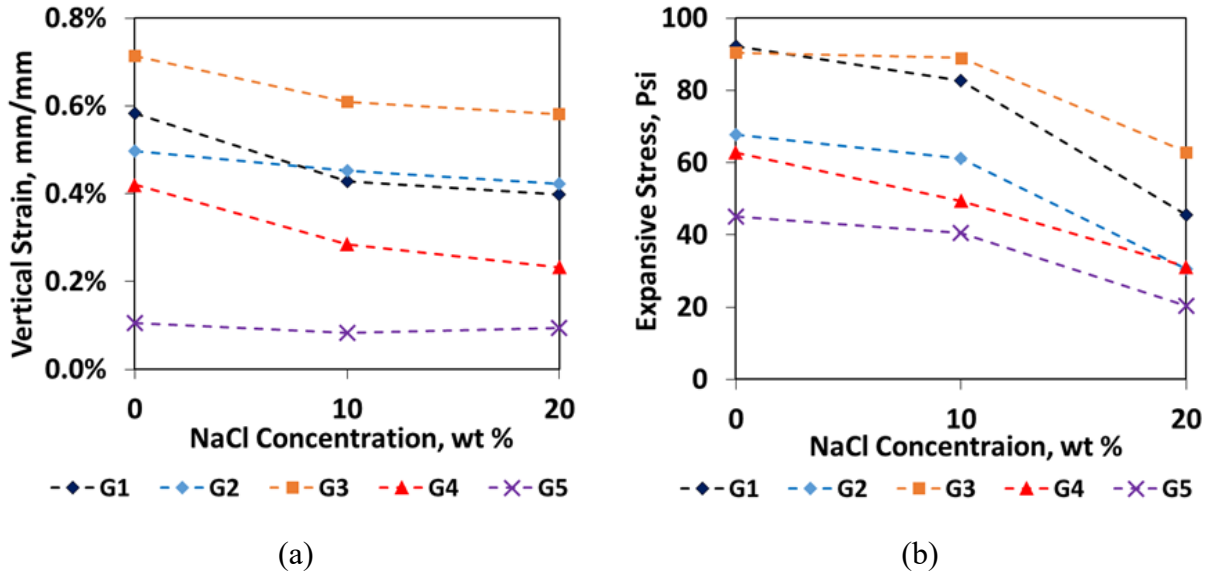


Figure 5-21. (a) ϵ_y and (b) σ at the end of water/brine imbibition experiment (6 days) versus NaCl concentration in the bulk solution.

5.6 Summary

The experiment results lead to the following conclusions:

- Water imbibition into the shale samples enhances the pore volume by up to 0.72% of sample initial bulk volume. The enhanced porosity contributes to the excess water imbibition into the shale samples.
- The induced strain is positively correlated to the imbibed water mass and clay content of the shale samples. The initial expansion of the samples enhances the existing microcracks, causing further water imbibition and expansion. Hence, shale expansion during water imbibition is a self-amplifying phenomenon.
- When the samples are confined in the vertical direction during water imbibition process, up to 92 psi of stress is induced in the vertical direction. The induced stress is proportional to the logarithmic function of confining pressure and is positively correlated to the clay content of shale samples.

- Sample expansion is more pronounced in the late stage of water imbibition. The early stage of imbibition is mainly controlled by the existing microcracks along the depositional lamination.
- The imbibition and swelling potentials of the shale samples are strongly anisotropic. Water imbibition along the depositional lamination is significantly higher than that perpendicular to the lamination. Consistently, the samples expand more in the direction perpendicular to the lamination.
- Increasing NaCl concentration in the imbibing water effectively restrains the induced strain and stress during the imbibition process.

Chapter 6: Modelling of Water Uptake into Shales

6.1 Introduction

Spontaneous imbibition has been identified as the main mechanism for the water retention in shales (Dutta et al., 2012; Holditch, 1979). A great interest has been devoted on modeling imbibition process into rocks over a century (Bell and Cameron, 1906; Lucas 1918; Washburn, 1921; Handy, 1960; Li and Horne, 2001; Rangel-German and Kovscek, 2002; Cai et al., 2014). Handy (1960) compared two equations for imbibition rates. One is diffusion-type equation derived from the Darcy's law, capillary pressure equation, and the continuity equation. This equation assumes that water and gas are continuous phases during imbibition and is given as:

$$\phi \frac{\partial S_w}{\partial t} = - \frac{\partial}{\partial x} \left[\left(\frac{k_w}{\mu_w} \frac{\partial P_c}{\partial S_w} \right) \frac{\partial S_w}{\partial x} \right] \quad (6.1)$$

Where, ϕ is fractional porosity, S_w is fractional water content at the imbibition front, k_w is effective water permeability in darcies, μ_w is water viscosity, x is distance in centimeters, t is time, P_c is capillary pressure. The second equation describing the imbibition rate is frontal-advance equation. This equation assumes that water imbibes as piston-like displacement and the effect of trapped gas on the capillary pressure gradient is negligible, which is given as:

$$\frac{dx}{dt} = \frac{k_w}{\phi \mu_w S_w} \left(\frac{P_c}{x} - \Delta \rho g \right). \quad (6.2)$$

Where, $\Delta \rho$ is the differential density of water and gas and g is gravitational acceleration. Comparing these two equations indicates that the capillary pressure is the primary driving force for spontaneous imbibition. The imbibed water volume proportional to the square root of time in one dimensional flow.

Recent imbibition studies (Makhanov et al., 2012; Dehghanpour et al., 2013) show a considerably higher water imbibition than oil imbibition into oil-wet shale samples. This cannot be traced by contact angle and capillary effect. Dutta et al. (2012) observed the non-uniform water saturation profile in tight sandstone during imbibition, and attributed the high water saturation to the clay-rich region. Zhou et al. (2016b) and Roychaudri et al. (2013) performed similar imbibition

experiments on shale samples with different clay contents. They observed that shale samples with higher clay content consistently imbibed more water. Shale is a clay-rich sedimentary rock. For example, the aggregate clay minerals can be up to 70% in Horn River shale samples (Ross and Bustin, 2008). Thus, the unexpectedly high water uptake could be correlated to the presence of clay minerals in shale samples, which can be briefly described as followings:

Osmotic Pressure. It has been known that clay can act as semipermeable membranes, which prevent the passage of a solute without affecting the passage of the solvent (i.e. water) (Bader and Kooi, 2005). When water imbibes into shales, the dissolution of precipitated salts and rock constituents leads to lower chemical potential of imbibed water compared with the bulk water. This generates the chemical potential difference across the semi-permeable clay membranes and attracts more water into the pores of shales (Cey et al., 2011). Neuzil (2000) reported the results of a field experiment that osmotic pressure could draw low salinity water from borehole into shale.

Water Adsorption. Most clay surfaces have a net negative surface charge due to isomorphic substitution (Sposito et al., 1999; Keijzer, 2000). The isomorphic substitution is the substitution of Al^{3+} for Si^{4+} in the silica tetrahedron and Mg^{2+} or Fe^{2+} for Al^{3+} in the octahedron of clay minerals. When clays are dehydrated during geologic compaction process, the laminated layers of clay come close to each other and creates electrical potential between the layers. The potential is developed midway between two layers and its magnitude increases as distance between the layers decreases (Lagaly, 2006). The layers with exchangeable cations provide a negatively charged environment which attracts polar molecules (i.e. water molecules) due to electrostatic force (Fripiat et al., 1984; Hensen and Smit, 2012). In addition to the electrostatic force, molecular forces (i.e. hydration force) may also contribute to the water adsorption on the surface of clays (Schoonheydt and Johnston, 2006). The water molecules in the interlayer spacing tend to be hydrated with cations (K^+ , Na^+ , Mg^{2+} , Ca^{2+}), adsorbed on the surface of clay and formed double-layer hydration shell (Li et al., 2016). For example, water molecules are easily adsorbed on the surface of kaolinite, and the adsorption rate is associated with the hydrogen in hydroxyl groups in kaolinite substituted by cations in water (Aylmore and Quirk, 1966; Yavuz et al., 2003; Hu and Michaelides, 2008). As a result of electrostatic and hydration forces, water can attach to clay surface areas and form clay-bound water (Churaev et al., 2013; Tuller and Dudley, 1999; Li et al., 2017). The clay-bound water content

could reach up to 7.19% of the total sample volume (Hill et al., 1979; Boyer et al., 2006). It makes these clays prone to adsorb and hold water into their layered structure.

Clay Swelling. Hydration of swelling clay (i.e. smectite) will result in increasing the interlayer spacing because of the relatively weak intercrystalline bonds in the clay structure (Laird, 2006). The clay swelling behavior can be generally divided into crystalline swelling osmotic swelling (Liu and Lu, 2006). Crystalline swelling occurs at inter-layer separations of 10-22 Å, with a limited amount of adsorbed water. In comparison, osmotic swelling occurs at inter-layer separations larger than 22 Å, which involves a much larger amount of adsorbed water (Rao et al., 2013). Hydration of packed Na⁺-smectite and Ca²⁺-smectite specimens can result in up to 58% and 102% volume increase, respectively (Likos and Lu, 2006). Chenevert (1970) conducted a water adsorption experiment on shale samples and observed shale alteration induced by clay swelling. Ghanbari and Dehghanpour (2015) compared the water uptake of confined and unconfined shale samples. They found unconfined shale samples consistently imbibed more water than confined shale samples. Induced microfractures have been observed during water uptake into shale samples (Ghanbari and Dehghanpour, 2015; Sun et al., 2015). During the Hydration stress is concentrated on the fracture tip or edge of pores and creates tensile fractures (Liang et al., 2015). Expanded pores and induced microfractures increases the total pore volume, which may result in excess water uptake into shales (Gupta et al., 2017).

The overall spontaneous imbibition in clay-rich shales is controlled by 1) capillary suction, 2) water adsorption on clay surface due to electrostatic force and hydration force, and 3) expanded pores and induced microfractures due to clay swelling. Of particular interest is understanding the role of each mechanism during water imbibition process. This article extends the previous studies (Xu and Dehghanpour, 2014) about water uptake in Horn River clay-rich shales. The rest of the paper is organized as follows: Section 2 describes the materials and methods of 1 dimensional imbibition experiments. Section 3 shows the sample expansion and imbibition profiles measured during imbibition experiments. Section 4 decouples the total imbibition profiles and evaluates the contribution of capillary suction and sample expansion in water imbibition. Section 5 presents a mathematical model, combined with experimental imbibition data, to obtain the adsorption

coefficient for shale samples. The obtained adsorption coefficient is useful for better understanding the mechanisms of water imbibition and predicting the water imbibition into shales.

6.2 Experiments

To investigate the mechanisms of water imbibition into shales, several experiments of contact angle, spontaneous imbibition and sample expansion are performed using shale samples. These tests are designed to measure 1) the contact angles of water and oil on the polished surface of shale samples, 2) mass of imbibed water and oil into shale samples, and 3) lateral and axial expansion during co-current water imbibition.

6.2.1 Materials

A total of 15 unpreserved shale samples from the same well in Horn River Basin (HRB) are selected. Ten samples are used to conduct the co-current imbibition experiments using de-ionized (DI) water and kerosene, the other five samples are tested for the axial and lateral expansion during co-current water imbibition. Density, viscosity and surface tension of DI water and kerosene are listed in Table 6-1. The porosity, permeability and the dimensions of the shale samples are listed in Table 6-2. The porosity is measured by helium porosimetry and the permeability is measured by pulse decay permeameter. Due to the heterogeneity of shale samples, the porosity and permeability may vary for each sample. It is assumed that the samples from the depth within ± 1 meter have the same porosity and permeability. The average mineral concentration of the shale samples within ± 1 meter is measured by x-ray diffraction (XRD) and is listed in Table 6-3. All the samples are mainly composed of quartz (52 – 84 wt. %) and clay (10 – 18 wt. %).

Before each set of experiment, the shale samples are dried in a convection oven at 100 °C until mass stabilization, to ensure complete moisture removal from the samples, which may affect the results of imbibition and expansion experiments.

Table 6-1. The dimensions and petrophysical data of shale samples used in 1-D imbibition experiments. The labels of “Water” and “Oil” stands for the samples are used for water and oil imbibition experiments. The label of “Exp” stands for the samples are used for sample expansion measurement.

Label	Depth, m	Porosity, %	Permeability, nD	Cross-sectional area, cm ²	Length, cm
-------	-------------	----------------	---------------------	--	---------------

Sample-1 (Water)	2588	5.39	414	25.52	4.76
Sample-1 (Oil)	2588	5.39	414	25.52	5.18
Sample-1 (Exp)	2588	5.39	414	25.52	4.51
Sample-2 (Water)	2596	4.72	310	25.52	4.02
Sample-2 (Oil)	2596	4.72	310	25.52	4.67
Sample-2 (Exp)	2596	4.72	310	25.52	5.08
Sample-3 (Water)	2612	4.66	276	25.52	4.29
Sample-3 (Oil)	2612	4.66	276	25.52	5.36
Sample-3 (Exp)	2612	4.66	276	25.52	4.37
Sample-4 (Water)	2681	4.98	384	25.52	5.57
Sample-4 (Oil)	2681	4.98	384	25.52	4.96
Sample-4 (Exp)	2681	4.98	384	25.52	4.54
Sample-5 (Water)	2695	5.83	396	25.52	5.13
Sample-5 (Oil)	2695	5.83	396	25.52	4.41
Sample-5 (Exp)	2695	5.83	396	25.52	4.82

Table 6-2. Representative mineralogy of shale samples used in 1-D imbibition experiments measured by XRD.

Mineral wt%	Quartz	Feldspar	Plagioclase	Carbonate	Pyrite	Illite / Smectite	Illite / Mica	Kaolinite	Total Clay
Sample-1	55	7	6	14	4	4	10	0	14
Sample-2	52	5	6	16	3	7	12	0	18
Sample-3	84	3	2	1	1	4	6	0	10
Sample-4	79	0	2	6	2	3	8	0	11
Sample-5	80	1	2	1	2	5	9	0	14

6.2.2 Contact Angle Measurements.

The objective of contact angle measurement is to evaluate its influence on the capillary pressure when shales in contact with water and oil. Samples prepared for contact angle measurements are cut using a table saw. The fresh break surfaces are then polished with abrasive sand belts of 600, 400, and 200 grit. The cutting and polishing of shale samples minimize the affect of surface contamination and roughness on contact angle measurements.

6.2.3 Imbibition Experiments.

The objective of imbibition experiments is to investigate the existence and volume of the excess water imbibition into HRB shale samples. The 1-D imbibition experimental set-up is shown in

Figure 6-1. Before the imbibition experiment, the dry mass of shale sample is measured. During the imbibition process, the total mass of the shale sample is measured at different time intervals using a balance with accuracy of ± 0.01 g. The imbibed fluid mass is then obtained by subtracting the measured mass of wet sample and the initial mass of dry sample.

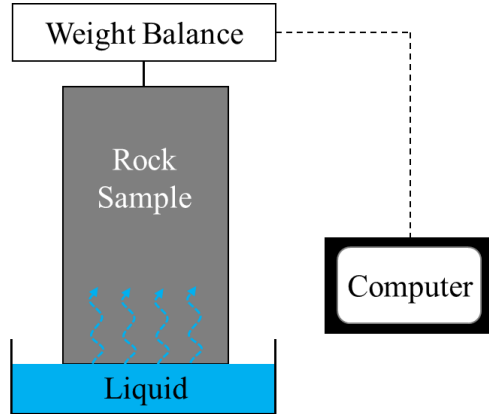


Figure 6-1. Schematic of 1-D imbibition set-up. Imbibed fluid (water or oil) is imbibed from the bottom to the top.

6.2.4 Sample Expansion Measurements.

The objective of the sample expansion measurement is to estimate the pore volume enhancement during the water imbibition process. The enhanced pore volume includes the volume of hydration induced microfractures and the volume of enlarged pore and natural fractures. Before the sample expansion measurement, the diameter (d) and height (h) of dry shale samples are measured using a caliper with 0.01 mm accuracy. As shown in Figure 6-2, the sample position is fixed by two stabilizer mounts. During water imbibition, the diameter change (Δd) and height change (Δh) of the sample are simultaneously measured using two linear variable differential transformers (LVDTs). The accuracy of the LVDT is ± 0.001 mm. Horizontal strain (ϵ_x) and vertical strain (ϵ_y) are then calculated using measured length changes in horizontal and vertical direction, which is

$$\epsilon_x = \frac{\Delta d}{d} \quad (6.3)$$

$$\epsilon_y = \frac{\Delta h}{h} \quad (6.4)$$

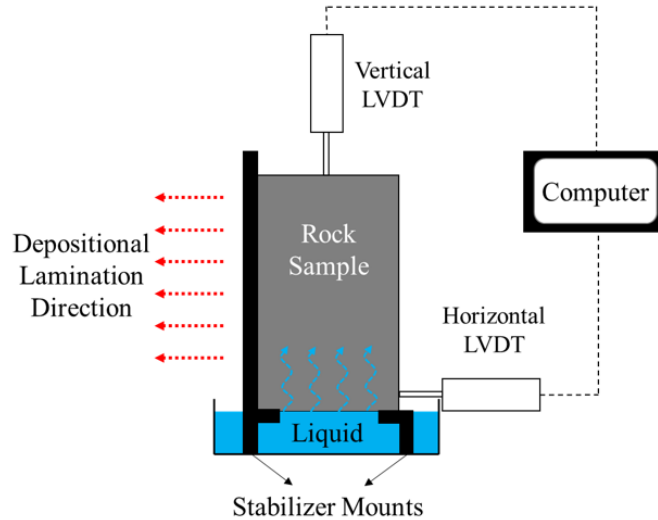


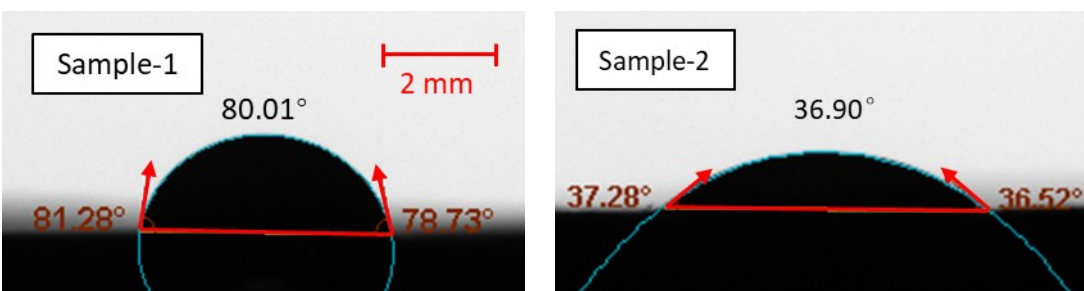
Figure 6-2. Schematic of the LVDT set-up for measuring sample expansion during 1-D imbibition set-up. Imbibed fluid (water or oil) is imbibed from the bottom to the top. Two LVDTs are placed horizontally and vertically to measure the sample expansion in the horizontal and vertical direction.

6.3 Experiments

This section presents the results of the contact angle, imbibition and expansion experiments

6.3.1 Contact Angle

Figure 6-3 shows the contact angles of DI water on the clean surface of the shale samples. The water droplets slowly spread on the surface of samples for one minute. The contact angles in Figure 6-3 are measured when the water droplets are no longer spreading on the samples' surface. Oil droplets completely spread on all the samples' surface within 5 seconds, which indicates the measured contact angles are 0° . Comparison between water and oil contact angles indicates that these samples are oil-wet.



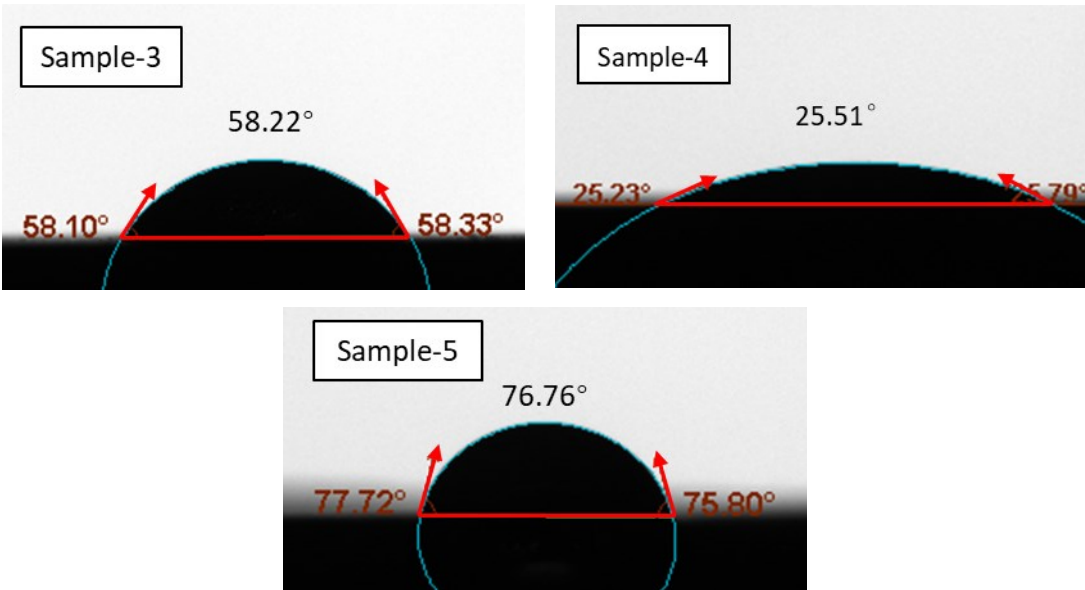


Figure 6-3. Water contact angles of the shale samples. Oil is completely spread on all the rock surface, which has 0° contact angles.

6.3.2 Imbibition

Figure 6-4 shows the cumulative water and oil imbibition volume versus time for 1-D imbibition experiments. It shows that all the samples consistently imbibe more water than oil. After 816 hours spontaneous imbibition, the water can fill up to 0.82 of the initial pore volume. However, the oil can only fill up to 0.39 of the initial pore volume. Although both oil and water imbibe at high rates for the first 100 hours, these rates generally decrease with time.

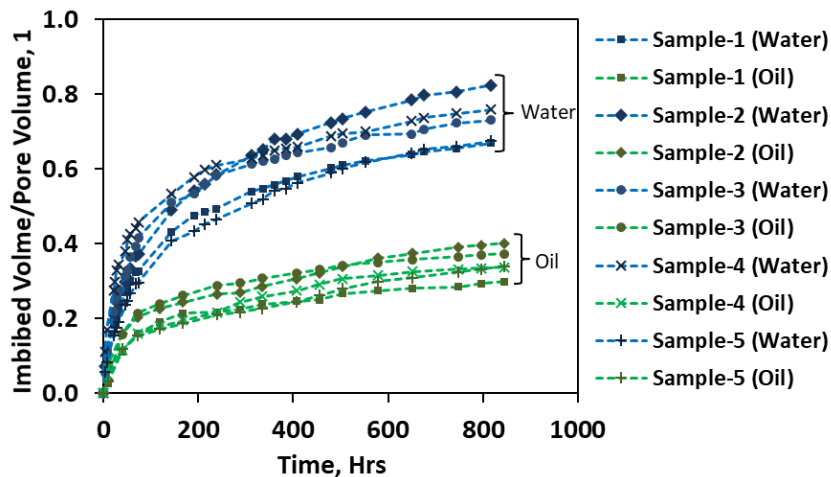


Figure 6-4. Results of 1-D spontaneous imbibition experiment.

6.3.3 Expansion

Figure 6-5 shows the horizontal and vertical strain versus the time of water imbibition into shale samples. Samples expand in both horizontal and vertical directions during water imbibition. The expansion in the vertical direction is higher than that in the horizontal direction, possibly due to the effect of depositional lamination of the shale sample in the horizontal direction. Assuming the enhanced pore volume is equal to the change in bulk volume of the sample, the enhanced pore volume (ΔV) for a cylindrical sample, can be determined as

$$\Delta V = V_{wet} - V_{dry} = \frac{\pi}{4}(d + \Delta d)^2 \times (h + \Delta h) - \pi r^2 \times h \quad (6.5)$$

where, V_{dry} and V_{wet} is the volume of shale samples before and after the water imbibition, respectively. Thus, the enhanced porosity ($\Delta\phi$) can be calculated as

$$\Delta\phi = \phi_{wet} - \phi_{dry} = \frac{\Delta V + V_{dry} \times \phi_{dry}}{\Delta V + V_{dry}} - \phi_{dry} \quad (6.6)$$

where, ϕ_{dry} is the original porosity of dry shale sample, as listed in Table 6-1. ϕ_{wet} is the porosity after water imbibition. The calculated pore volume enhancement, porosity enhancement, along with original porosity after 816 hours water imbibition experiment, are listed in Table 6-3. Water imbibition into shale samples significantly enhance the pore volume and porosity, resulting up to 1.07 porosity unit enhancement. Figure 6-6 shows the enhanced porosity increases with water imbibition time.

Table 6-3. The original porosity before water imbibition, pore volume enhancement, porosity and porosity enhancement after 815 hours water imbibition.

Sample	Sample-1 (Exp)	Sample-2 (Exp)	Sample-3 (Exp)	Sample-4 (Exp)	Sample-5 (Exp)
Original Porosity, %	5.39	4.72	4.66	4.98	5.83
Pore Volume Enhancement, cm ³	0.84	1.09	0.67	0.77	0.93
Porosity after Imbibition, %	6.24	5.71	5.37	5.44	5.87
Porosity Enhancement, %	0.85	0.99	0.71	0.78	0.89

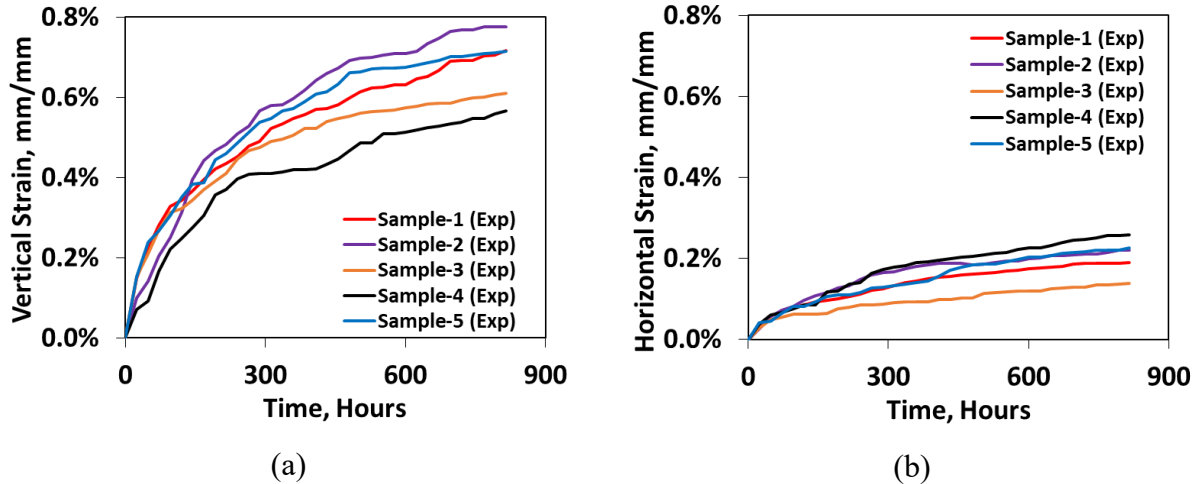


Figure 6-5. Sample expansion results on (a) vertical (perpendicular to the depositional lamination) and (b) horizontal (parallel to the depositional lamination) directions during water imbibition. Expansion curves in vertical direction is zoomed-in due to their relatively low values.

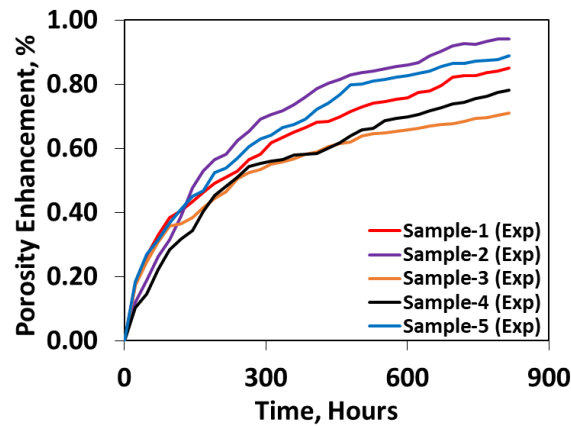


Figure 6-6. Porosity enhancement versus the time of water imbibition into shale samples.

6.4 Decoupling the Total Water Imbibition Profile

The objective of this section is to determine the contribution of capillary suction and sample expansion in water imbibition. A classic imbibition model, Handy's model, combined with the contact angle measured in the previous section, are used to estimate the imbibition due to capillary suction. In Handy's model, the piston-like spontaneous imbibition is assumed and the effect of gravity is ignored. If the imbibition is only controlled by the capillary pressure, the correlation between the time and the water imbibition volume can be evaluated by (Handy, 1960; Li and Horne, 2001):

$$Q_w^2 = \left(\frac{2P_c k k_r w \phi A^2 S_w}{\mu_w} \right) t \quad (6.7)$$

Here, the subscript “w” represents the water. Q is the cumulative volume of imbibed liquid, k is absolute permeability of rock sample, k_r is relative permeability of imbibed liquid, ϕ is fractional porosity, and A is cross-sectional area of sample perpendicular to the flow. S is the liquid saturation behind the imbibition front. μ_o is the liquid viscosity, and P_c is capillary pressure at the saturation of S . Similarly, oil imbibition can be evaluated by

$$Q_o^2 = \left(\frac{2P_c k k_r o \phi A^2 S_o}{\mu_o} \right) t \quad (6.8)$$

Where, the subscript “o” represents the oil. The capillary pressure of oil and water can be approximated using Young-Laplace equation. When the oil and water imbibition reach equilibrium, the effective permeability and fractional porosity are assumed to be the same for both oil and water. Assuming that oil imbibition is only due to capillary suction, thus, at the end of imbibition experiment (t=816 hours), the final imbibed water volume due to capillary suction (Q'_w) can be calculated based on the final imbibed oil volume (Q'_o), which is

$$Q'_w = Q'_o \times \frac{\sqrt{\left(\frac{P_c}{\mu}\right)_{water}}}{\sqrt{\left(\frac{P_c}{\mu}\right)_{oil}}} = Q'_o \times \frac{\sqrt{\left(\frac{\gamma \cos \theta}{\mu}\right)_{water}}}{\sqrt{\left(\frac{\gamma \cos \theta}{\mu}\right)_{oil}}} \quad (6.9)$$

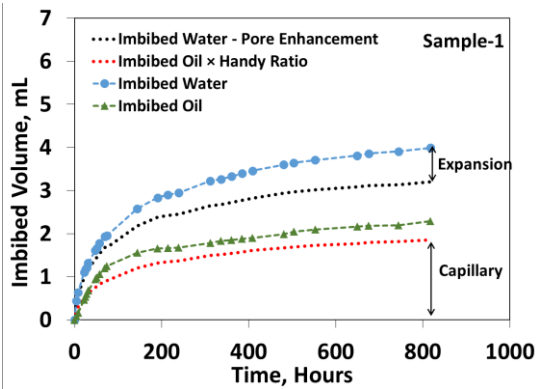
The calculated imbibed water volume due to sample expansion and capillary effect are shown in Figure 6-7. The red dotted line in Figure 6-7 shows the water imbibition driven by capillary effect (Q_{w-cap}), which is calculated by

$$Q_{w-cap} = Q_{o-imb} \times \frac{Q'_w}{Q'_o} \quad (6.10)$$

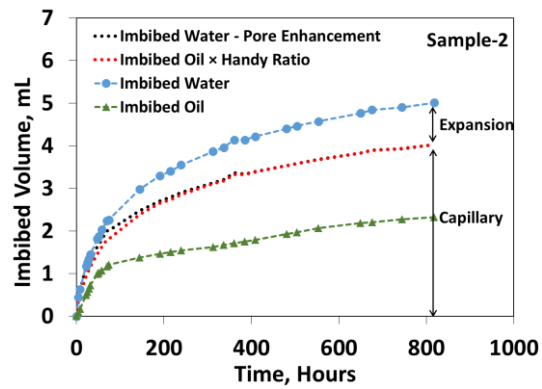
Where, Q_{o-imb} is the measured volume of imbibed oil. Assuming all the enhanced pore volume due to sample expansion can be accessed by imbibed water, the black dotted line in Figure 6-7 shows the water imbibition excluding the sample expansion effect (Q_{w-exp}), which is calculated by

$$Q_{w-exp} = Q_{w-imb} - \Delta V \quad (6.11)$$

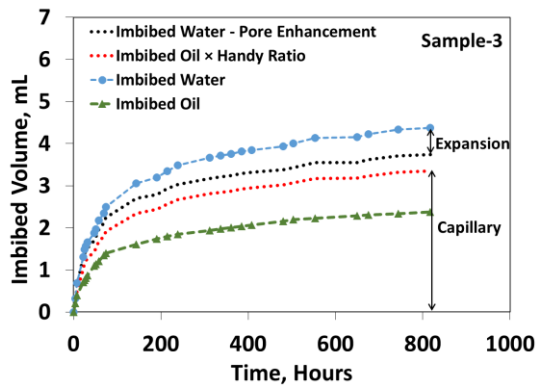
Where, Q_{w-imb} is the measured volume of imbibed water. The gap between Q_{w-imb} and Q_{w-imb} shows the water imbibition due to sample expansion effect. For samples 1, 3, 4 and 5 in Figure 6-7, there is still excess water imbibition after excluding the sample expansion and capillary effect, which is shown as the gap between red dashed line and black dotted line. This portion of water imbibition is possibly due to the water adsorption on clay platelets, which will be discussed in the next section.



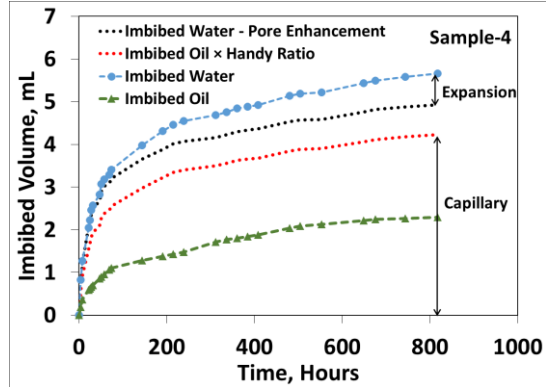
(a)



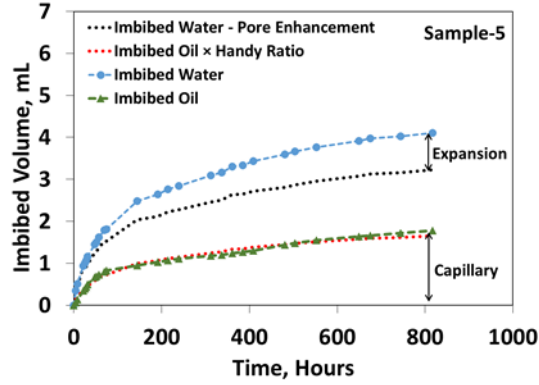
(b)



(c)



(d)



(e)

Figure 6-7. Experimental imbibition curve of oil (green dashed line) and water (blue dashed line), calculated water imbibition curve excluded expansion effect (black dotted line) and calculated water imbibition curve using Handy's model (red dotted line). (a) Sample-1, (b) sample-2, (c) sample -3, (d) sample-4 and (e) sample-5.

6.5 Decoupling the Imbibition and Adsorption

The objective of this section is to evaluate the portion of water imbibition due to water adsorption, using continuity equation. From the previous section, the total mass of water imbibed is equal to the summation of 1) the mass difference of water going in and leaving the matrix (capillary driven imbibition), 2) the water adsorbed in the shale matrix, and 3) excess pore volume induced by sample expansion. Excluding the effect of sample expansion, the water flow in the pores is single phase and 1-dimensional with capillary pressure as the only driving force responsible for the water movement into the pores. The spontaneous imbibition model can be derived based on conservation of mass, which is

$$\frac{\rho_w}{M_w} (q_w|_x - q_w|_{x+\Delta x}) \Delta t = \phi \frac{\rho_w A}{M_w} (S_w|_{t+\Delta t} - S_w|_t) \Delta x + (1 - \phi) \rho_r A (q_{ad}|_{t+\Delta t} - q_{ad}|_t) \Delta x \quad (6.12)$$

Where, M_w is the molar mass of water, ρ_w is the density of water, ρ_r is the density of rock matrix, q_w is the imbibition flow rate of water, q_{ad} is the water adsorption rate. The differential form of Eq. (6.12) is:

$$-\frac{\partial}{\partial x} \left(\frac{q_w}{M_w} \right) = \phi A \frac{\partial}{\partial t} \left(\frac{S_w}{M_w} \right) + (1 - \phi) A \frac{\partial}{\partial t} (\rho_r q_{ad}) \quad (6.13)$$

Since the rock sample is not compressed by external force, the density ρ_r will remain constant. By using Darcy law, the Eq. (6.14) becomes:

$$\frac{\partial}{\partial x} \left(-\frac{kk_{rw}}{M_w \mu_w} A \frac{\partial P}{\partial x} \right) = -\frac{A}{\rho_w} \frac{\partial C}{\partial t} + (1 - \phi) a A \rho_r \frac{\partial C}{\partial t} \quad (6.14)$$

Where C is concentration of water in the sample, which is $C = \frac{\rho_w \phi S_w}{M_w}$. Assuming linear Langmuir adsorption isotherm, then $q_{ad} = aC$, where a is adsorption coefficient. As capillary pressure is a function of water saturation, Eq. (6.15) can be rewrite as:

$$D \frac{\partial^2 C}{\partial x^2} = \frac{\partial C}{\partial t} + (1 - \phi) a \rho_r \frac{\partial C}{\partial t} \quad (6.15)$$

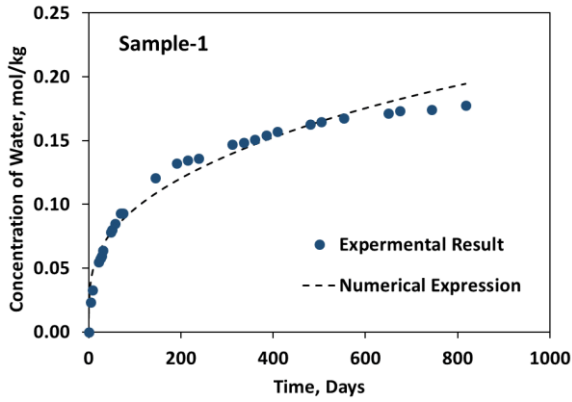
where $D = -\frac{kk_{rw}}{\phi \mu_w} \frac{\partial P}{\partial S_w}$. Assuming $\frac{\partial P}{\partial S_w}$ remains constant in the piston-like imbibition, D is mainly a function of k_{rw} . Using Corey correlation (Brooks and Corey, 1964), k_{rw} can be estimated as:

$$k_{rw} = K'_{rw} S_w^N \quad (6.16)$$

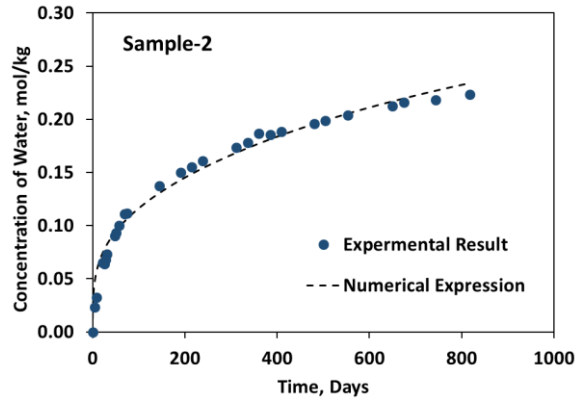
where K'_{rw} is the water relative permeability when the sample is fully saturated. N is empirical parameter. Since K'_{rw} and N are constants, the correlation between D with S_w can be written as:

$$D = K S_w^N \quad (6.17)$$

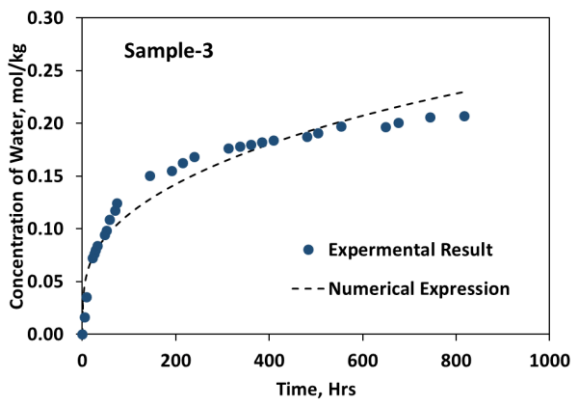
where, K is a constant obtained from analytical interpretation of experimental data. Applied the initial condition ($t = 0, C = 0$) and boundary condition ($x = h, \frac{\partial C}{\partial x} = 0; x = 0, C = C_0$) $L C_0$ is the concentration of the bulk water. Thus, the adsorption rate constant “a” can be evaluated by fitting water imbibition curves in Figure 6-8, and the values of the adsorption rate are listed in Table 6-4.



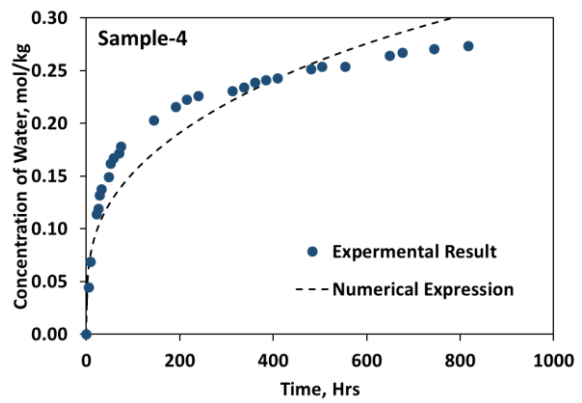
(a)



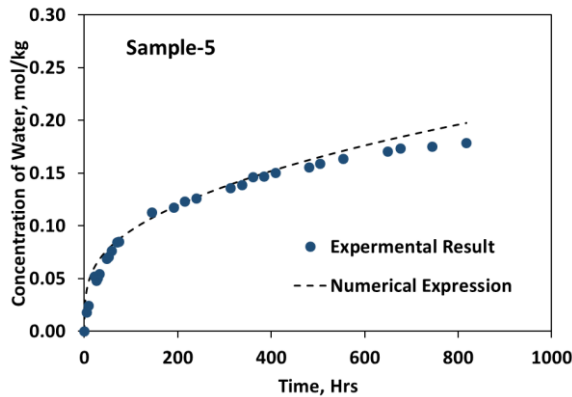
(b)



(c)



(d)



(e)

Figure 6-8. Comparisons of the imbibed water concentration predicted by the presented model (Eq. 6.16) with the imbibition experimental data excluding the sample expansion effect (Eq. 6.11). (a) Sample-1, (b) sample-2, (c) sample -3, (d) sample-4 and (e) sample-5.

Table 6-4. Values of adsorption coefficient from analytical interpretation of imbibition experimental data

Sample	Sample-1	Sample-2	Sample-3	Sample-4	Sample-5
Adsorption Coefficient, $\times 10^{-6} \text{ m}^3/\text{kg}$	4.89	0.00	1.34	2.42	4.64

6.6 Summary

This section investigates the role of capillary suction, water adsorption and sample expansion in water imbibition. Water imbibition profiles are decoupled to evaluate the contributions of capillary suction and sample expansion in water imbibition. A continuity equation is combined with experimental imbibition data to obtain the adsorption coefficient for shale samples.

Chapter 7: Conclusions and Recommendations for Future Work

In this study, I investigated the possible mechanisms responsible for the significantly high water uptake into gas shales. This is to shed light on the reasons for low water recovery after flowback and to quantify the impacts of the interactions between the unrecovered water and reservoir rocks.

7.1 Conclusions

Pore network connectivity, clay swelling of shales, salt concentration and dissolved gas concentration control excess water uptake into gas shales. The key conclusions for each mechanism are summarized below.

7.1.1 Effect of Pore Network Connectivity

- Hydrophobic organic pores are relatively small compared with the hydrophilic inorganic pores. The hydrophobic pore structure in shales may be poorly-connected and cause significantly higher water uptake than oil uptake.
- Wetting affinity of rock is affected by the initial saturated state. Initial exposure of the rock surface to a particular liquid phase increases its affinity to the same phase.

7.1.2 Effect of Salt Concentration

- Osmotic potential caused by salt concentration difference between water in pore space and bulk water acts as an additional driving force for water uptake.
- Imbibition of brine with low salinity (ionic strength) results in the formation of the thick electrical double layer on the surface of pore walls. The thickness of double layer represents the affinity of the aqueous solution to form a hydration shell around the charged shale surface.
- Increasing NaCl concentration in the imbibing water effectively restrains the induced strain and stress during imbibition. This is due to the double layer swelling of clays.

7.1.3 Effect of Dissolved Gas

- Initial degassed conditions in reservoir may accelerate water imbibition rate and minimize gas entrapment.
- Dissolved oxygen in fracturing fluid can react with pyrite-bearing components in shale to produce iron and sulfate ions.

7.1.4 Effect of Clay Swelling

- Water imbibition into the shale samples enhances the pore volume. The enhanced pore volume is positively correlated to the imbibed water mass and clay content of the shale samples. The initial expansion of the samples enhances the existing microcracks, causing further water imbibition and expansion. Hence, shale expansion during water imbibition is a self-amplifying phenomenon.
- Water imbibition into partially confined shale samples result in relatively low induced stress (up to 92 psi for 6 days water imbibition). The induced stress is proportional to the logarithmic function of confining pressure and is positively correlated to the clay content of shale samples.
- Sample expansion is more pronounced in the late stage of water imbibition. The early stage of imbibition is mainly controlled by the existing microcracks along the depositional lamination.
- The imbibition and swelling potentials of the shale samples are strongly anisotropic. Water imbibition along the depositional lamination is significantly higher than that perpendicular to the lamination. Consistently, the samples expand more in the direction perpendicular to the lamination.

7.2 Recommendations for Future Work

To further investigate the interactions of fracturing fluid with shale formations and their effects on hydrocarbon production, the following are recommended to improve the results of this research,

- To mimic actual imbibition process in reservoir conditions, forced imbibition experiments should be conducted in heated and pressurized imbibition cells with actual fracturing fluids.
- A comparison of rock permeability and porosity before and after imbibition experiments is needed to quantitatively investigate the effect of clay swelling and geochemical reactions on formation damage.
- Preserved samples with different initial water/oil saturation should be used to investigate the effect of water/oil saturation on water imbibition in unconventional rocks.
- Development of an imbibition model for field scale use in various shale and fluid types. The model needs to account for maximum and minimum principal stress, Young's modulus and Poisson's ratio of rock samples, and salinity, conductivity and ionic strength of formation water.
- Upscaling dynamic imbibition processes is needed for optimal water recovery using the knowledge of fluid retention in the matrix and fractures.

Bibliography

- Abbasi, M. A., Ezulike, D. O., Dehghanpour, H., Hawkes, R. V. 2014. A comparative study of flowback rate and pressure transient behavior in multifractured horizontal wells completed in tight gas and oil reservoirs. *Journal of Natural Gas Science and Engineering* 17: 82-93.
- Agbalaka, C. C., Dandekar, A. Y., Patil, S. L., Khataniar, S., Hemsath, J. 2008. The effect of wettability on oil recovery: A review. In *SPE Asia Pacific Oil and Gas Conference and Exhibition*. Society of Petroleum Engineers.
- Abdullah, W. S., Alshibli, K. A., Al-Zou'bi, M. S. 1999. Influence of pore water chemistry on the swelling behavior of compacted clays. *Applied Clay Science*, 15(5-6), 447-462.
- Akin, S., Schembre, J. M., Bhat, S. K., Kovsky, A. R. 2000. Spontaneous imbibition characteristics of diatomite. *Journal of Petroleum Science and Engineering*, 25(3-4), 149-165.
- Aksu, I., Bazilevskaya, E., Karpyn, Z. T. 2015. Swelling of clay minerals in unconsolidated porous media and its impact on permeability. *GeoResJ*, 7, 1-13.
- Al-Arfaj, M. K., Amanullah, M., Sultan, A. S., Hossain, M. E., Abdulraheem, A. 2014. Chemical and Mechanical Aspects of Wellbore Stability in Shale Formations: A Literature Review. In *Abu Dhabi International Petroleum Exhibition and Conference*. Society of Petroleum Engineers.
- Al-Maamari, R. S., Buckley, J. S. 2003. Asphaltene precipitation and alteration of wetting: the potential for wettability changes during oil production. *SPE Reservoir Evaluation & Engineering*, 6(04), 210-214.
- Alessi, D. S., Zolfaghari, A., Kletke, S., Gehman, J., Allen, D. M., Goss, G. G. 2017. Comparative analysis of hydraulic fracturing wastewater practices in unconventional shale development: Water sourcing, treatment and disposal practices. *Canadian Water Resources Journal/Revue canadienne des ressources hydriques*, 42(2), 105-121.
- Amott, E. (1959). Observations relating to the wettability of porous rock.
- Arthur, J. D., Bohm, B. K., Coughlin, B. J., Layne, M. A., Cornue, D. 2009. Evaluating the environmental implications of hydraulic fracturing in shale gas reservoirs. In *SPE Americas E&P environmental and safety conference*. Society of Petroleum Engineers.

Asadi, M., Woodroof, R.A. and Himes, R.E., 2008. Comparative study of flowback analysis using polymer concentrations and fracturing-fluid tracer methods: a field study. *SPE Production & Operations*, 23(02), pp.147-157.

Awaja, F. and Bhargava S. 2006. The prediction of clay contents in oil shale using DRIFTS and TGA data facilitated by multivariate calibration. *Fuel* 85(10-11): 1396-1402.

Aylmore, L. A. G., Quirk, J. P. 1966. Adsorption of water and electrolyte solutions by kaolin clay systems. *Soil Science*, 102(5), 339-345.

Bader, S., Kooi, H. 2005. Modelling of solute and water transport in semi-permeable clay membranes: comparison with experiments. *Advances in water resources*, 28(3), 203-214.

Balcerak, E. 2012. A general approach to spontaneous imbibition. *Eos, Transactions American Geophysical Union*, 93(16), 168-168.

Bahrami H.; Rezaee R.; Clennell B. 2012. Water blocking damage in hydraulically fractured tight sand gas reservoirs: An example from Perth Basin, Western Australia. *Journal of Petroleum Science and Engineering*. 88, 100-106.

Bai M, Green S, Suarez-Rivera R. Effect of leakoff variation on fracturing efficiency for tight shale gas reservoirs. *Alaska Rocks 2005, The 40th US Symposium on Rock Mechanics (USRMS)*. American Rock Mechanics Association, 2005.

B. C. Oil & Gas Commission. 2014. Horn River Basin unconventional shale gas play atlas. Report, BC Oil and Gas Commission.

Bai, M., Guo, Q., Jin, Z. H. 2008. Study of wellbore stability due to drilling fluid/shale interactions. In *The 42nd US Rock Mechanics Symposium (USRMS)*. American Rock Mechanics Association.

Bailey, L. K., Peters, E. 1976. Decomposition of pyrite in acids by pressure leaching and anodization: the case for an electrochemical mechanism. *Canadian Metallurgical Quarterly*, 15(4), 333-344.

Bearinger, D. 2013. Message in a Bottle. In *Unconventional Resources Technology Conference* (pp. 1455-1460). Society of Exploration Geophysicists, American Association of Petroleum Geologists, Society of Petroleum Engineers.

- Bell, J. M., Cameron, F. K. 1906. The flow of liquids through capillary spaces. *The Journal of Physical Chemistry*, 10(8), 658-674.
- Bergaya, F., Lagaly, G. 2013. *Handbook of clay science (Vol. 5)*. Newnes.
- Bell, J. S., Price, P. R., McLellan, P. J. 1990. In-situ stress in the western Canada Sedimentary Basin. *Bulletin of Canadian Petroleum Geology*, 38(1), 157-157.
- Bennion, D. B., Thomas, F. B., Bietz, R. F., Bennion, D. W. 1996. Water and hydrocarbon phase trapping in porous media-diagnosis, prevention and treatment. *Journal of Canadian Petroleum Technology*, 35(10).
- Bennion, D.B., Thomas, F.B. 2005. Formation Damage Issues Impacting the Productivity of Low Permeability, Low Initial Water Saturation Gas Producing Formations. *Journal of Energy Resources Technology-Transactions of the ASME* 127: 240-247.
- Bertoncello, A., Wallace, J., Blyton, C., Honarpour, M., Kabir, C. S. 2014, February. Imbibition and water blockage in unconventional reservoirs: well management implications during flowback and early production. In *SPE/EAGE European Unconventional Resources Conference and Exhibition*.
- Beverkog, B., Puigdomenech, I. 1996. Revised Pourbaix diagrams for iron at 25–300 C. *Corrosion Science*, 38(12), 2121-2135.
- Bhargava, S., Awaja, F., Subasinghe, N. 2005. Characterisation of some Australian oil shale using thermal, X-ray and IR techniques. *Fuel* 84(6): 707-715.
- Biegler, T., Swift, D. A. 1979. Anodic behaviour of pyrite in acid solutions. *Electrochimica Acta*, 24(4), 415-420.
- Binazadeh, M. 2013. *Effect of Secondary Structure on Surface Adsorption of Peptides (Doctoral dissertation, University of Alberta)*.
- Blanton, T. L. 1982. An experimental study of interaction between hydraulically induced and pre-existing fractures. In *SPE unconventional gas recovery symposium*. Society of Petroleum Engineers.

Blauch, M. E., Myers, R. R., Moore, T., Lipinski, B. A., Houston, N. A. 2009. Marcellus shale post-frac flowback waters-Where is all the salt coming from and what are the implications? In SPE Eastern Regional Meeting. Society of Petroleum Engineers.

Boek, E. S., Sprik, M. 2003. Ab initio molecular dynamics study of the hydration of a sodium smectite clay. *The Journal of Physical Chemistry B*, 107(14), 3251-3256.

Bostrom, N., Chertov, M., Pagels, M., Willberg, D., Chertova, A., Davis, M., Zagorski, W. 2014. The time-dependent permeability damage caused by fracture fluid. In SPE International Symposium and Exhibition on Formation Damage Control. Society of Petroleum Engineers.

Borysenko A., Clennell B., Sedev R., Burgar I., Ralston J., Raven M., Dewhurst D., Liu K. 2009. Experimental investigations of the wettability of clays and shales. *Journal of Geophysical Research: Solid Earth* (1978–2012). 114.

Boyer, C., Kieschnick, J., Suarez-Rivera, R., Lewis, R. E., Waters, G. 2006. Producing gas from its source. *Oilfield Review*, 18(3), 36-49.

Bray, H. J., Redfern, S. A., Clark, S. M. 1998. The kinetics of dehydration in Ca-montmorillonite: an in-situ X-ray diffraction study. *Mineralogical Magazine*, 62(5), 647-656.

Brooks, R.H., Corey, A.T. 1964. Hydraulic properties of porous media. *Hydrological Papers*. Colorado State University. 3.

Brigatti, M.F., Galan, E., Theng, B.K.G. 2006. Chapter 2 Structures and Mineralogy of Clay Minerals, In: F. Bergaya, B. K. G. Theng and G. Lagaly. Amsterdam, Editor(s), *Handbook of clay science*, Elsevier, 1: 19-86.

Brown, R. J., Fatt, I. 1956. Measurements of fractional wettability of oil fields' rocks by the nuclear magnetic relaxation method. In Fall Meeting of the Petroleum Branch of AIME. Society of Petroleum Engineers.

Cai, J., Perfect, E., Cheng, C. L., Hu, X. 2014. Generalized modeling of spontaneous imbibition based on Hagen–Poiseuille flow in tortuous capillaries with variably shaped apertures. *Langmuir*, 30(18), 5142-5151.

- Cai, J., Yu, B., Zou, M., Luo, L. 2010. Fractal characterization of spontaneous co-current imbibition in porous media. *Energy & Fuels*, 24(3), 1860-1867.
- Cey, B. D., Barbour, S. L., Hendry, M. J. 2001. Osmotic flow through a Cretaceous clay in southern Saskatchewan, Canada. *Canadian Geotechnical Journal*, 38(5), 1025-1033.
- Chakraborty, N., Karpyn, Z. T. 2015. Gas Permeability Evolution with Soaking Time in Ultra Tight Shales. In *SPE Annual Technical Conference and Exhibition*. Society of Petroleum Engineers.
- Chalmers, G. R., Ross, D. J., Bustin, R. M. 2012. Geological controls on matrix permeability of Devonian Gas Shales in the Horn River and Liard basins, northeastern British Columbia, Canada. *International Journal of Coal Geology*, 103, 120-131.
- Chalmers, G. R., Bustin, R. M., Power, I. M. 2012. Characterization of gas shale pore systems by porosimetry, pycnometry, surface area, and field emission scanning electron microscopy/transmission electron microscopy image analyses: Examples from the Barnett, Woodford, Haynesville, Marcellus, and Doig units. *AAPG bulletin*, 96(6), 1099-1119.
- Chakraborty, N., Karpyn, Z. T. 2015. Gas Permeability Evolution with Soaking Time in Ultra Tight Shales. In *SPE Annual Technical Conference and Exhibition*. Society of Petroleum Engineers.
- Chávez-Páez, M., Van Workum, K., De Pablo, L., de Pablo, J. J. 2001. Monte Carlo simulations of Wyoming sodium montmorillonite hydrates. *The Journal of chemical physics*, 114(3), 1405-1413.
- Cherry, J., Ben-Eli, M., Bharadwaj, L., Chalaturnyk, R., Dusseault, M. B., Goldstein, B., et al. 2014. Environmental impacts of shale gas extraction in Canada--The expert panel on harnessing science and technology to understand the environmental impacts of shale gas extraction. Council of Canadian Academies.
- Chen, G., Ewy, R. T., Yu, M. 2010. Analytic solutions with ionic flow for a pressure transmission test on shale. *Journal of Petroleum Science and Engineering*, 72(1-2), 158-165.

Chen, Q., Kang, Y., You, L., Yang, P., Zhang, X., Cheng, Q. 2017. Change in composition and pore structure of Longmaxi black shale during oxidative dissolution. *International Journal of Coal Geology*, 172, 95-111.

Cheng Y. 2012. Impact of water dynamics in fractures on the performance of hydraulically fractured wells in gas-shale reservoirs. *Journal of Canadian Petroleum Technology*, 51(02): 143-151.

Chenevert, M. E. 1970. Shale alteration by water adsorption. *Journal of petroleum technology*, 22(09), 1-141.

Chenevert, M. E. 1989. Lecture: diffusion of water and ions into shales. In *ISRM International Symposium*. International Society for Rock Mechanics.

Chenevert, M. E. K., Osisanya, S. O. K. 1992. Shale swelling at elevated temperature and pressure. In *The 33th US Symposium on Rock Mechanics (USRMS)*. American Rock Mechanics Association.

Cheng, Y. 2012. Impact of water dynamics in fractures on the performance of hydraulically fractured wells in gas-shale reservoirs. *Journal of Canadian Petroleum Technology*, 51(02), 143-151.

Chermak, J. A., Schreiber, M. E. 2014. Mineralogy and trace element geochemistry of gas shales in the United States: Environmental implications. *International Journal of Coal Geology*, 126, 32-44.

Cho, Y., Ozkan, E., Apaydin, O. G. 2013. Pressure-dependent natural-fracture permeability in shale and its effect on shale-gas well production. *SPE Reservoir Evaluation & Engineering*, 16(02), 216-228.

Churaev, N. V., Derjaguin, B. V., Muller, V. M. 2013. *Surface forces*. Springer Science & Business Media.

Ciminelli, V. S. T., Osseo-Asare, K. 1995. Kinetics of pyrite oxidation in sodium hydroxide solutions. *Metallurgical and Materials Transactions B*, 26(4), 677-685.

Civan, F. 2015. *Reservoir formation damage*. Gulf Professional Publishing.

Clarkson, C. R., Solano, N., Bustin, R. M., Bustin, A. M. M., Chalmers, G. R. L., He, L., Melnichenko Y. B., Radlinski A. P., Blach, T. P. 2013. Pore structure characterization of North American shale gas reservoirs using USANS/SANS, gas adsorption, and mercury intrusion. *Fuel*, 103, 606-616.

Crain's petrophysical handbook. 2012. Shale basics. <http://www.spec2000.net/11-vshbasics.htm> (accessed Jan 29, 2018).

CSUR (Canadian Society of Unconventional Resources). 2018. Understanding Tight Oil. Available at http://www.mpgpetroleum.com/home/docs/Understanding_TightOil_FINAL.pdf (accessed 08-01-2018)

Curtis, J. B. 2002. Fractured shale-gas systems. *AAPG bulletin*, 86(11), 1921-1938.

Davison, W., Seed, G. 1983. The kinetics of the oxidation of ferrous iron in synthetic and natural waters. *Geochimica et Cosmochimica Acta*, 47(1), 67-79.

de Carvalho Balaban, R., Vidal, E. L. F., Borges, M. R. 2015. Design of experiments to evaluate clay swelling inhibition by different combinations of organic compounds and inorganic salts for application in water base drilling fluids. *Applied Clay Science*, 105, 124-130.

Dehghanpour, H., Zubair, H. A., Chhabra, A., Ullah, A. 2012. Liquid intake of organic shales. *Energy & Fuels*, 26(9), 5750-5758.

Dehghanpour, H., Lan, Q., Saeed, Y., Fei, H., Qi, Z. 2013. Spontaneous imbibition of brine and oil in gas shales: effect of water adsorption and resulting microfractures. *Energy & Fuels*, 27(6), 3039-3049.

Dewhurst, D. N., Siggins, A. F. 2006. Impact of fabric, microcracks and stress field on shale anisotropy. *Geophysical Journal International*, 165(1), 135-148.

Derjaguin, B. V., Churaev, N. V., Muller, V. M., Forces, S. 1987. Consultants Bureau. New York, 266.

Descourvières, C., Hartog, N., Patterson, B. M., Oldham, C., Prommer, H. 2010. Geochemical controls on sediment reactivity and buffering processes in a heterogeneous aquifer. *Applied Geochemistry*, 25(2), 261-275.

Donaldson, E. C., Thomas, R. D., Lorenz, P. B. 1969. Wettability determination and its effect on recovery efficiency. *Society of Petroleum Engineers Journal*, 9(01), 13-20.

Dutta, R., Lee, C. H., Odumabo, S., Ye, P., Walker, S. C., Karpyn, Z. T., Ayala, L. F. 2012. Quantification of Fracturing Fluid Migration due to Spontaneous Imbibition in Fractured Tight Formations. In *SPE Americas Unconventional Resources Conference*. Society of Petroleum Engineers.

Ehlig-Economides, C. A., Economides, M. J. 2011. Water as proppant. In *SPE Annual Technical Conference and Exhibition*. Society of Petroleum Engineers.

Elie, M., Faure, P., Michels, R., Landais, P., Griffault, L. 2000. Natural and laboratory oxidation of low-organic-carbon-content sediments: comparison of chemical changes in hydrocarbons. *Energy & Fuels*, 14(4), 854-861.

EIA (U.S. Energy Information Administration). 2011. North America Shale Plays. Available at https://www.eia.gov/oil_gas/rpd/northamer_gas.jpg (accessed Aug 1, 2018)

EIA (U.S. Energy Information Administration). 2013. North America leads the world in production of shale gas. Available at <http://www.eia.gov/todayinenergy/detail.cfm?id=13491> (accessed Aug 1, 2018)

EIA (US Energy Information Administration). 2015. World Shale Resource Assessment. Available at <https://www.eia.gov/analysis/studies/worldshalegas/> (accessed Aug 1, 2018)

EIA (U.S. Energy Information Administration). 2016. International Energy Outlook 2016. [https://www.eia.gov/outlooks/ieo/pdf/0484\(2016\).pdf](https://www.eia.gov/outlooks/ieo/pdf/0484(2016).pdf) (accessed Aug 1, 2018).

Essington, M. E. 2005. *Soil and Water Chemistry: An Integrative Approach*, CRC Press, ISBN 0-8493-1258-2.

Evangelou, V. P., Zhang, Y. L. 1995. A review: pyrite oxidation mechanisms and acid mine drainage prevention. *Critical Reviews in Environmental Science and Technology*, 25(2), 141-199.

Ezulike, O. D. 2017. *Complementary Workflows for Analyzing Multiphase Flowback and Post-flowback Production Data In Unconventional Reservoirs* (Doctoral dissertation, UNIVERSITY OF ALBERTA).

Fakcharoenphol, P., Kurtoglu, B., Kazemi, H., Charoenwongsa, S., Wu, Y. S. 2014. The effect of osmotic pressure on improve oil recovery from fractured shale formations. In SPE unconventional resources conference. Society of Petroleum Engineers.

Fakcharoenphol, P., Kurtoglu, B., Kazemi, H., Charoenwongsa, S., Wu, Y. S. 2015. The Effect of Chemical Osmosis on Oil and Gas Production from Fractured Shale Formations. *Fluid Dynamics in Complex Fractured-Porous Systems*, 210, 85.

Fakcharoenphol, P., Torcuk, M., Kazemi, H., Wu, Y. S. 2016. Effect of shut-in time on gas flow rate in hydraulic fractured shale reservoirs. *Journal of Natural Gas Science and Engineering*, 32, 109-121.

Fan, L., Thompson, J. W., Robinson, J. R. 2010. Understanding gas production mechanism and effectiveness of well stimulation in the Haynesville Shale through reservoir simulation. In Canadian unconventional resources and international petroleum conference. Society of Petroleum Engineers.

Ferrari, A., Favero, V., Marschall, P., Laloui, L. 2014. Experimental analysis of the water retention behaviour of shales. *International Journal of Rock Mechanics and Mining Sciences*, 72, 61-70.

Fisher, M. K., Wright, C. A., Davidson, B. M., Goodwin, A. K., Fielder, E. O., Buckler, W. S., Steinsberger, N. P. 2002. Integrating fracture mapping technologies to optimize stimulations in the Barnett Shale. In SPE annual technical conference and exhibition. Society of Petroleum Engineers.

Fjar, E., Holt, R. M., Raaen, A. M., Risnes, R., Horsrud, P. 2008. Petroleum related rock mechanics (Vol. 53). Elsevier.

Fripiat, J. J., Letellier, M., Levitz, P. 1984. Interaction of water with clay surfaces. *Phil. Trans. R. Soc. Lond. A*, 311(1517), 287-299.

Gale, J. F., Reed, R. M., Holder, J. 2007. Natural fractures in the Barnett Shale and their importance for hydraulic fracture treatments. *AAPG Bulletin*, 91(4), 603-622.

Gale, J. F., Holder, J. 2010. Natural fractures in some US shales and their importance for gas production. In Geological Society, London, Petroleum Geology Conference Series (Vol. 7, No. 1, pp. 1131-1140). Geological Society of London.

- Gale, J. F., Laubach, S. E., Olson, J. E., Eichhubl, P., Fall, A. 2014. Natural fractures in shale: A review and new observations. *AAPG bulletin*, 98(11), 2165-2216.
- Gdanski, R. D., Fulton, D. D., Shen, C. 2006. Fracture face skin evolution during cleanup. In *SPE Annual Technical Conference and Exhibition*. Society of Petroleum Engineers.
- Geertsma, J., de Klerk, F. 1969. A rapid method of predicting width and extent of hydraulically induced fractures. *Journal of Petroleum Technology*, 21(12), 1-571.
- Ghanbari, E., Dehghanpour, H., 2015. Impact of Rock Fabric on Water Imbibition and Salt Diffusion in Gas Shales. *International Journal of Coal Geology* 138: 55–67.
- Ghanbari, E., Dehghanpour, H. 2016. The fate of fracturing water: A field and simulation study. *Fuel*, 163, 282-294.
- Gupta, A., Xu, M., Dehghanpour, H., Bearinger, D. 2017. Experimental investigation for microscale stimulation of shales by water imbibition during the shut-in periods. In *SPE Unconventional Resources Conference*. Society of Petroleum Engineers.
- Green W. D., Perry. W R. 2007. *Perry's Chemical Engineers' Handbook*, Eighth Edition McGraw-Hill.
- GWPC (Ground Water Protection Council) and ALL Consulting. 2009. *Modern Shale Gas Development in the United States: A Premier*. Available at [https://yosemite.epa.gov/sab%5CSABPRODUCT.NSF/98C1AE492F70249C852576EF004A35D6/\\$File/Bkgrd+Doc-+Modern+Shale+Gas+Dev+in+the+US-A+Primer.pdf](https://yosemite.epa.gov/sab%5CSABPRODUCT.NSF/98C1AE492F70249C852576EF004A35D6/$File/Bkgrd+Doc-+Modern+Shale+Gas+Dev+in+the+US-A+Primer.pdf) (accessed Aug 1, 2018)
- Gidley, J. L. 1989. Recent advances in hydraulic fracturing.
- Guo, B., Gao, D. 2014. The significance of fracture face matrix damage to the productivity of fractured wells in shale gas reservoirs. *Petroleum Science and Technology*, 32(2), 202-210.
- Guo, Q., Ji, L., Rajabov, V., Friedheim, J. E., Portella, C., Wu, R. 2012. Shale gas drilling experience and lessons learned from Eagle Ford. In *SPE Americas Unconventional Resources Conference*. Society of Petroleum Engineers.

- Harper J. 2008. The Marcellus Shale—An Old—New Gas Reservoir in Pennsylvania. *Pennsylvania Geology*, 28(1).
- Handy L. L. 1960. Determination of effective capillary pressures for porous media from imbibition data. *Trans. AIME*, 219, 75-80.
- Hensen, E. J., Smit, B. 2002. Why clays swell. *The Journal of Physical Chemistry B*, 106(49), 12664-12667.
- Helms, L. 2008. Horizontal drilling. *DMR newsletter*, 35(1), 1-3.
- Hensen, E. J., Smit, B. 2002. Why clays swell. *The Journal of Physical Chemistry B*, 106(49), 12664-12667.
- Hill, H. J., Klein, G. E., Shirley, O. J., Thomas, E. C., Waxman, W. H. 1979. Bound Water In Shaly Sands-Its Relation To Q And Other Formation Properties. *The log analyst*, 20(03).
- Hirasaki, G. J. 1991. Wettability: fundamentals and surface forces. *SPE Formation Evaluation*, 6(02), 217-226.
- Hu, X. L., Michaelides, A. 2008. Water on the hydroxylated (0 0 1) surface of kaolinite: From monomer adsorption to a flat 2D wetting layer. *Surface Science*, 602(4), 960-974.
- Huang, L., Wojciechowski, G., Ortiz de Montellano, P. R. 2005. Prosthetic heme modification during halide ion oxidation. Demonstration of chloride oxidation by horseradish peroxidase. *Journal of the American Chemical Society*, 127(15), 5345-5353.
- Hutcheon, I. 1998. The potential role of pyrite oxidation in corrosion and reservoir souring. *Journal of Canadian Petroleum Technology*, 37(01).
- Holditch S. 1979. Factors affecting water blocking and gas flow from hydraulically fractured gas wells. *Journal of Petroleum Technology*. 31, 1515-1524.
- Holtz, R.D. Kovacs, W.D. 1981. *An Introduction to Geotechnical Engineering*, Prentice Hall. (Chapter 4)
- Holmes, P. R., Crundwell, F. K. 2000. The kinetics of the oxidation of pyrite by ferric ions and dissolved oxygen: an electrochemical study. *Geochimica et Cosmochimica Acta*, 64(2), 263-274.

- Høgnesen, E. J., Standnes, D. C., Austad, T. 2006. Experimental and numerical investigation of high temperature imbibition into preferential oil-wet chalk. *Journal of Petroleum Science and Engineering*, 53(1), 100-112.
- Hirasaki G.J. 1991. Wettability: fundamentals and surface forces. *SPE Formation Evaluation*. 6, 217-226.
- Hsu, B. M., Huang, C. 2002. Influence of ionic strength and pH on hydrophobicity and zeta potential of Giardia and Cryptosporidium. *Colloids and Surfaces A: Physicochemical and Engineering Aspects*, 201(1), 201-206.
- Jamin, J. M. 1860. Memoir on equilibrium and movement of liquids in porous substances. *Compt. Rend*, 50, 172-176.
- Ji, L., Geehan, T. 2013. Shale failure around hydraulic fractures in water fracturing of shale gas. In *SPE Unconventional Resources Conference Canada*. Society of Petroleum Engineers.
- Jin, L., Mathur, R., Rother, G., Cole, D., Bazilevskaya, E., Williams, J., Brantley, S. 2013. Evolution of porosity and geochemistry in Marcellus Formation black shale during weathering. *Chemical Geology*, 356, 50-63.
- Johnson, M. F., Walsh, W., Budgell, P. A., Davidson, J. A. 2011. The ultimate potential for unconventional gas in the Horn River basin: integrating geological mapping with Monte Carlo simulations. In *Canadian Unconventional Resources Conference*. Society of Petroleum Engineers.
- Jones, S. C., Roszelle, W. O. 1978. Graphical techniques for determining relative permeability from displacement experiments. *Journal of Petroleum Technology*, 30(05), 807-817.
- Kanfar, M. S., Clarkson, C. R. 2016. Reconciling flowback and production data: A novel history matching approach for liquid rich shale wells. *Journal of Natural Gas Science and Engineering*, 33, 1134-1148.
- Kazemi, H., Gilman, J. R., Elsharkawy, A. M. 1992. Analytical and numerical solution of oil recovery from fractured reservoirs with empirical transfer functions (includes associated papers 25528 and 25818). *SPE Reservoir Engineering*, 7(02), 219-227.

- Keijzer, T. J. S. 2000. Chemical osmosis in natural clayey materials. *Geologica Ultraiectina* (196). Faculteit Aardwetenschappen.
- Keller, W. D., da Costa, L. M. 1989. Comparative chemical compositions of aqueous extracts from representative clays. *American Mineralogist*, 74(9-10), 1142-1146.
- Khan, S., Ansari, S. A., Han, H., Khosravi, N. 2011. Importance of shale anisotropy in estimating in-situ stresses and wellbore stability analysis in Horn River Basin. In *Canadian Unconventional Resources Conference*. Society of Petroleum Engineers.
- King, George Everette. 2012. Hydraulic fracturing 101: what every representative, environmentalist, regulator, reporter, investor, university researcher, neighbor and engineer should know about estimating frac risk and improving frac performance in unconventional gas and oil wells. *SPE Hydraulic Fracturing Technology Conference*. Society of Petroleum Engineers.
- King, G. E. 2012. What every representative, environmentalist, regulator, reporter, investor, university researcher, neighbor and engineer should know about estimating frac risk and improving frac performance in unconventional gas and oil wells. In *SPE Hydraulic Fracturing Technology Conference*, The Woodlands, Texas, USA (pp. 6-8).
- Kolev, N. I. 2011. Solubility of O₂, N₂, H₂ and CO₂ in water. In *Multiphase Flow Dynamics 4* (pp. 209-239). Springer Berlin Heidelberg.
- Kittrick, J. A. 1969. Interlayer forces in montmorillonite and vermiculite. *Soil Science Society of America Journal*, 33(2), 217-222.
- Kodikara, J., Barbour, S. L., Fredlund, D. G. 1999. Changes in clay structure and behaviour due to wetting and drying. In *Proceedings 8th Australia New Zealand Conference on Geomechanics: Consolidating Knowledge* (p. 179). Australian Geomechanics Society.
- Kuila, U., McCarty, D. K., Derkowski, A., Fischer, T. B., Prasad, M. 2014. Total porosity measurement in gas shales by the water immersion porosimetry (WIP) method. *Fuel*, 117, 1115-1129.
- Lagaly, G., 2011. Chapter 5: Colloid Clay Science. In: F. Bergaya, B. K. G. Theng and G. Lagaly. Amsterdam, Editor(s), *Handbook of clay science*, Elsevier, 1:141-245.

- Laird, D. A. 2006. Influence of layer charge on swelling of smectites. *Applied Clay Science*, 34(1), 74-87.
- Lal, M. 1999. Shale stability: drilling fluid interaction and shale strength. In *SPE Asia Pacific Oil and Gas Conference and Exhibition*. Society of Petroleum Engineers.
- Lan, Q., Ghanbari, E., Dehghanpour, H., Hawkes, R. 2014. Water Loss versus Soaking Time: Spontaneous Imbibition in Tight Rocks. *Energy Technology* 2.12: 1033-1039.
- Lan, Q., Xu, M., Binazadeh, M., Dehghanpour, H., Wood, J. M. 2015. A comparative investigation of shale wettability: The significance of pore connectivity. *Journal of Natural Gas Science and Engineering*.
- Leckband, D., Israelachvili, J. 1993. Molecular basis of protein function as determined by direct force measurements. *Enzyme and microbial technology*, 15(6), 450-459.
- Li K.; Horne R. 2001. Characterization of spontaneous water imbibition into gas-saturated rocks. *SPE Journal*. 6, 375-384.
- Li, Y. 2006. An empirical method for estimation of anisotropic parameters in elastic rocks. *The Leading Edge*, 25(6), 706-711.
- Likos, W. J., Lu, N. 2006. Pore-scale analysis of bulk volume change from crystalline interlayer swelling in Na⁺- and Ca²⁺-smectite. *Clays and Clay Minerals*, 54(4), 515-528.
- Liu, X. D., Lu, X. C. 2006. A thermodynamic understanding of clay - swelling inhibition by potassium ions. *Angewandte Chemie International Edition*, 45(38), 6300-6303.
- Lopes, P. E., Murashov, V., Tazi, M., Demchuk, E., MacKerell, A. D. 2006. Development of an empirical force field for silica. Application to the quartz– water interface. *The Journal of Physical Chemistry B*, 110(6), 2782-2792.
- Loucks, R. G., Reed, R. M., Ruppel, S. C., Hammes, U. 2012. Spectrum of pore types and networks in mudrocks and a descriptive classification for matrix-related mudrock pores. *AAPG bulletin*, 96(6), 1071-1098.
- Lucas R. 1918. Rate of capillary ascension of liquids. *Kolloid Z.* 23, 15-22.

- Ma, S. M., Zhang, X., Morrow, N. R., Zhou, X. 1999. Characterization of wettability from spontaneous imbibition measurements. *Journal of Canadian Petroleum Technology*, 38(13).
- Madsen, F. T., Müller-Vonmoos, M. 1989. The swelling behaviour of clays. *Applied Clay Science*, 4(2), 143-156.
- Makhanov, K. K. 2013. An experimental study of spontaneous imbibition in Horn River shales. University of Alberta (Canada).
- Makhanov, K., Dehghanpour, H., Kuru, E. 2012. An experimental study of spontaneous imbibition in Horn River shales. In SPE Canadian unconventional resources conference. Society of Petroleum Engineers.
- Makhanov, K., Habibi, A., Dehghanpour, H., Kuru, E. 2014. Liquid uptake of gas shales: A workflow to estimate water loss during shut-in periods after fracturing operations. *Journal of Unconventional Oil and Gas Resources* 7: 22-32.
- Manaka, M. 2009. Comparison of rates of pyrite oxidation by dissolved oxygen in aqueous solution and in compacted bentonite. *Journal of mineralogical and petrological sciences*, 104(2), 59-68.
- Manger, K.C., Oliver, S. J. P., Curtis, J. B. Scheper, R. J. 1991. Geologic influences on the location and production of Antrim shale gas, Michigan Basin. *Low Permeability Reservoirs Symposium*, Society of Petroleum Engineers.
- Mattax C. C.; Kyte J. R. 1962. Imbibition oil recovery from fractured, water-drive reservoir. *Old SPE Journal*. 2, 177-184.
- Matthew, E., Mantell, P.E. 2013. Recycling and reuse of produced water to reduce freshwater use in hydraulic fracturing operations. In: proceedings of the 2013 EPA hydraulic fracturing study water acquisition workshop, Arlington, VA, June 4th.
- Marcelja, S., Quirk, J. P. 1992. Salt penetration into electrical double layers. *Langmuir*, 8(11), 2778-2780.
- Marriott, R. A., Pirzadeh, P., Marrugo-Hernandez, J. J., Raval, S. 2015. Hydrogen sulfide formation in oil and gas. *Canadian Journal of Chemistry*, 94(4), 406-413.

- Marynowski, L., Szełęg, E., Jędrysek, M. O., Simoneit, B. R. 2011. Effects of weathering on organic matter: Part II: Fossil wood weathering and implications for organic geochemical and petrographic studies. *Organic Geochemistry*, 42(9), 1076-1088.
- Maxwell, S. C., Urbancic, T. I., Steinsberger, N., Zinno, R. 2002. Microseismic imaging of hydraulic fracture complexity in the Barnett shale. In SPE annual technical conference and exhibition. Society of Petroleum Engineers.
- Mayerhofer, M. J., Lonon, E. P., Youngblood, J. E., Heinze, J. R. 2006. Integration of microseismic-fracture-mapping results with numerical fracture network production modeling in the Barnett Shale. In SPE annual technical conference and exhibition. Society of Petroleum Engineers.
- McBride, M. B., Baveye, P. 2002. Diffuse double-layer models, long-range forces, and ordering in clay colloids. *Soil Science Society of America Journal*, 66(4), 1207-1217.
- McClure, M. W., Horne, R. N. 2014. An investigation of stimulation mechanisms in Enhanced Geothermal Systems. *International Journal of Rock Mechanics and Mining Sciences*, 72, 242-260.
- McKibben, M. A. 1985. Kinetics of aqueous oxidation of pyrite by ferric iron, oxygen, and hydrogen-peroxide from pH 1-4 and 20-40oC (Doctoral dissertation).
- Meng, M., Ge, H., Ji, W., Shen, Y., Su, S. 2015. Monitor the process of shale spontaneous imbibition in co-current and counter-current displacing gas by using low field nuclear magnetic resonance method. *Journal of Natural Gas Science and Engineering*, 27, 336-345.
- Millero, F. J. 1995. Thermodynamics of the carbon dioxide system in the oceans. *Geochimica et Cosmochimica Acta*, 59(4), 661-677.
- Mitchell A. G., Hazell L. B., Webb K. J. 1990. Wettability determination: pore surface analysis. SPE Annual Technical Conference and Exhibition. Society of Petroleum Engineers.
- Mitchell, J.K. 1993. *Fundamentals of Soil Behavior*, 2nd edition, John Wiley & Sons (Chapter 3).
- Mokhtari, M., Tutuncu, A. N. 2015. Characterization of anisotropy in the permeability of organic-rich shales. *Journal of Petroleum Science and Engineering*, 133, 496-506.

Moradian, Z., Fathi, A., Evans, B. 2016. Shear reactivation of natural fractures in hydraulic fracturing. In ARMA Symposium, Houston.

Morrow, N. R. 1990. Wettability and its effect on oil recovery. *Journal of Petroleum Technology*, 42(12), 1-476.

Morrow, N. R., Mason, G. 2001. Recovery of oil by spontaneous imbibition. *Current Opinion in Colloid & Interface Science*, 6(4), 321-337.

Morsy, S., Sheng, J. J. 2014. Imbibition characteristics of the Barnett Shale formation. In SPE Unconventional Resources Conference. Society of Petroleum Engineers.

Moses, C. O., Herman, J. S. 1991. Pyrite oxidation at circumneutral pH. *Geochimica et Cosmochimica Acta*, 55(2), 471-482.

Moses, C. O., Nordstrom, D. K., Herman, J. S., Mills, A. L. 1987. Aqueous pyrite oxidation by dissolved oxygen and by ferric iron. *Geochimica et Cosmochimica Acta*, 51(6), 1561-1571.

Mullen, J. 2010. Petrophysical characterization of the Eagle Ford Shale in south Texas. Canadian Unconventional Resources and International Petroleum Conference, Society of Petroleum Engineers.

Mullet, M., Fievet, P., Reggiani, J. C., Pagetti, J. 1997. Surface electrochemical properties of mixed oxide ceramic membranes: Zeta-potential and surface charge density. *Journal of Membrane Science*, 123(2), 255-265.

Nasralla, Ramez A., Hisham A. Nasr-El-Din. 2011. Coreflood study of low salinity water injection in sandstone reservoirs. SPE/DGS Saudi Arabia Section Technical Symposium and Exhibition. Society of Petroleum Engineers.

Nasralla, R. A., Nasr-El-Din, H. A. 2011. Impact of electrical surface charges and cation exchange on oil recovery by low salinity water. In SPE Asia Pacific Oil and Gas Conference and Exhibition. Society of Petroleum Engineers.

National Energy Borad. 2011. Available at <https://www.nerb-one.gc.ca/nrg/sttstc/ntrlgs/rprt/archive/ncnvntnlntrlgshrnrvrbsnhnrnrvr2011/ncnvntnlntrlgshrnrvrbsnhnrnrvr2011-eng.pdf> (accessed Aug 1, 2018)

- NaturPhilosophie. 2014. The Craic about “Fracking” – Technical Facts on Hydraulic Fracturing. Available at https://i1.wp.com/www.naturphilosophie.co.uk/wp-content/uploads/2014/06/Fracking_Explained.jpg (accessed Aug 1, 2018)
- Nejadi, S., Leung, J. Y., Trivedi, J. J., Virués, C. 2015. Integrated Characterization of Hydraulically Fractured Shale-Gas Reservoirs—Production History Matching. *SPE Reservoir Evaluation & Engineering*, 18(04), 481-494.
- Neuzil, C. E. 2000. Osmotic generation of ‘anomalous’ fluid pressures in geological environments. *Nature*, 403(6766), 182.
- Nelson, R. 2001. *Geologic analysis of naturally fractured reservoirs*. Elsevier.
- Nichols, G. 2009. *Sedimentology and stratigraphy* (Second ed.): Chichester, UK: Wiley-Blackwell.
- Nicholson, R. V., Gillham, R. W., Reardon, E. J. 1988. Pyrite oxidation in carbonate-buffered solution: 1. Experimental kinetics. *Geochimica et Cosmochimica Acta*, 52(5), 1077-1085.
- Nicot, J. P., Scanlon, B. R. 2012. Water use for shale-gas production in Texas, US. *Environmental science & technology*, 46(6), 3580-3586.
- Nitao, J. J., Bear, J. 1996. Potentials and Their Role in Transport in Porous Media. *Water Resources Research*. 32: 225-250.
- Nolen-Hoeksema, R. 2013. Elements of hydraulic fracturing. *Oilfield Review Summer, Schlumberger 2013: 25, no. 2*. Available at https://www.slb.com/-/media/Files/resources/oilfield_review/defining_series/Defining-Hydraulic-Fracturing.pdf?la=en&hash=221B2B0B90020732FE1D28A84CE3D1A1B74F369A (accessed Aug 1, 2018)
- Norrish, K. 1954. The swelling of montmorillonite. *Discussions of the Faraday society*, 18, 120-134.
- Northern Territory (Australia) Department of Mines and Energy. 2018. How do we access Unconventional Gas?. <http://www.virginiaplaces.org/geology/graphics/frack.png> (accessed Aug 1, 2018).

Novlesky A., Kumar A., Merkle S. 2011. Shale Gas Modeling Workflow: From Microseismic to Simulation--A Horn River Case Study. Canadian Unconventional Resources Conference.

Nygård, R., Gutierrez, M., Bratli, R. K., Høeg, K. 2006. Brittle–ductile transition, shear failure and leakage in shales and mudrocks. *Marine and Petroleum Geology*, 23(2), 201-212.

Odusina E.; Sondergeld C.; Rai C. 2011. NMR Study of Shale Wettability. Canadian Unconventional Resources Conference.

Oliver, H., Mojtaba R., Karsten, R., Moritz Z. 2016. WSM Team: World Stress Map Database Release 2016. GFZ Data Services.

Pagels M.; Hinkel J.; Willberg D. 2012a. Measuring Capillary Pressure Tells More Than Pretty Pictures. SPE International Symposium and Exhibition on Formation Damage Control.

Pagels M.; Hinkel J.; Willberg D. 2012b. Moving Beyond the Capillary Suction Time Test. SPE International Symposium and Exhibition on Formation Damage Control.

Paktinat, J., Pinkhouse, J. A., Johnson, N. J., Williams, C., Lash, G. G., Penny, G. S., Goff, D. A. 2006. Case Studies: Optimizing Hydraulic Fracturing Performance in Northeastern Fractured Shale Formations. SPE Eastern Regional Meeting.

Parmar, J., Dehghanpour, H., Kuru, E. 2014. Displacement of water by gas in propped fractures: Combined effects of gravity, surface tension, and wettability. *Journal of Unconventional Oil and Gas Resources*, 5, 10-21.

Petrowiki. 2018. https://petrowiki.org/Fracturing_fluids_and_additives (accessed Aug 1, 2018).

Pond, J., Zerbe, T., Odland, K. W. 2010. Horn River Frac Water: Past, Present, and Future. In Canadian Unconventional Resources and International Petroleum Conference. Society of Petroleum Engineers.

Quirein, J., Witkowsky, J., Truax, J. A., Galford, J. E., Spain, D. R., Odumosu, T. 2010. Integrating core data and wireline geochemical data for formation evaluation and characterization of shale-gas reservoirs. SPE Annual Technical Conference and Exhibition, Society of Petroleum Engineers.

Quirk, J. P., Aylmore, L. A. G. 1971. Domains and quasi-crystalline regions in clay systems. *Soil Science Society of America Journal*, 35(4), 652-654.

- Raaen, A. M., Skomedal, E., Kjørholt, H., Markestad, P., Økland, D. 2001. Stress determination from hydraulic fracturing tests: the system stiffness approach. *International Journal of Rock Mechanics and Mining Sciences*, 38(4), 529-541.
- Rangel-German E R, Kovscek A R. 2002. Experimental and analytical study of multidimensional imbibition in fractured porous media. *Journal of Petroleum Science and Engineering*, 36(1): 45-60.
- Rao, S. M., Thyagaraj, T., Rao, P. R. 2013. Crystalline and osmotic swelling of an expansive clay inundated with sodium chloride solutions. *Geotechnical and Geological Engineering*, 31(4), 1399-1404.
- Rapoport L A. 1955. Scaling laws for use in design and operation of water-oil flow models. *Trans. AIME*, 204, 143-150.
- Rathnaweera, T. D., Ranjith, P. G., Perera, M. S. A. 2014. Salinity-dependent strength and stress-strain characteristics of reservoir rocks in deep saline aquifers: an experimental study. *Fuel*, 122, 1-11.
- Reynolds, M. M., Munn, D. L. 2010. Development update for an emerging shale gas giant field-Horn River Basin, British Columbia, Canada. In *SPE Unconventional Gas Conference*. Society of Petroleum Engineers.
- Rickman, R., Mullen, M. J., Petre, J. E., Grieser, W. V., Kundert, D. 2008. A practical use of shale petrophysics for stimulation design optimization: All shale plays are not clones of the Barnett Shale. *SPE Annual Technical Conference and Exhibition*, Society of Petroleum Engineers.
- Roshan, H., Ehsani, S., Marjo, C. E., Andersen, M. S., Acworth, R. I. 2015. Mechanisms of water adsorption into partially saturated fractured shales: An experimental study. *Fuel*, 159, 628-637.
- Ross, D. J., Bustin, R. M. 2008. Characterizing the shale gas resource potential of Devonian–Mississippian strata in the Western Canada sedimentary basin: Application of an integrated formation evaluation. *AAPG bulletin*, 92(1), 87-125.

Rowan, E. L., Engle, M. A., Kraemer, T. F., Schroeder, K. T., Hammack, R. W., Doughten, M. W. 2015. Geochemical and isotopic evolution of water produced from Middle Devonian Marcellus shale gas wells, Appalachian basin, Pennsylvania. AAPG Bulletin, 99(2), 181-206.

Roychaudhuri, B., Tsotsis, T. T., Jessen, K. 2013. An experimental investigation of spontaneous imbibition in gas shales. Journal of Petroleum Science and Engineering, 111, 87-97.

Saidi, A. M. 1987. Reservoir Engineering of Fractured Reservoirs (fundamental and Practical Aspects). Total.

Santos, H., Diek, A., Roegiers, J. C., Fontoura, S. 1996. Can shale swelling be (easily) controlled?. In ISRM International Symposium-EUROCK 96. International Society for Rock Mechanics.

Salah, M., Orr, D., Meguid, A. A., Crane, B., Squires, S. 2016. Multistage Horizontal Hydraulic Fracture Optimization Through an Integrated Design and Workflow in Apollonia Tight Chalk, Egypt from the Laboratory to the Field. In Abu Dhabi International Petroleum Exhibition & Conference. Society of Petroleum Engineers.

Schlemmer, R., Friedheim, J. E., Growcock, F. B., Bloys, J. B., Headley, J. A., Polnaszek, S. C. 2003. Chemical osmosis, shale, and drilling fluids. SPE drilling & completion, 18(04), 318-331.

Schoonheydt, R. A. and C. T. Johnston 2006. Chapter 3 Surface and Interface Chemistry of Clay Minerals. In: F. Bergaya, B. K. G. Theng and G. Lagaly. Amsterdam, Editor(s), Handbook of clay science, Elsevier, 1: 87-113.

Settari, A., Sullivan, R. B., Bachman, R. C. 2002. The modeling of the effect of water blockage and geomechanics in waterfracs. In SPE Annual Technical Conference and Exhibition. Society of Petroleum Engineers.

Shaoul, J., van Zelm, L., de Pater, C. J. 2011. Damage Mechanisms in Unconventional-Gas-Well Stimulation--A New Look at an Old Problem. SPE Production & Operations 26: 388-400

Sharma, M., Agrawal, S. 2013. Impact of liquid loading in hydraulic fractures on well productivity. In SPE hydraulic fracturing technology conference. Society of Petroleum Engineers.

Shouxiang M.; Morrow N. R.; Zhang X. 1997. Generalized scaling of spontaneous imbibition data for strongly water-wet systems. Journal of Petroleum science and Engineering. 18, 165-178.

- Sierra, R., Tran, M. H., Abousleiman, Y. N., Slatt, R. M. 2010. Woodford Shale mechanical properties and the impacts of lithofacies. 44th US Rock Mechanics Symposium and 5th US-Canada Rock Mechanics Symposium, American Rock Mechanics Association.
- Singer, P. C., Stumm, W. 1968. Kinetics of the oxidation of ferrous iron. In Second Symposium Coal Mine Drainage Research (pp. 12-34).
- Singh, H. 2016. A critical review of water uptake by shales. *Journal of Natural Gas Science and Engineering*, 34, 751-766.
- Soeder, D. J., Kappel, W. M. 2009. Water resources and natural gas production from the Marcellus Shale (pp. 1-6). Reston, Virginia: US Department of the Interior, US Geological Survey.
- Sondergeld, C. H., Ambrose, R. J., Rai, C. S., Moncrieff, J. 2010a. Micro-structural studies of gas shales: SPE Unconventional Gas Conference, Pittsburgh, Pennsylvania, February 23–25, 2010.
- Sondergeld, C. H., Newsham, K. E., Comisky, J. T., Rice, M. C., Rai, C. S. 2010b. Petrophysical considerations in evaluating and producing shale gas resources. SPE Unconventional Gas Conference.
- Sposito, G., Skipper, N. T., Sutton, R., Park, S. H., Soper, A. K., Greathouse, J. A. 1999. Surface geochemistry of the clay minerals. *Proceedings of the National Academy of Sciences*, 96(7), 3358-3364.
- Sprycha, R. 1989. Electrical double layer at alumina/electrolyte interface: I. Surface charge and zeta potential. *Journal of colloid and interface science*, 127(1), 1-11.
- Stuart, M. C., Mulder, J. W. 1985. Adsorbed polymers in aqueous media the relation between zeta potential, layer thickness and ionic strength. *Colloids and Surfaces*, 15, 49-55.
- Stevens P. 2012. The ‘shale gas revolution’: Developments and changes. Chatham House Briefing Paper.
- Strand, S., Puntervold, T., Austad, T. 2008. Effect of temperature on enhanced oil recovery from mixed-wet chalk cores by spontaneous imbibition and forced displacement using seawater. *Energy & Fuels*, 22(5), 3222-3225.

- Sun, Y., Bai, B., Wei, M. 2015. Microfracture and surfactant impact on linear cocurrent brine imbibition in gas-saturated shale. *Energy & Fuels*, 29(3), 1438-1446.
- Tambach, T. J., Bolhuis, P. G., Hensen, E. J., Smit, B. 2006. Hysteresis in clay swelling induced by hydrogen bonding: accurate prediction of swelling states. *Langmuir*, 22(3), 1223-1234.
- Takahashi, S., Kovsky, A. R. 2010. Spontaneous countercurrent imbibition and forced displacement characteristics of low-permeability, siliceous shale rocks. *Journal of Petroleum Science and Engineering*, 71(1-2), 47-55.
- Tang, G. Q., Morrow, N. R. 1997. Salinity, temperature, oil composition, and oil recovery by waterflooding. *SPE Reservoir Engineering*, 12(04), 269-276.
- Tansel, B., Sager, J., Rector, T., Garland, J., Strayer, R. F., Levine, L., Roberts, M., Hummerick, M. Bauer, J. 2006. Significance of hydrated radius and hydration shells on ionic permeability during nanofiltration in dead end and cross flow modes. *Separation and Purification Technology* 51(1): 40-47.
- Taylor, K. C., Nasr-El-Din, H. A., Al-Alawi, M. J. 1999. Systematic study of iron control chemicals used during well stimulation. *SPE Journal*, 4(01), 19-24.
- Tissot, B., Durand, B., Espitalie, J., Combaz, A. 1974. Influence of nature and diagenesis of organic matter in formation of petroleum. *AAPG bulletin*, 58(3), 499-506.
- Toumelin E, Torres-Verdín C, Sun B, Dunn K. 2006. Limits of 2D NMR interpretation techniques to quantify pore size, wettability, and fluid type: a numerical sensitivity study. *SPE Journal*. 11(03): 354-363.
- Tuller, M., Or, D., Dudley, L. M. 1999. Adsorption and capillary condensation in porous media: Liquid retention and interfacial configurations in angular pores. *Water Resources Research*, 35(7), 1949-1964.
- Urbancic, T. I., Shumila, V., Rutledge, J. T., Zinno, R. J. 1999. Determining hydraulic fracture behavior using microseismicity. In *Vail Rocks 1999, The 37th US Symposium on Rock Mechanics (USRMS)*. American Rock Mechanics Association.

US Energy Information Administration, North America leads the world in production of shale gas. 23 Oct. 2013. Available at <http://www.eia.gov/todayinenergy/detail.cfm?id=13491> (accessed Feb 18, 2018)

Van Olphen, H., Hsu, P. H. 1978. An introduction to clay colloid chemistry. *Soil Science*, 126(1), 59.

van Olphen, H., 1977. *An Introduction to Clay Colloid Chemistry*, 2nd edition. Wiley, New York.

Van Oort, E. 2003. On the physical and chemical stability of shales. *Journal of Petroleum Science and Engineering*, 38(3-4), 213-235.

van Oort, E., Hale, A. H., Mody, F. K., Roy, S. 1996. Transport in shales and the design of improved water-based shale drilling fluids. *SPE Drilling & Completion*, 11(03), 137-146.

Van Oss C.J, 2006. *Interfacial forces in aqueous media*, 2nd Edition,. Chapter 13, 165-178.

Vandecasteele, I., Rivero, I. M., Sala, S., Baranzelli, C., Barranco, R., Batelaan, O., Lavalle, C. 2015. Impact of shale gas development on water resources: a case study in northern Poland. *Environmental management*, 55(6), 1285-1299.

Wang, D., Butler, R., Liu, H., Ahmed, S. 2011. Flow-rate behavior and imbibition in shale. *SPE Reservoir Evaluation & Engineering*, 14(04), 485-492.

Wang, D., Butler, R., Zhang, J., Seright, R. 2012. Wettability survey in Bakken shale with surfactant-formulation imbibition. *SPE Reservoir Evaluation & Engineering*, 15(06), 695-705.

Wangler, T., Scherer, G. W. 2008. Clay swelling mechanism in clay-bearing sandstones. *Environmental Geology*, 56(3-4), 529-534.

Warpinski, N. R., Teufel, L. W. 1987. Influence of geologic discontinuities on hydraulic fracture propagation (includes associated papers 17011 and 17074). *Journal of Petroleum Technology*, 39(02), 209-220.

Washburn E. W. 1921. The dynamics of capillary flow. *Physical review*. 17, 273.

- Walsh, J. B. 1981. Effect of pore pressure and confining pressure on fracture permeability. In *International Journal of Rock Mechanics and Mining Sciences & Geomechanics Abstracts* (Vol. 18, No. 5, pp. 429-435). Pergamon.
- Wu, K., Chen, Z., Li, J., Li, X., Xu, J., Dong, X. 2017. Wettability effect on nanoconfined water flow. *Proceedings of the National Academy of Sciences*, 114(13), 3358-3363.
- Xie, X., Ellis, A., Wang, Y., Xie, Z., Duan, M., Su, C. 2009. Geochemistry of redox-sensitive elements and sulfur isotopes in the high arsenic groundwater system of Datong Basin, China. *Science of the total environment*, 407(12), 3823-3835.
- Xu, Y., Adefidipe, O. A., Dehghanpour, H. 2015. Estimating fracture volume using flowback data from the Horn River Basin: A material balance approach. *Journal of Natural Gas Science and Engineering*, 25, 253-270.
- Xu, Y., Adefidipe, O., Dehghanpour, H. 2016. A flowing material balance equation for two-phase flowback analysis. *Journal of Petroleum Science and Engineering*, 142, 170-185.
- Yan, Q., Lemanski, C., Karpyn, Z. T., Ayala, L. F. 2015. Experimental investigation of shale gas production impairment due to fracturing fluid migration during shut-in time. *Journal of Natural Gas Science and Engineering*, 24, 99-105.
- Yang, L., Ge, H., Shen, Y., Zhang, J., Yan, W., Wu, S., Tang, X. 2015. Imbibition inducing tensile fractures and its influence on in-situ stress analyses: a case study of shale gas drilling. *Journal of Natural Gas Science and Engineering*, 26, 927-939.
- Yang, F., Ning, Z., Liu, H. 2014. Fractal characteristics of shales from a shale gas reservoir in the Sichuan Basin, China. *Fuel* 115: 378-384.
- Yavuz, Ö., Altunkaynak, Y., Güzel, F. 2003. Removal of copper, nickel, cobalt and manganese from aqueous solution by kaolinite. *Water research*, 37(4), 948-952.
- Yu B., Li J. 2011. Some fractal characters of porous media. *Fractals*. 9, 365-372.
- Yun M. Yu B. Cai J. 2008. A fractal model for the starting pressure gradient for Bingham fluids in porous media. *International Journal of Heat and Mass Transfer*. 51, 1402-1408.

- Zambrano, L., Pedersen, P. K., Aguilera, R. 2016. Geologic Controls on Gas Production and Hydraulic-Fracturing Flowback in Tight Gas Sandstones of the Late Jurassic Monteith Formation, Deep Basin, Alberta, Canada. *SPE Reservoir Evaluation & Engineering*, 19(01), 24-40.
- Zhang X.; Morrow N.; Ma S. 1996. Experimental verification of a modified scaling group for spontaneous imbibition. *SPE Reservoir Engineering*. 11, 280-285.
- Zhou, Q., Dilmore, R., Kleit, A. and Wang, J.Y., 2016. Evaluating fracture-fluid flowback in Marcellus using data-mining technologies. *SPE Production & Operations*, 31(02), pp.133-146.
- Zhou, D., Jia, L., Kamath, J., Kovscek, A. R. 2002. Scaling of counter-current imbibition processes in low-permeability porous media. *Journal of Petroleum Science and Engineering*, 33(1-3), 61-74.
- Zhou, Z., Abass, H., Li, X., Teklu, T. 2016. Experimental investigation of the effect of imbibition on shale permeability during hydraulic fracturing. *Journal of Natural Gas Science and Engineering*, 29, 413-430.
- Zhou, Z., Hoffman, B. T., Bearinger, D., Li, X. 2014. Experimental and numerical study on spontaneous imbibition of fracturing fluids in shale gas formation. In *SPE/CSUR Unconventional Resources Conference—Canada*. Society of Petroleum Engineers.
- Zolfaghari, A., Dehghanpour, H., Holyk, J. 2017. Water sorption behaviour of gas shales: I. Role of clays. *International Journal of Coal Geology*, 179, 130-138.
- Zolfaghari, A., Dehghanpour, H., Noel, M., Bearinger, D. 2016. Laboratory and field analysis of flowback water from gas shales. *Journal of Unconventional Oil and Gas Resources*, 14, 113-127.
- Zolfaghari, A., Tang, Y., Holyk, J., Binazadeh, M., Dehghanpour. H., Bearinger D., 2015. *Advances in Flowback Chemical Analysis of Gas Shales*, SPE-175154-MS, SPE Annual Technical Conference and Exhibition held in Houston, Texas, USA.

Appendix A: Permeability Measurement

Permeability is an important physical property for analysing and scaling imbibition data. Here the permeability test is set based on Darcy's Law. The schematic of permeability test apparatus is shown in Figure A-1. The procedure of permeability test includes the following steps:

- 1). Set the water pump flow rate as 0.1 ml/min, and read the water level in the manometer after reaching the equilibrium.
- 2). Change the water pump flow rate to 0.2 ml/min, 0.3 ml/min and etc. Read the water level in the manometer under different flow rates.
- 3). Calculate the inlet pressure from gas volume change (ideal gas law) and accounting for gravity effect. The outlet pressure is atmospheric pressure.
- 4). Calculate the permeability of the crushed sample pack using the measured pressure drop and flowrate and Darcy's Law.

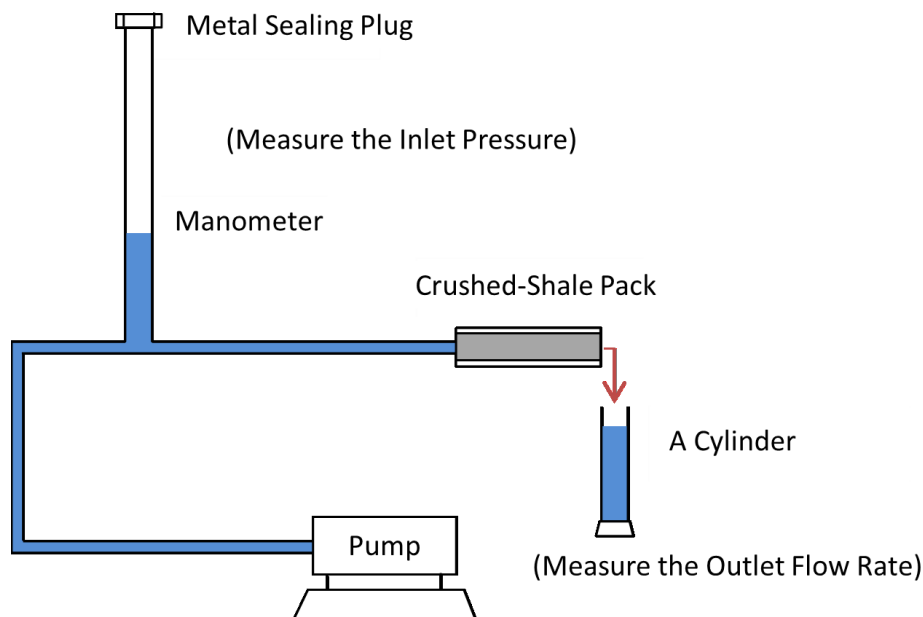


Figure A-1. The schematic of permeability test.

Appendix B: Calculation of Average Pore Diameter

Assuming that pore size distribution is Gaussian and pore tortuosity is equal to 1, the effective pore diameter (λ) becomes equal to the average pore diameter. This can be calculated by (Yun et al., 2008) as:

$$\lambda_{av} = \lambda_{max} \left(\frac{D_f}{4-D_f} \right)^{\frac{1}{4}} \quad (\text{B.1})$$

The pore fractal dimension, D_f , and the maximum pore diameter, λ_{max} , can be estimated using the theoretical models (Yu and Li, 2001)

$$D_f = d - \frac{\ln \emptyset}{\ln \xi} \quad (\text{B.2})$$

Where, $\xi = \frac{\lambda_{min}}{\lambda_{max}}$, d is the Euclidean dimension (a value of 2 is used in this work), \emptyset is the total porosity of shale sample. The maximum pore diameter can be calculated based on combining the model of equilateral-triangle arrangement and square arrangement of circular particles:

$$\lambda_{max} = \frac{D_s}{4} \left[\sqrt{\frac{2\phi}{1-\phi}} + \sqrt{\frac{\phi}{1-\phi}} + \sqrt{\frac{\pi}{4(1-\phi)}} - 1 \right] \quad (\text{B.3})$$

Where, D_s is characteristic particle diameter.

Appendix C: Chemical Analysis of Precipitated Salts

Electrical conductivity (EC) and concentration of different ions in the salt solutions after each washing stages are shown in Figures C-1 and C-2. As can be seen from Figures C-1 and C-2, neither EC nor the final ion concentration approaches to zero after 10 times washing.

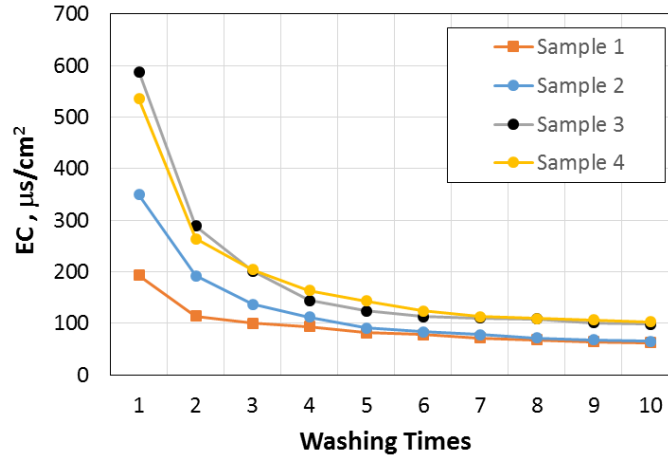
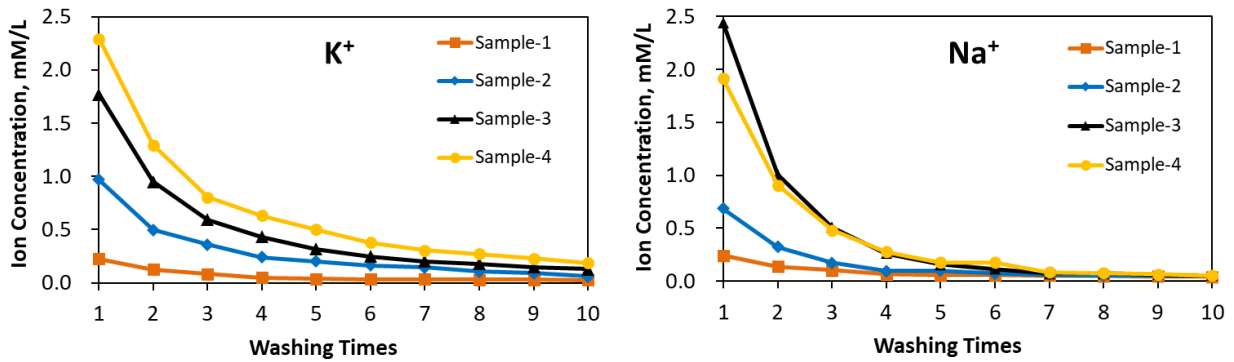


Figure C-1. The EC of salt solutions obtained after washing of HRB shale powders with DI water as a function of number of washing stages



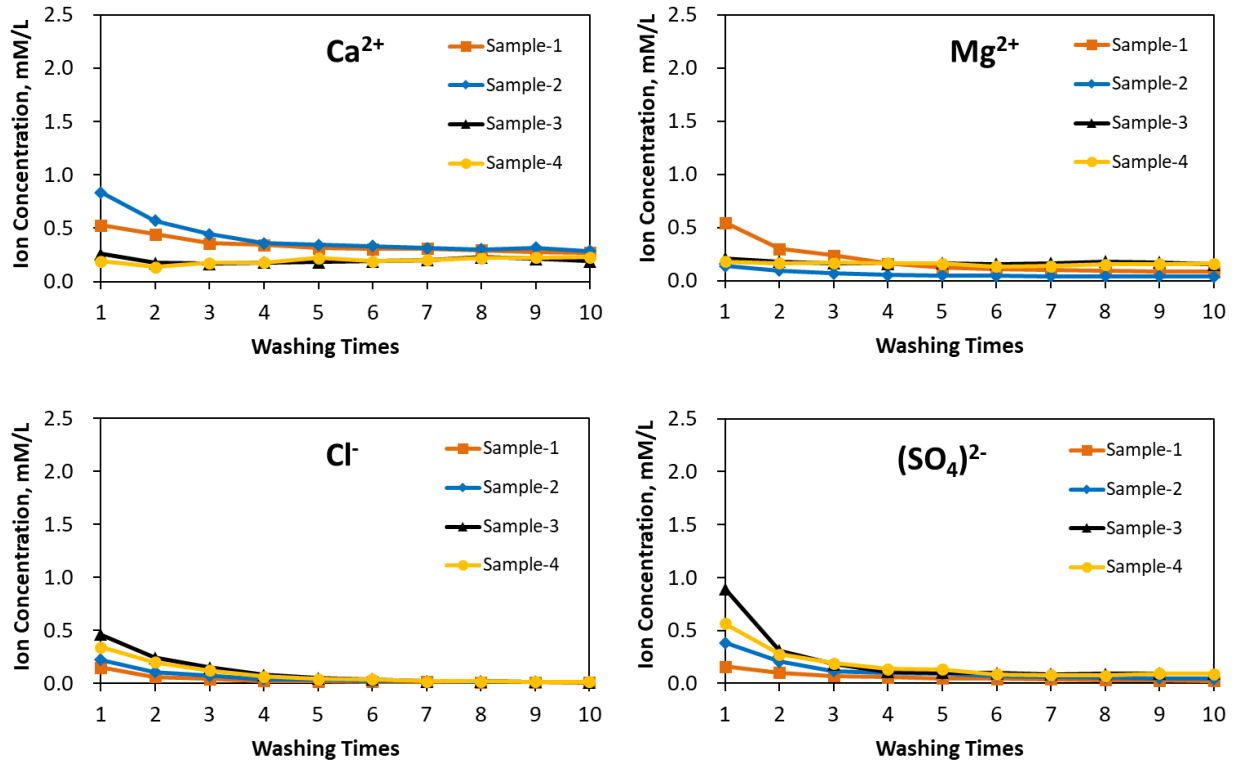


Figure C-2. Individual ion concentration of the salt solutions obtained after washing of HRB shale powders with DI water as a function of number of washing stages.

Appendix D: Oven Heating Process

In the oven heating process, the high temperature may break hydrogen bonding between water and clay, resulting in clay dehydration and further induce permanent deformations of clay structure (Bray et al., 1998). At the beginning of oven heating process, shale samples are heated at 50 °C until no mass change (~ 24 hours). Then, the temperature is increased by 10 °C for every 24 hours, until reaching 100 °C. The weight of sample is measured after every 24 hours of oven heating process. Figure D-1 shows the weight loss of samples at different heating temperatures. The weight loss is negligible when increasing the temperature from 90 °C to 100 °C. To avoid the effects of clay dehydration on shale expansion during water imbibition, the shale samples are not heated at the temperature higher than 100 °C. Figure D-2 shows the weight change of samples heated at 100°C versus time. The weight of samples does not change after 24 hours of oven heating.

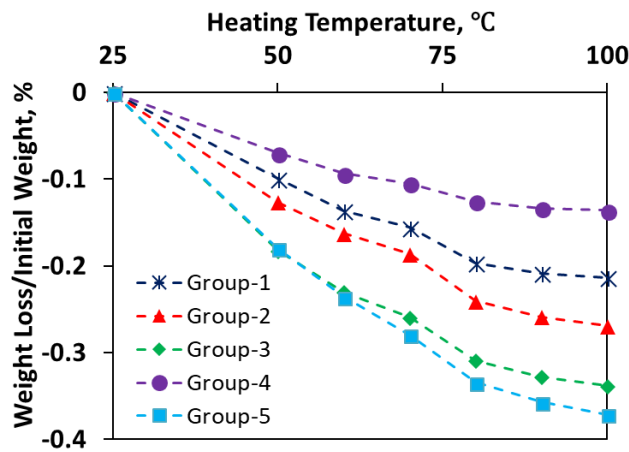


Figure D-1. Normalized weight loss of shale samples at different temperatures. The weight-loss is normalized by dividing by the initial weight of dry sample.

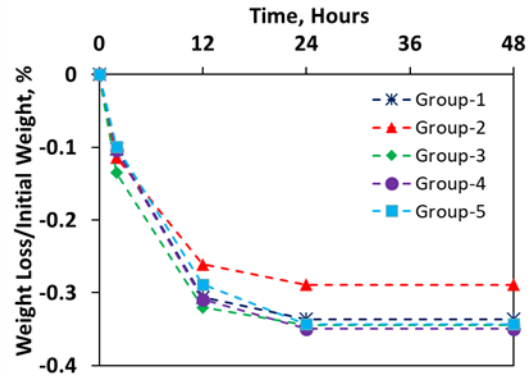


Figure D-2. Normalized weight loss of shale samples heated at 100°C. The measured weight does not change after 24 hours.

Appendix E: Effect of Heterogeneity on Expansion Behavior

To evaluate the variation in measured stress and strain values of the samples from the same group due to the heterogeneity. Ten HR shale samples are selected from the depth of 2694 in Evie member. All the samples are cut into the similar size ($52.0 \pm 3.0 \text{ cm}^2$ cross-sectional area and $3.8 \pm 0.5 \text{ cm}$ length). ϵ_y is measured on five samples and σ is measured on the other five samples during water imbibition. Experimental set-ups for Set 2 and Set 3 are used for ϵ_y and σ measurement. Figure E-1 shows the values of ϵ_y and σ measured during water imbibition into shale samples selected from similar depth. As shown in Figures. E-1a and E-1b, the maximum differences in measured values of ϵ_y and σ are 0.10% and 7.01-psi, respectively, with the standard deviations of 0.03% and 2.07 psi, respectively.

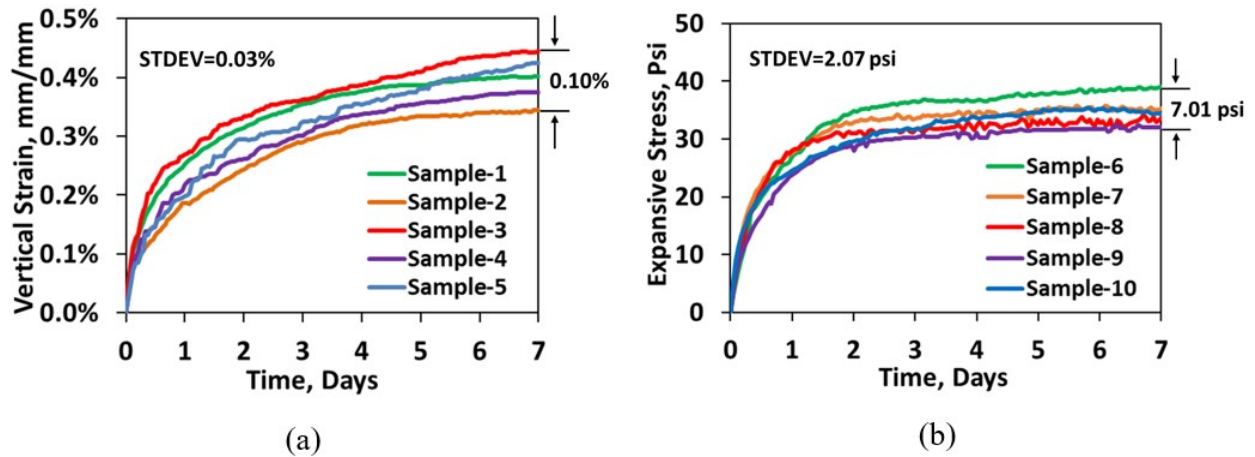


Figure E-1. (a) ϵ_y and (b) σ of ten shale samples from HR Formation during water imbibition process. The maximum differences and standard deviations in measured values of ϵ_y and σ are 0.10% and 7.01 psi and 0.03% and 2.07 psi respectively.

Appendix F: Mechanisms of Clay Swelling

Among the clay minerals found in shales, smectite and illite/smectite mixed layers are particularly prone to swelling. These clays have a layered structure, where each aluminosilicate layer is composed of an octahedral sheet placed in between two tetrahedral sheets (Quirk and Aylmore, 1971; Brigatti et al., 2006; Nichols, 2009).

Figure F-1 shows the structure of smectite before and after hydration. Cations are found in the interlayer spacing, weakly bound to the negatively charged layers permitting water molecules to enter this spacing with relative ease (Brigatti et al., 2006). The interlayer bonding is due to the cations balancing the charge deficiencies and van der Waals forces (van Olphen, 1977). Subsequently, water molecules adsorb into the interlayer spacing due to 1) hydrogen bonds between water molecules and silicate sheets (Tambach et al., 2006), 2) electrostatic attraction between polar water molecules and available interlayer cations (i.e. K^+ , Na^+ , Mg^{2+} , Ca^{2+} , etc.) and 3) osmosis potential due to higher cation concentration in interlayer spacing and lower cation concentration in the injected water (Lagaly, 2011). By this process, each cation in the interlayer spacing becomes surrounded by water molecules.

Addition of water molecules significantly increases the interlayer spacing in the structure of clay minerals. For example, the crystal radii of a Na^+ monolayer increases by 200% when Na^+ get hydrated (from 0.1 nm to 0.3 nm) (Tansel et al., 2006). Similarly, hydration-induced volumetric strain of a Na^+ -smectite and Ca^{2+} -smectite specimen can be up to 57.9% and 102.0%, respectively (Likos and Lu, 2006). The expansion of interlayer spacing is responsible for swelling of clays and shales commonly observed in laboratory experiments and in reservoirs. Other swelling mechanisms include crystalline swelling (Marcelja and Quirk, 1992; Norrish, 1954; Kittrick, 1969), double-layer swelling (McBride and Baveye, 2002), co-volume swelling and Brownian swelling (Laird, 2006).

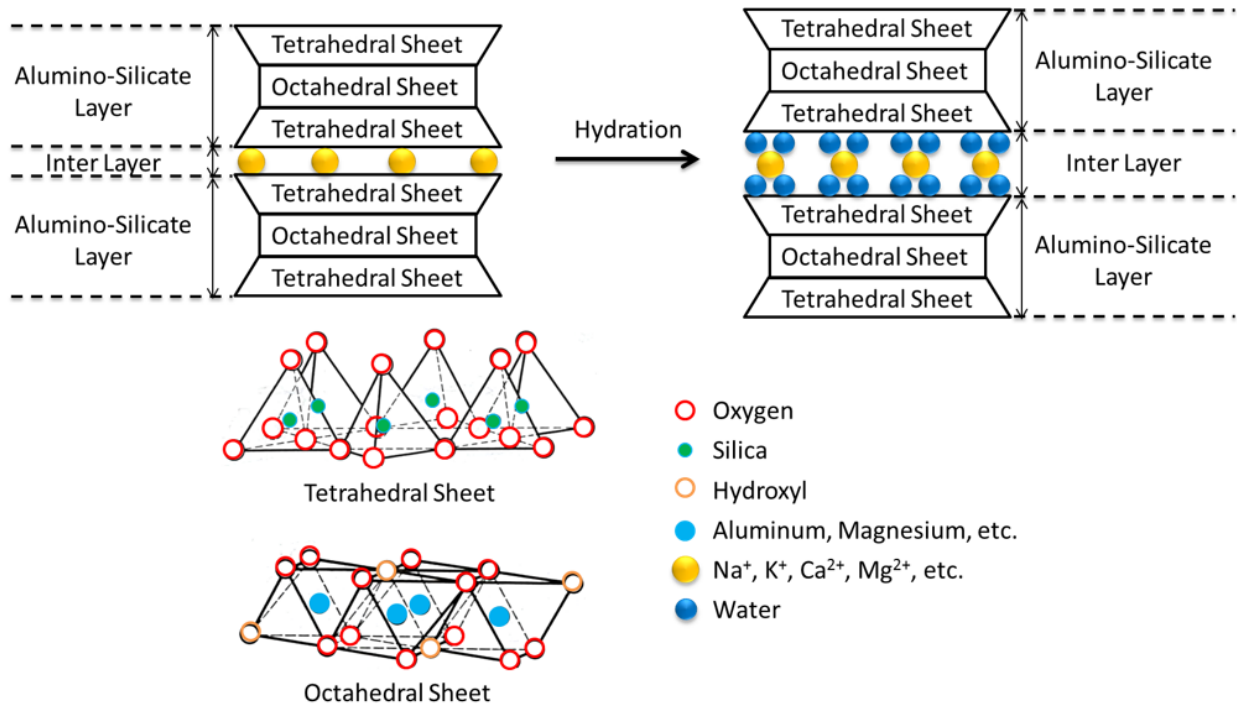


Figure F-1. Structure of smectite clay before and after hydration. Water molecules bind to the cations in interlayer spaces, resulting in clay swelling. (b) Structure of tetrahedral and octahedral sheets. Modified from Holtz and Kovacs (1981) and Mitchell, J.K. (1993).